이학박사 학위논문

Black Hole Masses, Scaling Relations, and The Co-Evolution of Black Holes and Galaxies

블랙홀 질량, 척도 관계, 블랙홀과 은하의 공동 진화

2013년 8월

서울대학교 대학원

물리·천문학부 천문학 전공

박 대 성

Black Hole Masses, Scaling Relations, and The Co-Evolution of Black Holes and Galaxies

by

Daeseong Park

A dissertation submitted in partial fulfillment of the requirements for the degree of

Doctor of Philosophy

in

Astronomy

in

Astronomy Program, Department of Physics and Astronomy
Seoul National University

Committee:

Professor	Hyung Mok Lee, Chair
Professor	Jong-Hak Woo, Advisor
Professor	Myungshin Im
Professor	Woong-Tae Kim
Professor	Aeree Chung

dedicated to my parents

진실로 성실하고 정직한 삶이 무엇인지 평생 당신들의 삶을 통해 몸소 보여 주고 계시는
사랑하는 어머니 아버지께

ABSTRACT

To better understand the cosmic growth of supermassive black hole (BH) population and the co-evolution with their host galaxies, we first perform three studies for improving determination of AGN BH masses, i.e., 1) investigating the uncertainties of Hβ single-epoch (SE) virial BH mass estimates, 2) constraining the virial factor of the BH mass estimators, and 3) improving the calibration of the C IV SE virial BH mass estimators for high-redshift AGNs. Then we present a study for direct observational constraints on the redshift evolution of the black hole mass – bulge luminosity relation.

We investigate the calibration and uncertainties of the black hole mass estimates based on the single-epoch method, using homogeneous and high-quality 428 multi-epoch spectra obtained by the Lick AGN Monitoring Project 2008 for 9 local Seyfert 1 galaxies with black hole masses $< 10^8$ $M_\odot$. By decomposing the spectra into their AGN and stellar components, we study the variability of the single-epoch Hβ line width (full width at half-maximum intensity, $\mathrm{FWHM_{H\beta}}$; or dispersion, $\sigma_{\mathrm{H}\beta}$) and of the AGN continuum luminosity at 5100 Å (L_{5100}). From the distribution of the "virial products" ($\propto \mathrm{FWHM_{H\beta}}^2\ L_{5100}^{0.5}$ or $\sigma_{\mathrm{H}\beta}{}^2\ L_{5100}^{0.5}$) measured from SE spectra, we estimate the uncertainty due to the combined variability as ~ 0.05 dex (12%). This is subdominant with respect to the total uncertainty in SE mass estimates, which is dominated by uncertainties in the size-luminosity relation and virial coefficient, and is estimated to be ~ 0.46 dex (factor of ~ 3). By comparing the Hβ line profile of the SE, mean, and root-mean-square (rms) spectra, we find that the Hβ line is broader in the mean (and SE) spectra than in the rms spectra by ~ 0.1 dex (25%) for our sample with $\mathrm{FWHM_{H\beta}} < 3000$ km s^{-1}. This result is at variance with larger mass black holes where the difference is typically found to be much less than 0.1 dex. To correct for this systematic difference of the Hβ line profile, we introduce a line-width dependent virial factor, resulting in a recalibration of SE black hole mass estimators for low-mass AGNs.

Determining the virial factor of the broad-line region gas is crucial for calibrating AGN black hole mass estimators, since the measured line-of-sight velocity needs to be converted into the intrinsic virial velocity. The average virial factor has been empirically calibrated based on the $M_{\mathrm{BH}}-\sigma_*$ relation of quiescent galaxies, but the claimed values differ by a factor of two in recent studies. We investigate the origin of the difference by measuring the $M_{\mathrm{BH}}-\sigma_*$ relation using an updated galaxy sample from the literature, and explore the dependence of the virial factor on various fitting methods. We find that the discrepancy is primarily

caused by the sample selection, while the difference stemming from the various regression methods is marginal. However, we generally prefer the `FITEXY` and `Bayesian` estimators based on Monte Carlo simulations for the $M_{\rm BH}-\sigma_*$ relation. In addition, the choice of independent variable in the regression leads to ~ 0.2 dex variation in the virial factor inferred from the calibration process. Based on the determined virial factor, we present the updated $M_{\rm BH}-\sigma_*$ relation of local active galaxies.

We present the single-epoch black hole mass estimators based on the C IV λ1549 broad emission line, using the updated sample of the reverberation-mapped AGNs and high-quality UV spectra. By performing multi-component spectral fitting analysis, we measure the C IV line widths (FWHM$_{\rm CIV}$ and line dispersion, $\sigma_{\rm CIV}$) and the continuum luminosity at 1350 Å (L_{1350}) to calibrate the C IV-based mass estimators. By comparing with the Hβ reverberation-based masses, we provide new mass estimators with the best-fit relationships, i.e., $M_{\rm BH} \propto L_{1350}^{0.50\pm0.07}\sigma_{\rm CIV}^2$ and $M_{\rm BH} \propto L_{1350}^{0.52\pm0.09}{\rm FWHM}_{\rm CIV}^{0.56\pm0.48}$. The new C IV-based mass estimators show significant mass-dependent systematic difference compared to the estimators commonly used in the literature. Using the published Sloan Digital Sky Survey QSO catalog, we show that the black hole mass of high-redshift QSOs decreases on average by ~ 0.25 dex if our recipe is adopted.

We investigate the cosmic evolution of the black hole mass – bulge luminosity relation with a sample of 52 moderate luminosity galaxies at $z \sim 0.36$ and $z \sim 0.57$, corresponding look-back times of 4 and 6 Gyrs. By employing multicomponent spectral and structural decomposition methods to the high-quality Keck spectra and high-resolution *HST* images, black hole masses ($M_{\rm BH}$) are estimated using the Hβ broad emission line with the 5100Å nuclear luminosity, and bulge luminosities ($L_{\rm bul}$) are derived from the surface photometry. Taking into account selection effects, we obtain the evolution trend of the form $M_{\rm BH}/L_{\rm bul} \propto (1+z)^{1.9\pm0.7}$, which is consistent with previous studies based on the bulge luminosity, as well as on the bulge mass and stellar velocity dispersion. This result indicates that black holes in the non-local universe live in smaller bulges than today, thus implying that black holes grow first and then the host galaxies follow up in the context of the co-evolution of black holes and galaxies.

Keywords: black hole physics – galaxies: active – galaxies: nuclei – methods: statistical

Student Number: 2005-20522

Contents

List of Figures

List of Tables

Chapter 1

Introduction

For more than a decade, it has been thought that supermassive black holes (BHs) are ubiquitous at the centers of almost all bulge dominated galaxies from many dynamical evidences of the spatially resolved kinematics (Kormendy & Richstone 1995; Richstone et al. 1998). Understanding the cosmic growth of the supermassive BHs and the co-evolution with their host galaxies is now one of the major challenges in extragalactic astronomy (see reviews by Ferrarese & Ford 2005 and Kormendy & Ho 2013).

The observational discoveries of the tight local BH-galaxy correlations such as $M_{\rm BH}-\sigma_*$, $M_{\rm BH}-L_{\rm bul}$, and $M_{\rm BH}-M_{\rm bul}$ relations (e.g., Magorrian et al. 1998; Ferraresse & Merritt 2000; Gebhardt et al. 2000; Tremaine et al. 2002; Marconi & Hunt 2003; Häring & Rix 2004; see also Figure 1.1 for the recent versions of the relations) have brought a paradigm shift on galaxy formation and evolution theory by introducing the framework of a co-evol growth between black holes and galaxies. These close connections are indeed surprising given the huge difference in scales between BH and galaxy (8 orders of magnitude in size) and have been motivated numerous studies to investigate the fundamental questions about the physical origin and cosmic evolution.

Although the AGN feedback mechanism (e.g., Volonteri et al. 2003; Di Matteo et al. 2005; Croton et al. 2006; Hopkins et al. 2009) and random merging events in hierarchical assembly (e.g., Peng 2007; Hirschmann et al. 2010; Jahnke & Macciò 2011) from the theoretical approaches have been suggested for the origin of this coupling, the exact cause is still unclear due to many ad hoc prescriptions and approximations involved to deal with daunting and complex physical processes in huge ranges of scales. Taking into account the BHs and AGNs as fundamental ingredients, Hopkins et al. (2006) schematized an overall picture

for the model of galaxy formation and evolution connected to the self-regulated growth of black holes in mergers (see Figure 1.2). However, since the details of the model are not fully established yet, it should be more developed by confronting with observations. In this regard, observational approaches can give direct constraints on how black holes and galaxies co-evolve, by investigating the BH-galaxy scaling relations over the cosmic time. These empirical constraints can provide essential inputs on which physical mechanisms are more important and what physical phenomena should be reproduced in theoretical modelings for the co-evolution of BH and galaxies.

In past years, several observational studies have attempted to quantify the cosmic evolution of the scaling relations either by using global constraints on the BH mass density as a function of redshift from the galaxy distribution functions and AGN luminosity function (e.g., Shankar et al. 2009; Zhang et al. 2012) or by directly measuring BH masses and their host properties such as masses, luminosities, and stellar velocity dispersions for samples of objects at high-redshift (e.g., Treu et al. 2004, 2007; Walter et al. 2004; McLure et al. 2006; Peng et al. 2006; Woo et al. 2006, 2008; Jahnke et al. 2009; Decarli et al. 2010; Merloni et al. 2010; Bennert et al. 2010, 2011; Wang et al. 2010; Cisternas et al. 2011; Targett et al. 2012; Hiner et al. 2012; Canalizo et al. 2012; Schramm & Silverman 2013; see Figure 1.3 for the recent compilation of the samples available from literature). While the global constraining favors a mile or no positive evolution and some studies based on the σ_* measurement from the [O III] line as a proxy (e.g., Shields et al. 2003 and Gaskell 2009) find no evolution, a majority of the direct measurements claims that the black hole growth seems to precede the bulge growth with a exception for the high-z submillimeter-emitting galaxies (e.g., Borys et al. 2005; Alexander et al. 2008; Coppin et al. 2008; Carrera et al. 2011; see also Lamastra et al. 2010).

However, these direct observational results are still not only subject to large uncertainties in black hole mass estimates, but also affected by several selection biases as well as a small number and limited dynamic ranges of the sample (e.g., Lauer et al. 2007; Shen & Kelly 2010; Schulze & Wisotzki 2011; Salviander & Shields 2013). Given the uncertain and tentative understanding for the BH-galaxy co-evolution, it is essential to give more accurate and direct empirical constraints on the black hole growth and galaxy evolution from the distant universe by taking advantages of high-quality datasets obtained from the advanced observational facilities for the well defined sample with a large number and wider dynamic ranges, as well as by using the more sophisticated statistical techniques to account for systematic uncertainties and selection effects.

The first crucial step is measuring BH masses accurately at all redshifts. It is of fundamental importance to investigate the evolution of the scaling relations by probing the BH population over cosmic time. Beyond the local universe, however, BH masses can be obtained only via an observation of the broad-line (Type 1) AGNs, which are powered by mass accretion onto black holes, since a dynamical measurement method is limited to the very local universe ($\lesssim$ 150 Mpc; $z \simeq 0.04$) due to the required high spatial resolution for resolving the BH sphere-of-influence. Rooted in the results from the reverberation mapping (RM; Peterson 1993) method applied to a limited sample of AGNs ($\lesssim$ 50, to date), the virial black hole mass estimates using the single-epoch (SE) spectra (i.e., the so-called SE method; Wandel et al. 1999) have been widely used and become a standard practice for BH mass measurements in AGNs by its practicality and efficiency. However, estimating BH masses using AGN single spectra is subject to various systematic uncertainties (see recent review by Shen 2013 and references therein), thus it is still requiring a refinement of the method and better understanding of the systematic biases and uncertainties.

Sources of uncertainties in SE virial BH mass estimates include (1) the virial factor f, which is related to the unknown geometry and kinematics of the broad-line region and constitutes the major portion of the overall uncertainty (Woo et al. 2010), (2) the intrinsic scatter in the empirical size-luminosity relation (Bentz et al. 2009), (3) the intrinsic variability of AGNs, which makes the line width and luminosity variable as a function of time, thus leading to varying mass measurements for the different epochs (Denney et al. 2009), (4) systematic differences between the broad-line profile measured from SE spectra and those measured from root-mean-square (rms) spectra which represent only the varying part of the line profile (Collin et al. 2006), and (5) the limited size and inhomogeneity in the current RM AGN sample as a calibration standard. Thus it is required to understand, quantify, and possibly correct for the random and systematic uncertainties listed above to improve the precision and accuracy of BH mass estimations in AGNs. In addition, in high-z universe, the C IV line is usually adopted for BH mass estimation since it can be observed in optical spectra for AGNs at $2 \lesssim z \lesssim 5$. Achieving correct and accurate calibrations for C IV based $M_{\rm BH}$ estimators are crucial for studying high-z AGNs, thus for the scaling relationships.

In Chapter 2, taking advances of the homogeneous and high-quality reverberation-mapping data for 9 local Seyfert 1 galaxies, which are extending the previous RM sample to relatively unexplored regime of low-mass BHs ($10^{6-7} M_{\odot}$), we investigate the random uncertainty in mass estimates due to the AGN variability, the systematic uncertainty from differences in emission line profiles, and the calibration of the SE BH mass estimators for

low-mass AGNs. For the uniform and consistent analysis of these multi-epoch data, we develop the multi-component spectral decomposition method, which consists of a power-law function, a Fe II template, and host galaxy templates for the model of the continuum and absorption features and Gaussian and Gauss-Hermite series functions for the model of the Hβ, [O III], and He II emission line features. We present a test of the virial assumption of the SE BH mass estimation and discuss an overall uncertainties in SE BH mass estimates.

In Chapter 3, we revisit the empirical calibration of the virial factor for the better determination and to constrain the uncertainties. For this purpose, we employ the three $M_{\rm BH}-\sigma_*$ data sets recently complied in literature to investigate differences from the samples and the four different methods for linear regression analysis to check possible biases from the fitting techniques. We discuss a difference in the derived virial factors for the adopted direction of regression and present the $M_{\rm BH}-\sigma_*$ relation for local active galaxies based on the updated virial factor using the preferred regression method with the most recent data.

In Chapter 4, we improve the calibration of C IV SE BH mass estimators using the highest quality UV spectra (mostly from *HST*) and the most updated local RM AGN sample. We use the multi-component fitting method for consistent measurements and perform calibrations by adopting the proper regression approach to minimize systematic uncertainties in C IV-based BH mass estimates. We discuss a systematic difference in the derived BH masses based on our new estimators to those from literature.

Equipped with techniques and understanding for the BH mass measurements in AGNs, as well as that the bulge luminosity can be estimated within a reasonable accuracy (~ 0.2 dex) for AGN host galaxies with the high-resolution *HST* images (Treu et al. 2007; Kim et al. 2008a,b), we can directly investigate the cosmic evolution of the scaling relations with samples of active galaxies as a function of redshift to give better observational constraints on the BH growth and galaxy evolution. In Chapter 5, We directly measure the BH masses and bulge luminosities by performing spectroscopic decomposition analysis on the high-quality Keck spectra and photometric decomposition analysis on the high-resolution *HST* images for a sample of 52 Seyfert galaxies at $z \simeq 0.36$ and 0.57. Based on the measurements, we constrain the redshift evolution of the $M_{\rm BH}-L_{\rm bul}$ relation by performing the Monte Carlo simulations to account for selection effects. We provide the implication of our results in terms of the BH-galaxy co-evolution and discuss the possible bulge growth mechanisms.

In this context, this thesis is dedicated to improve the BH mass estimates using AGNs by understanding their uncertainties and updating the calibrations and to give more accurate observational constraints on a co-evol growth of the BH and galaxy over cosmic time.

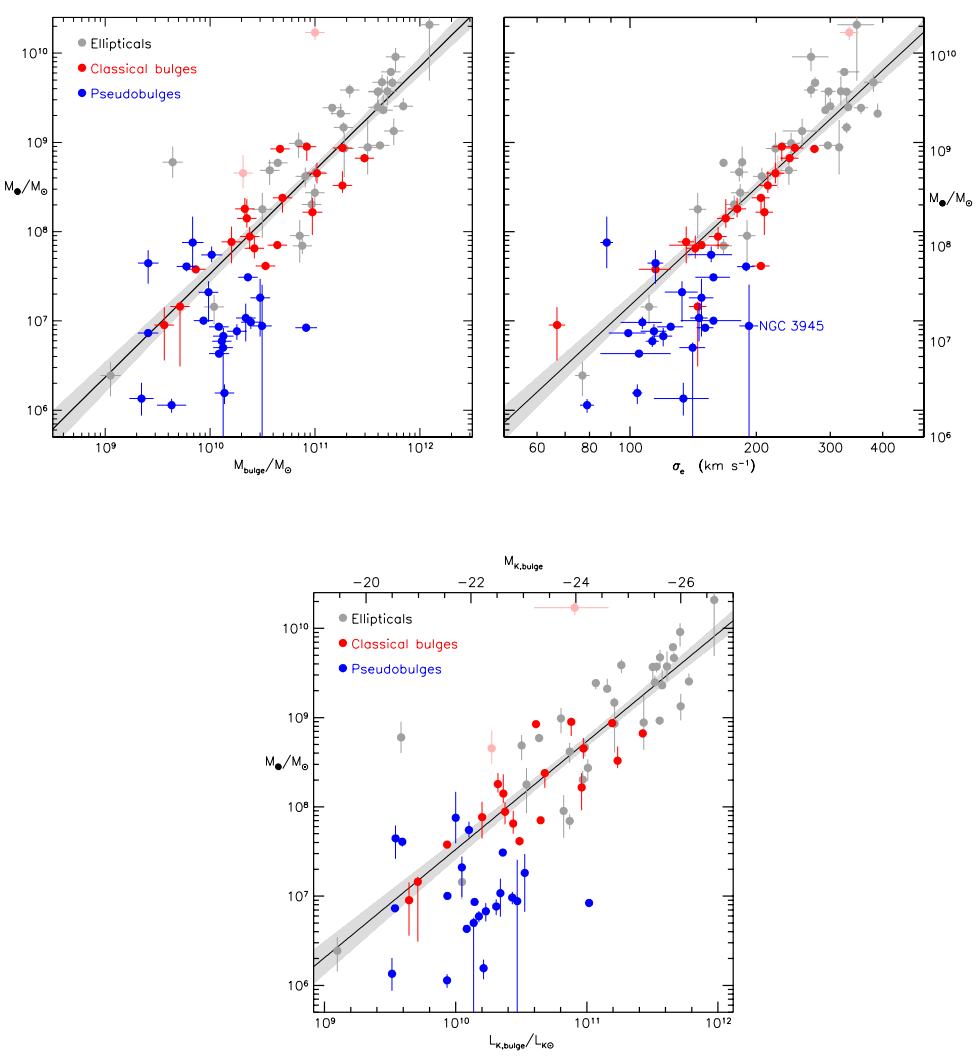

Figure 1.1 (From Kormendy & Ho 2013). The most recent versions of the local quiescent BH-bulge correlations. The best-fit relation for ellipticals and classical bulges is plotted with a solid black line in each panel with gray shade for 1σ error. The BHs in pseudobulges seem to be offset under the best-fit relation in all panels.

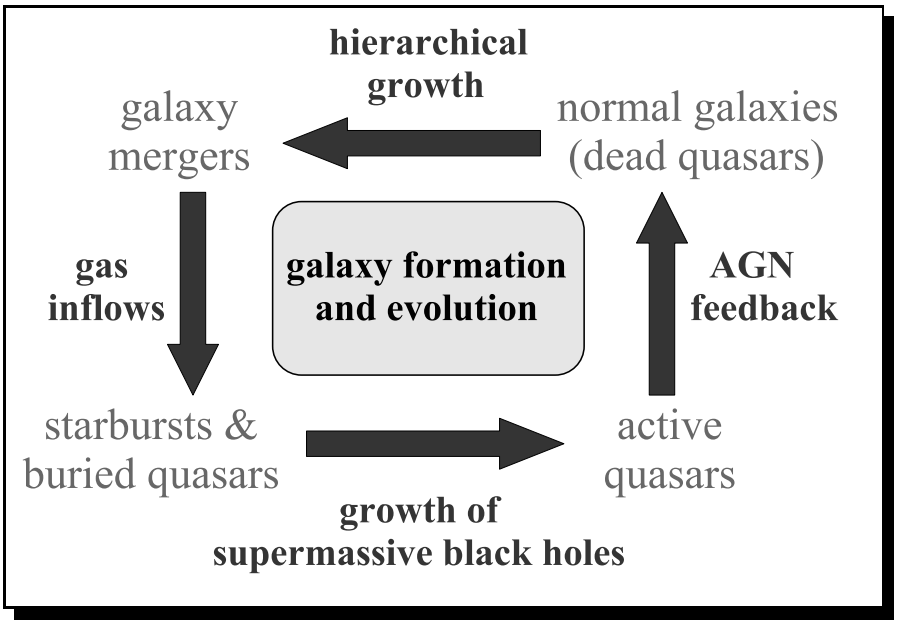

Figure 1.2 (From Hopkins et al. 2006). A schematic picture for galaxy formation and evolution regulated from the interplay of galaxy merging and AGN feedback. In this picture, AGNs (i.e., accreting BHs) comprise integral phase in galaxy evolution by the feeding and feedback processes.

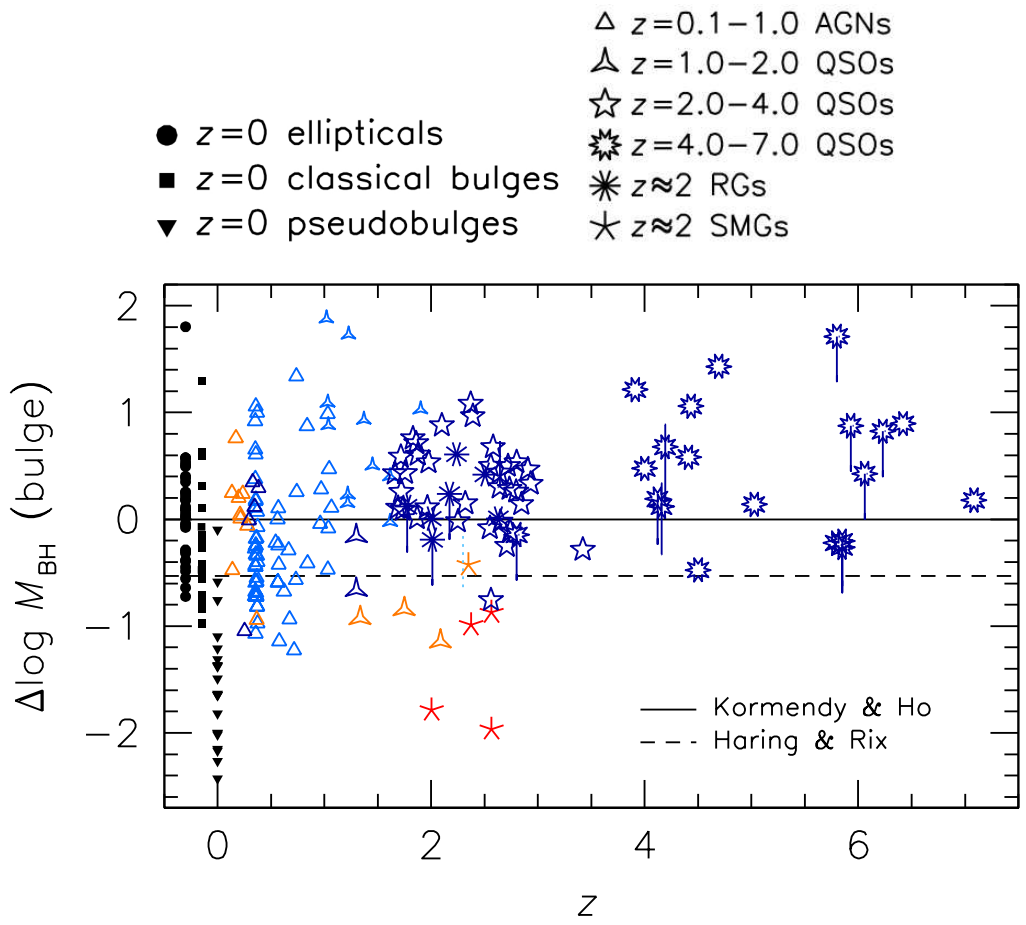

Figure 1.3 (From Kormendy & Ho 2013). Redshift distribution of the offsets in $\log M_{\rm BH}$ for AGNs at $z \simeq 0.1-7.1$ available from literature with respect to the local $M_{\rm BH}-M_{\rm bul}$ relations from Häring & Rix (2004) and Kormendy & Ho (2013). Black filled symbols, which are slightly offset from $z = 0$ for clarity, indicate the local inactive samples. Although there is a significant scatter, it shows on average the positive evolutionary trend except for a sample of submm galaxies (SMGs).

References

Alexander, D. M., Brandt, W. N., Smail, I., et al. 2008, AJ, 135, 1968

Bennert, V. N., Treu, T., Woo, J.-H., et al. 2010, ApJ, 708, 1507

Bennert, V. N., Auger, M. W., Treu, T., Woo, J.-H., & Malkan, M. A. 2011, ApJ, 742, 107

Bentz, M. C., Peterson, B. M., Netzer, H., Pogge, R. W., & Vestergaard, M. 2009, ApJ, 697, 160

Borys, C., Smail, I., Chapman, S. C., et al. 2005, ApJ, 635, 853

Canalizo, G., Wold, M., Hiner, K. D., et al. 2012, ApJ, 760, 38

Carrera, F. J., Page, M. J., Stevens, J. A., et al. 2011, MNRAS, 413, 2791

Cisternas, M., Jahnke, K., Bongiorno, A., et al. 2011, ApJ, 741, L11

Collin, S., Kawaguchi, T., Peterson, B. M., & Vestergaard, M. 2006, A&A, 456, 75

Coppin, K. E. K., Swinbank, A. M., Neri, R., et al. 2008, MNRAS, 389, 45

Croton, D. J., Springel, V., White, S. D. M., et al. 2006, MNRAS, 365, 11

Decarli, R., Falomo, R., Treves, A., et al. 2010, MNRAS, 402, 2453

Denney, K. D., Peterson, B. M., Dietrich, M., Vestergaard, M., & Bentz, M. C. 2009, ApJ, 692, 246

Di Matteo, T., Springel, V., & Hernquist, L. 2005, Nature, 433, 604

Ferrarese, L., & Ford, H. 2005, Space Sci. Rev., 116, 523

Ferrarese, L., & Merritt, D. 2000, ApJ, 539, L9

Gaskell, C. M. 2009, arXiv:0908.0328

Gebhardt, K., Bender, R., Bower, G., et al. 2000, ApJ, 539, L13

Häring, N., & Rix, H.-W. 2004, ApJ, 604, L89

Hiner, K. D., Canalizo, G., Wold, M., Brotherton, M. S., & Cales, S. L. 2012, ApJ, 756, 162

Hirschmann, M., Khochfar, S., Burkert, A., et al. 2010, MNRAS, 407, 1016

Hopkins, P. F., Hernquist, L., Cox, T. J., et al. 2006, ApJS, 163, 1

Hopkins, P. F., Murray, N., & Thompson, T. A. 2009, MNRAS, 398, 303

Jahnke, K., Bongiorno, A., Brusa, M., et al. 2009, ApJ, 706, L215

Jahnke, K., & Macciò, A. V. 2011, ApJ, 734, 92

Kim, M., Ho, L. C., Peng, C. Y., et al. 2008a, ApJ, 687, 767

Kim, M., Ho, L. C., Peng, C. Y., Barth, A. J., & Im, M. 2008b, ApJS, 179, 283

Kormendy, J., & Ho, L. C. 2013, arXiv:1304.7762

Kormendy, J., & Richstone, D. 1995, ARA&A, 33, 581

Lauer, T. R., Tremaine, S., Richstone, D., & Faber, S. M. 2007, ApJ, 670, 249

Magorrian, J., Tremaine, S., Richstone, D., et al. 1998, AJ, 115, 2285

Marconi, A., & Hunt, L. K. 2003, ApJ, 589, L21

McLure, R. J., Jarvis, M. J., Targett, T. A., Dunlop, J. S., & Best, P. N. 2006, MNRAS, 368, 1395

Merloni, A., Bongiorno, A., Bolzonella, M., et al. 2010, ApJ, 708, 137

Peng, C. Y., Impey, C. D., Rix, H.-W., et al. 2006, ApJ, 649, 616

Peng, C. Y. 2007, ApJ, 671, 1098

Peterson, B. M. 1993, PASP, 105, 247

Richstone, D., Ajhar, E. A., Bender, R., et al. 1998, Nature, 395, A14

Salviander, S., & Shields, G. A. 2013, ApJ, 764, 80

Schramm, M., & Silverman, J. D. 2013, ApJ, 767, 13

Shankar, F., Bernardi, M., & Haiman, Z. 2009, ApJ, 694, 867

Shen, Y., & Kelly, B. C. 2010, ApJ, 713, 41

Shen, Y. 2013, Bulletin of the Astronomical Society of India, 41, 61

Shields, G. A., Gebhardt, K., Salviander, S., et al. 2003, ApJ, 583, 124

Schulze, A., & Wisotzki, L. 2011, A&A, 535, A87

Targett, T. A., Dunlop, J. S., & McLure, R. J. 2012, MNRAS, 420, 3621

Tremaine, S., Gebhardt, K., Bender, R., et al. 2002, ApJ, 574, 740

Treu, T., Malkan, M. A., & Blandford, R. D. 2004, ApJ, 615, L97

Treu, T., Woo, J.-H., Malkan, M. A., & Blandford, R. D. 2007, ApJ, 667, 117

Volonteri, M., Haardt, F., & Madau, P. 2003, ApJ, 582, 559

Walter, F., Carilli, C., Bertoldi, F., et al. 2004, ApJ, 615, L17

Wandel, A., Peterson, B. M., & Malkan, M. A. 1999, ApJ, 526, 579

Wang, R., Carilli, C. L., Neri, R., et al. 2010, ApJ, 714, 699

Woo, J.-H., Treu, T., Malkan, M. A., & Blandford, R. D. 2006, ApJ, 645, 900

Woo, J.-H., Treu, T., Malkan, M. A., & Blandford, R. D. 2008, ApJ, 681, 925

Woo, J.-H., Treu, T., Barth, A. J., et al. 2010, ApJ, 716, 269

Zhang, X., Lu, Y., & Yu, Q. 2012, ApJ, 761, 5

Chapter 2

The Lick AGN Monitoring Project: Recalibrating Single-Epoch Virial Black Hole Mass Estimates

(This chapter is published in The Astrophysical Journal[1]*.)*

2.1 Introduction

Supermassive black holes (BHs) are believed to play a key role in galaxy evolution. Evidence for this connection comes from the tight correlations observed in the local universe between BH masses and the global properties of their host galaxies (Magorrian et al. 1998; Ferrarese & Merritt 2000; Gebhardt et al. 2000; Gültekin et al. 2009; Bentz et al. 2009a; Woo et al. 2010). Establishing the cosmic evolution of these correlations is a powerful way to understand the feedback mechanisms connecting BHs and galaxies (e.g., Kauffmann & Haehnelt 2000; Robertson et al. 2006; Hopkins et al. 2006). Recent observational studies have found that these correlations may evolve over cosmic time, in the sense that BHs of a given mass appeared to live in smaller galaxies in the past (e.g., Woo et al. 2006; Peng et al. 2006; Treu et al. 2007; Woo et al. 2008; Merloni et al. 2010; Decarli et al. 2010; Bennert et al. 2010).

In order to investigate the nature of BH-galaxy coevolution, as well as virtually all

[1] Park et al. 2012, ApJ, 747, 30

aspects of active galactic nucleus (AGN) physics (e.g., Woo & Urry 2002; Kollmeier et al. 2006; Davis et al. 2007), BH masses must be accurately determined at large distances. Dynamical methods based on high angular resolution kinematics of stars and gas are the most common approach to measuring masses of quiescent BHs (e.g., Kormendy & Gebhardt 2001; Ferrarese & Ford 2005). However, owing to the parsec-size scale of the sphere of the influence of typical BHs, they are limited to galaxies within a distance of few tens of Mpc with current technology.

In the case of BHs powering an AGN, the presence of a variable broad-line region (BLR) provides an alternative way that is in principle applicable to much larger distances. The geometry and kinematics of the BLR gas can be mapped in the time domain using the so-called reverberation (or echo) mapping technique (Blandford & McKee 1982; Peterson 1993). In turn, these quantities can be converted into BH mass estimates under appropriate assumptions about the dynamics of the system (Peterson 1993; Pancoast, Brewer, & Treu 2011). Estimators of the form $M_{\rm BH} \propto R_{\rm BLR}\, V^2$, where $R_{\rm BLR}$ and V are (respectively) size and velocity estimators of the BLR, are often referred to as "virial" mass estimators. However, due to the observational challenges of reverberation mapping campaigns, fewer than 50 BH masses have been measured to date using this technique (Wandel, Peterson, & Malkan 1999; Kaspi et al. 2000; Peterson et al. 2004; Bentz et al. 2009c; Denney et al 2009; Barth et al. 2011).

In light of the scientific importance of determining BH masses, it is critical to develop alternative BH mass estimators that are observationally less demanding. A popular BH mass estimator, based on the results of reverberation mapping studies, is the so-called single-epoch (SE) method. It exploits the empirical correlation between the size of the BLR and the AGN continuum luminosity ($R_{\rm BLR} \propto L^{\alpha}$, with $\alpha \approx 0.5$), as expected from the photoionization model predictions (Wandel, Peterson, & Malkan 1999; Kaspi et al. 2000, 2005; Bentz et al. 2006, 2009b), to bypass the expense of a monitoring campaign. Thus, the AGN luminosity is used as a proxy for the BLR size and, in combination with the square of a velocity estimate from a broad line, to estimate BH masses from single spectroscopic observations. Typically, SE mass estimators are based on optical/ultraviolet lines (e.g., Hβ or Mg II) and optical/ultraviolet continuum luminosity (e.g., at 5100 Å or 3000 Å). A summary and cross-calibration of commonly adopted recipes is given by McGill et al. (2008).

Due to its convenience, the SE method has been widely applied from the study of BH demographics (e.g., Shen et al. 2008; Fine et al. 2008) to the characterization of galaxy-AGN scaling relations at low and high redshift (e.g., Treu et al. 2004; Barth et al. 2005;

Greene & Ho 2006; Woo et al. 2006; Bennert et al. 2010, Bennert et al. 2011a). For this reason it is of paramount importance to quantify, understand, and (possibly) correct for random and systematic uncertainties in the method. In addition to the random and systematic errors, selection bias can play a role in studying statistical properties of AGN samples selected from a flux-limited survey since BH mass from SE data is proportional to the AGN continuum luminosity at 5100Å (L_{5100}) (e.g., Lauer et al. 2007; Treu et al. 2007; Shen & Kelly 2010). Naturally, the strength of the selection bias depends on the uncertainty of the SE mass estimates, providing another compelling reason to quantify it accurately.

The largest uncertainty comes from the unknown "virial" factor f, connecting the observable size and velocity to the actual BH mass, $M_{\rm BH} \equiv f R_{\rm BLR}\, V^2/G$, where G is the gravitational constant. In general, f cannot be determined for individual sources due to limited spatial information except a few cases (Davies et al. 2006, Onken et al. 2007; Hicks & Malkan 2008; see, however, Brewer et al. 2011 and references therein). Therefore, an average virial factor is typically applied. This average is determined by forcing active and quiescent galaxies to obey the same BH mass-galaxy velocity dispersion ($M_{\rm BH}-\sigma_*$) relation (Onken et al. 2004; Woo et al. 2010), even though the virial factor of individual AGNs may be different from the mean value. Thus, using an average virial factor introduces an uncertainty in the SE mass estimates. It is not known precisely how large the uncertainty of the virial factor is (see Collin et al. 2006), and whether this uncertainty is stochastic (random) or has a systematic component that can be reduced using additional observables. An upper limit to the uncertainty is derived from the intrinsic scatter of the AGN $M_{\rm BH}-\sigma_*$ relation (0.43 dex; Woo et al. 2010), assuming that the samples used to calibrate f are representative of the class of broad-line AGNs targeted for the SE study.

A second source of uncertainty is the variability of AGNs: line width and continuum luminosity will vary as a function of time, while the BH mass is not expected to change significantly over time scales of order a few years. Thus, AGN variability introduces an uncertainty in the SE mass estimates, which is believed to be stochastic in nature. Previous studies based on multi-epoch spectra reported that the random error due to the variability is $\sim$15–25% (e.g., Woo et al. 2007; Denney et al. 2009).

A third source of error is the intrinsic scatter in the size-luminosity relation used to infer the size of the BLR. Recent studies, based on reverberation mapping results and *Hubble Space Telescope (HST)* imaging analysis, report $\sim$40% scatter in the size-luminosity relation (Bentz et al. 2009b).

A fourth source of uncertainty in SE mass estimates is due to differences in the BLR

line profile as measured from SE spectra and those measured from root-mean-square (rms) spectra. In reverberation mapping studies, BH mass determinations rely on the line width measured from the rms spectra, which reflect the varying part of the line profile. In contrast, for SE mass determinations line widths are measured from single spectra since such equivalent measurements as in the rms spectra are not available. Thus, it is necessary to investigate and quantify the line-width difference between SE and rms spectra. Previous studies based on multi-epoch data showed that the Hβ line widths in the mean spectra are broader than those in the rms spectra (e.g., Sergeev et al. 1999; Shapovalova et al. 2004; Collin et al. 2006; Denney et al. 2009). The difference is presumably due to the different kinematics of the gas responding over various time scales, indicating that a different normalization is required in order to consistently estimate virial masses based on the SE method.

In this work, we focus on the uncertainties of SE mass estimators due to the variability, and those due to differences in line profiles. By comparing measurements from single-epoch, mean, and rms spectra using the high-quality multi-epoch spectra of 9 local Seyfert galaxies in the relatively unexplored regime of low-mass BHs from the Lick AGN monitoring project (Bentz et al. 2009c), we provide new quantitative estimates for the uncertainties and recipes to correct for them. The chapter is organized as follows. In §2.2, we describe the observations and data reduction. Section 2.3 discusses the measurement method for SE spectra as well as for mean and rms spectra. In § 2.4, we present the main results including a test of the virial assumption, a quantification of the random errors due to AGN variability, and the systematic differences in line width between SE and rms spectra. We also present a recalibration of standard recipes that corrects for the systematic differences. We conclude and summarize our findings in § 2.5. Throughout the chapter we adopt the following cosmological parameters to calculate distances: $H_0 = 70$ km s^{-1} Mpc^{-1}, $\Omega_{\rm m} = 0.30$, and $\Omega_\Lambda = 0.70$.

2.2 Observations and Data Reduction

We use the homogeneous and high-quality multi-epoch spectra from the Lick AGN monitoring project (LAMP; Bentz et al. 2009c), which was designed to measure the reverberation time scales of 13 local Seyfert 1 galaxies. Here, we briefly summarize the observations and data reduction.

The LAMP campaign was carried out using the Kast spectrograph at the 3-m Shane telescope at the Lick Observatory in Spring 2008. Among 13 Seyfert 1 galaxies, we selected 9 objects for which the Hβ line variability was sufficiently large to measure the reverberation

time lag (Bentz et al. 2009c). During the LAMP campaign, each object was observed multiple times (43 to 51 epochs with an average of 47), enabling us to construct high-quality mean and r.m.s. spectra.

After performing standard spectroscopic reductions using IRAF[2], one-dimensional spectra were extracted with an aperture window of 13 pixels (10.″1). Flux calibrations utilized nightly spectra of spectrophotometric standard stars. As described by Bentz et al. (2009c), the spectral rescaling was performed using the algorithm of van Groningen & Wanders (1992) in order to mitigate the effects of slit loss, variable seeing, and transparency. By rescaling, shifting, and smoothing each spectrum, the algorithm minimizes the difference of flux of the [O III] lines between each spectrum and a reference spectrum created from the mean of individual spectra. The quality of each individual spectrum is sufficient to perform SE measurements (average signal-to-noise ratio S/N $\approx$ 66 per pixel at rest-frame 5100 Å).

2.3 Measurements

Two quantities, the line width and the continuum luminosity, are required to determine $M_{\rm BH}$ using single spectra. Uniform and consistent analysis is crucial for investigating systematic uncertainties and minimizing additional errors. In this section, we present the multi-component spectral fitting process and describe the measurements using single-epoch, mean, and rms spectra.

2.3.1 Multi-Component Fitting

To measure the line width of Hβ and the continuum luminosity at 5100 Å, we follow the procedure given by Woo et al. (2006) and McGill et al. (2008), but with significant modifications as described below (cf., McLure & Dunlop 2004; Dietrich et al. 2005; Denney et al. 2009). The multi-component fitting processes were carried out in a simultaneous and automated fashion, using the nonlinear Levenberg-Marquardt least-squares fitting routine `mpfit` (Markwardt 2009) in IDL.

First, all single spectra were converted to the rest frame. Second, we modelled the observed continuum with three components: the featureless AGN continuum, the Fe II emission blends, and the host-galaxy starlight, using respectively a single power-law continuum,

[2]IRAF is distributed by the National Optical Astronomy Observatories, which are operated by the Association of Universities for Research in Astronomy, Inc., under cooperative agreement with the National Science Foundation (NSF).

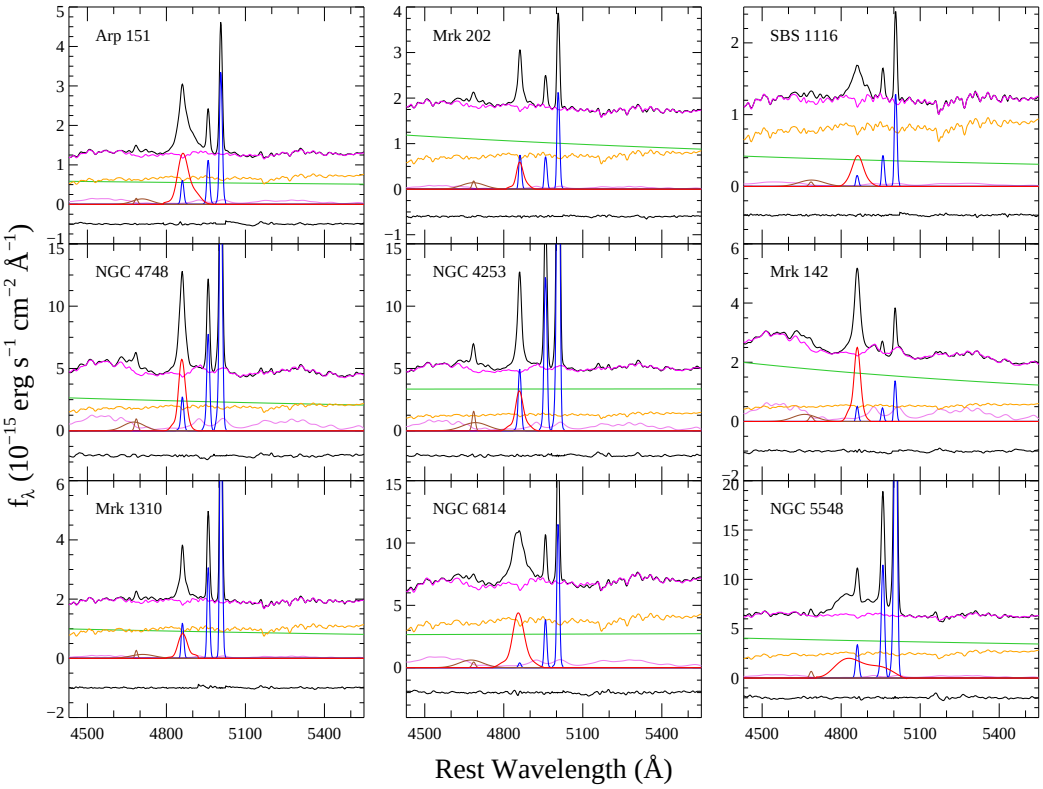

Figure 2.1 Multi-component spectral fitting in the mean spectra. The mean spectra of all 9 Seyfert galaxies are presented along with multi-component models. In each panel, observed spectra (black) and the continuum+Fe II+stellar best-fit model (magenta) are shown in the upper part, and the best-fit power-law continuum (green), stellar spectrum (yellow), and Fe II template (violet) models are presented in the middle part. Three narrow lines [Hβ, [O III] $\lambda\lambda$4959, 5007 (blue)], broad Hβ (red), and the broad and narrow He II λ4686 components (brown) are presented in the bottom part. The residuals (black), representing the difference between the observed spectra and the sum of all model components, are arbitrarily shifted downward for clarity.

Table 2.1. Hβ Integration Ranges, and Hβ narrow ratios

Object	$H\beta_{BC}$ Line Ranges (Å)	$f(H\beta_{NC})/f$([O III] λ5007)
Arp 151	4790–4980	0.18
NGC 4748	4790–4920	0.12
Mrk 1310	4800–4920	0.13
Mrk 202	4810–4920	0.35
NGC 4253 (Mrk 766)	4790–4930	0.13
NGC 6814	4760–4950	0.03
SBS 1116+583A	4795–4940	0.12
Mrk 142	4790–4910	0.37
NGC 5548	4705–5040	0.10

Note. — All values in the table are given in the rest frame.

an Fe II template from Boroson & Green (1992), and a host-galaxy template from Bruzual & Charlot (2003). A simple stellar population synthesis model with solar metallicity and age of 11 Gyr was found to reproduce the observed stellar lines reasonably well (see Figure 2.1). The Fe II emission blends and the host-galaxy template were convolved with appropriate Gaussian velocities to reproduce kinetic and instrumental broadening during the fitting process as described below. The best continuum models were determined based on the χ^2 statistic in the regions 4430–4600 Å and 5080–5550 Å where Fe II emission dominates. The three components were varied simultaneously with six free parameters: the normalization and the slope of the power-law continuum, the strength and the broadening velocity of the Fe II, and the line strength and the velocity dispersion of the host-galaxy templates. We masked out the typical weak AGN narrow emission lines (e.g., He I λ4471, [Fe VII] λ5160, [N I] λ5201 , [Ca V] λ5310; Vanden Berk et al. 2001) during the fitting process. The best-fit continuum models (the power-law component + the Fe II template + the host-galaxy template) were subtracted from each spectrum, leaving the broad and narrow AGN emission lines.

Third, we subtracted the narrow lines around the Hβ region before fitting the broad

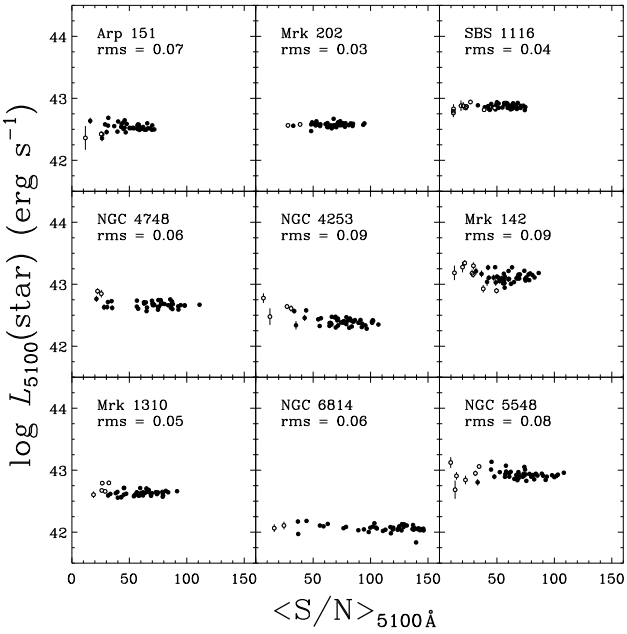

Figure 2.2 The host-galaxy luminosity at 5100 Å, measured from each SE spectrum based on the spectral decomposition analysis, as a function of S/N. A few low-S/N spectra (open circles) are removed from further analysis to avoid biases due to low-quality data. Measurement uncertainties estimated from the method given in §3.2.3 are expressed by vertical error bars.

component. We first made a template for the Hβ narrow-line profile by fitting a tenth-order Gauss-Hermite series (cf., van der Marel & Franx 1993) model to the [O III] λ5007 line. We then subtracted the [O III] λ4959 line by blueshifting and scaling the flux of the template by $1/3$. The Hβ narrow line was also subtracted by scaling the [O III] λ5007 line. The ratios of the narrow Hβ to [O III] λ5007 were determined from the χ^2 minimization in the mean spectra and then forced to be the same for all SE spectra of each object. Applied scaling ratios for the Hβ narrow component range from 0.03 to 0.37 (Table 2.1).

Lastly, we modelled the broad component of the Hβ line using a sixth-order Gauss-Hermite series. We also used a two-component Gaussian model to describe the broad and narrow components of the He II λ4686 emission line whenever it affected the blue wing of the Hβ profile. Figure 2.1 shows the fitting results for the mean spectra.

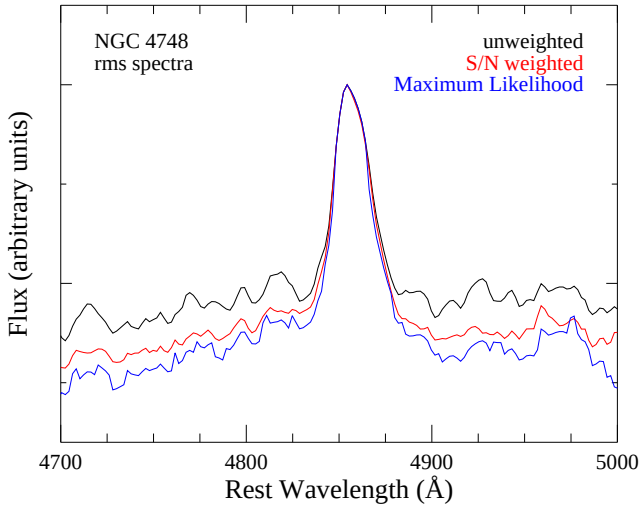

Figure 2.3 Comparison of the rms spectra of NGC 4748 generated with three different methods: unweighted rms (black), S/N weighted (red), and maximum likelihood (blue). For this object, two bad epochs with low-S/N data were removed as described in § 3.2.

2.3.2 Single-Epoch Spectra

We performed the multi-component fitting procedure using individual SE spectra, and measured the line width and continuum luminosity for each epoch. The vast majority of SE spectra have sufficiently high quality to perform the analysis (S/N $\approx$ 66 per pixel at rest-frame 5100 Å). However, a small fraction of spectra have significantly lower S/N owing to bad weather during the LAMP monitoring campaign. In addition, there are a few epochs with artificial signatures, such as bad pixels, abnormal curvature, or fluctuations in the reduced spectra. Those SE spectra were discarded to avoid possible biases due to much larger measurement errors (see Fig. 2.2). On average, four bad epochs out of 47 nights were removed for each object, except for SBS 1116, for which 11 epochs were eliminated because of a defect between the Hβ and [O III] λ4959 lines due to bad pixels in the detector.

Emission-Line Width

We measured the full width at half-maximum intensity (FWHM$_{\rm H\beta}$) and the dispersion ($\sigma_{\rm H\beta}$) (the second moment of line profile; Peterson et al. 2004) of the broad component of Hβ directly from the data as well as from the fits to the continuum-subtracted spectra. Line-

Table 2.2. Mean continuum luminosities and host-galaxy contributions

Object	λL_λ(tot) (10^{42} erg s^{-1})	λL_λ(AGN) (10^{42} erg s^{-1})	λL_λ(star) (10^{42} erg s^{-1})	$\frac{\lambda L_\lambda(\mathrm{star})}{\lambda L_\lambda(\mathrm{tot})}$
(1)	(2)	(3)	(4)	(5)
Arp 151	6.11	2.76	3.42	0.56
NGC 4748	10.05	5.55	4.69	0.47
Mrk 1310	8.10	3.79	4.32	0.53
Mrk 202	8.78	5.02	3.75	0.43
NGC 4253	8.87	6.41	2.47	0.28
NGC 6814	1.93	0.83	1.15	0.59
SBS 1116+583A	10.52	3.15	7.44	0.71
Mrk 142	47.89	35.64	12.73	0.27
NGC 5548	20.86	12.42	8.37	0.40

Note. — Col. (1): object name. Col. (2): the total continuum luminosity at 5100 Å. Col. (3): the AGN luminosity estimated from the power-law continuum fit. Col. (4): the host-galaxy luminosity estimated from the host-galaxy template fit. Col. (5): the host-galaxy fraction.

width measurements are corrected for the instrumental resolution in a standard way (Barth et al. 2002; Woo et al. 2004; Bentz et al. 2009c), by subtracting in quadrature the instrumental resolution (Table 11 of Bentz et al. 2009c) from the measured line width.

By comparing line widths measured from Gauss-Hermite series fits with those directly measured from the data, we found less than a 3% systematic difference (with considerable rms scatter of $\sim 5\%$) as expected given the high S/N of individual spectra. The small systematic trend between $\mathrm{FWHM}_{\mathrm{H}\beta}$ and $\sigma_{\mathrm{H}\beta}$ shows opposite directions. In the case of $\mathrm{FWHM}_{\mathrm{H}\beta}$, the measurements from the fit were $2.6 \pm 0.2\%$ larger than those from the data while $\sigma_{\mathrm{H}\beta}$ measurements from the fit were $1.9 \pm 0.1\%$ smaller than those from the data, showing a trend consistent with that reported by Denney et al. (2009). For consistency with other studies on the reverberation and single-epoch masses, we focus on the line-width measurements from the fits in the rest of the chapter unless explicitly noted.

Continuum Luminosity

We measured the monochromatic continuum luminosity at 5100 Å from the observed spectra at each epoch by calculating the average flux in the rest-frame 5080–5120 Å region. The luminosity at 5100 Å (total luminosity, $L_{5100,\mathrm{t}}$) is strongly contaminated by the host-galaxy starlight when the AGN luminosity is comparable to or smaller than the host-galaxy stellar luminosity as in the Seyfert galaxies in our sample.

To obtain the AGN continuum luminosity (nuclear luminosity, $L_{5100,\mathrm{n}}$), the host-galaxy contribution to the total luminosity should be subtracted from the measured total luminosity. In principle, the host-galaxy luminosity can be determined by separating a stellar component from a point source using surface brightness fitting analysis based on a high-resolution image. Such an analysis is in progress based on the *HST* WFC3 images of the LAMP sample (GO-11662, PI. Bentz). For this chapter, however, we used the information obtained from the spectral decomposition. We note that, although the host-galaxy flux should be constant, the amount of host-galaxy contribution to the total flux can vary in each epoch's spectrum because of seeing variations and miscentering in the slit. Thus, the nuclear luminosity, $L_{5100,\mathrm{n}}$, needs to be estimated for each individual spectrum from which Fe II and starlight have been subtracted.

Figure 2.2 shows the starlight luminosity measured from each SE spectrum as a function of S/N. As expected, the starlight is not constant due to the effects of seeing and miscentering. The variability ranges from 10% to 20% with an average of 0.06 ± 0.01 dex. These results underscore the importance of subtracting the host-galaxy starlight in making the rms spectra. Otherwise, the rms spectra may contain a contribution from the variable amount of starlight observed through the slit (see § 3.3 and Figure 2.5).

As a consistency check, we directly compare the host-galaxy flux of NGC 5548 measured from our spectral decomposition with that from the *HST* imaging analysis as similarly done by Bentz et al. (2009b). In order to calculate the amount of light observed through the spectroscopic aperture, we used an aperture size of $4'' \times 10\farcs1$ as used in the LAMP spectroscopy analysis, after smearing the point-spread-function (PSF) subtracted *HST* image with a $2''$ Gaussian seeing disk. The host-galaxy flux of NGC 5548 based on the spectral decomposition is 2.47×10^{-15} erg s^{-1} cm^{-2} Å^{-1}, while the *HST* imaging-based galaxy flux is 2.73×10^{-15} erg s^{-1} cm^{-2} Å^{-1}. Thus, the small difference ($\sim$ 10%) between the two analyses shows the consistency in host-galaxy flux measurements. When we use a smaller seeing disk (e.g., a $1\farcs5$ Gaussian disk), the host-galaxy flux measured from the *HST* imag-

ing analysis increases by $\sim 13\%$, indicating that the actual seeing size will slightly change the host-galaxy flux measurements.

Error Estimation

To estimate the uncertainties of the line-width and luminosity measurements from SE spectra, we adopted the Monte Carlo flux randomization method (e.g., Bentz et al. 2009c; Shen et al. 2011). First, we generated 50 mock spectra for each observed spectrum by adding Gaussian random noise based on the flux errors at each spectral pixel. Then we measured the line widths and AGN luminosities from the simulated spectra using the method described in §3.2.1 and §3.2.2. We adopted the standard deviation of the distribution of measurements from 50 mock spectra as the measurement uncertainty. For a consistency check, we increased the number of mock spectra up to 100 and found that the results remain the same. In the case of the total luminosity ($L_{5100,\mathrm{t}}$), we measured the uncertainty as the square root of the quadratic sum of the standard deviation of fluxes and average flux errors in the continuum-flux window.

2.3.3 Mean and RMS Spectra

In this section, we describe the process of generating mean and rms spectra, and present the method for measuring the line width and continuum luminosity. The mean spectra are representative of all single spectra, thus they are useful to constrain the random errors of measurements from single-epoch spectra. In contrast, reverberation mapping studies generally use rms spectra to map the geometry and kinematics of the same gas that responds to the continuum variation. By comparing the line profiles between rms and single spectra, one can investigate any systematic differences of the corresponding line widths, and therefore improve the calibration of BH mass estimators.

Method

We generated mean and rms spectra for each object using the following equations:

$$\langle f(\lambda)\rangle = \frac{1}{N}\sum_{i=1}^{N} f_i(\lambda), \tag{2.1}$$

$$\mathrm{rms}(\lambda) = \sqrt{\frac{1}{N-1}\sum_{i=1}^{N}\left[f_i(\lambda) - \langle f(\lambda)\rangle\right]^2}, \tag{2.2}$$

where $f_i(\lambda)$ is the flux of i-th SE spectrum (out of N spectra).

The unweighted rms spectra can be biased by low-S/N spectra, often showing peaky residual features in the continuum. These spurious features in continuum can affect the wings of the emission lines and therefore the measurement of line dispersion. To mitigate this effect it is best to consider more robust procedures. We considered the following two schemes. First, we used the S/N as a weight, with the following equations:

$$\langle f^w(\lambda)\rangle = \sum_{i=1}^{N} w_i f_i(\lambda), \tag{2.3}$$

$$\mathrm{rms}^w(\lambda) = \sqrt{\frac{1}{1-\sum_{i=1}^{N} w_i^2} \sum_{i=1}^{N} w_i \left[f_i(\lambda) - \langle f^w(\lambda)\rangle\right]^2}, \tag{2.4}$$

where w_i is the normalized S/N weight defined by

$$w_i = \frac{\left(S_i/N_i\right)}{\sum_{i=1}^{N}\left(S_i/N_i\right)}. \tag{2.5}$$

Alternatively, we considered the maximum likelihood method. Assuming Gaussian errors, the logarithm of the likelihood function (up to a normalization constant) is given by

$$2\ln\mathcal{L} = -\sum_{i=1}^{N} \ln\epsilon_{\mathrm{tot},i}^2(\lambda) - \sum_{i=1}^{N} \frac{\left[f_i(\lambda) - \langle f(\lambda)\rangle\right]^2}{\epsilon_{\mathrm{tot},i}^2(\lambda)}, \tag{2.6}$$

where

$$\epsilon_{\mathrm{tot},i}^2(\lambda) \equiv \epsilon_i^2(\lambda) + \mathrm{rms}^2(\lambda), \tag{2.7}$$

and $\epsilon_i(\lambda)$ is the error in the flux $f_i(\lambda)$. Here $\langle f(\lambda)\rangle$ is the mean flux while rms(λ) is the intrinsic scatter – that is, the rms flux after removing measurement errors. By maximizing the log-likelihood, we obtain the mean and rms spectra. The maximum likelihood method also provides proper errors in the rms spectra. We calculated errors in the inferred mean and rms spectra in a standard way, by computing their posterior probability distribution after marginalizing over the other parameters. We adopt $1-\sigma$ errors as symmetric intervals around the posterior peak containing 68.3% of the posterior probability.

Figure 2.3 compares rms spectra of NGC 4748 generated with the unweighted rms method, the S/N weighted method, and the maximum likelihood method, after removing

two bad epochs as described in § 3.2. As expected, the S/N weighted rms spectrum is less noisy than the unweighted rms spectrum. The rms spectrum based on the maximum likelihood method is similar to but slightly noisier than the S/N weighted spectrum. In particular, the maximum likelihood method generates noisy patterns around the [O III] line region, presumably due to the fact that the error statistics have changed owing to the subtraction of the strong [O III] line signals. In the case of the mean spectrum, all three methods produce almost identical results. Thus, we choose the S/N weighting scheme to generate the mean and the rms spectra, and adopt the errors of the rms spectra from the maximum likelihood method. We note that using the rms spectra based on the maximum likelihood method does not significantly change the results in the following analysis. If more bad epochs with low S/N are removed in generating rms spectra (as practiced in the reverberation studies; e.g., Bentz et al. 2009c), the difference among the three methods tends to be smaller.

We note that there may be a potential bias in the S/N weighted method owing to the fact that in the high continuum state the S/N is higher while emission lines are narrower. Thus, the S/N weighted rms spectra can be slightly biased toward having narrower lines. On the other hand, the time lag between the luminosity change and the corresponding velocity change will reduce the bias since the high luminosity and the corresponding narrow line width are not observed at the same epoch.

To test this potential bias, we compared the line-width measurements based on S/N weighted and unweighted rms spectra, respectively. We find that the line width decreases by $2.6 \pm 2.1\%$ for $\sigma_{\rm H\beta}$ and $2.7 \pm 1.3\%$ for $\rm FWHM_{H\beta}$ when the S/N weighted rms spectra are used, indicating that the bias is not significant for our sample AGNs. However, this offset is not due to the luminosity bias since the S/N ratio does not correlate with AGN luminosity. Instead, the change of the S/N ratio is mostly due to the effects of seeing and miscentering within the slit since different amounts of stellar light were observed within the slit on different nights. Considering the low level of luminosity variability and the time lag, the night-to-night seeing and weather variations would be the predominant factors affecting the S/N ratio. The average offset of $\sim$3% is dominated by two objects, NGC 6814 (0.07 dex for $\sigma_{\rm H\beta}$, 0.02 dex for $\rm FWHM_{H\beta}$) and SBS 1116 (0.04 dex for $\sigma_{\rm H\beta}$, 0.05 dex for $\rm FWHM_{H\beta}$), which showed the largest stellar fraction in Fig. 2.1, thus supporting our conclusion. By excluding these two objects, the average offset decreases to $\sim$1%. Thus, we conclude that the potential AGN luminosity bias in the S/N weighted method is not significant, at least for our sample.

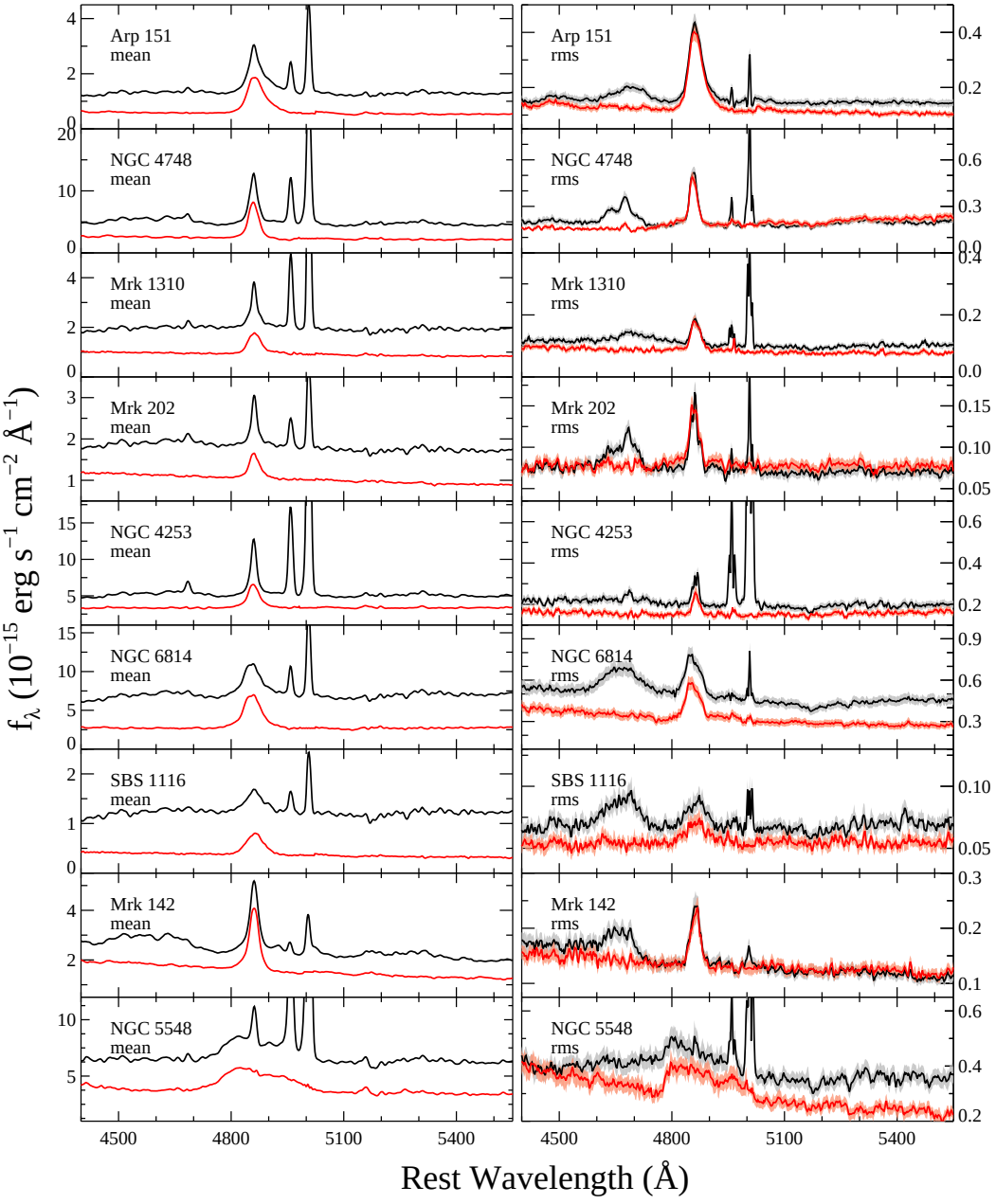

Figure 2.4 *Left:* S/N weighted mean spectra of 9 Seyfert galaxies. *Right:* S/N weighted rms spectra. In each panel, red lines represent spectra obtained after removing narrow lines, Fe II emission, He II lines, and host-galaxy starlight from each individual SE spectrum. Black lines represent rms spectra obtained without removing the same components from each individual spectrum. Shaded regions show the errors from the maximum likelihood method described in §3.3.

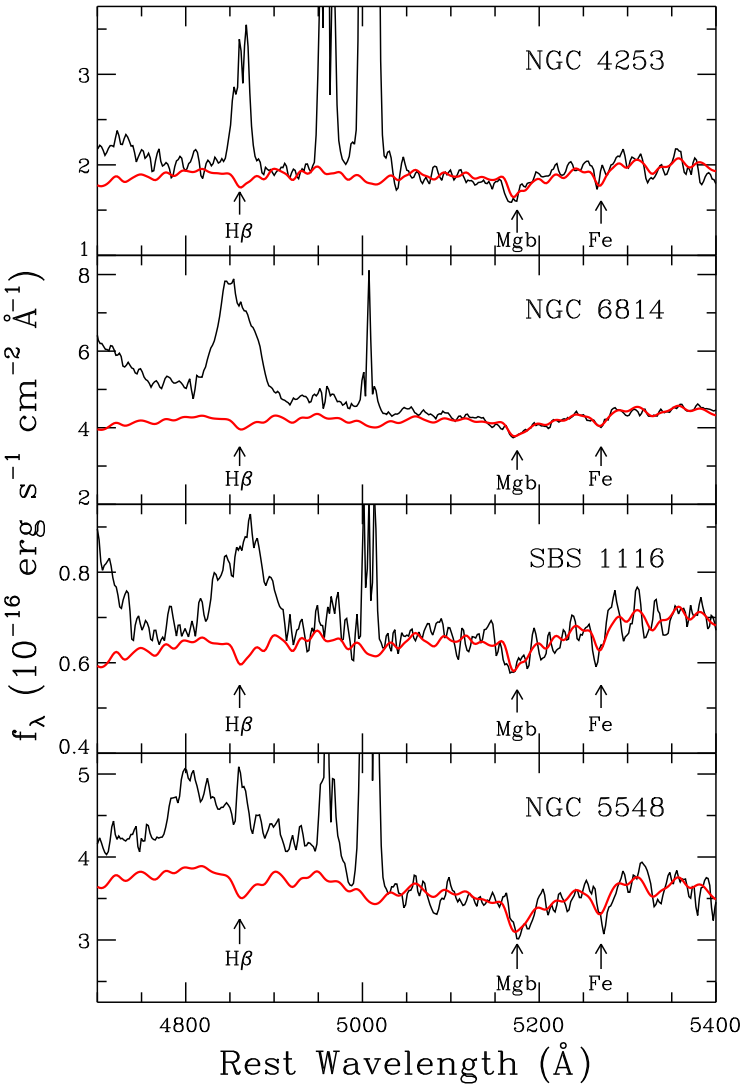

Figure 2.5 The rms spectra of 4 Seyfert 1 galaxies with strong stellar features. Black (red) solid lines represent rms spectra (stellar model fit). Strong absorption lines are labelled with arrows.

The Effect of Host Galaxy, Fe II, and He II

Although the rms spectra are supposed to contain only varying components of AGN spectra, residuals of narrow lines (e.g., [O III]) are often present due to residual systematic errors (due to calibration issues; Bentz et al. 2009c). Additionally, the variation of the host-galaxy starlight contribution to the total flux can be significant (10–20%) in the extracted SE spectra as discussed in §3.2.2. This variable starlight is responsible for the stellar absorption features often visible in the rms spectra. To demonstrate the presence of stellar absorption lines in the rms spectra, we fit the continuum with a stellar-population model. As shown in Figure 2.5, it is clear that the rms spectra show stellar absorption lines [such as the Mg *b* triplet ($\sim$ 5175 Å), Fe (5270 Å), and possibly Hβ (4861 Å)] for Seyfert 1 galaxies having strong starlight contribution. Thus, for AGNs with high starlight fraction, like the ones considered here, it is important to remove the variable starlight in order to generate pure AGN rms spectra and correctly measure the widths of the broad lines.

To minimize these residual features in the rms spectra, we subtracted the narrow lines in all SE spectra before making mean and rms spectra. We also subtracted the Fe II emission blends, host-galaxy starlight, and the He II emission line from each SE spectrum. In Figure 2.4, we show the S/N weighted mean and rms spectra with and without prior removal of narrow-line components, the Fe II blend, He II lines, and host-galaxy starlight. Clearly, the rms spectra are significantly affected by this procedure. In particular, removing the Fe II and He II emission changes the continuum shape around Hβ. For the objects with higher starlight fraction, stellar Hβ absorption is present in the rms spectra, if starlight is not removed from each SE spectrum.

To quantify the change of the line widths due to prior removal of the starlight, He II, and Fe II components, we compared the line-width measurements from rms spectra generated with/without prior removal. Each panel in Fig. 2.6 shows the effects of individual components by comparing the line-width measurements from the rms spectra with prior removal of all three components (i.e., host-galaxy stellar features, He II, and the Fe II blend) with those from the rms spectra without subtracting one of the three components, respectively. We found that the effect of host-galaxy stellar features is stronger than those of He II and the Fe II blend. Without subtracting host-galaxy stellar features, the rms line widths decrease by 18 ± 5% for $\sigma_{\rm H\beta}$ and 4 ± 3% for FWHM$_{\rm H\beta}$, indicating that the line wings are more affected than the line core. The large increase of $\sigma_{\rm H\beta}$ can be understood as the buried Hβ line wings within the residual of stellar features are restored by subtracting the host stellar lines,

leading to a lower continuum level and larger line width.

The subtraction of He II changes the line width of objects that show strong blending with the Hβ line (e.g., Mrk 1310 and NGC 6814). On average, the effect of He II on the Hβ line width is at the 4.7 ± 2.2% level for $\sigma_{\mathrm{H}\beta}$ and the 1.6 ± 0.6% level for $\mathrm{FWHM}_{\mathrm{H}\beta}$. In the case of the Fe II subtraction, the effect on the rms line widths is more complex. Line widths increase for some objects and decrease for other objects, depending on whether the Fe II emission residual is strong. For example, if the Fe II residual is prominent in the continuum region (i.e., 5080–5550Å), then the removal of Fe II will lower the continuum level, increasing the Hβ line width. In contrast, if the Fe II residual is strong under Hβ, then the Hβ line width will decrease by subtracting Fe II. On average, the effect of Fe II on the Hβ line width is at the 1.2 ± 2.9% level for $\sigma_{\mathrm{H}\beta}$ and the 1.6 ± 2.2% level for $\mathrm{FWHM}_{\mathrm{H}\beta}$.

Without prior removal of all three components (i.e., host-galaxy stellar features, He II, and the Fe II blend), the line widths are underestimated by 18 ± 6% for $\sigma_{\mathrm{H}\beta}$ and 5 ± 4% for $\mathrm{FWHM}_{\mathrm{H}\beta}$, due to the combined effects as described above. Subtracting stellar features has the most significant impact on the measurements of rms line dispersion, demonstrating the importance of prior removal of starlight when stellar contribution is significant. Moreover, in order to successfully remove the He II blending in the rms spectra, the host-galaxy component as well as Fe II emission blends should be simultaneously fitted in the modeling of the continuum. Thus, we conclude that for AGNs with strong host galaxy starlight, strong Fe II, or blended He II, it is necessary to remove all non-broad-line components from SE spectra in order to generate the cleanest rms spectra and reduce errors in measuring the Hβ line width.

Mean Spectra

We generated the S/N weighted mean spectra without prior removal of narrow lines, iron emission, and host-galaxy starlight. Then, we used the same multi-component spectral fitting procedure as used for the SE spectra (see Fig. 2.1). Note that in the case of mean spectra, removing the narrow lines, Fe II blends, and host-galaxy absorption features before or after generating the mean spectra results in almost identical Hβ broad-line profiles.

Error Estimation

Using the S/N weighted rms and mean spectra, we measured the widths of the Hβ line from the continuum-subtracted spectra and determined the continuum luminosity at 5100 Å, as

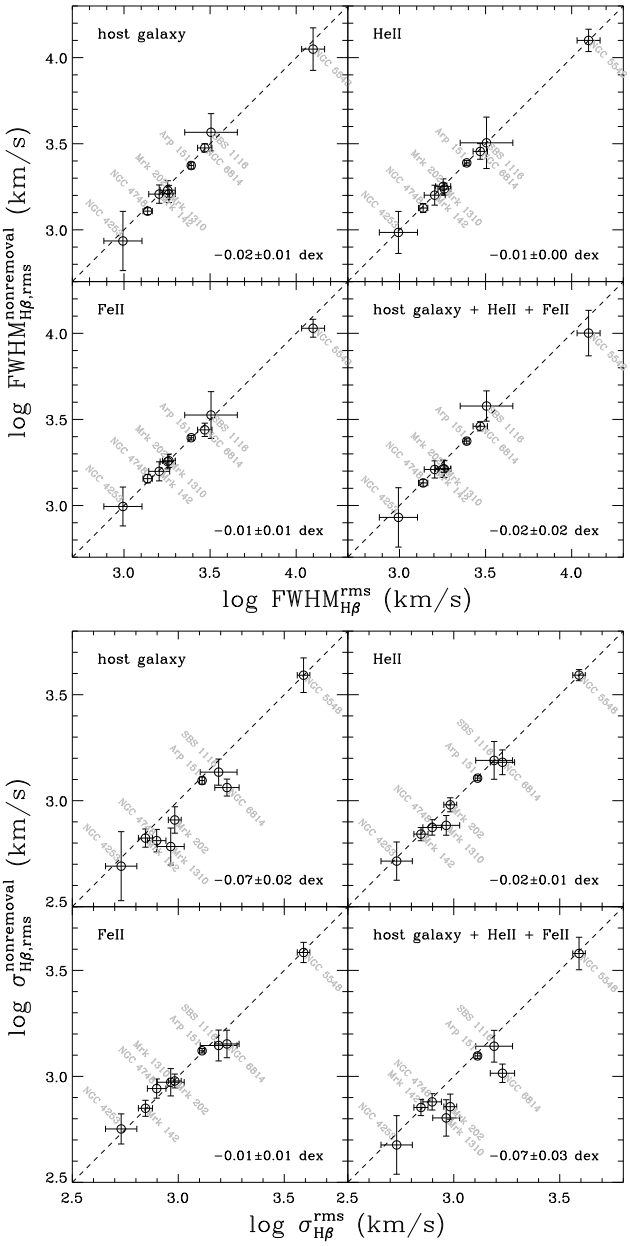

Figure 2.6 The effect of each blended component on the rms line widths using the $\mathrm{FWHM}_{\mathrm{H}\beta}$ (top) and $\sigma_{\mathrm{H}\beta}$ (bottom). In each panel, the rms line widths without prior removal of each component (given in the upper-left corner) are plotted as a function of final rms line widths (all non-broad-line components removed). The dashed line indicates an identity relationship. The average offsets with their standard errors are given in the lower-right corner of each panel.

Table 2.3. Rest-Frame Broad Hβ Line-Width Measurements

Object	Mean Spectrum		RMS Spectrum	
	$\sigma_{H\beta}$ (km s^{-1})	FWHM$_{H\beta}$ (km s^{-1})	$\sigma_{H\beta}$ (km s^{-1})	FWHM$_{H\beta}$ (km s^{-1})
Arp 151	1726 ± 17	3076 ± 39	1295 ± 37	2458 ± 82
NGC 4748	952 ± 6	1796 ± 8	791 ± 80	1373 ± 86
Mrk 1310	1229 ± 12	2425 ± 19	921 ± 135	1823 ± 157
Mrk 202	1047 ± 8	1787 ± 15	962 ± 67	1794 ± 181
NGC 4253	1232 ± 9	1946 ± 10	538 ± 92	986 ± 251
NGC 6814	1744 ± 12	3129 ± 14	1697 ± 224	2945 ± 283
SBS 1116+583A	1460 ± 23	3135 ± 36	1550 ± 310	3202 ± 1127
Mrk 142	970 ± 5	1671 ± 6	700 ± 54	1601 ± 224
NGC 5548	4354 ± 25	12402 ± 111	3900 ± 266	12539 ± 1927

described in §3.2.1 and §3.2.2. We estimated the uncertainty of the line-width measurements in the S/N weighted mean and rms spectra using the bootstrap method (e.g., Peterson et al. 2004). One thousand samples per object were generated. The median and standard deviation of the distribution of measurements were adopted as our line-width estimate and uncertainty; these are listed in Table 2.3. We also estimated the line-width uncertainties for the rms spectra using the method given in §3.2.3. We found that the errors estimated from both the Monte Carlo flux randomization and the bootstrapping were consistent within a few percent on average, which yielded almost identical fitting results.

2.4 Analysis and Results

2.4.1 Testing the Assumptions of SE BH Mass Estimators

Single-epoch M_{BH} estimates are based on the "virial" assumption and on the empirical relation between BLR size and AGN luminosity. Since M_{BH} does not vary over the time scale of our campaign, AGN luminosity and line velocity should obey the relation $V^2 \propto L^{-0.5}$. In this section, we test this assumption by studying the relation between the line width and continuum luminosity from individual SE spectra of Arp 151, the object with the

highest variability during the LAMP campaign.

In Figure 2.7 we present the time variation of the line width and luminosity of Arp 151. Line width and luminosity are inversely correlated, although the variability amplitude is smaller in luminosity than in line width. Ideally, the luminosity variability should be four times as large as the line-width variability (0.042 ± 0.001 dex and 0.027 ± 0.003 dex, respectively, for $\mathrm{FWHM}_{\mathrm{H}\beta}$ and $\sigma_{\mathrm{H}\beta}$). However, one must take into account the residual contamination from nonvariable sources to the observed continuum. In fact, the amplitude of the luminosity variability is significantly smaller than expected based on the line-width variability if the total luminosity is used (bottom panel). In contrast, providing a validation of our constant continuum subtraction procedure, the variability amplitude of the nuclear continuum is consistent with that expected from the line width, as we will further quantify below.

In Figure 2.8, we compare measured luminosities and line widths in order to test whether they obey the expected relation $V^2 \propto L^{-0.5}$. The continuum variation is shifted by the measured time lag, 4 days, to account for the time delay between the central engine and BLR variations and then matched with the corresponding epochs of line-width variations. Note that densely sampled light curves are required for this correction. As expected, the observed correlation between total flux $L_{5100,\mathrm{t}}$ and line width is steeper than the theoretical correlation. In contrast, the correlation between nuclear flux and line width is consistent with the theoretical expectation. The best-fit slopes[3] are -1.46 ± 0.31 (with intrinsic scatter 0.05 ± 0.01 dex) for $\mathrm{FWHM}_{\mathrm{H}\beta}$, and -1.09 ± 0.15 (with intrinsic scatter 0.02 ± 0.01 dex) for $\sigma_{\mathrm{H}\beta}$, which is consistent with the expected value of -1. The linear correlation coefficients between the nuclear luminosity and the line widths are -0.86 for the line dispersion and -0.77 for the FWHM, indicating the tighter inverse correlation of continuum luminosity with the line dispersion than with the FWHM.

The agreement of the observed correlations with those expected for an ideal system is remarkable, considering the many sources of noise in the observed velocity-luminosity relation. They include residual errors in the subtraction of the host-galaxy starlight contribution and the measurement uncertainties of line widths and luminosities. The inverse correlation

[3]We used the Bayesian linear regression routine `linmix_err` developed by Kelly (2007) in the NASA IDL Astronomy User's Library. This method is currently the most sophisticated regression technique, which takes into account intrinsic scatter and nondetections as well as the measurement errors in both axes, generating the random draws from posterior probability distribution of each parameter for the given data using MCMC sampling. In this study, we take best-fit values and uncertainties of parameters as the median values and $\pm 1\sigma$ standard deviation of $10,000$ random draws from corresponding posterior distributions.

between line width and luminosity further corroborates the use of SE mass estimates (Peterson & Wandel 1999, 2000; Kollatschny 2003; Peterson et al. 2004).

2.4.2 Uncertainties Due to Variability

Since the line width and continuum luminosity of an AGN vary as a function of time, mass estimates from SE spectra may also vary. Owing to its stochastic nature, this variability can be considered a source of random error in SE mass estimates. In this section, we quantify this effect by comparing SE measurements with measurements from the mean spectra.

The Effect of Line-Width Variability

We quantify the dispersion of the distribution of line-width measurements using all SE spectra. This dispersion can be interpreted as a random error due to the combined effect of variability and measurement errors. In Figure 2.9, we present the distributions of $\mathrm{FWHM}_{\mathrm{H}\beta}$ measurements from all SE spectra, after normalizing them by the measurement from the mean spectra. All SE values are normalized to the FWHM measured from the mean spectra. The standard deviation of the FWHM distributions ranges from 0.009 dex to 0.042 dex, with an average of 0.021 ± 0.004 dex ($\sim$5%) across all objects. Note that the standard deviation includes the variability and the measurement error.

In Figure 2.10, we plot the distributions of line dispersion for all objects. The dispersion of distributions ranges from 0.013 dex to 0.040 dex, with an average and rms of 0.023 ± 0.003 dex ($\sim$5%) for the entire sample. SBS 1116 shows the broadest distribution; however, part of this scatter can be attributed to the residual systematic in the red wing of Hβ due to the bad pixels in the original spectra, as discussed previously.

By averaging the standard deviation of the distribution of the line-width measurements for all 9 objects in the sample, we find that the uncertainty of SE BH mass estimates due to the line-width variation and measurement errors is on average 0.044 dex. Note that the dispersion of the line-width distribution strongly depends on the variability. For example, Arp 151 has the largest variability amplitude and also the largest variability in the line width. This is expected if line flux correlates with BLR size and both are connected to the BH mass. Based on these results, we conclude that the typical uncertainty of SE mass estimates due to line-width variability is $\sim$10%. However, as discussed below, this uncertainty is partly cancelled out in the virial product by the inverse correlation with the variability of the continuum.

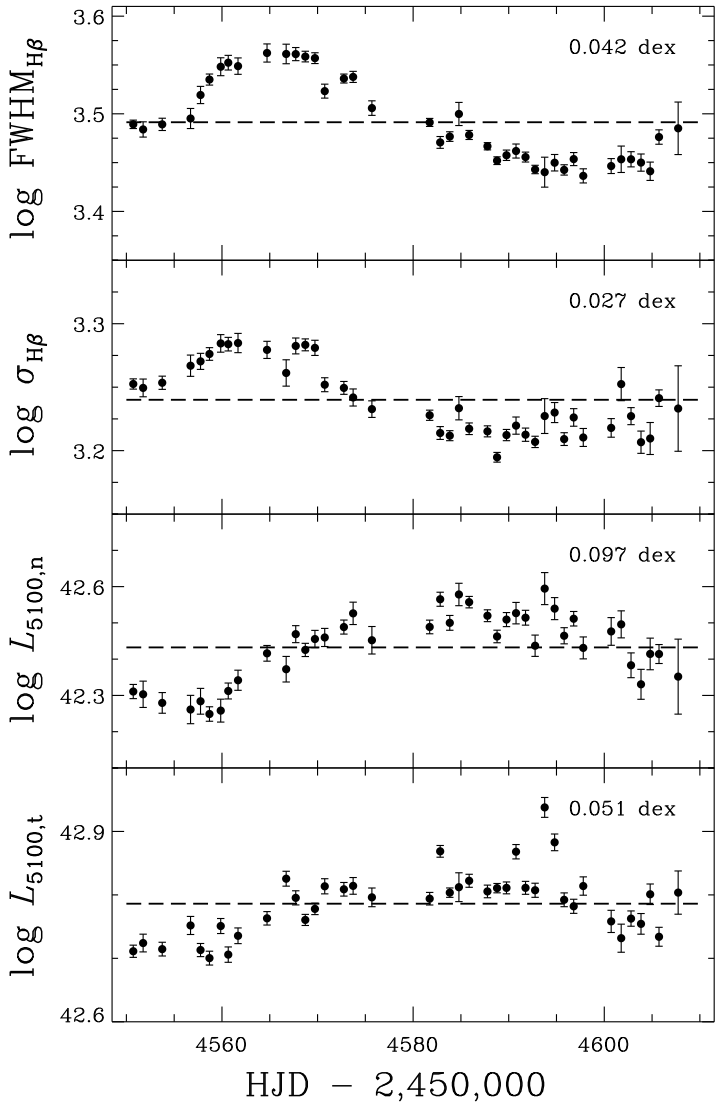

Figure 2.7 Time variations of the Hβ line width (*top:* FWHM$_{H\beta}$; *upper middle:* $\sigma_{H\beta}$) and the continuum luminosity at 5100 Å (*lower middle:* nuclear; *bottom:* total) of Arp 151. The dashed lines represent the average values over the monitoring period. The rms dispersion values are given in each panel.

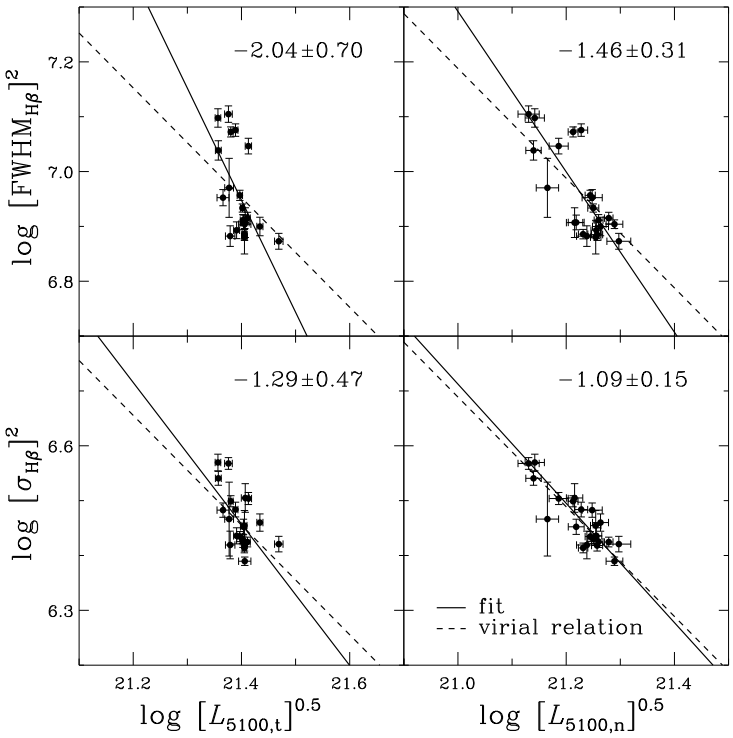

Figure 2.8 Test of SE mass estimates for Arp 151. Each filled circle represents SE measurements after shifting luminosity measurements by the average lag of 4 days (*left:* total luminosity; *right:* nuclear luminosity). Dashed lines represent the correlation $L^{0.5} \propto V^{-2}$ expected from the virial theorem and the size-luminosity relation, while solid lines are the best-fit slopes. The values of best-fit slopes and its uncertainties are given in each panel.

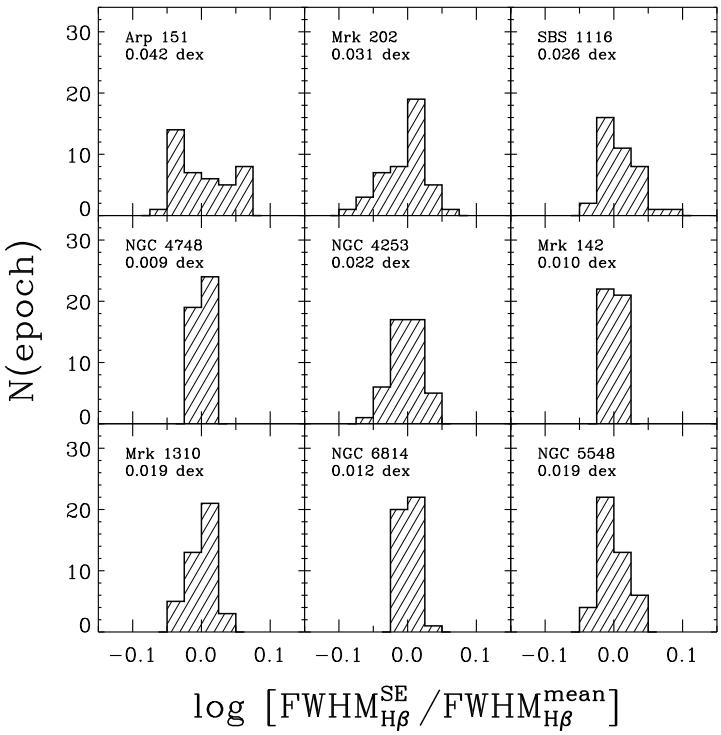

Figure 2.9 Distribution of the $\mathrm{FWHM}_{\mathrm{H}\beta}$ measured from all SE spectra. Each $\mathrm{FWHM}_{\mathrm{H}\beta}$ value is normalized to the $\mathrm{FWHM}_{\mathrm{H}\beta}$ measured from the mean spectra. The average rms dispersion of 9 objects is 0.021 ± 0.004 dex.

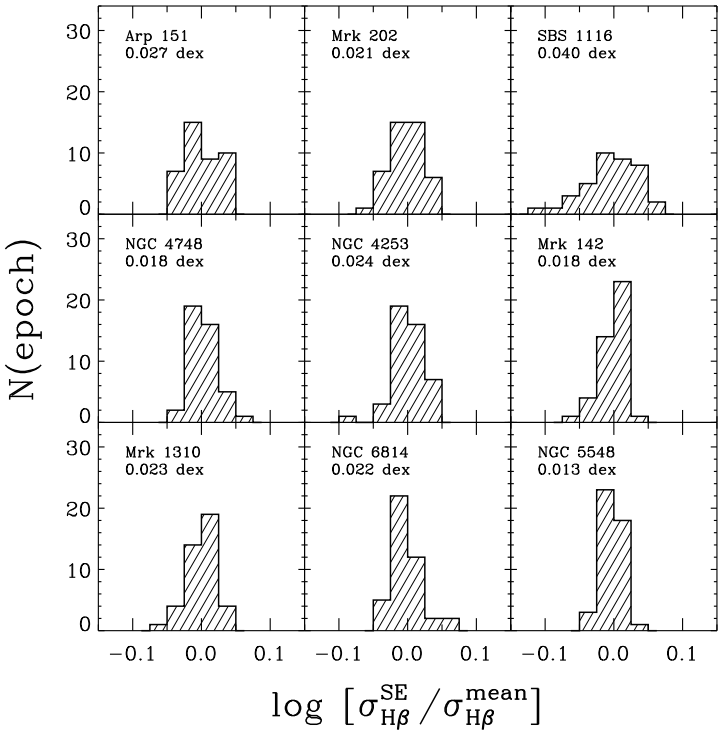

Figure 2.10 Same as in Fig. 2.9, but for $\sigma_{\rm H\beta}$. The average rms dispersion of 9 objects is 0.023 ± 0.003 dex.

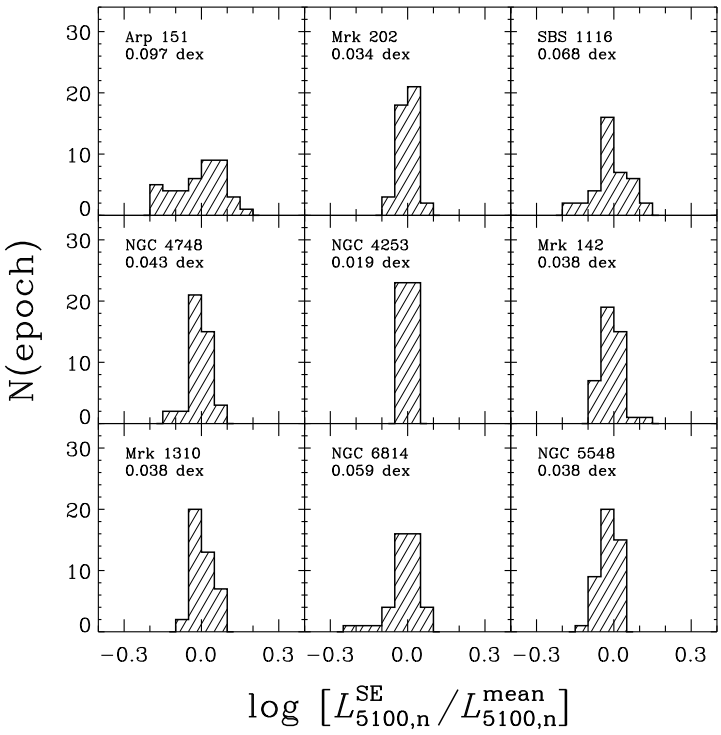

Figure 2.11 Distribution of nuclear luminosities measured from single-epoch spectra (see §2.3.2). Each luminosity value is normalized to the nuclear luminosity measured from the mean spectra. The standard deviation of the distribution is given in each panel. The average standard deviation of all 9 objects is 0.048 ± 0.008 dex.

The Effect of Luminosity Variability

We now consider the effect of luminosity variability on SE mass estimates. In Figure 2.11, we present the distributions of the nuclear luminosities at 5100 Å, after normalizing them by the nuclear luminosity measured from the mean spectra. The standard deviation of the luminosity distributions ranges from 0.019 to 0.097 dex, with an average of 0.048 ± 0.008 dex ($\sim$12%), which can be treated as a random error of the continuum luminosity measured from a SE spectrum due to the luminosity variability and measurement error.

Based on the empirical size-luminosity relation, the random errors of the luminosity enter the uncertainty of the SE mass estimates as the square root (i.e., 0.024 dex). This is somewhat smaller than the uncertainty of SE mass estimates due to the line-width variabil-

ity, 0.044 dex, as determined in the previous section, indicating that the two do not cancel each other exactly.

Combined Effect

Since the luminosity and the line width are inversely correlated as $V^2 \propto L^{-0.5}$, one may expect that the variability of luminosity and line width cancel out in the SE mass estimates. However, the two effects may not compensate each other exactly, for a variety of reasons. First, there is a time lag between continuum and emission-line variability. Second, variations such as in the ionizing flux may indicate that the luminosity at 5100 Å traces the broad-line size only approximately. In order to quantify the combined effect of the continuum luminosity and line-width variability, we thus investigate the distribution of the virial product $L_{5100,n}^{0.5} \times \sigma_{\rm H\beta}^2$ as measured from SE spectra.

In Figure 2.12, we present the distribution of the SE virial products, normalized by the virial product measured from the mean spectra. The standard deviation of the distributions can be treated as a random error due to the combined variability and measurement errors. The average rms scatter (corresponding to a source of random measurement errors when using the SE estimator) of the virial products is 0.052 ± 0.006 dex when the line dispersion ($\sigma_{H\beta}$) is used, and 0.049 ± 0.006 dex when $\rm FWHM_{H\beta}$ is used.

In agreement with previous studies (Wilhite et al. 2007; Woo et al. 2007; Denney et al. 2009), these results suggest that BH masses based on SE spectra taken at different epochs are consistent within ~ 0.05 dex ($\sim 12\%$) uncertainty, negligible with respect to other sources of uncertainty which are believed to add up to $\sim$0.4–0.5 dex (see §5.1).

2.4.3 Systematic Difference between SE and Reverberation Masses

In order to assess the accuracy of the SE mass estimates, we need to compare the SE masses with the masses determined from reverberation mapping. Setting aside potential differences in the virial coefficient, there are two main sources of systematic uncertainties in SE mass estimates. One is the potential difference of the line profile between SE spectra and the rms spectra. The other is the systematic uncertainty of the size-luminosity relation. We postpone discussion of the latter to a future paper when more accurate *HST*-based nuclear luminosities will be available. Therefore, in this section we focus on the systematic difference of the Hβ line profile and derive new SE mass estimators recalibrated to account for the difference found.

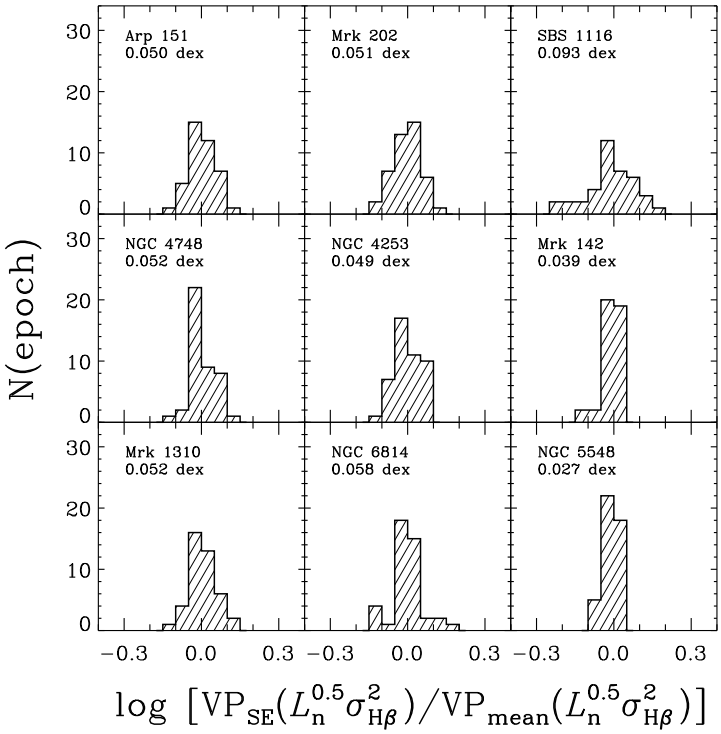

Figure 2.12 Distribution of the SE virial product ($V^2 \times L^{0.5}$) normalized to that of the mean spectra. Hβ line dispersion is used for the velocity and the nuclear luminosity at 5100 Å, corrected for the host galaxy, is used for the luminosity. The average rms dispersion of all 9 objects is 0.052 ± 0.006 dex.

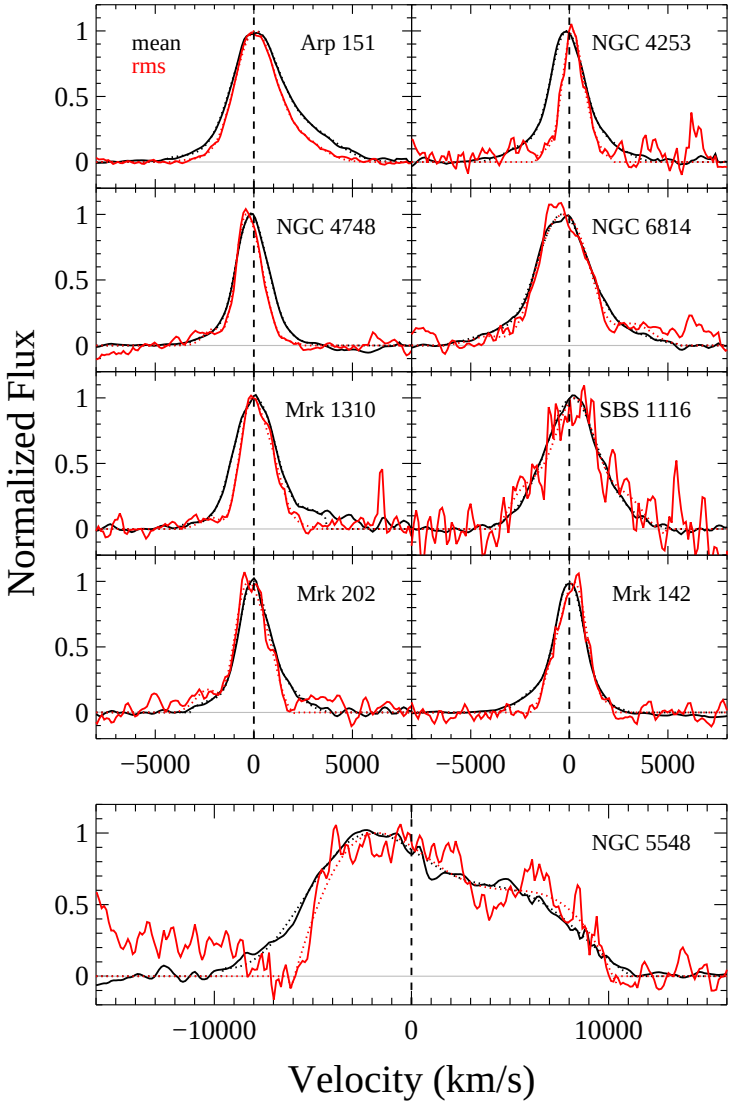

Figure 2.13 Comparison of the Hβ broad-line profiles in the mean (black) and rms (red) spectra. In each panel, solid lines represent the data, while dotted lines represent the Gauss-Hermite series fitting results. Each line profile is normalized by the maximum value of the fit. Dashed vertical lines indicate the center of the Hβ line.

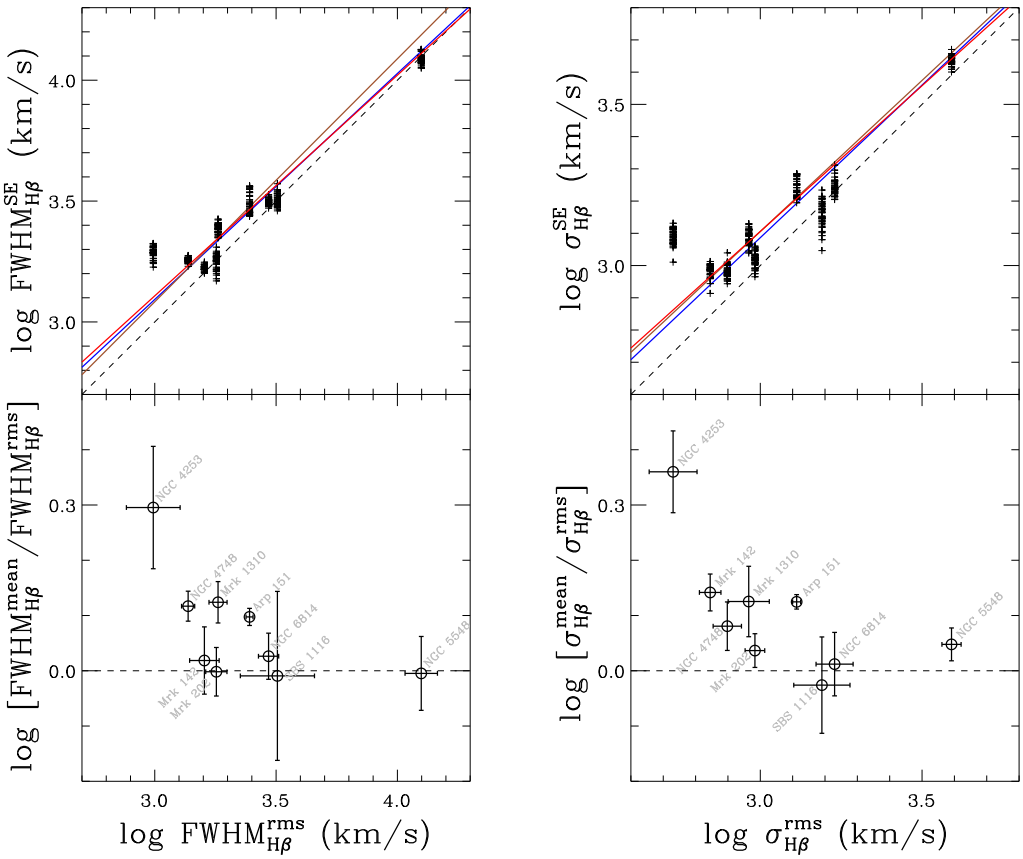

Figure 2.14 Direct comparisons of line widths and their ratios, i.e., $\mathrm{FWHM}_{\mathrm{H}\beta}$ (left) and $\sigma_{\mathrm{H}\beta}$ (right), measured from SE (or mean) and rms spectra, as a function of line width. Average offset is 0.07 ± 0.03 dex for $\mathrm{FWHM}_{\mathrm{H}\beta}$ and 0.10 ± 0.04 dex for $\sigma_{\mathrm{H}\beta}$. Dashed lines indicate an identity relation while solid lines are the best-fit results using all objects (red), excluding NGC 4253 (blue), or excluding NGC 5548 (brown) using bootstrap errors.

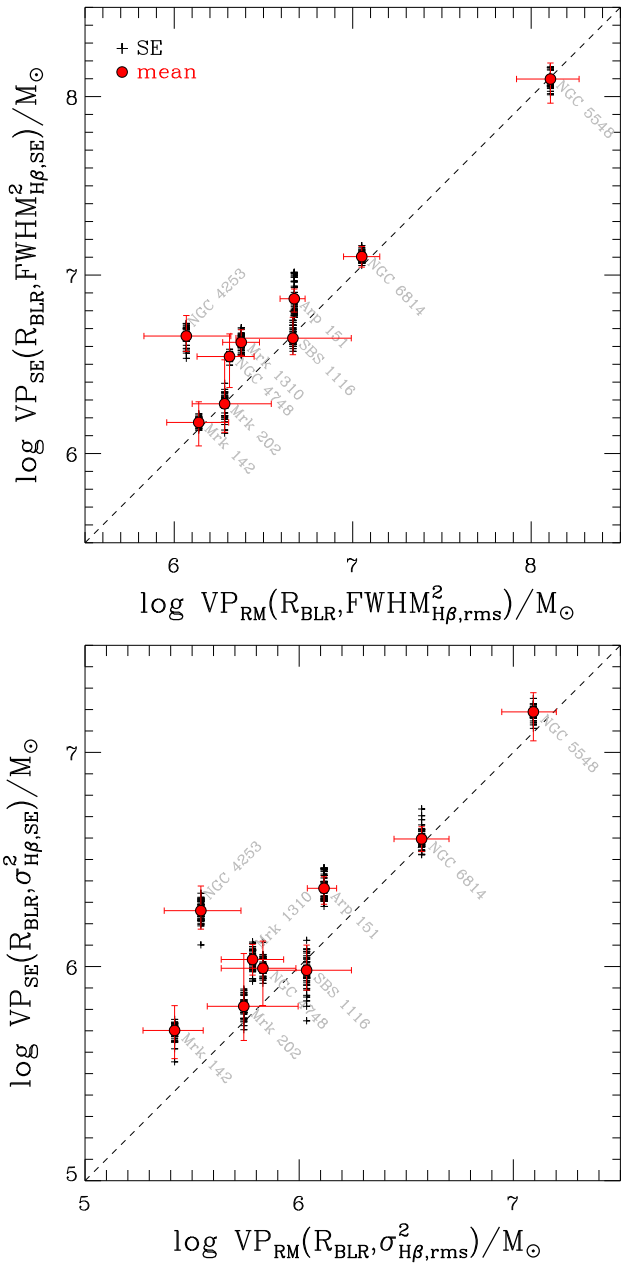

Figure 2.15 Comparison of the virial products measured from SE spectra and rms spectra. Virial products are calculated using $\mathrm{FWHM}_{\mathrm{H}\beta}$ (top) or $\sigma_{\mathrm{H}\beta}$ (bottom). In addition to measurements from each SE spectrum (crosses), we show those from the mean spectra (filled circles). The average offset of all mean measurements is 0.201 ± 0.075 (0.147 ± 0.066) dex when $\sigma_{\mathrm{H}\beta}$ ($\mathrm{FWHM}_{\mathrm{H}\beta}$) is used for the virial products.

Comparing Line Profiles

In Figure 2.13 we compare the broad Hβ line profiles measured from the mean and rms spectra after normalizing by the peak flux. Generally the Hβ line is broader in the mean spectra than in the rms spectra, indicating that the variation is weaker in the line wings than in the line core. It is worth noting that the observed offset cannot be explained by the contamination of the narrow Hβ component or the Fe II blends since we consistently subtracted them in both the mean and rms spectra. To verify this we arbitrarily decreased the amount of narrow component subtracted from the observed Hβ profile, and found that the large offsets between rms and mean spectra are virtually unchanged.

The broader line width in the mean spectra has been noted in previous reverberation studies (e.g., Sergeev et al. 1999; Shapovalova et al. 2004). Collin et al. (2006) reported that the line widths in the mean spectra were typically broader by $\sim 20\%$ than those in the rms spectra. Denney et al. (2010) also found that some objects in their reverberation sample clearly showed narrower line widths in the rms spectra than in the mean spectra. Several different and somewhat mutually exclusive explanations have been suggested for this difference. For example, Shields et al. (1995) explained the systematic difference of the line width as being due to the high-velocity gas in the inner BLR being optically thin to the ionizing continuum and hence fully ionized. In this way, the line wings have weak variability and are suppressed in the rms spectra. In contrast, Korista & Goad (2004) suggested a distance-dependent responsivity of optically thick clouds to explain the weak variability of Balmer line wings.

We quantify the systematic offset in line width in Figure 2.14 by showing the ratios of the line width measured from the mean (and SE) spectra to those measured from the rms spectra as a function of line width. The average offset in $\mathrm{FWHM}_{\mathrm{H}\beta}$ is 0.07 ± 0.03 dex (0.05 ± 0.02 dex, if NGC 4253, the object with the narrowest line, is excluded). In the case of line dispersion ($\sigma_{\mathrm{H}\beta}$), the offset is slightly larger, 0.10 ± 0.04 dex (0.07 ± 0.02 dex if NGC 4253 is excluded). The larger offset of the line dispersion in comparison with FWHM is consistent with there being mainly a difference between variability in the wings and in the core.

There seems to be a systematic trend, in the sense that the offset becomes relatively larger for the narrower line objects, but its origin is not clear. In particular, the narrow-line Seyfert 1 galaxy NGC 4253 (Mrk 766) has the narrowest Hβ line in the sample and shows the largest systematic difference. It is possible that the systematic difference for this partic-

ular object with very narrow Hβ (FWHM$_{\rm H\beta}$ (rms) $<$ 1000 km s^{-1}) may be amplified due to imperfect subtraction of the narrow component, the Fe II blends, or starlight. However, the trend is present even if we remove this object from the sample.

In order to correct for this potential bias, we derive a relation between Hβ line width as measured from rms and SE spectra by fitting the trend as shown in Figure 2.14. Using the linear regression routine `linmix_err` (Kelly 2007), we fit the linear relationship in log-scale using bootstrap errors determined in §3.3. We also determined the slope excluding the narrowest-line object (NGC 4253) or the broadest-line object (NGC 5548) from the sample. As shown in Figure 2.13, removing either NGC 4253 or NGC 5548 from the sample does not significantly change the slope.

In addition, we fit the slope using a fixed error for all objects. Since the bootstrap errors on the rms line widths are significantly different for each object owing to the different quality and S/N ratios of individual single-epoch spectra, we assigned a fixed error, such as 20% on both axes, to test the effect of errors. The best-fit slope using a fixed error is slightly shallower than that with bootstrap errors since the most offset object, NGC 4253 has a large bootstrap error and consequently has smaller weight in the fitting process.

To secure a large dynamic range, we decided to use all 9 objects for the fit and adopt the best-fit result using bootstrap errors. The adopted best fits are expressed as

$$\log \mathrm{FWHM}_{\rm H\beta}(\mathrm{rms}) = -0.405(\pm 0.051) + 1.095(\pm 0.015)\ \log \mathrm{FWHM}_{\rm H\beta}(\mathrm{SE}), \tag{2.8}$$

$$\log \sigma_{\rm H\beta}(rms) = -0.434(\pm 0.060) + 1.106(\pm 0.019)\ \log \sigma_{\rm H\beta}(SE). \tag{2.9}$$

However, these fits should not be extrapolated to high-velocity objects; otherwise, negative bias will be introduced. Since our sample consists of relatively narrow-line Seyfert 1 galaxies, we recommend that readers use Eqs. 2.8 and 2.9 for objects with FWHM$_{\rm H\beta,SE} < 3,000$ km s^{-1} and $\sigma_{\rm H\beta,SE} < 2,000$ km s^{-1}, respectively.

Systematic Offset of Mass Estimates

The systematically broader line width in SE spectra would result in overestimates of SE masses if unaccounted for. In Figure 2.15 we plot the ratio of the SE virial product (VP) with respect to the virial product based on the reverberation studies as a function of the virial product. Note that to demonstrate the effect of the systematic difference between SE and rms spectra, we simply used the measured $R_{\rm BLR}$ for all SE virial products, instead of using L_{5100} and the size-luminosity relation. As expected, virial products exhibit a biased systematic

trend. The average offset of all SE measurements is 0.152 ± 0.009 dex when FWHM is used in the virial product (top), and 0.204 ± 0.011 dex for the $\sigma_{\rm H\beta}$-based virial product (bottom). The average offset of all measurements based on mean spectra is 0.147 ± 0.066 (0.201 ± 0.075) dex when $\rm FWHM_{H\beta}$ ($\sigma_{\rm H\beta}$) is used in the virial product. To avoid potential biases from the narrowest-line object, we recalculate the average offset after removing NGC 4253. The average offset of all SE measurements is now 0.093 ± 0.006 dex and 0.135 ± 0.007 dex for $\rm FWHM_{H\beta}$ and $\sigma_{\rm H\beta}$, respectively. When the measurements from mean spectra are used in comparison, the average offsets are 0.092 ± 0.040 dex and 0.136 ± 0.043 dex for $\rm FWHM_{H\beta}$ and $\sigma_{\rm H\beta}$, respectively. Thus, the SE BH masses of broad-line AGNs with virial products in the range $\sim 10^{5-7}$ $\rm M_{\odot}$ can be overestimated by $\sim$25–35% if the same recipe used for rms spectra is adopted.

These results are similar to the findings by Collin et al. (2006), who investigated the systematic offset of virial product estimates between rms and mean spectra using a different sample of reverberation mapping measurements. Although it is not straightforward to directly compare their results with ours since the methods of generating rms spectra and measuring line widths are substantially different, the similar systematic offset between SE and reverberation masses clearly demonstrates the importance of calibrating SE masses.

Comparing $\rm FWHM_{H\beta}$ and $\sigma_{\rm H\beta}$

We compare $\rm FWHM_{H\beta}$ and $\sigma_{\rm H\beta}$ in Figure 2.15. As previously noticed in other studies (e.g., Collin et al. 2006; McGill et al. 2008), the shape of the Hβ line is different from a Gaussian profile, for which $\rm FWHM_{H\beta}/\sigma_{H\beta}$ is expected to be 2.35. As shown in Figure 2.16, narrower lines tend to have stronger wings leading to a lower $\rm FWHM_{H\beta}/\sigma_{H\beta}$ ratio, while broader lines are more core dominated with a higher $\rm FWHM_{H\beta}/\sigma_{H\beta}$ ratio. These results are consistent with those of previous studies, although our sample is composed of objects with narrower lines than previously studied.

The best-fit correlation based on the rms spectra is

$$\log \sigma_{\rm H\beta}({\rm rms}) = 0.401(\pm 0.395) + 0.792(\pm 0.117)\ \log {\rm FWHM_{H\beta}(rms)}. \quad (2.10)$$

In the case of measurements from the SE spectra, the best fit is expressed as

$$\log \sigma_{\rm H\beta}({\rm SE}) = 0.567(\pm 0.027) + 0.753(\pm 0.008)\ \log {\rm FWHM_{H\beta}(SE)}. \quad (2.11)$$

We note that these results are somewhat limited by the small dynamic range of our sample and the lack of objects with FWHM $>$ 3000 km $\rm s^{-1}$. Further analysis with broader line

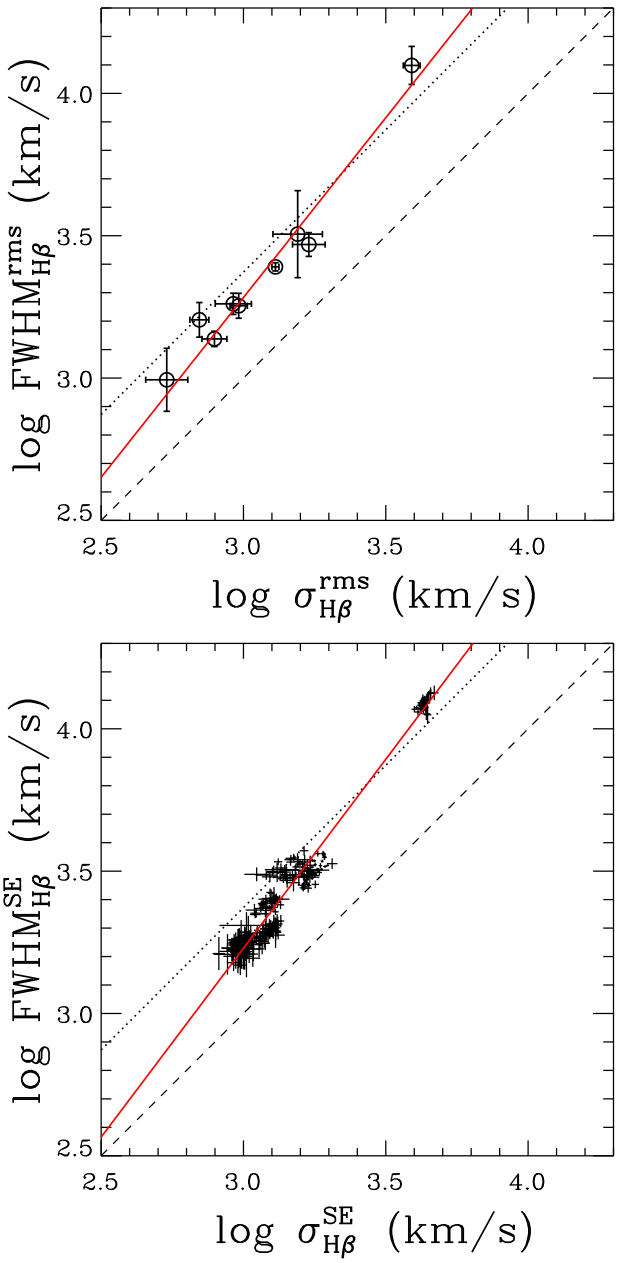

Figure 2.16 Comparisons of $FWHM_{H\beta}$ and $\sigma_{H\beta}$, using measurements from rms spectra (top) and SE spectra (bottom). The dashed line indicates an identity relationship while the dotted line represents the Gaussian profile, i.e., $FWHM_{H\beta}/\sigma_{H\beta}$ = 2.35. The red solid line shows the best-fit relation.

objects is required. However, in the case of broader line objects in the literature, we do not have consistently measured line widths from rms spectra as described in §3.3. Nevertheless, we will use this fit to convert $\mathrm{FWHM}_{\mathrm{H}\beta}$ to $\sigma_{\mathrm{H}\beta}$ in §4.3.4.

Line-Width Dependent Mass Estimators

In order to avoid potential systematic biases in SE spectra, we derive line-width dependent mass estimators, using the best-fit relations derived above (see Fig. 2.14). As a reference, we use the mass estimator normalized for the virial product from rms spectra (reverberation results) using the virial factor $\log f = 0.72$ determined from the $M_{\mathrm{BH}} - \sigma_*$ relation of reverberation mapped AGNs (Woo et al. 2010):

$$M_{\mathrm{BH}} = 10^{7.602}\mathrm{M}_{\odot} \left(\frac{\sigma_{\mathrm{H}\beta}(\mathrm{rms})}{1000 \text{ km s}^{-1}} \right)^{2} \left(\frac{\lambda L_{5100,n}}{10^{44} \text{ erg s}^{-1}} \right)^{0.518} . \quad (2.12)$$

If we replace $\sigma_{\mathrm{H}\beta}$ from rms spectra with $\sigma_{\mathrm{H}\beta}$ measured from SE spectra using Eq. 2.9, the mass estimator changes to

$$M_{\mathrm{BH}} = 10^{7.370}\mathrm{M}_{\odot} \left(\frac{\sigma_{\mathrm{H}\beta}(\mathrm{SE})}{1000 \text{ km s}^{-1}} \right)^{2.212} \left(\frac{\lambda L_{5100,n}}{10^{44} \text{ erg s}^{-1}} \right)^{0.518} . \quad (2.13)$$

As in the case of Eq. 2.9, we recommend readers use Eq. 2.13 for AGNs with $\sigma_{\mathrm{H}\beta} < 2{,}000$ km s^{-1}.

In the case of $\mathrm{FWHM}_{\mathrm{H}\beta}$, the virial factor has not been determined by Woo et al. (2010), but we can use the relations found above to derive a consistent expression. If we replace $\sigma_{\mathrm{H}\beta}$ with $\mathrm{FWHM}_{\mathrm{H}\beta}$ using Eq. 2.10, then Eq. 2.12 becomes

$$M_{\mathrm{BH}} = 10^{7.156}\mathrm{M}_{\odot} \left(\frac{\mathrm{FWHM}_{\mathrm{H}\beta}(\mathrm{rms})}{1000 \text{ km s}^{-1}} \right)^{1.584} \left(\frac{\lambda L_{5100,n}}{10^{44} \text{ erg s}^{-1}} \right)^{0.518} . \quad (2.14)$$

In order to use $\mathrm{FWHM}_{\mathrm{H}\beta}$ measured from SE spectra, $\mathrm{FWHM}_{\mathrm{H}\beta}$ from rms spectra in Eq. 2.14 can be replaced by $\mathrm{FWHM}_{\mathrm{H}\beta}$ from SE spectra, using Eq. 2.8. Then, the mass estimator becomes

$$M_{\mathrm{BH}} = 10^{6.966}\mathrm{M}_{\odot} \left(\frac{\mathrm{FWHM}_{\mathrm{H}\beta}(\mathrm{SE})}{1000 \text{ km s}^{-1}} \right)^{1.734} \left(\frac{\lambda L_{5100,n}}{10^{44} \text{ erg s}^{-1}} \right)^{0.518} . \quad (2.15)$$

Alternatively, we can use Eq. 2.13 and replace $\sigma_{\mathrm{H}\beta}$ with $\mathrm{FWHM}_{\mathrm{H}\beta}$ measured from SE spectra using Eq. 2.11. Then Eq. 2.13 becomes

$$M_{\mathrm{BH}} = 10^{6.985}\mathrm{M}_{\odot} \left(\frac{\mathrm{FWHM}_{\mathrm{H}\beta}(SE)}{1000 \text{ km s}^{-1}} \right)^{1.666} \left(\frac{\lambda L_{5100,n}}{10^{44} \text{ erg s}^{-1}} \right)^{0.518} , \quad (2.16)$$

which is almost identical to Eq. 2.15. For a consistency check, we compared the SE masses estimated from Eq. 2.15 with those from Eq. 2.16. They are consistent within ∼1%, indicating that Eq. 15 and 16 are essentially equivalent. As in the case of Eq. 2.8, for AGNs with $\mathrm{FWHM}_{\mathrm{H}\beta}$< 3,000 km s^{-1} we recommend readers use Eq. 2.16 instead of Eq. 2.15, since the SE masses derived from Eq. 16 are slightly more consistent with the masses determined from Eqs. 12 and 14.

The BH masses derived from the new mass estimators are consistent with each other within a ∼2% offset, indicating that the systematic difference in the line widths between SE and rms spectra is well calibrated. In contrast, the ∼0.2 dex scatter between various mass estimators reflects a lower limit to the uncertainties of our line-width dependent calibrations. In a sense, these new estimators can be thought of as introducing a line-width dependent virial factor to correct for the systematic difference of the geometry and kinematics of the gas contributing to the SE line profile and that contributing to the rms spectra. Regardless of the physical interpretation, these new recipes ensure that mass estimates from SE spectra and rms spectra can be properly compared.

2.5 Discussion and Conclusions

2.5.1 Random Uncertainty

We investigated the precision and accuracy of BH mass estimates based on SE spectra, using the homogeneous and high-quality spectroscopic monitoring of 9 local Seyfert 1 galaxies obtained as part of the LAMP project. We find that the uncertainty of SE mass estimates due to the AGN variability is ∼ 0.05 dex (∼12%). Our result is slightly less than that of Denney et al. (2009), who reported ∼ 0.1 dex random error due to the variability based on the investigation of Seyfert 1 galaxy NGC 5548 using data covering ∼10 years. For higher luminosity AGNs, the uncertainty due to variability can be smaller since the amplitude of variability inversely correlates with the luminosity (e.g., Cristiani et al. 1997). For example, by comparing SE spectra with mean spectra averaged over ∼10 multi-epoch data of 8 moderate-luminosity AGN, Woo et al. (2007) reported that intrinsic FWHM variation of the Hβ line is ∼7%, resulting in ∼15% random error in mass estimates.

In addition to the uncertainty related to variability, the total random uncertainty of SE mass estimators includes the uncertainty in the virial factor, and the scatter of the size-luminosity relation. The scatter of the AGN $M_{\mathrm{BH}}-\sigma_*$ relation (Woo et al. 2010) provides

an upper limit to the random object-to-object scatter in the virial factor of 0.43 dex. By adding 0.1 dex due to variability and 0.13 dex scatter from the size-luminosity relation in quadrature (assuming they are uncorrelated), the upper limit of the overall uncertainty of SE mass estimates is found to be 0.46 dex. This is consistent with the uncertainty of 0.4–0.5 dex estimated by Vestergaard & Peterson (2006). If we assume more realistically that 0.3 dex of the scatter in the $M_{\rm BH}-\sigma_*$ relation measured by Woo et al. (2010) is intrinsic scatter (e.g., Gültekin et al. 2010) and not due to uncertainties in the virial coefficient, then the uncertainty of the virial factor becomes 0.31 dex, resulting in an overall uncertainty of $\sim$0.35 dex in SE mass estimates. More direct measurements of the virial coefficient (e.g., Davies et al. 2006; Onken et al. 2007; Hicks & Malkan 2008; Brewer et al. 2011) are needed to break this degeneracy.

Note that measurement errors in the line width and continuum luminosity are negligible in our study owing to the high quality of the data. However, often such high-quality data are not available, and measurement errors of the line width in particular can be a significant contribution to the total error budget. For example, Woo et al. (2007) estimated the propagated uncertainty in the SE mass estimates due to the FWHM measurement errors as 0.11 dex (30%) based on spectra with a S/N of 10–15. Therefore, the estimated overall uncertainty of $\sim$0.35 dex should be taken as a lower limit for typical SE mass estimates based on optical spectra such as those from the Sloan Digital Sky Survey.

2.5.2 Difference in Line Profile between SE and RMS spectra

We confirmed that the Hβ line width measured from a mean or SE spectrum is systematically larger than that measured from an rms spectrum. The systematic difference corresponds to an average difference in virial product of $\sim$0.15–0.20 dex. However, the average difference is dominated by the narrowest line objects in the sample, with a decreasing trend toward broader line objects as shown in Fig. 2.15 (cf., Collin et al. 2006). These results indicate that for narrow-line AGNs (FWHM$_{\rm H\beta} < 3000$ km s^{-1}), BH masses based on SE spectra can be overestimated by $\sim$25–35% if standard recipes are used. In order to correct for the systematic difference of the line profile, we derive new empirically calibrated line-width dependent SE mass estimators.

It is important to notice that line-width measurements from rms spectra can also be systematically biased by residuals of narrow-line components, Fe II, and host-galaxy starlight. Fluctuations of these components can generate signatures in the rms spectra, resulting in

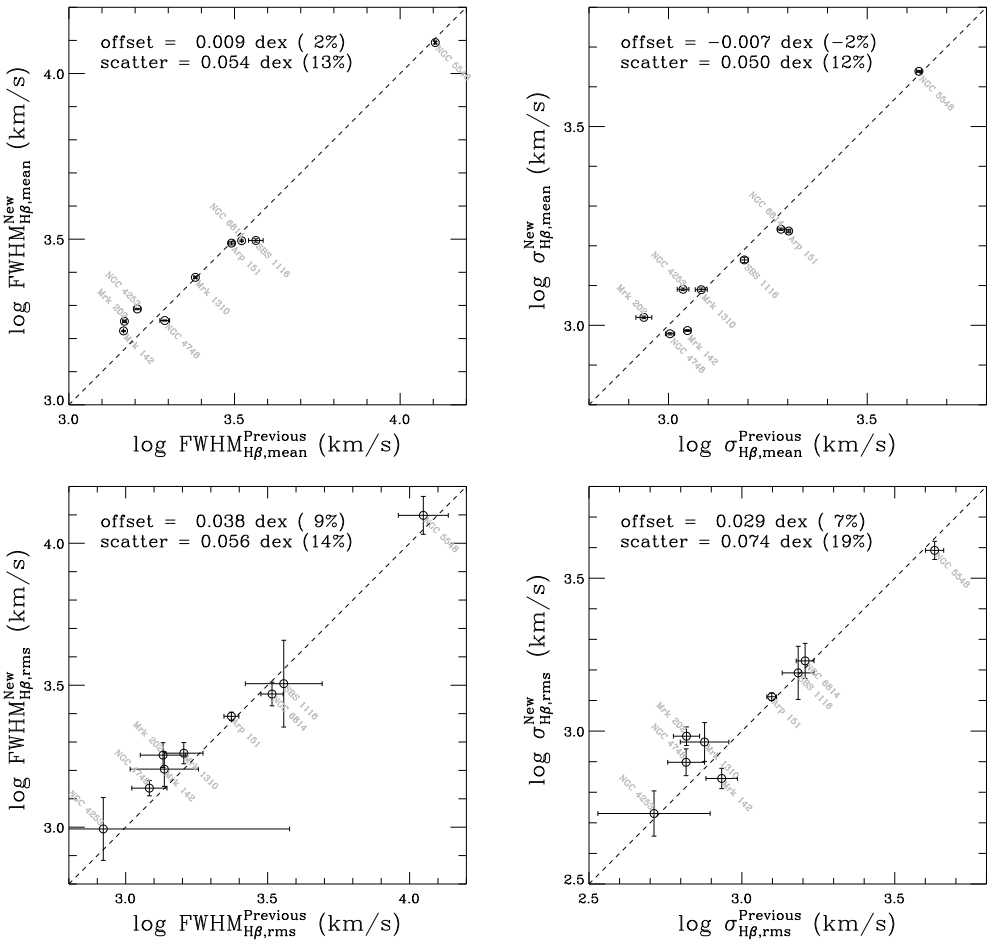

Figure 2.17 Comparison of $\mathrm{FWHM}_{\mathrm{H}\beta}$ (left) and $\sigma_{\mathrm{H}\beta}$ measurements (right) based on the new methods (this work) and the previous traditional methods (Bentz et al. 2009c), using the mean (top) and rms spectra (bottom). The average difference of the Hβ line widths between two methods is relatively small. However, the large scatter (12–19%) indicates that the contribution from individual effects, e.g., subtraction of starlight, Fe II, or He II varies on an object-by-object basis.

a biased line profile and an improper continuum fit. We have demonstrated several new strategies to mitigate these effects. First, we adopt two robust methods to derive rms spectra — using S/N weights and adopting a maximum likelihood approach — that minimize the contamination of low-S/N spectra when there is a large range in S/N. Second, we subtract Fe II and host-galaxy starlight based on spectral decomposition analysis of each individual-epoch spectrum before making the rms and mean spectra. These new methods substantially improve the quality of rms spectra in measuring the width of the Hβ line for AGNs with strong starlight, Fe II, or blended He II. Especially in these cases we recommend the new methods as an useful alternative to the traditional simple methods in future reverberation mapping studies (and possibly to revisit previous studies).

The new methods introduced here differ from previous ones. The overall goal is to account for systematic uncertainties and correct for biases stemming from known effects such as stellar line contamination. However, it is possible that they might introduce biases due to unknown systematics, especially when directly compared to other measurements obtained with previous techniques. An absolute comparison would require a third way to measure the same quantities (e.g., BH mass); however, we can estimate any differential bias by comparing our measurements to those given by Bentz et al. (2009c) using traditional methods. On average, $\sigma_{\rm H\beta}$ measured with our new methods increases by 7 ± 6% and FWHM$_{\rm H\beta}$ increases by 9 ± 4% (see Fig. 2.17), suggesting that the systematic uncertainties due to the new methods is lower than 10%, although we assume the difference is entirely caused by the systematic uncertainty of the new scheme.

The average small difference between our new measurements and those of Bentz et al. (2009c) is due to the fact that various effects, e.g., S/N weighting, prior subtraction of host galaxy starlight and blended emission lines, line profile fitting, and removal of narrow Hβ, are mixed together and canceled out for individual objects. For example, if we separate the effect of host galaxy starlight, the difference of the line dispersion measurements with/without removal of host galaxy starlight is much larger than the average difference between Bentz et al. (2009c) and ours (see §3.3.2). The 10-20% rms scatter between previous (Bentz et al. 2009c) and new measurements indicates that the contribution of each effect varies on an object-by-object basis (see Fig. 2.17). The new methods are useful for reducing the uncertianites of individual BH masses due to those various effects, and better constraining the intrinsic scatter of the $M_{\rm BH} - \sigma_*$ relation (e.g., Woo et al. 2010). When other systematic uncertainites, i.e., the virial coefficient, can be constrained and reduced in the future, the new methods will become more important for BH mass determination.

From the point of view of interpretation, the systematically narrower line width in the rms spectra can be explained by the photoionization calculations of Korista & Goad (2004), which predict that high-velocity gas in the inner BLR has lower responsivity, leading to lower variability of the line wings and therefore a narrower profile in the rms spectrum. However, it is not clear why the effect should be stronger for the narrower line AGNs. Further investigations are required to reveal the nature of this systematic trend. We conclude by noting that our study is limited to relatively low luminosity and narrow line width (and hence small BH mass) AGNs. In future work we plan to expand our study to cover a larger dynamic range in luminosity and line width.

2.5.3 Implications for the Evolution of BH Host-Galaxy Scaling Relations

Virtually all observational studies of the evolution of the BH host-galaxy scaling relations over cosmic time are based on SE mass estimates. Evolutionary trends are generally established by comparing measurement of distant samples (based on SE BH mass estimates) with the local scaling relations. The latter can be determined either based on SE BH mass estimates, or on reverberation BH mass estimates, or on spatially resolved kinematics. In the case of comparison between SE mass estimates at high redshift and mass estimates of local objects based on different methods, it is essential that the mass estimates be properly calibrated. For example, the positive bias of Hβ line width of SE spectra compared to the rms spectra could lead to overestimation of BH masses for distant samples, if compared with local samples based on rms spectra.

However, as shown in Figures 2.13 and 2.14, this bias is only significant for the narrower line objects with BH mass $< 10^7$ $M_\odot$). Typically, high-redshift studies such as those by Bennert et al. (2010) and Merloni et al. (2010) focus on higher mass BHs, where the bias is believed to be negligible. We note that one could completely eliminate this bias by comparing distant and local BH mass estimates based entirely on self-consistent SE BH mass estimates (Woo et al. 2008;Bennert et al. 2011a,b). Even then, of course, one must keep in mind the differential nature of the measurement. For example, the slope inferred for the local scaling relations based on SE spectra (e.g., Greene & Ho 2006) may be biased with respect to the true slope if the mass estimator is biased at low masses, and yet one may still infer the correct evolution even for low masses if the bias does not change with redshift.

References

Barth, A. J., Greene, J. E., & Ho, L. C., 2005, ApJ, 619, L151

Barth, A. J., et al. 2011, ApJ, 732, 121

Bennert, V. N., et al. 2010, ApJ, 708, 1507

Bennert, V. N., et al. 2011a, ApJ, 726, 59

Bennert, V. N., et al. 2011b, arXiv:1102.1975

Bentz, M. C., Peterson, B. M., Pogge, R. W., Vestergaard, M., & Onken, C. A. 2006, ApJ, 644, 133

Bentz, M. C., Peterson, B. M., Pogge, R. W., & Vestergaard, M. 2009a, ApJ, 694, L166

Bentz, M. C., et al. 2009b, ApJ, 697, 160

Bentz, M. C., et al. 2009c, ApJ, 705, 199

Brewer, B. J., et al. 2011, ApJ, 733, L33

Blandford, R. D., & McKee, C. F. 1982, ApJ, 225, 419

Boroson, T. A., & Green, R. F. 1992, ApJS, 80, 109

Bruzual, G., & Charlot, S. 2003, MNRAS, 344, 1000

Cristiani, S., Trentini, S., La Franca, F., & Andreani, P. 1997, A&A, 321, 123

Collin, S., Kawaguchi, T., Peterson, B. M., & Vestergaard, M. 2006, A&A, 456, 75

Davies, R. I., et al. 2006, ApJ, 646, 754

Davis, S. W., Woo, J.-H., & Blaes, O. M., 2007, ApJ, 668, 682

Decarli, R., Falomo, R., Treves, A., Labita, M., Kotilainen, J. K., & Scarpa, R., 2010, MNRAS, 402, 2453

Denney, K. D., et al. 2009, ApJ, 692, 246

Denney, K. D., et al. 2010, ApJ, 721, 715

Dietrich, M., Crenshaw, D. M., & Kraemer, S. B., 2005, ApJ, 623, 700

Ferrarese, L., & Ford, H. 2005, Space Sci. Rev., 116, 523

Ferrarese, L., & Merritt, D. 2000, ApJ, 539, L9

Fine, S., et al. 2008, MNRAS, 390, 1413

Gebhardt, K., et al. 2000, ApJ, 539, L9

Greene, J. E., & Ho, L. C. 2006, ApJ, 641, 21

Gultekin, K., et al. 2009, ApJ, 698, 198

Hicks, E. K. S., & Malkan, M. A. 2008, ApJS, 174, 31

Hopkins, P. F., et al. 2006, ApJS, 163, 1

Kaspi, S., Maoz, D., Netzer, H., Peterson, B. M., Vestergaard, M., & Jannuzi, B. T. 2005, ApJ, 629, 61

Kaspi, S., Smith, P. S., Netzer, H., Maoz, D., Jannuzi, B. T., & Giveon, U. 2000, ApJ, 533, 631

Kauffmann, G., & Haehnelt, M. 2000, MNRAS, 311, 576

Kelly, B. C., 2007, ApJ, 665, 1489

Kollatschny, W., 2003, A&A, 407, 461

Kollmeier, J., A., 2006, ApJ, 648, 128

Kormendy, J., & Richstone, D. 1995, ARA&A, 33, 581

Kormendy, J., & Gebhardt, K. 2001, in 20th Texas Symposium on Relativistic Astrophysics, ed. J. C. Wheeler & H. Martel (New York: AIP, vol. 586), 363

Korista, K. T., & Goad, M. R., 2004, ApJ, 606, 749

Lauerrconi, T., R., et al. 2007, ApJ, 670, 249

Marconi, A., & Hunt, L. K. 2003, ApJ, 589, L21

Marconi, A., et al. 2008, ApJ, 678, 693

Magorrian, J. et al. 1998, AJ, 115, 2285

Markwardt, C. B. 2009, in Astronomical Data Analysis Software and Systems XVIII, ed. D. A. Bohlender, D. Durand, & P. Dowler (San Francisco: ASP), 251

McGill, K. L., Woo, J.-H., Treu, T., & Malkan, M. A. 2008, ApJ, 673, 703

McLure, R. J., & Dunlop, J. S. 2004, MNRAS, 352, 1390

Merloni, A. et al. 2010, ApJ, 708, 137

Onken, C. A., Ferrarese, L., Merritt, D., Peterson, B. M., Pogge, R. W., Vestergaard, M., & Wandel, A. 2004, ApJ, 615, 645

Netzer, H., & Marziani, P. 2010, ApJ, 724, 318

Onken, C. A., et al. 2007, ApJ, 670, 105

Pancoast, A., Brewer, B. J., & Treu, T. 2011, ApJ, 730, 139

Peng, C. Y., Impey, C. D., Rix, H.-W., Kochanek, C. S., Keeton, C. R., Falco, E. E., Lehár, J., & McLeod, B. A. 2006, ApJ, 649, 616

Peterson, B. M., 1993, PASP, 105, 247

Peterson, B. M., & Wandel, A., 1999, ApJ, 521, L95

Peterson, B. M., & Wandel, A., 2000, ApJ, 540, L13

Peterson, B. M., et al. 2004, ApJ, 613, 682

Robertson, B. et al. 2006, ApJ, 641, 90

Sergeev, S. G., Pronik, V. I., Sergeeva, E. A., Malkov, Yu. F. Sergeev, S. G., Pronik, V. I., Sergeeva, E. A., & Malkov, Yu. F., 1999, AJ, 118, 2658

Shapovalova, A. I., et al. 2004, å, 422, 925

Shen, Y., Greene, J. E., Strauss, M. A., Richards, G. T., & Schneider, D. P. 2008, ApJ, 680, 169

Shen, Y., & Kelly, B. C., 2010, ApJ, 713, 41

Shen, Y., et al. 2011, ApJS, 194, 45

Shields, J. W., Ferland, G. J., & Peterson, B. M. 1995, ApJ, 441, 507

Tremaine, S., et al. 2002, ApJ, 574, 740

Treu, T., Woo, J.-H., Malkan, M. A., & Blandford, R. D. 2007, ApJ, 667, 117

van Groningen, E., & Wanders, I. 1992, PASP, 104, 700

van der Marel, R. P., & Franx, M. 1993, ApJ, 407, 525

Vanden Berk, D. E., et al. 2001, AJ, 122, 549

Vestergaard, M., & Peterson, B. M. 2006, ApJ, 641, 689

Wandel, A., Peterson, B. M., & Malkan, M. A. 1999, ApJ, 526, 579

Wilhite, B. C., Brunner, R. J., Schneider, D. P., & Vanden Berk, D. E. 2007, ApJ, 669, 791

Woo, J.-H., & Urry, M., 2002, ApJ, 579, 530

Woo, J.-H., Urry, C. M., Lira, P., van der Marel, R. P., & Maza, J., 2004, ApJ, 617, 903

Woo, J.-H., Treu, T., Malkan, M. A., & Blandford, R. D. 2006, ApJ, 645, 900

Woo, J.-H., Treu, T., Malkan, M. A., Ferry, M. A., & Misch, T. 2007, ApJ, 661, 60

Woo, J.-H., Treu, T., Malkan, M. A., & Blandford, R. D., 2008, ApJ, 681, 925

Woo, J.-H., et al. 2010, ApJ, 716, 269

Chapter 3

Recalibration of the virial factor and $M_{\rm BH}-\sigma_*$ relation for local active galaxies

(This chapter is published in The Astrophysical Journal Supplement Series[1]*.)*

3.1 Introduction

Supermassive black holes (SMBHs) are thought to be ubiquitous in the centers of virtually all massive galaxies (e.g., Kormendy & Richstone 1995; Richstone et al. 1998; Ferrarese & Ford 2005). The close connection of black hole growth to galaxy evolution is inferred from the discovery of tight correlations between the masses of SMBHs ($M_{\rm BH}$) and the global properties of host galaxies, such as the stellar velocity dispersion (σ_*; Ferraresse & Merritt 2000; Gebhardt et al. 2000) bulge luminosity ($L_{\rm bul}$; Magorrian et al. 1998; Marconi & Hunt 2003), and bulge mass ($M_{\rm bul}$; Häring & Rix 2004). The origin of these connections has been investigated in theoretical studies of galaxy evolution either through the introduction of active galactic nucleus (AGN) feedback (e.g., Kauffmann & Haehnelt 2000; Di Matteo et al. 2005; Croton et al. 2006; Hopkins et al. 2006; Bower et al. 2006; Somerville et al. 2008; Booth & Schaye 2009) or as simply being the result of a hierarchical merging framework (e.g., Peng 2007; Hirschmann et al. 2010; Janke & Maccio 2011). The interplay between

[1] Park et al. 2012, ApJS, 203, 6

the black holes and galaxies is now one of the basic ingredients in our understanding of galaxy formation and evolution.

In order to better understand the origin and evolution of the SMBH-host galaxy connection, AGN demographics, and the growth of the SMBHs through cosmic time, an accurate and precise measurement of black hole mass is essential. Stellar/gas dynamical modeling is commonly used to measure the black hole masses in quiescent galaxies. However, this technique requires high spatial resolution to resolve the sphere-of-influence of the black hole, thereby limiting it to the local universe. In active galaxies, the black hole mass can be determined by utilizing AGN variability. The reverberation mapping technique (Blandford & McKee 1982; Peterson 1993) has been used to estimate the mean size of the broad line region (BLR, $R_{\rm BLR}$) by cross-correlating the continuum light curve with the broad emission line light curve. Combining $R_{\rm BLR}$ with the line-of-sight velocity width (ΔV) measured from the variable component of the broad emission line provides a virial black hole mass estimate as $M_{\rm BH} \equiv f \Delta V^2 R_{\rm BLR}/G$, where G is the gravitational constant and f is the virial factor that converts the measured virial product into the actual black hole mass. This technique is also limited to around 50 AGNs to date since it requires extensive photometric and spectroscopic monitoring observations. This technique has established the empirical size-luminosity relation (Wandel et al. 1999; Kaspi et al. 2000; Bentz et al. 2006a, 2009a), which is the basis for the single-epoch (SE) method. In the SE method, one simply substitutes the time-consuming BLR size measurement with AGN luminosity using the size-luminosity relation. This therefore provides estimates of black hole masses for broad line AGNs from a single spectroscopic observation, thus expanding the sample size substantially at any redshift. However, both methods suffer from the large uncertainty stemming from the unknown virial factor (see Park et al. 2012), which depends on the geometry and kinematics of BLR of individual AGNs.

Instead, an empirically calibrated average virial factor has been applied to most AGN black hole mass estimates, except for only a few objects where dynamical mass measurements can be obtained (e.g., Davies et al. 2006; Onken et al. 2007; Hicks & Malkan 2008). The first calibration of the virial factor was performed by Onken et al. (2004). They derived $\langle f \rangle = 5.5 \pm 1.8$ based on a sample of 14 AGNs, for which both reverberation masses and stellar velocity dispersions were available, by forcing the AGN host galaxies to obey the same $M_{\rm BH} - \sigma_*$ relationship as for quiescent galaxies. By enlarging the dynamical range of the AGN sample, Woo et al. (2010) determined the virial factor as $\log\langle f \rangle = 0.72^{+0.09}_{-0.10}$ (i.e., $\langle f \rangle = 5.2 \pm 1.2$) based on an updated reverberation sample of 24 AGNs, which included

8 low-mass local Seyfert 1 galaxies from the Lick AGN Monitoring project (Bentz et al. 2009b). They provided the upper limit of uncertainty in the derived virial factor as 0.43 dex based on the intrinsic scatter in the relation. In contrast, Graham et al. (2011) reported $\langle f \rangle = 2.8^{+0.7}_{-0.5}$, based on their updated $M_{\rm BH} - \sigma_*$ relation of quiescent galaxies, and an upated AGN sample, which is a factor of 2 smaller than the aforementioned values. Graham et al. (2011) commented that the value of $\langle f \rangle$ might be even further lowered due to the effect of radiation pressure (see Marconi et al. 2008). This correspondingly reduces the black hole mass estimates for most AGNs by that amount, influencing all of the studies incorporating single-epoch AGN black hole masses. Thus it is important to investigate the origin of this difference and check for possible biases in the calibration process.

Since the derived $M_{\rm BH} - \sigma_*$ relation of quiescent galaxies is used to calibrate the virial factor in AGN mass estimators, under the assumption that the same $M_{\rm BH} - \sigma_*$ relation holds for AGN host galaxies, it is important to investigate the differences in the $M_{\rm BH} - \sigma_*$ relations of quiescent galaxies reported in the literature, and to study their effect on the derived virial factors. Originally the slopes of the $M_{\rm BH} - \sigma_*$ relation reported by Ferrarese & Merritt (2000) and Gebhardt et al. (2000) were 4.8 ± 0.5 and 3.75 ± 0.3 based on 12 and 26 galaxy samples, respectively. After that, various slopes have been reported in the literature, ranging from 3.68 to 5.95. Although the slopes are roughly consistent with the theoretical expectations of $M \propto \sigma^5$ (Silk & Rees 1998) and $M \propto \sigma^4$ (Fabian 1999), their difference and change are noteworthy. The possible origin of the difference in slopes has been investigated in the literature. The related factors are: (1) the type of regression method adopted (Tremaine et al. 2002; Novak et al. 2006; see Kelly 2007 for general applications of regression), (2) the size of the assigned uncertainty on the velocity dispersion (Merritt & Ferrarese 2001; Tremaine et al. 2002), (3) the velocity dispersion measures used (Tremaine et al. 2002), (4) the adopted value of velocity dispersion for the Milky Way (Merritt & Ferrarese 2001; Tremaine et al. 2002), (5) the spatial resolution of the data for the resolved BH sphere-of-influence (Ferrarese & Ford 2005; see also Gültekin et al. 2009, 2011; Batcheldor 2010) (6) the morphological type of the sample used (Hu 2008; Graham 2008; Gültekin et al. 2009; Greene et al. 2010; Graham et al. 2011).

To understand the origin of the differences in the derived $M_{\rm BH} - \sigma_*$ relationships, we investigate in this work 3 main issues: the difference in samples, the difference in regression methods, and the direction of the regression analysis. Recently, with new measurements and improved modeling the number of dynamical mass measurements is continuously growing both at the high-mass and low-mass end regimes. To date, a total of 67 black hole masses in

quiescent galaxies has been measured via stellar/gas/maser kinematics (see the most recent compilation from McConnell et al. 2011 and references therein). Therefore, it is presently a good time to investigate what effect the difference in samples has on the derived $M_{\rm BH}-\sigma_*$ relation using the largest sample ever. In addition, various estimators have been used for the regression analysis in the black hole scaling relation studies: `FITEXY` (e.g., Tremaine et al. 2002, Novak et al. 2006, Kim et al. 2008, Li et al. 2011, Beifiori et al. 2012, Vika et al. 2012, McConnell et al. 2011), `BCES` (e.g., Ferrarese & Merritt 2000, Ferrarese & Ford 2005, Hu 2008, Bentz et al. 2009a, Bennert et al. 2010, Graham et al. 2011), `Maximum likelihood` (e.g., Gültekin et al. 2009, Greene et al. 2010, Schulze & Gebhardt 2011), Bayesian approach (`linmix_err`) (e.g., Sani et al. 2011, Xiao et al. 2011, Mancini & Feoli 2012). Thus, in order to investigate the difference in the derived scaling relationships caused by the sample selection, it is important to investigate differences between the estimators for the $M_{\rm BH}-\sigma_*$ relation analysis. Finally, adopting the choice of independent variable is another issue for determining the $M_{\rm BH}-\sigma_*$ relation. Motivated by the suggestion by Graham et al. (2011) to use the 'inverse' fit to calibrate the single-epoch AGN mass estimates, we present results based on both of the forward and inverse regressions.

This chapter is organized as follows. In the next section, we describe the most commonly used regression methods in astronomy with their explicit implementations. In Section 3.3, we re-measure the $M_{\rm BH}-\sigma_*$ relation using 3 different samples from the literature and investigate the difference due to the regression methods and samples. In Section 3.4 we present our main result for the calibrated virial factors and discuss the difference based on the regression methods and samples. The difference from the direction of regression is discussed in Section 3.5. Finally, we summarize and conclude in Section 5.5.

3.2 Linear regression techniques

Linear regression methods[2] in astronomy were exhaustively discussed in the pioneering paper, Isobe et al. (1990). They provided formulae for 5 unweighted bivariate linear regression coefficients with their error estimates, and recommended the bisector line for the case of treating the variables symmetrically. The second paper in the series, Feigelson & Babu (1992), extended their work by accommodating bootstrap and jackknife resampling procedures for error estimation, weighted regression, and truncated/censored regressions. In addition, they suggested practical strategies for linear regression problems in astronomy.

[2]For recent reviews, please see Hogg et al. (2010) and Caimmi (2011a,b).

The `BCES` estimator (Bivariate Correlated Errors and intrinsic Scatter) was proposed by Akritas & Bershady (1996) in order to incorporate, heteroscedastic measurement errors, intrinsic scatter, and correlation in the measurement errors. The method of minimizing a χ^2 statistic (`FITEXY`), which account for measurement error in both the dependent and independent variable, was modified by Tremaine et al. (2002) to incorporate intrinsic scatter. They added the unknown constant intrinsic variance term in quadrature to the error of the dependent variable and determined it so that the reduced χ^2 is equal to a value of unity. Based on the Monte Carlo simulations performed by Tremaine et al. (2002) and Novak et al. (2006), they concluded that the modified `FITEXY` is a better estimator than the `BCES`. In particular, Tremaine et al. (2002) concluded that the `BCES` tends to be biased when the sample size is small or the mean square of the x errors is comparable to the variance of x distribution, and that it becomes inefficient when there is a single measurement with much larger error than others.

Kelly (2007) developed a sophisticated Bayesian linear regression technique, termed `linmix_err`. It accounts for intrinsic scatter in the relationship, heteroscedastic measurement errors in both the independent and dependent variables, and correlation between the measurement errors. This method uses a Gaussian mixture model for the distribution of independent variables, which is shown to work well particularly when the measurement errors are large by avoiding the bias incorporated if the choice of x-distribution model is incorrect (also noted in Auger et al. 2010). The method assumes that the measurement errors and intrinsic scatter are Gaussian, and it accommodates multiple independent variables, nondetections, and selection effects.

Recently, Gültekin et al. (2009) applied a `maximum likelihood` method to determine the $M-\sigma$ and $M-L$ relations by naturally incorporating an intrinsic scatter and upper limits. They also extensively investigated the distributional forms for the measurement error and intrinsic scatter. However, they did not include a model for the distribution of the independent variable, but instead used Monte Carlo sampling to assess the impact of the measurement errors in the independent variable on the parameter estimates.

To sum up, the four methods for linear regression that have been used to characterize the black hole/host galaxy scaling relationships are: (1) `BCES` (Akritas & Bershady 1996), (2) `FITEXY` (Tremaine et al. 2002), (3) `Maximum likelihood` (Gültekin et al. 2009), (4) `LINMIX_ERR` (Kelly 2007). In this section we explicitly show our implementation and usage of each method. We assume the model of $y = \alpha + \beta x$ in the following analysis.

3.2.1 BCES estimator

The `BCES`($Y|X$) estimator is implemented using the formula described in Akritas & Bershady (1996),

$$\beta = \frac{\mathrm{cov}(x,y) - \langle \sigma_{xy} \rangle}{\mathrm{var}(x) - \langle \sigma_x^2 \rangle}, \tag{3.1}$$

$$\alpha = \langle y \rangle - \beta \langle x \rangle , \tag{3.2}$$

where cov(x,y) is the covariance of x and y, σ_x is the standard deviation of the measurement error (i.e., standard measurement error) in x, var(x) is the variance of x, and σ_{xy} is the covariance between the measurement errors in x and y. The intrinsic variance (i.e., variance in the intrinsic scatter) is estimated following the expression given in Cheng & Riu (2006) and Kelly (2007),

$$\sigma_{\mathrm{int}} = \sqrt{\mathrm{var}(y) - \langle \sigma_y^2 \rangle - \beta \left[\mathrm{cov}(x,y) - \langle \sigma_{xy} \rangle \right]}. \tag{3.3}$$

The uncertainties in the parameters can be estimated with the bootstrap or using analytical estimates given in Akritas & Bershady (1996). In this work we assume $\sigma_{xy} = 0$ (i.e., uncorrelated measurement errors), as most values of x and y in the $M_{\mathrm{BH}} - \sigma_*$ samples were independently measured and the covariances between the measurement errors are not provided in the literature. Thus, simply assuming the zero covariance seems to be more reasonable for these very heterogeneously collected $M_{\mathrm{BH}} - \sigma_*$ samples. In addition, there is no result incorporating the correlated measurement errors (i.e., σ_{xy}) to $M_{\mathrm{BH}} - \sigma_*$ fitting in the literature at least to our knowledge. Thus, to compare consistently with the results from the literature we here set $\sigma_{xy} = 0$.

3.2.2 FITEXY estimator

The `FITEXY` (Press et al. 1992), modified by Tremaine et al. (2002), is implemented in our work in IDL using the `mpfit` (Markwardt 2009) Levenberg-Marquardt least-squares minimization routine. Note that our implementation is basically similar to that given in Williams et al. (2010) [3]. It performs the linear regression by minimizing

$$\chi^2 = \sum_{i=1}^{N} \frac{(y_i - \alpha - \beta x_i)^2}{\sigma_{y,i}^2 + \beta^2 \sigma_{x,i}^2 + \sigma_{\mathrm{int}}^2}, \tag{3.4}$$

[3] http://purl.org/mike/mpfitexy

where α and β are the regression coefficients, σ_x and σ_y are the standard deviation in the measurement errors, and $\sigma^2_{\rm int}$ is the intrinsic variance. The value of $\sigma_{\rm int}$ is iteratively adjusted as an effective additional *y* error by repeating the fit until one obtains $\chi^2/(N-2) = 1$ (i.e., following the suggested iterative procedure given in Bedregal et al. 2006 and Bamford et al. 2006). If after the initial iteration the reduced χ^2 is less than one, then no further iterations occur and one sets $\sigma_{\rm int} = 0$. We estimate uncertainties in the regression parameters with the bootstrap method.

3.2.3 Maximum Likelihood estimator

The method of `maximum likelihood` is implemented similarly as given in Gültekin et al. (2009) (see also Woo et al. 2010). Under the assumptions of uncorrelated Gaussian measurement errors in both coordinates and Gaussian intrinsic scatter along *y*, the Gaussian likelihood function is given by

$$\mathcal{L} = \prod_{i=1}^{N} \frac{1}{\sqrt{2\pi\sigma_i^2}} \exp\left[-\frac{(y_i-\alpha-\beta x_i)^2}{2\sigma_i^2}\right], \tag{3.5}$$

where

$$\sigma_i^2 = \sigma_{y,i}^2 + \beta^2\sigma_{x,i}^2 + \sigma_{\rm int}^2. \tag{3.6}$$

Note that this likelihood function implicitly assumes that the independent variable is uniformly distributed (i.e., a uniform prior for the intrinsic distribution of *x*). Then the log-likelihood function is

$$\begin{aligned} -2\ln\mathcal{L} &= \sum_{i=1}^{N} \ln\left(2\pi\sigma_i^2\right) + \sum_{i=1}^{N} \frac{(y_i-\alpha-\beta x_i)^2}{\sigma_i^2} \\ &= \sum_{i=1}^{N} \ln\left(2\pi\sigma_i^2\right) + \chi^2. \end{aligned} \tag{3.7}$$

This likelihood approach is more complete than the χ^2 method given in Equation (3.4) in a sense that it includes the intrinsic variance term in both the normalization and exponent of the likelihood function, and determines it simultaneously with the other regression coefficients. To estimate the best-fit parameters of $(\alpha, \beta, \sigma_{\rm int})$ using the maximum likelihood estimate (MLE), we minimize $-2\ln\mathcal{L}$ using the downhill simplex method implemented as `AMOEBA` (Press et al. 1992) in IDL. Then we adopt uncertainties in parameters as the average difference where $\ln\mathcal{L}$ decreases from its maximum value by 0.5. We also estimate the parameter errors using the bootstrap method.

3.2.4 Bayesian estimator (linmix_err)

The Bayesian linear regression routine, `linmix_err`, developed by Kelly (2007) is available from the NASA IDL astronomy user's library[4]. Here we briefly summarize the method. For details, please refer to Kelly (2007).

This method assumes Gaussian intrinsic scatter, Gaussian measurement errors, and a weighted sum of K Gaussian functions for the distribution of the independent variable. The choice of a Gaussian mixture model was motivated in that it can not only approximate well various intrinsic distributions of the independent variable, but it is also a mathematically convenient conjugate family. The full measured data likelihood function is expressed as a mixture of bivariate normal distributions

$$\mathcal{L} = \prod_{i=1}^{N} \sum_{k=1}^{K} \frac{\pi_k}{2\pi |V_{k,i}|^{1/2}} \exp\left[-\frac{1}{2} (z_i - \zeta_k)^T V_{k,i}^{-1} (z_i - \zeta_k) \right], \tag{3.8}$$

where $\sum_{k=1}^{K} \pi_k = 1$ and the measured data, means, and covariance matrices are, respectively,

$$z_i = \begin{pmatrix} y_i \\ x_i \end{pmatrix}, \tag{3.9}$$

$$\zeta_k = \begin{pmatrix} \alpha + \beta\mu_k \\ \mu_k \end{pmatrix}, \tag{3.10}$$

$$V_{k,i} = \begin{pmatrix} \beta^2\tau_k^2 + \sigma_{\rm int}^2 + \sigma_{y,i}^2 & \beta\tau_k^2 + \sigma_{xy,i} \\ \beta\tau_k^2 + \sigma_{xy,i} & \tau_k^2 + \sigma_{x,i}^2 \end{pmatrix}. \tag{3.11}$$

In order to calculate the posterior probability distribution of the model parameters for the given measured data, it adopts uniform prior distributions on the regression parameters $(\alpha, \beta, \sigma_{\rm int}^2)$. It also adopt a Dirichlet, normal, and scaled inverse-χ^2 prior on the mixture model parameters (π_k, μ_k, τ_k^2), respectively. The data is 'fit' using a Markov Chain Monte Carlo (MCMC) sampler. For each regression parameter, we take the best-fit value and uncertainty as the posterior median and posterior standard deviation from the marginal posterior distributions using the 100,000 random draws returned by the MCMC sampler. Note that the likelihood function given in Equation (3.8) converges to that of the `maximum likelihood` method given in Equation (3.5) if the distribution for the independent variable is assumed to be uniform rather than a mixture of normals and the measurement errors are uncorrelated.

[4] http://idlastro.gsfc.nasa.gov/

As an illustration, we also used the likelihood function in the case of a single Gaussian model ($K = 1, \pi_k = 1$) for the distribution of independent variable with uncorrelated measurement errors ($\sigma_{xy,i} = 0$). For comparison with the procedure assuming a uniform intrinsic distribution (MLE) given in Section 3.2.3, we compute the maximum likelihood estimate (i.e., $\mathrm{MLE_{1G}}$) utilizing the likelihood function derived from assuming the distribution of independent variable is a Gaussian.

In the following sections, we determine the α, β, and $\sigma_{\rm int}$ parameters with the corresponding error estimates for the $M_{\rm BH}-\sigma_*$ relation using each regression technique described above.

3.3 The $M_{\rm BH}-\sigma_*$ relations

The $M_{\rm BH}-\sigma_*$ relation is generally expressed as the log-linear form,

$$\log(M_{\rm BH}/M_\odot) = \alpha + \beta \log(\sigma_*/200 \text{ km s}^{-1}). \tag{3.12}$$

Here $y = \log(M_{\rm BH}/M_\odot)$ and $x = \log(\sigma_*/200 \text{ km s}^{-1})$. We assume that the measurement errors in the logarithms of mass and stellar velocity dispersion are symmetric by taking the symmetric interval in log space, i.e., $\epsilon_{\log M_{\rm BH}} = \left(\log M_{\rm BH}^{\rm upper} - \log M_{\rm BH}^{\rm lower}\right)/2$ and $\epsilon_{\log \sigma_*} = \left(\log \sigma_*^{\rm upper} - \log \sigma_*^{\rm lower}\right)/2$. Following Graham et al., for their data we assume that the measurement errors on the logarithm of mass are symmetric by taking the average of upper and lower 1σ uncertainties on the linear scale and propagating it onto the logarithmic scale, i.e., $\epsilon_{\log M_{\rm BH}} = 0.5\left(\epsilon_{M_{\rm BH}}^{\rm upper} + \epsilon_{M_{\rm BH}}^{\rm lower}\right)/(M_{\rm BH}\ln 10)$. The measurement errors in the logarithm of the dispersion are $\epsilon_{\log \sigma_*} = 0.5\left(\epsilon_{\sigma_*}^{\rm upper} + \epsilon_{\sigma_*}^{\rm lower}\right)/(\sigma_*\ln 10)$. However, note that this choice of error bars does not significantly affect our results.

3.3.1 Re-measuring the relation with four methods

In this section we consistently re-derive the $M_{\rm BH}-\sigma_*$ relation using three literature samples to check our implementation of the fitting methods. Figure 3.1 shows the re-estimated $M_{\rm BH}-\sigma_*$ relations of the data from Gültekin et al. 2009 (*top*), McConnell et al. 2011 (*middle*), and Graham et al. 2011 (*bottom*) using the various methods described in the previous section. We also include the ordinary least squares (hereafter `OLS`) line as a reference. For the sample of 49 galaxies without upper limits from Table 1 in Gültekin et al. (2009), we also follow the same fitting scheme of their maximum likelihood estimator, which is slightly different to the method described in Section 3.2.3. Using the Gültekin et al. (2009) procedure,

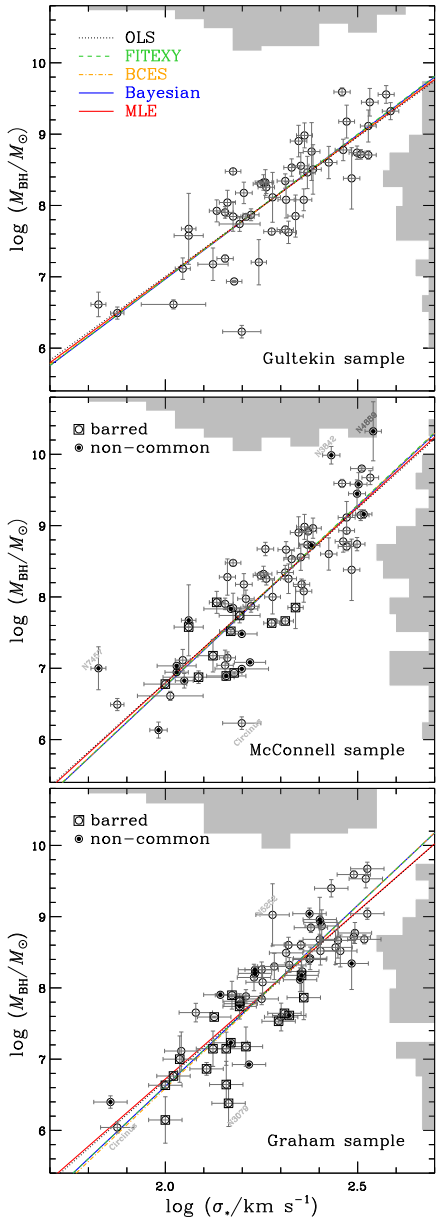

Figure 3.1 The $M_{\rm BH}-\sigma_*$ relations using each dataset from Gültekin et al. 2009 (*top*), McConnell et al. 2011 (*middle*), and Graham et al. 2011 (*bottom*). Each regression line is derived from five different methods (see the text and Table 3.1). The sample distributions for the logarithms of black hole masses and stellar velocity dispersions are shown in the right side and top side of each panel as grey histograms. The non-overlapping sample in between the McConnell and Graham data are marked with a filled dot inside open circles. Note that the common sample has 50 galaxies. The barred galaxies are marked with an open square enclosing open circles.

Table 3.1. Re-estimation of Parameters for the $M_{\rm BH}-\sigma_*$ Relation of Quiescent Galaxy Samples: $\log(M_{\rm BH}/M_\odot) = \alpha + \beta\log(\sigma_*/200\ {\rm km\ s^{-1}})$

Method	Forward regression			Inverse regression[a]		
	α	β	$\sigma_{\rm int}$	$\alpha=-\alpha_{\rm inv}/\beta_{\rm inv}$	$\beta=1/\beta_{\rm inv}$	$\sigma_{\rm int}=\sigma_{\rm int,inv}/\beta_{\rm inv}$
Gültekin et al. (2009) Sample[b]						
OLS	8.18 ± 0.06	3.91 ± 0.28	···	8.21 ± 0.07	5.60 ± 0.68	···
MLE	8.19 ± 0.06	3.97 ± 0.31	0.39 ± 0.06	8.22 ± 0.07	5.61 ± 0.70	0.47 ± 0.08
BCES	8.18 ± 0.06	4.01 ± 0.32	0.38 ± 0.07	8.20 ± 0.07	5.27 ± 0.70	0.43 ± 0.10
FITEXY	8.19 ± 0.06	4.06 ± 0.32	0.39 ± 0.06	8.21 ± 0.07	5.35 ± 0.66	0.45 ± 0.09
Bayesian	8.19 ± 0.07	4.04 ± 0.40	0.42 ± 0.05	8.21 ± 0.08	5.44 ± 0.56	0.49 ± 0.09
McConnell et al. (2011) Sample[c]						
OLS	8.27 ± 0.06	4.87 ± 0.37	···	8.33 ± 0.06	6.55 ± 0.50	···
MLE	8.28 ± 0.06	4.92 ± 0.34	0.41 ± 0.05	8.33 ± 0.06	6.43 ± 0.51	0.47 ± 0.06
BCES	8.28 ± 0.06	5.06 ± 0.41	0.43 ± 0.05	8.33 ± 0.06	6.36 ± 0.51	0.48 ± 0.07
FITEXY	8.28 ± 0.06	5.07 ± 0.36	0.43 ± 0.05	8.32 ± 0.06	6.29 ± 0.49	0.47 ± 0.06
Bayesian	8.27 ± 0.06	5.06 ± 0.36	0.44 ± 0.05	8.32 ± 0.07	6.31 ± 0.46	0.49 ± 0.07
Graham et al. (2011) Sample						
OLS	8.13 ± 0.05	4.75 ± 0.29	···	8.16 ± 0.06	6.22 ± 0.46	···
MLE	8.14 ± 0.05	4.72 ± 0.29	0.30 ± 0.04	8.17 ± 0.06	6.06 ± 0.46	0.33 ± 0.05
BCES	8.13 ± 0.05	5.13 ± 0.35	0.31 ± 0.04	8.15 ± 0.06	5.95 ± 0.45	0.34 ± 0.05
FITEXY	8.15 ± 0.05	5.08 ± 0.34	0.31 ± 0.04	8.16 ± 0.05	5.84 ± 0.42	0.33 ± 0.05
Bayesian	8.15 ± 0.05	5.08 ± 0.36	0.31 ± 0.05	8.17 ± 0.06	5.85 ± 0.42	0.34 ± 0.06

Note. — Forward regression=fit $\log M_{\rm BH}$ on $\log\sigma_*$; Inverse regression=fit $\log\sigma_*$ on $\log M_{\rm BH}$; OLS=Ordinary Least Squares; MLE=Maximum Likelihood Estimates; BCES=estimator of Akritas & Bershady (1996); FITEXY=estimator of Tremaine et al. (2002); Bayesian=Bayesian posterior median estimates using `linmix_err` procedure of Kelly (2007).

[a]Inverse regression and its results will be discussed in Section 3.5.

[b]We used 49 galaxies listed in Table 1 in Gültekin et al. (2009) without upper limits for comparison with other samples. For the MLE estimate, we also estimate the parameters using the same likelihood function and error estimation method given in Gültekin et al. (2009). The result is $(\alpha,\beta,\sigma_{\rm int}) = (8.18\pm0.06, 3.97\pm0.39, 0.42\pm0.05)$. Note that there are two different mass measurements for NGC 1399 and NGC 5128.

[c]We used all of the 67 galaxies listed in Table 4 in McConnell et al. (2011), while they used only 65. We found that there is a typo in the $M_{\rm BH}$ of NGC 1023 in their Table 4. Thus we corrected the value from 14.6×10^7 to 4.6×10^7. Note that there are two different mass measurements for the NGC 1399 and for the NGC 5128. Following their scheme, if we apply half weights for them, then we get the same result with that of McConnell et al. (2011), i.e., $(\alpha,\beta,\sigma_{\rm int}) = (8.28\pm0.06, 5.13\pm0.34, 0.42\pm0.05)$ for the FITEXY estimate.

we first perform the fit without accounting for the measurement errors in the independent variables. Then, we incorporate the effects of measurement errors in x into the parameter uncertainties by adding in quadrature the standard deviations estimated from the Monte Carlo fitting results for 10^4 realizations of the independent variables. Recently, McConnell et al. (2011) have updated the compiled sample of 49 galaxies from Gültekin et al. (2009) by including new black hole mass measurements and revising earlier black hole masses based on improved stellar orbit modeling, which accounts for dark matter halos (Gebhardt & Thomas 2009; van den Bosch & de Zeeuw 2010; Shen & Gebhardt 2010; Schulze & Gebhardt 2011). We have consistently re-estimated slopes of the $M_{\rm BH}-\sigma_*$ relation using the 67 galaxies listed in Table 4 of McConnell et al. (2011). The independently compiled sample of 64 galaxies from Graham et al. (2011) is also used. Table 3.1 lists all regression results. Note that we get consistent results with each paper if we choose the same method and setting used by the respective papers.

For the Gültekin et al. sample the difference between fitted lines is only marginal since they assumed a minimum of 5% measurement errors on σ_*; such small errors in σ_* are found to have relatively small impact on the regression result, as described in the next section. However, the slope of the $M_{\rm BH}-\sigma_*$ relation derived from the updated sample of McConnell et al. is significantly larger than that of the Gültekin et al., increasing from ~ 4 to ~ 5. As implied by the histograms for the black hole mass distributions shown in grey in the figures, this increase is mostly due to inclusion of both the low-mass and high-mass sample, which generally show an offset trend to the relation of the Gültekin et al. sample. For the Graham et al. sample the difference between fitted lines is marginally significant, and the slope is apparently divided into two groups, since they assigned relatively large (10%) measurement errors in σ_*. It seems that the bias of the `maximum likelihood` estimator starts to become non-negligible for x-errors of this magnitude. Therefore we investigate in details the effect of the amplitude of the x-error on these estimators in the following sections.

3.3.2 The effect of the adopted measurement uncertainty of σ_*

Merritt & Ferrarese (2001) first noted that ignoring the measurement errors in the velocity dispersion leads to a biased slope (i.e., underestimates) in the $M_{\rm BH}-\sigma_*$ relation. However, Tremaine et al. (2002) argued that the effect of the measurement errors in the velocity dispersion is not significant even at the 10% error level using two estimators, `BCES` and `FITEXY`, based on their simulation results. Indeed, the measurement errors in the independent vari-

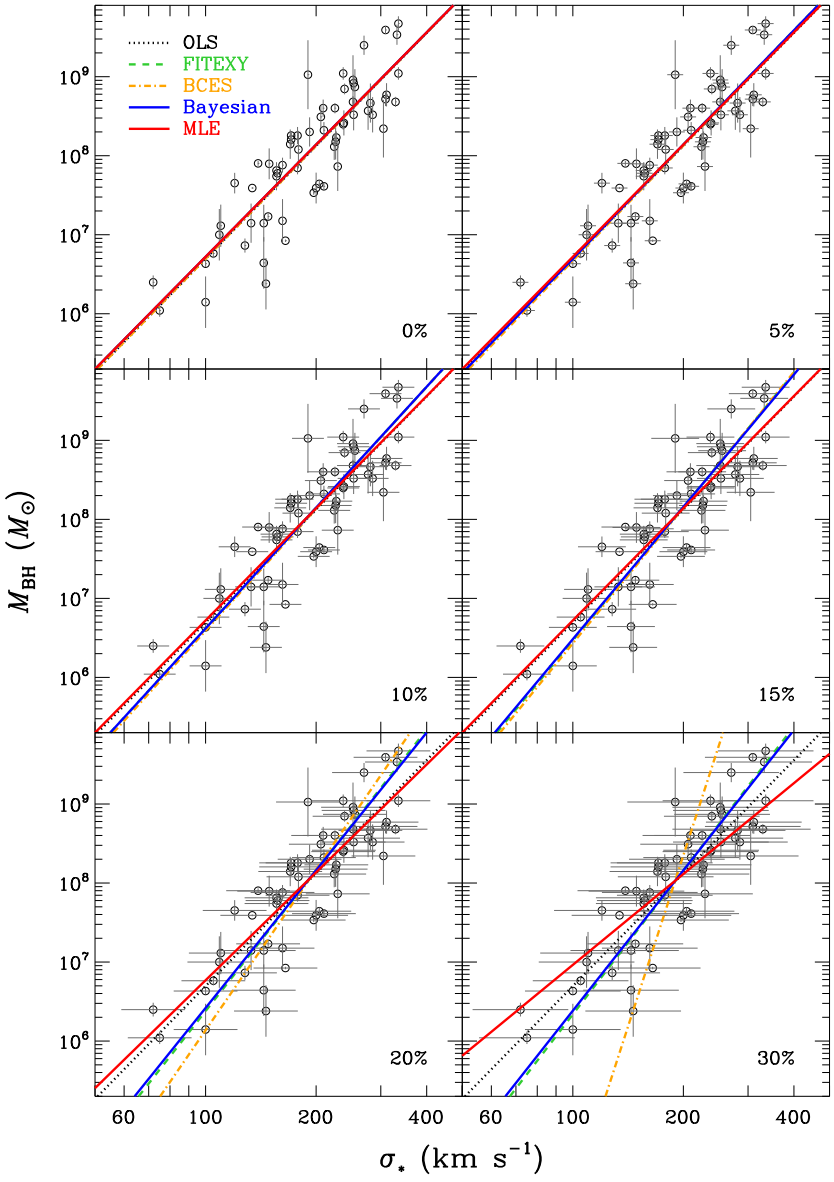

Figure 3.2 Comparison of five regression lines as a function of the assigned amount of measurement errors on σ_* using Graham et al. (2011) sample. The percentages of assigned errors are given at lower right corners in each panel. In the case of measurement errors on independent variables above 10%, the difference between the fitted lines is clearly visible.

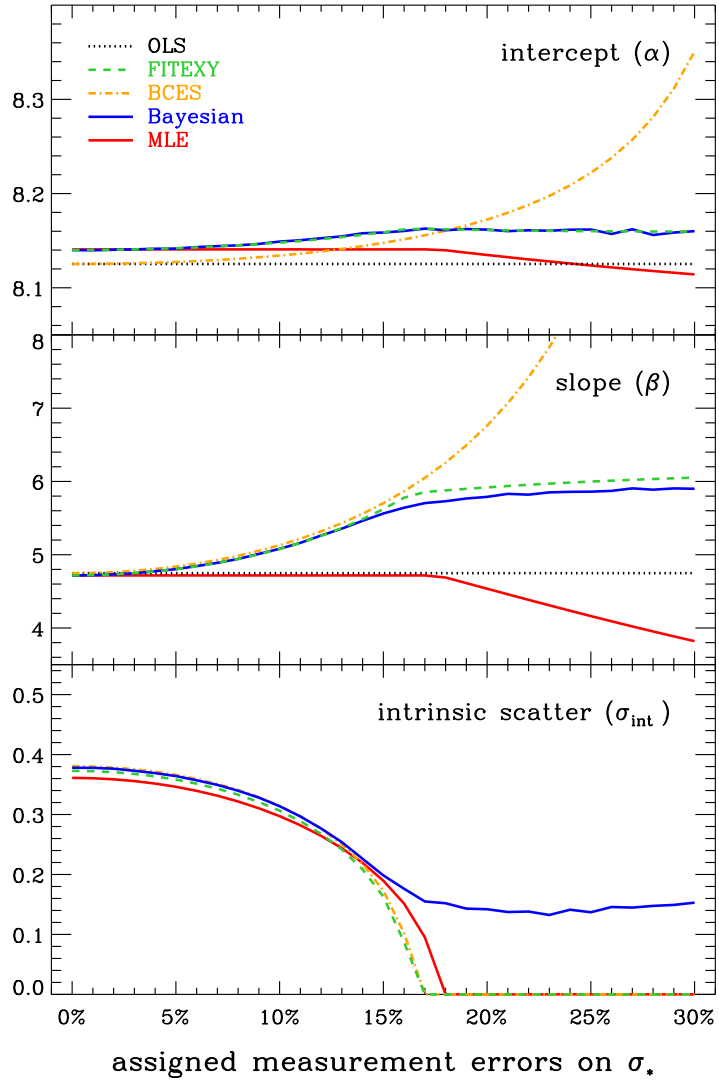

Figure 3.3 Direct comparison of regression results for the intercept (*top*), slope (*middle*), and intrinsic scatter (*bottom*) from the analysis of Figure 3.2. For the 5% errors the difference is only marginal. When the measurement errors are larger than 15% there is significant deviation between the estimators.

ables can have significant impact on the regression analysis as also investigated by Kelly (2007), although the effect is only marginal in current datasets of the $M_{\rm BH}-\sigma_*$ relation. Typically the measurement errors in the velocity dispersion are assumed to be 5% or 10% in literature.

In Figure 3.2 we compare the fitted lines to the Graham et al. $M_{\rm BH}-\sigma_*$ dataset assuming measurement errors on σ_* ranging from 0% to 30%. The difference between the fitted lines is noticeable and obvious when the measurement errors are large. Figure 3.3 compares the regression coefficients and intrinsic scatter derived from the five estimators as a function of the assigned errors. As a reference we show the results from the `OLS` estimator, i.e., for the unweighted fitting scheme without accounting for the intrinsic scatter as described in Isobe et al. (1990). This estimator is biased when there are measurement errors.

For the intercept, the estimators do not give significantly different results except for the case of the `BCES` estimator. Both the intercept and slope estimated from the `BCES` estimator show very different behaviour in the high measurement error regime, which is consistent with the result from Tremaine et al. (2002).

For the slope, it is noted that all converge to the same value as the measurement errors in the velocity dispersion approach zero. Moreover, the estimators `BCES`, `FITEXY`, and `Bayesian` are very similar up to the 15% error level, thus indicating consistent estimation for these three estimators. The value of the slope from the `BCES` estimator becomes higher compared to the others as the assumed errors on σ_* increase. This is expected from the denominator term in Equation (3.1). As can be seen, the estimated slope from the `maximum likelihood` estimator is almost identical to the `OLS` result up to measurement error amplitudes of $\sim 16\%$ on the independent variable. As noted and discussed in Kelly (2007) this biased behaviour is due to the implicit adoption of a naive uniform prior for the intrinsic distribution of the independent variables; this bias is also noted in Körding et al (2006). Based on this, we do not recommend the `maximum likelihood` method as outlined in Section 3.2.3. It is surprising that the `FITEXY` with an ad hoc iterative approach gives fairly consistent results with that of the fully Bayesian approach (`linmix_err`). This is inconsistent with the result of the simulations performed by Kelly (2007). The source of this discrepancy is that for the `FITEXY` estimator Kelly (2007) did not refit the slope and intercept each time after the intrinsic scatter term is iteratively adjusted (see also, Kelly 2011). Instead, he just assigned the intrinsic scatter value such that the reduced χ^2 is equal to unity using the first minimization result of α and β for the zero intrinsic scatter case (i.e., just simply increasing $\sigma_{\rm int}$ without re-optimization each time).

For the intrinsic scatter, its level is very sensitive to the magnitude of the assumed measurement errors. Only `linmix_err` recovers a non-zero intrinsic scatter amplitude even in the case of assuming large measurement errors on σ_*.

3.3.3 Monte Carlo simulations

An incorrect model for the distribution of the true values of x and y can lead to biased slope estimates, especially in the case of relatively large measurement errors on the independent variables, as pointed out by Gull (1989) and Kelly (2007) (see also, Auger et al. 2010, Mantz et al. 2010, and March et al. 2011). Here we use Monte Carlo simulations to investigate the effect of an incorrect assumption on the intrinsic distribution of the independent variables. First, we generate three 10,000 simulated datasets by assuming respectively uniform, normal, and power-law distributions for x. The number of data points in each realization is set to be the same as that of the Graham $M_{\rm BH}-\sigma_*$ data set (i.e., 64). The true intercept, slope, and standard deviation of Gaussian intrinsic scatter are assumed to be 8, 5, and 0.3 dex respectively, similar to typical values from the regression results given in Table 3.1. In other words, the sample points (y) from the given intrinsic relation ($y = 8+5x$) are scattered by the Gaussian random offsets with $\sigma = 0.3$. Then Gaussian random noises, having zero mean and standard deviations equal to the measurement errors from the Graham et al. (2011) data set, are added to both x and y. We fit the simulated data sets using the regression methods described in Section 3.2.

Figure 3.4 shows the simulation results for the uniform, normal, and power-law distributions of x, respectively. As already pointed above, the estimated intercept and slope from `MLE` are biased and distributed similarly to that of the `OLS` estimator. This bias is regardless of the form for the intrinsic distribution, and surprisingly the `MLE` still has a bias for the simulated sample from the uniform distribution. This is because the the `maximum-likelihood` method assumes a uniform distribution for the independent variable in the range of $-\infty$ to ∞, while in the simulations performed here the uniformly distributed data have some finite range (i.e., fixed to be same as the range of Graham et al. data). As can be seen, the true values are well recovered if the likelihood function is changed to assuming a Gaussian for the distribution of independent variables, as described in Section 3.2.4 ($\rm MLE_{1G}$). This modified maximum likelihood estimates give very similar distributions to that of the fully Bayesian estimates based on the `linmix_err` procedure ($\rm BPME_{3G}$). Here we also show the result of the version of `FITEXY` estimator used by Kelly (2007) to compare directly

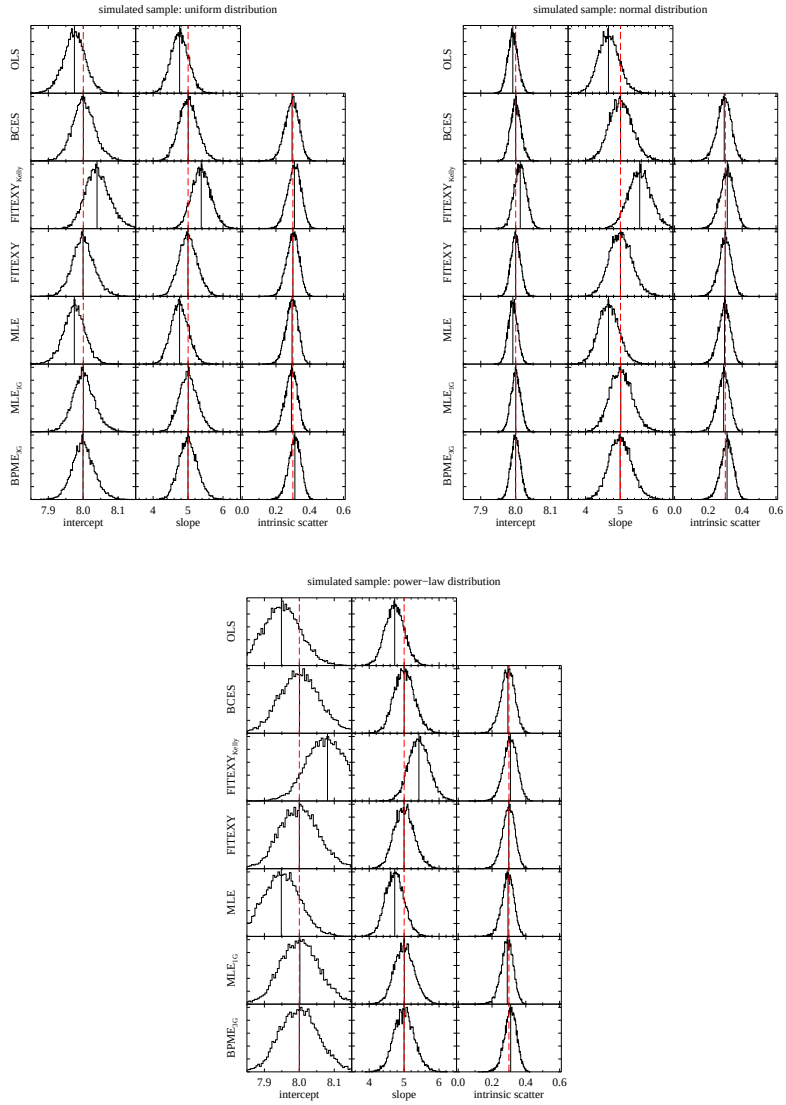

Figure 3.4 Monte Carlo simulation results for the cases of the given uniform (*upper left*), normal (*upper right*), and power-law (*bottom*) distributions on *x*. Each column shows the distribution of intercept, slope, and intrinsic scatter estimated from the simulated datasets using the various estimators. $\mathrm{FITEXY}_{\mathrm{Kelly}}$ is the version of `FITEXY` estimator implemented by Kelly (2007). $\mathrm{MLE}_{1\mathrm{G}}$ means the `maximum likelihood` estimator with a single Gaussian model for the distribution of independent variable as described in Section 3.2.4. $\mathrm{BPME}_{3\mathrm{G}}$ is the Bayesian posterior median estimate using `linmix_err` procedure based on the normal mixture model with 3 Gaussians. The median value of the simulated distribution is plotted as a vertical solid black line while the true value is indicated by the red dashed line in each panel.

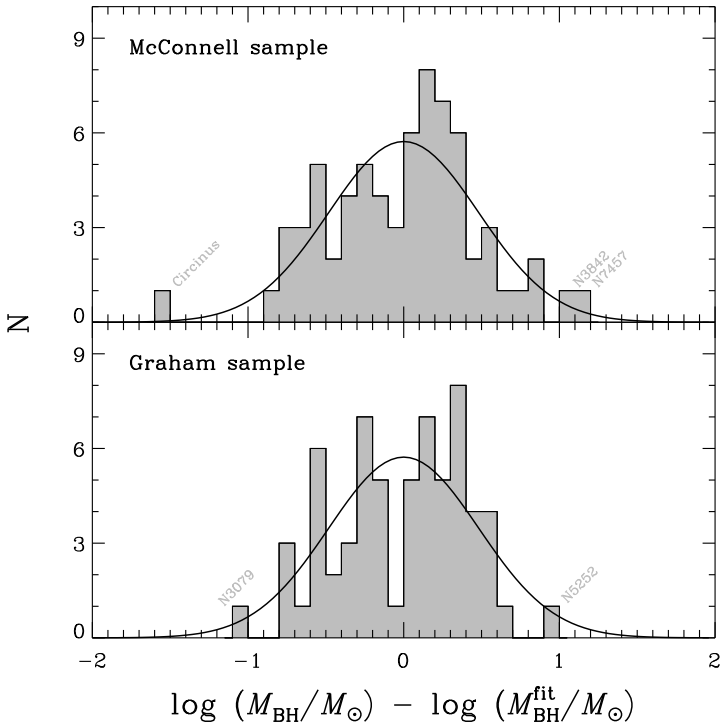

Figure 3.5 Histograms of mass residuals from the $M_{\rm BH}-\sigma_*$ relation based on the `FITEXY` estimator. A single Gaussian fit with the center fixed to zero is expressed as a solid line.

(FITEXY$_{\rm Kelly}$). The biased behaviour is same as noted in Kelly (2007). Thus this means that his implementation of `FITEXY` is inefficient compared to the one implemented here. From a viewpoint of how well the true values are recovered, all of `BCES`, `FITEXY`, and `Bayesian` estimators performed very well in this test.

3.3.4 The sample difference

In this section we investigate the sample discrepancy in detail using the most updated samples of McConnell et al. and Graham et al. We do this because the $M_{\rm BH}-\sigma_*$ relations derived from these two datasets show a difference in the intercept (see Table 3.1), which consequently affects the value of the virial factor. Note that the change in the $M_{\rm BH}-\sigma_*$ relation from the Gültekin sample to the McConnell sample is obvious because there was a major update of the sample as discussed in Section 3.3.1. However, the difference between

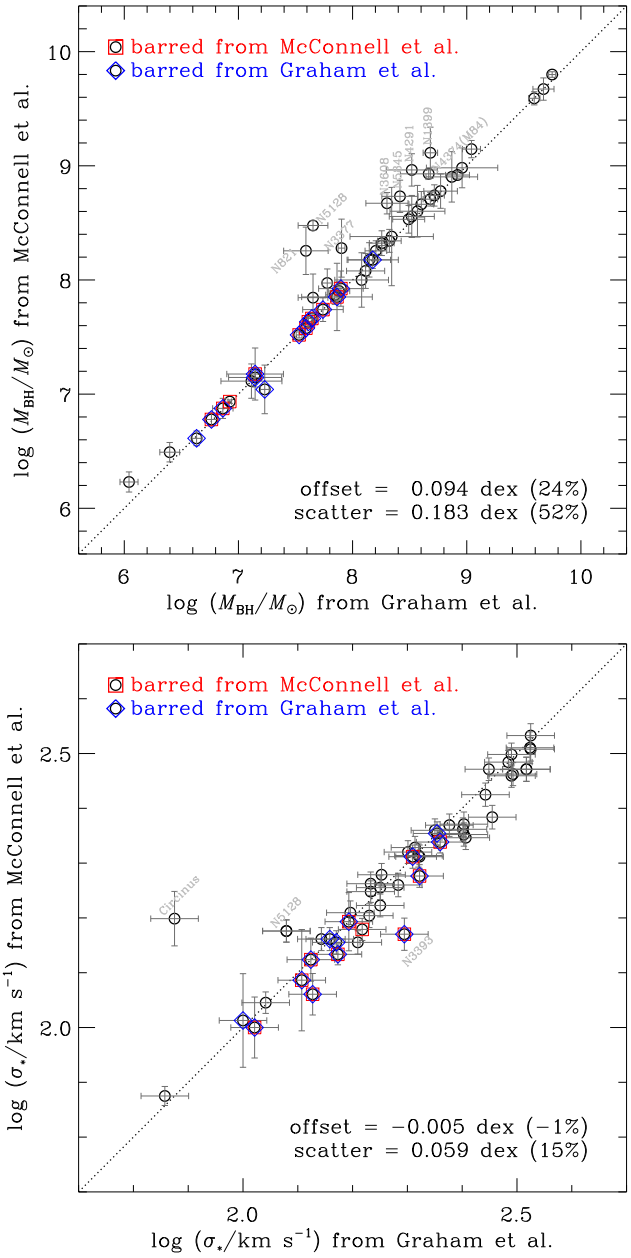

Figure 3.6 Comparison of the values of $M_{\rm BH}$ and σ_* for the galaxies in the set defined by the intersection of the McConnell et al. (2011) and Graham et al. (2011) samples. The barred sample defined by McConnell et al. (2011) is marked with a red open square, while that defined by Graham et al. (2011) is marked with a blue open diamond. The dotted line indicates the identity relationship.

the McConnell and Graham data is not clear since these two sample have 50 galaxies in common.

Figure 3.5 shows the mass residuals from the best-fit $M_{\rm BH}-\sigma_*$ relation derived from the McConnell and Graham data. As can be seen, there is one extreme outlier, Circinus, in the McConnell sample. Note that the central velocity dispersions of Circinus used in McConnell (i.e., 158 km/s) and Graham (i.e., 75 km/s) data are different from each other even though they were both taken from the HyperLEDA[5] database. The central velocity dispersion for this object currently given in the HyperLEDA is 157.6 ± 18.8 km/s. We verified that the value listed by Graham et al. was a typo (Alister W. Graham 2012, private communication).

In order to investigate the difference in the sample in common between Graham and McConnell, in Figure 3.6 we compare the values of the black hole masses and stellar velocity dispersions. For the $M_{\rm BH}$ values, there are quite a few galaxies deviating from the identity relation. This is mostly due to recent updates of the black hole masses by Schulze & Gebhardt (2011) in the McConnell data. For the σ_*, the values of the Graham sample are slightly larger on average than those of the McConnell sample, except for a few outliers. This slight average difference stems from the difference in the adopted velocity dispersion measures. Graham et al. (2011) used the central velocity dispersion provided in HyperLEDA, while McConnell et al. (2011) mostly used the effective velocity dispersion whenever it was available. This leads to systematic differences in the dispersion values as discussed in Tremaine et al. (2002). These mass and dispersion differences work to make the intercept smaller in the Graham sample compared to the McConnell sample. However, we note that the barred sample does not show any significant difference between these datasets. We also performed the regression for the common sample only, and found that the intercepts remained almost the same while the slopes were reduced by $0.2-0.3$ compared to that of the entire sample. Therefore, the difference of the intercepts between McConnell and Graham samples is due to the different values adopted for the common sample, while the difference in slopes is primarily due to the non-overlapping sample.

3.4 The virial factor

The virial factor is of fundamental importance for estimating AGN black hole masses in that it properly calibrates the measured virial product to a black hole mass for both the reverberation mapping method and the single-epoch method. Following Onken et al. (2004),

[5] http://leda.univ-lyon1.fr/

Table 3.2. AGN black hole masses and stellar velocity dispersions

Galaxy	$\mathrm{VP_{BH}}$ $(c\tau_{\mathrm{cent}}\sigma_{\mathrm{line}}^2/G)$ $10^6\ M_\odot$	$\mathrm{VP_{BH}}$ ref.	σ_* km s^{-1}	σ_* ref.
(1)	(2)	(3)	(4)	(5)
3C 120	$10.1^{+5.7}_{-4.1}$	1	162 ± 20	2
3C 390.3	$52.2^{+11.7}_{-11.7}$	1	273 ± 16	1
Ark 120	$27.2^{+3.5}_{-3.5}$	1	221 ± 17	1
Arp 151	$1.31^{+0.18}_{-0.23}$	4 & 6	118 ± 4	6
Mrk 50	$6.2^{+0.9}_{-0.9}$	7	109 ± 14	7
Mrk 79	$9.52^{+2.61}_{-2.61}$	1	130 ± 12	1
Mrk 110	$4.57^{+1.1}_{-1.1}$	1	91 ± 7	3
Mrk 202	$0.55^{+0.32}_{-0.22}$	4 & 6	78 ± 3	6
Mrk 279	$6.35^{+1.67}_{-1.67}$	1	197 ± 12	1
Mrk 590	$8.64^{+1.34}_{-1.34}$	1	189 ± 6	1
Mrk 817	$11.3^{+2.7}_{-2.8}$	5	120 ± 15	1
Mrk 1310	$0.61^{+0.20}_{-0.20}$	4 & 6	84 ± 5	6
NGC 3227	$1.39^{+0.29}_{-0.31}$	5	136 ± 4	1
NGC 3516	$5.76^{+0.51}_{-0.76}$	5	181 ± 5	1
NGC 3783	$5.42^{+0.99}_{-0.99}$	1	95 ± 10	4
NGC 4051	$0.31^{+0.10}_{-0.09}$	5	89 ± 3	1
NGC 4151	$8.31^{+1.04}_{-0.85}$	2	97 ± 3	1
NGC 4253 (Mrk 766)	$0.35^{+0.15}_{-0.14}$	4 & 6	93 ± 32	6
NGC 4593	$1.78^{+0.38}_{-0.38}$	3	135 ± 6	1
NGC 4748	$0.68^{+0.24}_{-0.30}$	4 & 6	105 ± 13	6
NGC 5548	$12.41^{+3.06}_{-4.21}$	4 & 6	195 ± 13	6
NGC 6814	$3.73^{+1.10}_{-1.11}$	4 & 6	95 ± 3	6
NGC 7469	$2.21^{+0.25}_{-0.25}$	1	131 ± 5	1
PG 1426+015	236^{+70}_{-70}	1	217 ± 15	5
SBS 1116+583A	$1.08^{+0.52}_{-0.49}$	4 & 6	92 ± 4	6

Note. — Col. (1) name. Col. (2) virial product ($\mathrm{VP_{BH}} = M_{\mathrm{BH}}/f$) based on the line dispersion (σ_{line}) from reverberation mapping. Col. (3) reference for virial product. 1. Peterson et al. 2004; 2. Bentz et al. 2006b; 3. Denney et al. 2006; 4. Bentz et al. 2009b; 5. Denney et al. 2010; 6. Park et al. 2012; 7. Barth et al. 2011. Col. (4) stellar velocity dispersion. Col. (5) reference for stellar velocity dispersion. 1. Nelson et al. 2004; 2. Nelson & Whittle 1995; 3. Ferrarese et al. 2001; 4. Onken et al. 2004; 5. Watson et al. 2008; 6. Woo et al. 2010; 7. Barth et al. 2011.

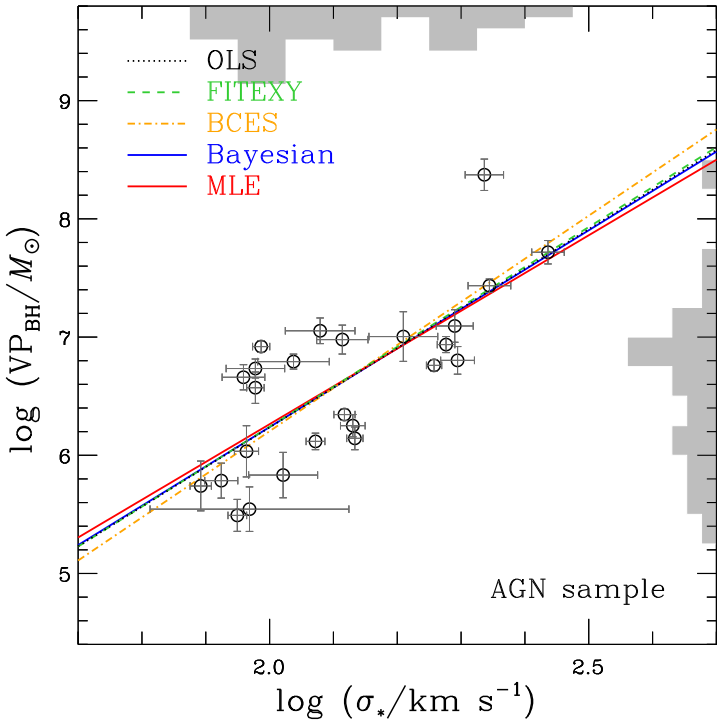

Figure 3.7 The $VP_{BH} - \sigma_*$ relation for the AGN sample (25). As shown in the right-hand side grey histogram, we are currently suffering from a lack of high mass AGN sample. Here we can clearly see the variability of the BCES estimator due to the effect of a single point (i.e., NGC 4253) that is subject to much larger measurement error than others.

we determine the average virial factor $\langle f \rangle$ by forcing the AGN black hole masses onto the $M_{\rm BH} - \sigma_*$ relation of quiescent galaxies. The AGN sample used here is listed in Table 3.2 with the corresponding references. We updated the AGN sample given in Table 2 of Woo et al. (2010) by updating the virial products from Denney et al. (2010), revising the rms line widths from Park et al. (2012), and including the new $M_{\rm BH}$ estimate for Mrk 50 from Barth et al. (2011). In Figure 3.7, we estimate the $\mathrm{VP_{BH}} - \sigma_*$ relation with four regression methods, as in Figure 3.1. The regression results are listed in Table 3.3. The slope appears to be marginally lower than that for quiescent galaxies. This small difference in slopes might be due to noise and AGN selection effects or it could be intrinsic, indicating a difference between passive and active galaxies (see Greene & Ho 2006 and Schulze & Wisotzki 2011). Note that the current sample is not representative of the AGN population since there is a deficit of high-mass AGNs, for which stellar velocity dispersion is extremely difficult to measure due to the overwhelming AGN luminosity.

To determine the average virial factor we use the `FITEXY` estimator, fixing the intercept and slope to be the same as that of the $M_{\rm BH} - \sigma_*$ relation for the quiescent galaxies,

$$\chi^2 = \sum_{i=1}^{N} \frac{(y_i + \log f - \alpha - \beta x_i)^2}{\sigma_{y,i}^2 + \beta^2 \sigma_{x,i}^2 + \sigma_{\rm int}^2}. \tag{3.13}$$

Here, $y = \log(\mathrm{VP_{BH}}/\mathrm{M_\odot})$ and $x = \log(\sigma_*/200\ \mathrm{km\ s^{-1}})$. The free parameters are only f and $\sigma_{\rm int}$. Adopting the regression results listed in Table 3.1, we estimate the virial factor and list the result in Table 3.4.

Figure 3.8 shows the dependency of the virial factor on the adopted slope and intercept based on three datasets with four regression methods. As expected, the difference of f between the different regression methods for a particular dataset is small, with the only exception being the value of f obtained from MLE (red symbols). Estimated virial factors vary as much as a factor of 2 among the data sets, larger than the typical uncertainties. The difference in f factors derived from the McConnell and Graham data is mostly due to the difference in the values from the sample of galaxies that overlap in these two data sets, as discussed in Section 3.3.4. The recent updates of $M_{\rm BH}$ measurements by Schulze & Gebhardt (2011) lead to a smaller mean mass in the Graham sample compared to that in the McConnell sample. The difference of the adopted velocity dispersion measures results in a slightly larger velocity dispersion on average in the Graham sample compared to that of the McConnell sample. These combined differences make the intercept of the $M_{\rm BH} - \sigma_*$ relationship smaller in the Graham sample than in the McConnell sample, thus reducing

Table 3.3. The $VP_{BH}-\sigma_*$ Relation for the Active Galaxy Sample:
$\log(VP_{BH}/M_\odot) = \alpha+\beta\log(\sigma_*/200\ \mathrm{km\ s^{-1}})$

Method	α	β	σ_{int}
Forward regression			
OLS	7.25 ± 0.14	3.35 ± 0.57	$\cdots$
MLE	7.23 ± 0.14	3.20 ± 0.59	0.41 ± 0.06
BCES	7.30 ± 0.17	3.65 ± 0.75	0.41 ± 0.06
FITEXY	7.26 ± 0.15	3.38 ± 0.63	0.43 ± 0.06
Bayesian	7.24 ± 0.17	3.33 ± 0.69	0.47 ± 0.09
Inverse regression			
OLS	7.74 ± 0.23	5.93 ± 0.82	$\cdots$
MLE	7.72 ± 0.33	5.88 ± 1.21	0.57 ± 0.13
BCES	7.70 ± 0.30	5.72 ± 1.10	0.51 ± 0.12
FITEXY	7.68 ± 0.26	5.68 ± 0.95	0.56 ± 0.11
Bayesian	7.68 ± 0.37	5.67 ± 1.87	0.62 ± 0.28

the f factor in the Graham sample regardless of the adopted regression methods. As can be seen, the derived virial factor is susceptible to the small variation of the quiescent galaxy $M_{BH}-\sigma_*$ relation within the current calibration process.

With the current AGN dataset, we are unable to constrain the f factor as a function of the mass range or host galaxy morphological type, since the number of sources in our sample is small and the morphology of our sample is biased toward late-type galaxies. We note that a larger AGN sample (e.g., high-mass AGNs, especially) is needed for better statistical calibration.

3.5 Inverse fit

In addition to the conventional forward fit relation (i.e., fitting M_{BH} for a given σ_*, as we performed in previous sections), Graham et al. (2011) used an inverse fit for the $M_{BH}-\sigma_*$ relation, suggesting that it corrects for possible sample selection bias due to non-detection of

Table 3.4. The derived average virial factor and intrinsic scatter based on the adopted $M_{\rm BH}-\sigma_*$ relation given in Table 3.1

Method	$\log\langle f\rangle$	$\sigma_{\rm int}$	$\log\langle f\rangle$	$\sigma_{\rm int}$
	From Gültekin et al. (2009) Sample			
	using forward relation		using inverse relation	
MLE	0.82 ± 0.09	0.43 ± 0.05	0.55 ± 0.12	0.54 ± 0.06
BCES	0.81 ± 0.10	0.43 ± 0.05	0.60 ± 0.11	0.51 ± 0.05
FITEXY	0.81 ± 0.10	0.43 ± 0.05	0.59 ± 0.11	0.52 ± 0.06
Bayesian	0.81 ± 0.10	0.43 ± 0.05	0.57 ± 0.12	0.52 ± 0.06
	From McConnell et al. (2011) Sample			
	using forward relation		using inverse relation	
MLE	0.74 ± 0.11	0.48 ± 0.05	0.51 ± 0.14	0.62 ± 0.07
BCES	0.72 ± 0.11	0.49 ± 0.05	0.52 ± 0.13	0.62 ± 0.07
FITEXY	0.71 ± 0.11	0.49 ± 0.05	0.53 ± 0.13	0.61 ± 0.06
Bayesian	0.71 ± 0.11	0.49 ± 0.05	0.52 ± 0.13	0.61 ± 0.07
	From Graham et al. (2011) Sample			
	using forward relation		using inverse relation	
MLE	0.64 ± 0.10	0.47 ± 0.05	0.42 ± 0.13	0.58 ± 0.06
BCES	0.55 ± 0.11	0.50 ± 0.05	0.42 ± 0.13	0.57 ± 0.06
FITEXY	0.58 ± 0.11	0.49 ± 0.05	0.45 ± 0.12	0.56 ± 0.06
Bayesian	0.58 ± 0.11	0.49 ± 0.05	0.46 ± 0.12	0.56 ± 0.06

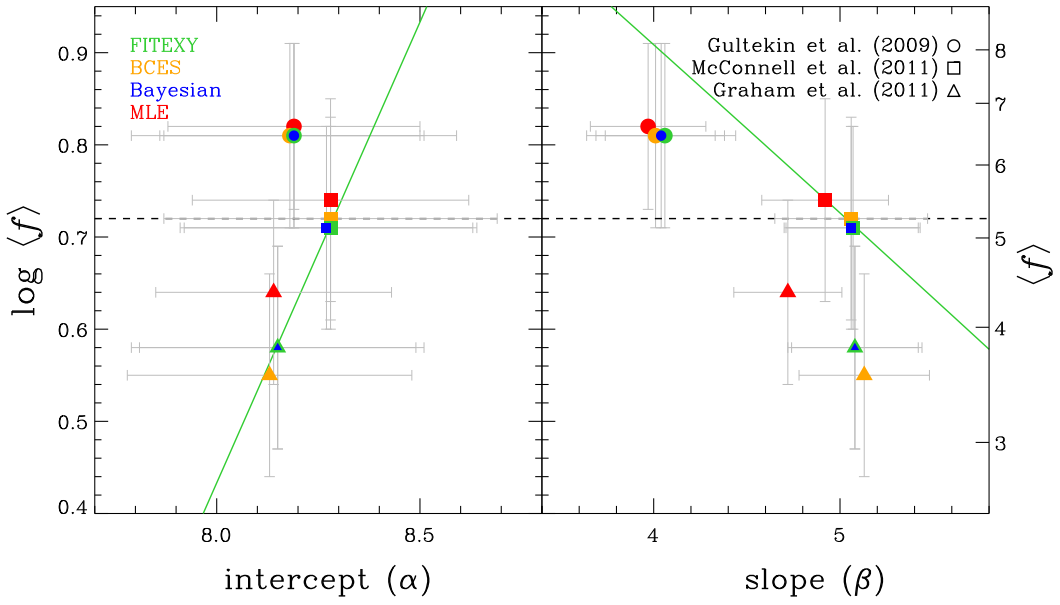

Figure 3.8 Variation of the estimated virial factor as a function of the adopted intercept (left) and slope (right) of the quiescent galaxy $M_{\rm BH}-\sigma_*$ relations taken from Table 3.1. Symbols mean the corresponding dataset used for estimation of the intercept and slope as expressed in upper right corner, while the colors of symbols indicate the regression methods used for them as given in the upper left corner. The horizontal dashed line indicates the value of the virial factor estimated from Woo et al. (2010) (i.e., 0.72). As an illustration, we add the green solid lines which show the dependence of the virial factor on the arbitrarily varied intercept (left) and slope (right) by fixing respectively the slope (left) and intercept (right) taken from the `FITEXY` estimates in the sample of McConnell et al. (2011).

intermediate-mass black holes ($< 10^6 M_\odot$). We also follow their argument, refit all relations, and derive the average virial factors based on the inverse relations (see Table 3.1, 3.3, and 3.4). Note that basically forward and inverse fittings are not the same in the presence of intrinsic scatter. Depending on the direction of regression (i.e., whether to choose $M_{\rm BH}$ or σ_* as the independent variable) the regressed slopes show large differences, leading to substantial changes in the virial factors. Therefore, we investigate and discuss the inverse fit in the context of the $M_{\rm BH}-\sigma_*$ relation. Now we have three factors related to the linear regression, which make the problem more complicated: measurements errors, intrinsic scatter, and truncation.

If there is a truncation in the y-axis (i.e., $\log M_{\rm BH}$) as argued by Graham et al. (2011), the conventional forward fit (fit y on x) causes a flattening in the estimated slope due to the increased loss of low mass black holes in the low σ_* regime (e.g., see Appendix A in Mantz et al. 2010). The inverse fit (i.e., fit x on y) is not sensitive to this Malmquist-type bias, so long as incompleteness only exist in black hole mass. As shown by Kelly (2007), in order to avoid this selection bias on the regression result, it is necessary to assign the 'independent variable' as the variable used to select a sample. This approach has been generally adopted in the Tully-Fisher relation studies since its sample is magnitude-selected and errors are smaller in magnitude than in velocity (e.g., Willick 1994; Tully & Pierce 2000; Bamford et al. 2006; Weiner et al. 2006; Koen & Lombard 2009; Williams et al. 2010; Miller et al. 2011).

In our sample, the measurement errors in the truncated coordinate ($M_{\rm BH}$) are larger than in the other coordinate (σ_*). Moreover, the sample selection might be highly inhomogeneous and simple selection criteria may not be sufficient for describing it. The situation is more complex in the AGN sample selection. According to Schulze & Wisotzki (2011), even though the inverse relation is insensitive to the mass-dependent selection, it does not yield the intrinsic true relation without incorporating the knowledge of the underlying host galaxy distribution function, which is currently hard to measure precisely. Furthermore, the AGN sample likely exhibits incompleteness in σ_* as well, as it is harder to measure σ_* for AGN hosting more massive black holes due to their tendency to have higher luminosities. Thus there are good reasons to use either type of regression, but neither of them is completely free of bias.

We provide both regression results in Table 3.1, 3.3, and 3.4. Inverse regression results in a steeper slope compared to that of forward regression in the $M_{\rm BH}-\sigma_*$ relation of quiescent galaxies. The calibration based on the inverse regression makes black hole masses inferred

from the AGN virial products smaller, since most of the AGN sample is located at the low-mass regime, thus leading to a reduction in the average virial factor. This biased dependency toward the low-mass regime motivates expansion in the dynamic range of sample of AGN containing both reverberation mapping data and measurement of σ_*. Based on these results, we conclude that the origin of the difference in the recently reported virial factors (Woo et al. 2010 based on forward regression *vs*. Graham et al. 2011 based on inverse regression) is mostly due to the direction of regression adopted (i.e., whether $M_{\rm BH}$ is considered the independent or dependent variable), as well as the difference in the samples used to calibrate the mass estimates.

Feigelson & Babu (1992) suggested that we should choose the regression method for individual cases depending on the scientific question being investigated. Here the purpose of deriving the $M_{\rm BH}-\sigma_*$ relation for local quiescent galaxies is to calibrate AGN black hole masses with determining the virial factor. By properly comparing the black hole masses of inactive galaxies to virial products of active galaxies, the average virial factor is constrained as discussed in the previous section. Thus it is desirable to adopt the type of regression which yields the relation that minimizes the scatter in the black hole mass estimates (Graham & Driver 2007). It is more common to adopt the host spheroidal quantity as the independent variable because the scaling relations are often used to infer black hole mass using the host spheroidal quantities as a proxy. Considering this, and the fact that the AGN sample likely suffers from Malmquist bias in both $M_{\rm BH}$ and σ_*, we prefer the calibration from the traditional forward regression.

3.6 Discussion and Conclusion

We investigated the differences in the derived $M_{\rm BH}-\sigma_*$ relation and virial factor using the recently compiled datasets of quiescent and active galaxies. The investigated possible origins of the difference are the fitting methodology and the sample difference.

For the difference in regression methods, we utilized and compared four linear regression techniques: `FITEXY`, `Bayesian`, `BCES`, and `Maximum likelihood`. With the current level of measurement errors of the $M_{\rm BH}-\sigma_*$ dataset, all estimators except for the `maximum likelihood` estimator show good performance and consistent results with each other. There is no significant difference between the estimators. However, the assigned size of measurement errors on σ_* can have a significant impact on the regression results, especially for the `BCES` and `Maximum likelihood` estimators. The `Maximum`

`likelihood` method using an implicit assumption of a uniform distribution for the intrinsic distribution of the independent variables introduces a bias which is clearly noticeable when the measurement errors on the independent variable are large (e.g., above 10% errors in the Graham sample as shown in Figure 3.2). Without properly accounting for the form of the intrinsic distribution of the independent variable, MLE estimates are very similar to the OLS results. Therefore we do not recommend this method for regression analysis in general. Of course for the $M_{\rm BH}-\sigma_*$ regression analysis the difference in the estimated slope is only marginal at the current adopted level of uncertainty on σ_* (5%). The `BCES` estimator is also one of the good estimators based on the current measurement error level on σ_*, although it may be problematic if the error is larger. Based on our simulation results, the `FITEXY` estimator shows slightly better performance and the least-biased result compared to the other methods, although the others also perform well and the differences are marginal. This is consistent with the result of Novak et al. (2006), although they did not provide an explicit implementation of all of the methods, nor a specific quantitative comparison. In general, we recommend both the `FITEXY` and `Bayesian` estimators, although the latter is computationally more intensive, especially when the measurement errors are large. However, we note that the `Bayesian` estimator has the advantage over the method of `FITEXY` in that it calculates the full probability distribution function (i.e., posterior) of the parameters for the given data, and hence provides well-defined and reliable parameter uncertainties. In addition, the `Bayesian` method can incorporate upper limits, as can the method of Gültekin et al. (2009), whereas the `FITEXY` cannot. If we perform the regression using the `Bayesian` method, for the Gültekin sample including upper limits as well as secure measurements, the result changes from ($\alpha = 8.19 \pm 0.07$, $\beta = 4.04 \pm 0.40$, $\sigma_{\rm int} = 0.42 \pm 0.05$) to ($\alpha = 8.13 \pm 0.07$, $\beta = 4.32 \pm 0.38$, $\sigma_{\rm int} = 0.43 \pm 0.05$), thus $\log\langle f \rangle$ correspondingly decreases from 0.81 ± 0.10 to 0.70 ± 0.10. As discussed in Tremaine et al. (2002), accurate and consistent estimation of an individual stellar velocity dispersion with a correct measurement uncertainty is still required and it will be an important factor for better constraining the $M_{\rm BH}-\sigma_*$ relation and virial factor.

The difference in sample is the most important factor contributing to the differences in derived $M_{\rm BH}-\sigma_*$ relations. Gültekin et al. (2009) noted that the late-type galaxy and pseudobulge population in their sample is the source of the difference in intrinsic scatter measurements by comparing their sample to that of Tremaine et al. (2002). Greene et al. (2010) found that the late-type low-mass galaxies show large scatter and are offset relative to the $M_{\rm BH}-\sigma_*$ relation of elliptical galaxies using the sample of megamaser disk galaxies.

By extending the work of Graham et al. (2008), recently Graham et al. (2011) showed that the fraction of barred galaxies in their sample alters the $M_{\rm BH}-\sigma_*$ relationship by dividing their sample into barred and non-barred galaxies.

According to these previous studies, the $M_{\rm BH}-\sigma_*$ relation seems to be not universal. It varies depending on the mass range and galaxy type. Correspondingly, the average f factor is also significantly affected by the sample population, since the intercept and slope from the quiescent galaxy $M_{\rm BH}-\sigma_*$ relation are directly used in the calibration process. As investigated in this study, the differences in the adopted sample contribute to the change of the virial factor. Moreover, the direction of regression (forward *vs.* inverse) causes further changes in the virial factor. We showed that the derived f factors vary as much as a factor of 2, which is from a combined effect of the sample and regression used. These differences could be thought of as an additional systematic uncertainty in the AGN black hole mass estimation via the current calibration process of the virial factor, since there is no obvious physical foundation for the selection of the appropriate sample and direction of regression.

The true average f factor should not be changed by the host galaxy type since there should be no direct physical link between the AGN BLR geometry and the global morphology of host galaxies. Unfortunately, the estimated average f factor may be subject to biases due to its calibration based on a single $M_{\rm BH}-\sigma_*$ relationship. However, since the current sample is not large enough to calibrate the virial factor as a function of galaxy type, it is better to use a single value of the mean f factor for AGN $M_{\rm BH}$ estimation in order to avoid additional systematic errors until we get enough direct measurements of the structure of the BLR for an each individual AGN. We note that an alternative method to measure AGN black hole mass that derives the virial factor through BLR modeling has been recently developed and applied to the reverberation data (e.g., Pancoast, Brewer, & Treu 2011; Brewer et al. 2011; Pancoast et al. 2012). Given the uncertainties in the f factor, when investigating evolutionary trends in the $M_{\rm BH}-\sigma_*$ relation based on SE estimates, we recommend to use self consistent samples and techniques at different redshifts. In other words, one should measure the SE black hole masses consistently for AGN samples at different redshifts by using the cross-calibrated recipes based on the same virial factor. In this way the virial factor should be very similar for all samples and cancel out in the determination of the evolution of $\log M_{\rm BH}$ under the assumption that the virial factor is not a function of redshift (e.g., Woo et al. 2008).

Finally, we present the updated $M_{\rm BH}-\sigma_*$ relation for local active galaxies based on the `FITEXY` estimator in Figure 3.9, where the forward (inverse) regression result is α =

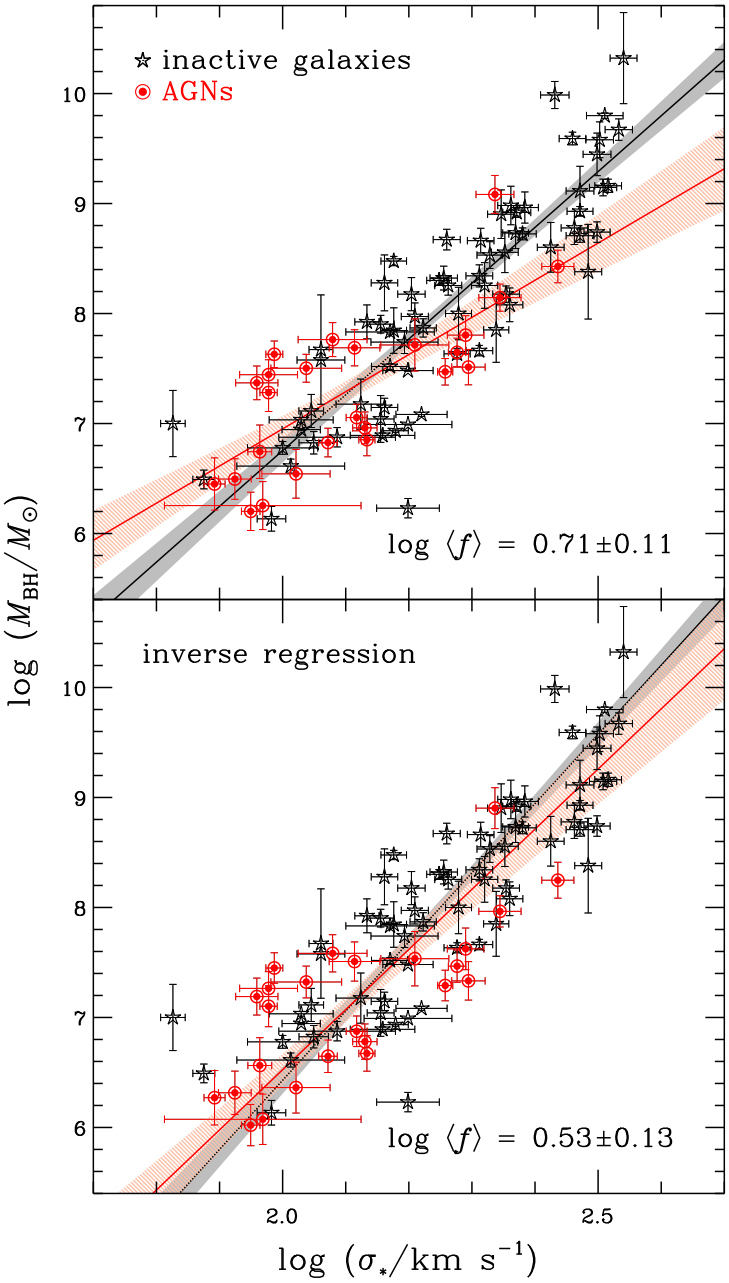

Figure 3.9 The updated $M_{\rm BH}-\sigma_*$ relations for the inactive (black) and active (red) samples using the FITEXY estimator for the forward regression (upper) and inverse regression (lower). Shaded regions show the 1σ (68%) confidence intervals on the best-fit line. The inactive sample is from McConnell et al. (2011) and is the most recent one. The active sample is given in Table 3.2.

7.97 ± 0.14, $\beta = 3.38 \pm 0.61$, and $\sigma_{\rm int} = 0.42 \pm 0.06$ ($\alpha = 8.17 \pm 0.27$, $\beta = 5.47 \pm 1.01$, and $\sigma_{\rm int} = 0.52 \pm 0.11$). The AGN black hole masses were converted from the virial products using the virial factor $\log\langle f \rangle = 0.71 \pm 0.11$ ($\log\langle f \rangle = 0.53 \pm 0.13$) derived in Section 3.4. From a methodological point of view, we prefer the forward regression as discussed in Section 3.5. Thus our preferred value for the virial factor is 0.71 based on the preferred forward `FITEXY/Bayesian` estimation with the most recent sample (McConnell et al. 2011). This value is consistent with that of Woo et al. (2010) (i.e., 0.72) and differs from that of Graham et al. (2011) (i.e., 0.45) by ~ 0.26 dex. The difference arises from the combination of sample differences and regression differences. It is worth noticing that the bottom panel of Figure 3.9 shows slightly better agreement between the non-AGN and AGN $M_{\rm BH} - \sigma_*$ relations, which may indicate that the inverse regression has less bias than the forward one and thus might be more reliable. However, this conclusion only holds if we assume that the active and inactive galaxies share the same $M_{\rm BH} - \sigma_*$ relationship. Considering these issues, it is still not conclusive whether the inverse method is preferable with the current datasets owing to selection effects and limited dynamic range of the AGN sample.

References

Akritas, M. G., & Bershady, M. A. 1996, ApJ, 470, 706

Auger, M. W., Treu, T., Bolton, A. S., et al. 2010, ApJ, 724, 511

Bamford, S. P., Aragón-Salamanca, A., & Milvang-Jensen, B. 2006, MNRAS, 366, 308

Barth, A. J., Pancoast, A., Thorman, S. J., et al. 2011, ApJ, 743, L4

Batcheldor, D. 2010, ApJ, 711, L108

Bedregal, A. G., Aragón-Salamanca, A., & Merrifield, M. R. 2006, MNRAS, 373, 1125

Beifiori, A., Courteau, S., Corsini, E. M., & Zhu, Y. 2012, MNRAS, 419, 2497

Bennert, V. N., Treu, T., Woo, J.-H., et al. 2010, ApJ, 708, 1507

Bentz, M. C., Peterson, B. M., Pogge, R. W., Vestergaard, M., & Onken, C. A. 2006a, ApJ, 644, 133

Bentz, M. C., Denney, K. D., Cackett, E. M., et al. 2006b, ApJ, 651, 775

Bentz, M. C., Peterson, B. M., Pogge, R. W., & Vestergaard, M. 2009a, ApJ, 694, L166

Bentz, M. C., Walsh, J. L., Barth, A. J., et al. 2009b, ApJ, 705, 199

Blandford, R. D., & McKee, C. F. 1982, ApJ, 255, 419

Booth, C. M., & Schaye, J. 2009, MNRAS, 398, 53

Bower, R. G., Benson, A. J., Malbon, R., et al. 2006, MNRAS, 370, 645

Brewer, B. J., Treu, T., Pancoast, A., et al. 2011, ApJ, 733, L33

Caimmi, R. 2011a, NewA., 16, 337

Caimmi, R. 2011b, arXiv:1111.2680

Cheng, C. L., & Riu, J. 2006, Technometrics, 48, 511

Croton, D. J., Springel, V., White, S. D. M., et al. 2006, MNRAS, 365, 11

Di Matteo, T., Springel, V., & Hernquist, L. 2005, Nature, 433, 604

Denney, K. D., Bentz, M. C., Peterson, B. M., et al. 2006, ApJ, 653, 152

Denney, K. D., Watson, L. C., Peterson, B. M., et al. 2009, ApJ, 702, 1353

Denney, K. D., Peterson, B. M., Pogge, R. W., et al. 2010, ApJ, 721, 715

Fabian, A. C. 1999, MNRAS, 308, L39

Feigelson, E. D., & Babu, G. J. 1992, ApJ, 397, 55

Ferrarese, L., & Ford, H. 2005, Space Sci. Rev., 116, 523

Ferrarese, L., & Merritt, D. 2000, ApJ, 539, L9

Ferrarese, L., Pogge, R. W., Peterson, B. M., et al. 2001, ApJ, 555, L79

Gebhardt, K., Bender, R., Bower, G., et al. 2000, ApJ, 539, L13

Gebhardt, K., & Thomas, J. 2009, ApJ, 700, 1690

Graham, A. W. 2008, ApJ, 680, 143

Graham, A. W., & Driver, S. P. 2007, ApJ, 655, 77

Graham, A. W., Onken, C. A., Athanassoula, E., & Combes, F. 2011, MNRAS, 412, 2211

Greene, J. E., & Ho, L. C. 2006, ApJ, 641, L21

Greene, J. E., Peng, C. Y., Kim, M., et al. 2010, ApJ, 721, 26

Gull, S. F. 1989, Bayesian Data Analysis: Straight-line fitting, in Maximum Entropy and Bayesian Methods, ed. J. Skilling, (Dordrecht:Kluwer Academic Publishers) 511

Gültekin, K., Richstone, D. O., Gebhardt, K., et al. 2009, ApJ, 698, 198

Gültekin, K., Tremaine, S., Loeb, A., & Richstone, D. O. 2011, ApJ, 738, 17

Häring, N., & Rix, H.-W. 2004, ApJ, 604, L89

Hogg, D. W., Bovy, J., & Lang, D. 2010, arXiv:1008.4686

Hopkins, P. F., Hernquist, L., Cox, T. J., et al. 2006, ApJS, 163, 1

Hu, J. 2008, MNRAS, 386, 2242

Isobe, T., Feigelson, E. D., Akritas, M. G., & Babu, G. J. 1990, ApJ, 364, 104

Jiang, Y.-F., Greene, J. E., & Ho, L. C. 2011, ApJ, 737, L45

Kaspi, S., Smith, P. S., Netzer, H., et al. 2000, ApJ, 533, 631

Kaspi, S., Maoz, D., Netzer, H., et al. 2005, ApJ, 629, 61

Kauffmann, G., & Haehnelt, M. 2000, MNRAS, 311, 576

Kelly, B. C. 2007, ApJ, 665, 1489

Kelly, B. C. 2011, arXiv:1112.1745

Kim, M., Ho, L. C., Peng, C. Y., et al. 2008, ApJ, 687, 767

Koen, C., & Lombard, F. 2009, MNRAS, 395, 1657

Körding, E., Falcke, H., & Corbel, S. 2006, A&A, 456, 439

Kormendy, J., Bender, R., & Cornell, M. E. 2011, Nature, 469, 374

Kormendy, J., & Richstone, D. 1995, ARA&A, 33, 581

Li, G., Conroy, C., & Loeb, A. 2011, arXiv:1110.0017

Magorrian, J., Tremaine, S., Richstone, D., et al. 1998, AJ, 115, 2285

Mancini, L., & Feoli, A. 2012, A&A, 537, A48

Mantz, A., Allen, S. W., Ebeling, H., Rapetti, D., & Drlica-Wagner, A. 2010, MNRAS, 406, 1773

March, M. C., Trotta, R., Berkes, P., Starkman, G. D., & Vaudrevange, P. M. 2011, MNRAS, 418, 2308

Marconi, A., Axon, D. J., Maiolino, R., et al. 2008, ApJ, 678, 693

Marconi, A., & Hunt, L. K. 2003, ApJ, 589, L21

Markwardt, C. B. 2009, Astronomical Data Analysis Software and Systems XVIII, 411, 251

McConnell, N. J., Ma, C.-P., Gebhardt, K., et al. 2011, Nature, 480, 215

McLure, R. J., & Dunlop, J. S. 2002, MNRAS, 331, 795

Merritt, D., & Ferrarese, L. 2001, ApJ, 547, 140

Miller, S. H., Bundy, K., Sullivan, M., Ellis, R. S., & Treu, T. 2011, ApJ, 741, 115

Nelson, C. H., Green, R. F., Bower, G., Gebhardt, K., & Weistrop, D. 2004, ApJ, 615, 652

Nelson, C. H., & Whittle, M. 1995, ApJS, 99, 67

Novak, G. S., Faber, S. M., & Dekel, A. 2006, ApJ, 637, 96

Onken, C. A., Ferrarese, L., Merritt, D., et al. 2004, ApJ, 615, 645

Pancoast, A., Brewer, B. J., & Treu, T. 2011, ApJ, 730, 139

Pancoast, A., Brewer, B. J., Treu, T., et al. 2012, ApJ, 754, 49

Park, D., Woo, J.-H., Treu, T., et al. 2012, ApJ, 747, 30

Peterson, B. M. 1993, PASP, 105, 247

Peterson, B. M., Ferrarese, L., Gilbert, K. M., et al. 2004, ApJ, 613, 682

Press, W. H., Teukolsky, S. A., Vetterling, W. T., & Flannery, B. P. 1992, Numerical recipes in C. The art of scientific computing, Cambridge: University Press, 2nd ed.

Richstone, D., Ajhar, E. A., Bender, R., et al. 1998, Nature, 395, A14

Sani, E., Marconi, A., Hunt, L. K., & Risaliti, G. 2011, MNRAS, 413, 1479

Schulze, A., & Gebhardt, K. 2011, ApJ, 729, 21

Schulze, A., & Wisotzki, L. 2011, A&A, 535, A87

Shen, J., & Gebhardt, K. 2010, ApJ, 711, 484

Silk, J., & Rees, M. J. 1998, A&A, 331, L1

Somerville, R. S., Hopkins, P. F., Cox, T. J., Robertson, B. E., & Hernquist, L. 2008, MNRAS, 391, 481

Tremaine, S., Gebhardt, K., Bender, R., et al. 2002, ApJ, 574, 740

Tully, R. B., & Pierce, M. J. 2000, ApJ, 533, 744

van den Bosch, R. C. E., & de Zeeuw, P. T. 2010, MNRAS, 401, 1770

Vika, M., Driver, S. P., Cameron, E., Kelvin, L., & Robotham, A. 2012, MNRAS, 419, 2264

Wandel, A., Peterson, B. M., & Malkan, M. A. 1999, ApJ, 526, 579

Watson, L. C., Martini, P., Dasyra, K. M., et al. 2008, ApJ, 682, L21

Weiner, B. J., Willmer, C. N. A., Faber, S. M., et al. 2006, ApJ, 653, 1049

Williams, M. J., Bureau, M., & Cappellari, M. 2010, MNRAS, 409, 1330

Willick, J. A. 1994, ApJS, 92, 1

Woo, J.-H., Treu, T., Malkan, M. A., & Blandford, R. D. 2008, ApJ, 681, 925

Woo, J.-H., Treu, T., Barth, A. J., et al. 2010, ApJ, 716, 269

Xiao, T., Barth, A. J., Greene, J. E., et al. 2011, ApJ, 739, 28

Chapter 4

Calibrating C IV-based virial black hole mass estimators

(This chapter is published in The Astrophysical Journal[1]*.)*

4.1 Introduction

Understanding the growth history of supermassive black holes (SMBHs) is one of the fundamental issues in studies of galaxy formation and evolution. The intimate connection between SMBHs and host galaxies is evidenced through empirical correlations between the masses of SMBHs ($M_{\rm BH}$) and the overall properties of the host galaxy spheroids (e.g., Magorrian et al. 1998; Ferraresse & Merritt 2000; Gebhardt et al. 2000). The cosmic evolution of these scaling relationships has been investigated in the literature, where a tentative evolution has been reported utilizing observational approaches (e.g., Peng et al. 2006; Woo et al. 2006, 2008; Treu et al. 2007; Merloni et al. 2010; Bennert et al. 2010, 2011; Hiner et al. 2012; Canalizo et al. 2012). In order to provide better empirical constraints on the cosmic growth of SMBHs and its connection to galaxy evolution, reliable $M_{\rm BH}$ estimation at low and high redshifts is of paramount importance.

The $M_{\rm BH}$ can be determined for Type 1 AGN with the reverberation mapping (RM, Peterson 1993) method or the single-epoch (SE, Wandel et al. 1999) method under the virial assumption: $M_{\rm BH} = fR_{\rm BLR}\Delta V^2/G$, where G is the gravitational constant. The size

[1] Park et al. 2013, ApJ, 770, 87

of the broad-line region (BLR), $R_{\rm BLR}$, can be directly measured from RM analysis (e.g., Peterson et al 2004; Bentz et al. 2009; Denney et al. 2010; Barth et al. 2011b; Grier et al. 2012) or indirectly estimated from the monochromatic AGN luminosity measured from SE spectra based on the empirical BLR size-luminosity relation (Kaspi et al. 2000, 2005; Bentz et al. 2006, 2009, 2013). The line-of-sight velocity dispersion, ΔV, of BLR gas can be measured either from the broad emission line width in the rms spectrum (e.g., Peterson et al. 2004) obtained from multi-epoch RM data or in the SE spectra (e.g., Park et al. 2012b), while the virial factor, f, is the dimensionless scale factor of order unity that depends on the geometry and kinematics of the BLR. Currently, an ensemble average, $\langle f \rangle$, is determined empirically under the assumption that local active and inactive galaxies have the same $M_{\rm BH}-\sigma_*$ relationship (e.g., Onken et al. 2004; Woo et al. 2010; Graham et al. 2011; Park et al. 2012a; Woo et al. 2013) and recalibrated to correct for the systematic difference of line widths in between the SE and rms spectra (e.g., Collin et al. 2006; Park et al. 2012b).

The RM method has been applied to a limited sample (~ 50) to date, due to the practical difficulty of the extensive photometric and spectroscopic monitoring observations and the intrinsic difficulty of tracing the weak variability signal across very long time-lags for high-z, high-luminosity QSOs. In contrast, the SE method can be applied to any AGN if a single spectrum is available, although this method is subject to various random and systematic uncertainties (see, e.g., Vestergaard & Peterson 2006, Collin et al. 2006; McGill et al. 2008; Shen et al. 2008; Denney et al. 2009, 2012; Richards et al. 2011; Park et al. 2012b).

In the local universe, the SE mass estimators based on the Hβ line are well calibrated against the direct Hβ RM results (e.g., McLure & Jarvis 2002; Vestergaard 2002; Vestergaard & Peterson 2006; Collin et al. 2006; Park et al. 2012b). For AGNs at higher redshift ($z \gtrsim 0.7$), rest-frame UV lines, i.e., Mg II or C IV, are frequently used for $M_{\rm BH}$ estimation since they are visible in the optical wavelength range. Unfortunately the kinds of accurate calibration applied to Hβ-based SE BH masses are difficult to achieve for the mass estimators based on the Mg II and C IV lines, since the corresponding direct RM results are very few (see Peterson et al. 2005; Metzroth et al. 2006; Kaspi et al. 2007). Instead, SE $M_{\rm BH}$ based on these lines can be calibrated indirectly against either the most reliable Hβ RM based masses (e.g., Vestergaard & Peterson 2006; Wang et al. 2009; Rafiee & Hall 2011a) or the best calibrated Hβ SE masses (McGill et al. 2008; Shen & Liu 2012, SL12 hereafter) under the assumption that the inferred $M_{\rm BH}$ is the same whichever line is used for the estimation.

While several studies demonstrated the consistency between Mg II based and Hβ based

masses (e.g., McLure & Dunlop 2004; Salviander et al. 2007; McGill et al. 2008; Shen et al. 2008; Wang et al. 2009; Rafiee & Hall 2011a; SL12), the reliability of utilizing the C IV line is still controversial, since C IV can be severely affected by non-virial motions, i.e., outflows and winds, and strong absorption (e.g, Leighly & Moore 2004; Shen et al. 2008; Richards et al. 2011; Denney 2012). Other related concerns for the C IV line include the Baldwin effect, the strong blueshift or asymmetry of the line profile, broad absorption features, and the possible presence of a narrow line component (see Denney 2012 for discussions and interpretations of the issues). Several studies have reported a poor correlation between C IV and Hβ line widths and a large scatter between C IV and Hβ based masses (e.g., Baskin & Laor 2005; Netzer et al. 2007; Sulentic et al. 2007; SL12; Ho et al. 2012; Trakhtenbrot & Netzer 2012). On the other hand, other studies have shown a consistency between them and/or suggested additional calibrations for bringing C IV and Hβ based masses further into agreement. (e.g., Vestergaard & Peterson 2006; Kelly & Bechtold 2007; Dietrich et al. 2009; Greene et al. 2010; Assef et al. 2011; Denney 2012).

Given the practical importance of the C IV line, which can be observed with optical spectrographs over a wide range of redshifts ($2 \lesssim z \lesssim 5$), in studying high-z AGNs, it is important and useful to calibrate the C IV based $M_{\rm BH}$ estimators. Vestergaard & Peterson 2006 (VP06 hereafter) have previously calibrated C IV mass estimators against Hβ RM masses, providing widely used $M_{\rm BH}$ recipes. Since then, however, the Hβ RM sample has been expanded and many of RM masses have been updated based on various recent RM campaigns (e.g., Bentz et al. 2009; Denney et al. 2010; Barth 2011a,b; Grier et al. 2012). At the same time, new UV data became available for the RM sample, substantially increasing the quality and quantity of available UV spectra for the RM sample.

In this chapter we present the new calibration of the C IV based $M_{\rm BH}$ estimators utilizing the highest quality UV spectra and the most updated RM sample. In section 2 we describe the sample of Hβ reverberation mapped AGN having available UV spectra. Section 3 describes our detailed spectral analysis of the C IV emission line complex to obtain the relevant luminosity and line width measurements necessary for estimating SE $M_{\rm BH}$. We provide the updated SE C IV $M_{\rm BH}$ calibration in Section 4 and conclude with a discussion and summary in Section 5. We adopt the following cosmological parameters to calculate distances in this work: $H_0 = 70$ km s^{-1} Mpc^{-1}, $\Omega_{\rm m} = 0.30$, and $\Omega_\Lambda = 0.70$.

4.2 Sample and Data

For our analysis, we start with the reverberation mapped AGN sample, which is considered as a calibration base with reliable mass estimates. To date, there are 47 AGNs, for which Hβ reverberation based masses are available (Peterson et al. 2004; Denney et al. 2006; Bentz et al. 2009; Denney et al. 2010; Barth et al. 2011a,b; Grier et al. 2012). Of those 47 objects, we selected 39 AGNs[2] whose archival UV spectra are available from *International Ultraviolet Explorer* (*IUE*) or *Hubble Space Telescope* (*HST*) data archives[3]. First, we collected all available UV spectra covering the C IV spectral region from the public archives. If there were multiple spectra for a given individual object, either multiple epochs taken with the same instrument or from multiple instruments, we combined the spectra for each instrument by using a standard weighted average method to get the better signal-to-noise (S/N) ratio. At the same time, we tried to keep contemporaneity as far as possible. Then we selected the best quality spectra for each object based on visual inspection and by setting a limiting S/N ratio of ~ 10 per pixel, which was measured in an emission-line free region of the continuum near 1450Å or 1700Å (see Denney et al. 2013 for the S/N related issues). Among these 39 objects, we excluded four AGNs (i.e., NGC 3227, NGC 4151, PG 1411+442, PG 1700+518) because they are severely contaminated with absorption features. Other 9 AGNs (i.e., Mrk 79, Mrk 110, Mrk 142, Mrk 1501, NGC 4253, NGC 4748, NGC 6814, PG 0844+349, PG 1617+175) were also excluded due to the low quality and unreliability of UV spectra. Thus, our sample contains 26 AGNs. Table 4.1 lists the AGNs in the sample and their properties. Note that we adopt the updated virial factor, $\log f = 0.71$ (Park et al. 2012a; Woo et al. 2013).

Compared to the previous sample of VP06, one object, Mrk 290, is newly included and seven objects (i.e., 3C 120, Mrk 335, NGC 3516, NGC 4051, NGC 4593, NGC 5548, PG 2130+099) have updated reverberation $M_{\rm BH}$ (Denney et al. 2006, Bentz et al. 2009; Denney et al. 2010; Grier et al. 2012). One object, PG 0804+761, that was excluded by VP06, is included since it has a new high-quality UV spectrum from the *Cosmic Origins Spectrograph* (COS) aboard *HST*. Contrary to VP06, NGC 4151 is omitted in this work due to the strong absorption features near the line center (see Section 3). In summary, 13 AGNs

[2]Note that we also excluded two objects in the list from Peterson et al. 2004 (i.e., PG 1211+143 and IC 4329A) due to the unreliable RM measurements as done in VP06, while we included NGC 4593 since a new RM mass became available by Denney et al. (2006).

[3]http://archive.stsci.edu/iue/ & http://archive.stsci.edu/hst/

have recent high-quality UV spectra from *HST* COS [4] compared to VP06. For the remaining objects, UV spectra were obtained from the *Space Telescope Imaging Spectrograph* (STIS) aboard *HST* for one object, from the *Faint Object Spectrograph* (FOS) aboard *HST* for eight objects, and from *Short-Wavelength Prime* (SWP) camera aboard *IUE* for four objects as listed in Table 4.2. We corrected the Galactic extinction using the values of $E(B-V)$ from the recalibration of Schlafly & Finkbeiner (2011) listed in the NASA/IPAC Extragalactic Database (NED) and the reddening curve of Fitzpatrick (1999).

4.3 Spectral Measurements

In order to calibrate the C IV $M_{\rm BH}$ estimator, we measured the line width of C IV and the continuum luminosity at 1350 Å, following the multi-component fitting procedure developed by Park et al. (2012b) with a modification for the C IV region. We first fitted a single power-law continuum using the typical emission-line-free windows in both sides of C IV (i.e., $\sim 1340-1360$ Å or $\sim 1430-1470$ Å and $\sim 1700-1730$ Å), which were slightly adjusted for each spectrum to avoid the contaminating absorption and emission features. We did not subtract the iron emission, since it is generally too weak to constrain at least in our data sets, although we indeed tested the pseudocontinuum model by including the UV Fe II template from Vestergaard & Wilkes (2001). After subtracting the best-fit power-law continuum, we simultaneously fitted the C IV complex region with the multi-component model consisting of a Gaussian function for the N IV] λ1486Å, a Gaussian function for the Si II λ1531Åwhenever clearly seen, a Gaussian function + a sixth-order Gauss-Hermite series for the C IV λ1549Å, two Gaussian functions for the He II λ1640Å, and a Gaussian function for the O III] λ1663Å. Note that we fitted the 1600 Å feature, which is contaminating the red wing of C IV, with a broad He II component (cf. Appendix A. in Fine et al. 2010; Marziani et al. 2010). In the fitting process, the centers of He II, O III], N IV], and Si II emission line components were fixed to be laboratory wavelengths. We suppressed some components in He II, O III], N IV], and Si II lines based on empirical tests with and without such components. Narrow absorption features were excluded automatically in the calculation of χ^2 statistics by masking out the 3 sigma outliers below the smoothed spectrum (cf. Shen et al. 2011). Strong broad absorption features around the C IV line center were also masked out

[4] For the COS data, we performed a co-addition of multiple exposures with the upgraded costools routine (v2.0; Keeney et al. 2012) and then binned the spectra to a COS resolution element (~ 0.07 Å, ~ 17 km s^{-1}) by smoothing and re-binning by 7-pixels.

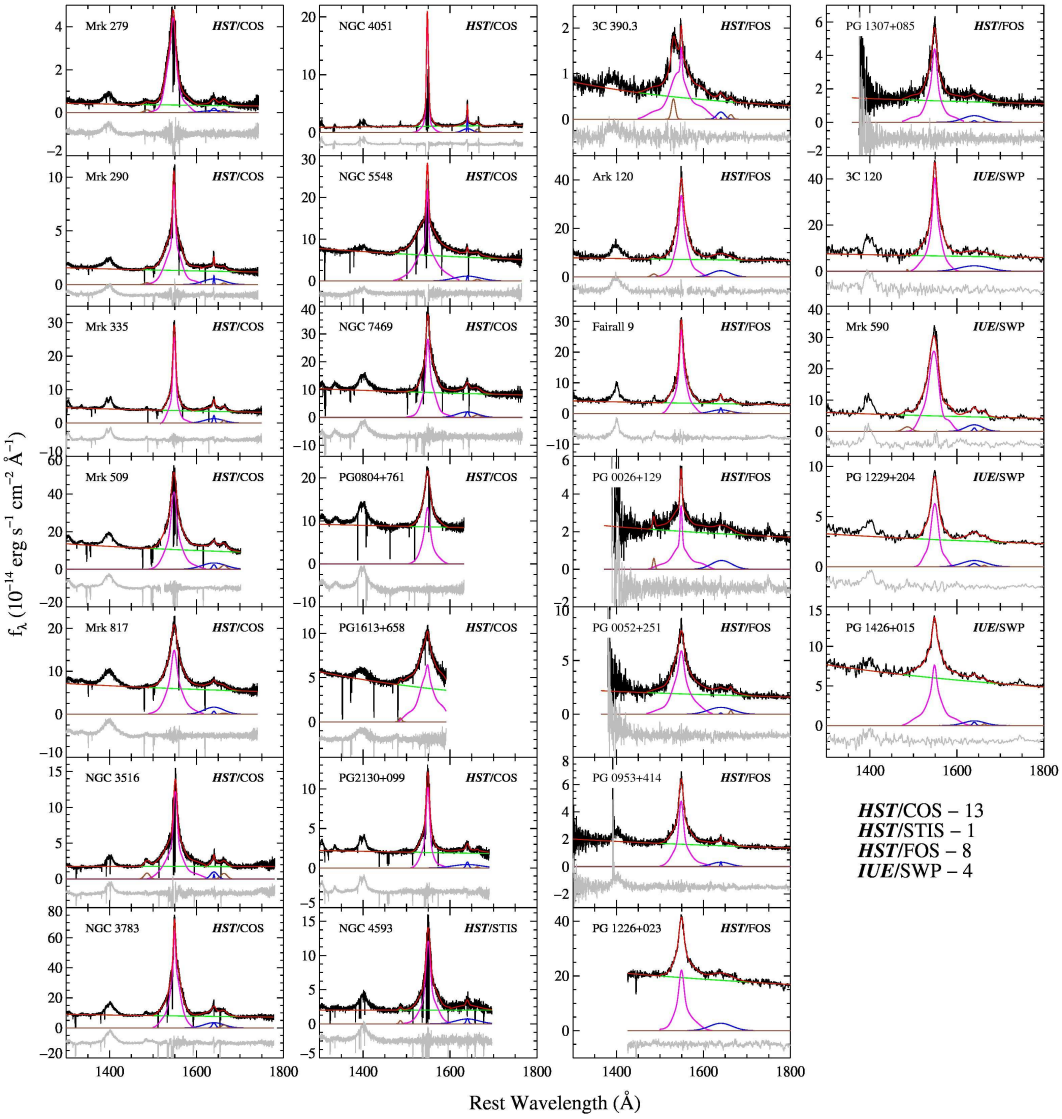

Figure 4.1 Multi-component fitting results for the sample of 26 objects. In each panel, the observed UV spectrum (black) is overplotted with the best-fit model (red), which consists of a single power-law continuum (green), C IV λ1549Å emission line (magenta), He II λ1640Å emission line (blue), O III] λ1663Å emission line (brown), and N IV] λ1486Å emission line (brown). The residual (gray), differences between black and red lines, is presented at the bottom of each panel.

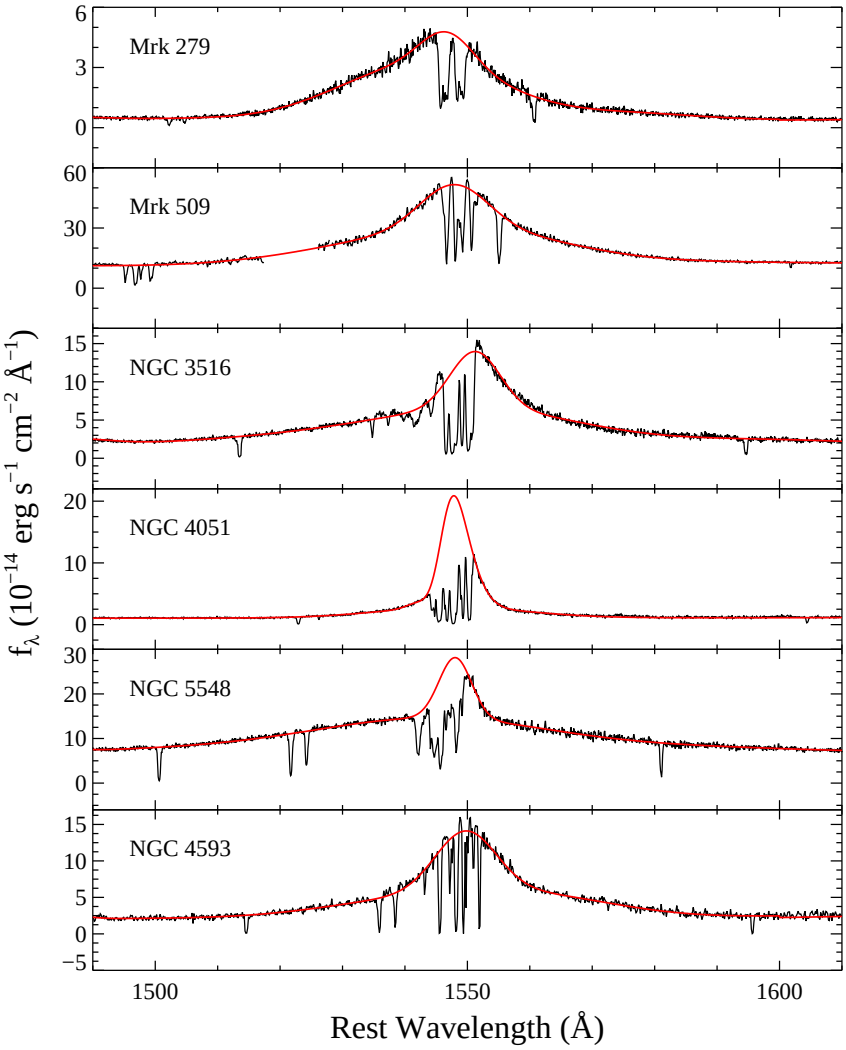

Figure 4.2 The zoom-in view of the C IV for 6 objects, for which fitting results are uncertain due to the absorption at the line center. Black and red solid lines represent the observed spectra and the best-fit models, respectively.

manually by setting exclusion windows from visual inspection.

Although it is still controversial whether or not to remove a narrow emission-line component from C IV before measuring the width, we use the full line profile of C IV, i.e., without subtracting a narrow emission-line component, in order to be consistent with other studies (VP06, Shen et al. 2011, Assef et al. 2011; Ho et al. 2012). We measured the continuum luminosities at 1350 Å and 1450 Å from the power-law model and measured the C IV line widths (FWHM and σ) from the best-fit model (i.e., a Gaussian function + a sixth-order Gauss-Hermite series) as shown in Figure 4.1. The measured line widths were corrected for the instrumental resolution following the standard practice by subtracting the instrumental resolution from the measured velocity in quadrature. In Figure 4.2, we explicitly show spectra and best-fit models for the objects showing absorption features at the center of C IV. Note that the fitting results are uncertain for these objects, in particular NGC 4051 (see Section 4.1).

To assess measurement uncertainties of the line width and continuum luminosity, we applied the Monte Carlo flux randomization method used by Park et al. (2012b; see also Shen et al. 2011). Using the $1,000$ realizations of resampled spectra made by randomly scattering flux values based on the flux errors, we fitted and measured the line width and continuum flux, and adopted the standard deviation of the distribution as the measurement uncertainties for individual objects as listed in Table 4.2.

4.3.1 Continuum Luminosities and Line Widths

Figure 4.3 presents the continuum luminosities measured at 1350 Å and 1450 Å, respectively, which are commonly adopted for the C IV $M_{\rm BH}$ estimator. Since they are almost identical, we choose to use L_{1350} for the mass estimator. The comparison between FWHM and σ of C IV is plotted in the bottom panel of Figure 4.3. It shows on average, a one-to-one relation between FWHM and σ, indicating that the C IV profile is more peaky than a Gaussian profile, although there is large scatter.

4.3.2 Comparison to Previous Measurements

We compare our measurements with those in VP06 in Figure 4.4, using the common sample (23 out of 27 objects given in their Table 2, except for Mrk 79, Mrk 110, NGC 4151, and PG 1617+175). Since there are multiple measurements in VP06, we here show weighted average values of VP06 measurements for the purpose of comparison.

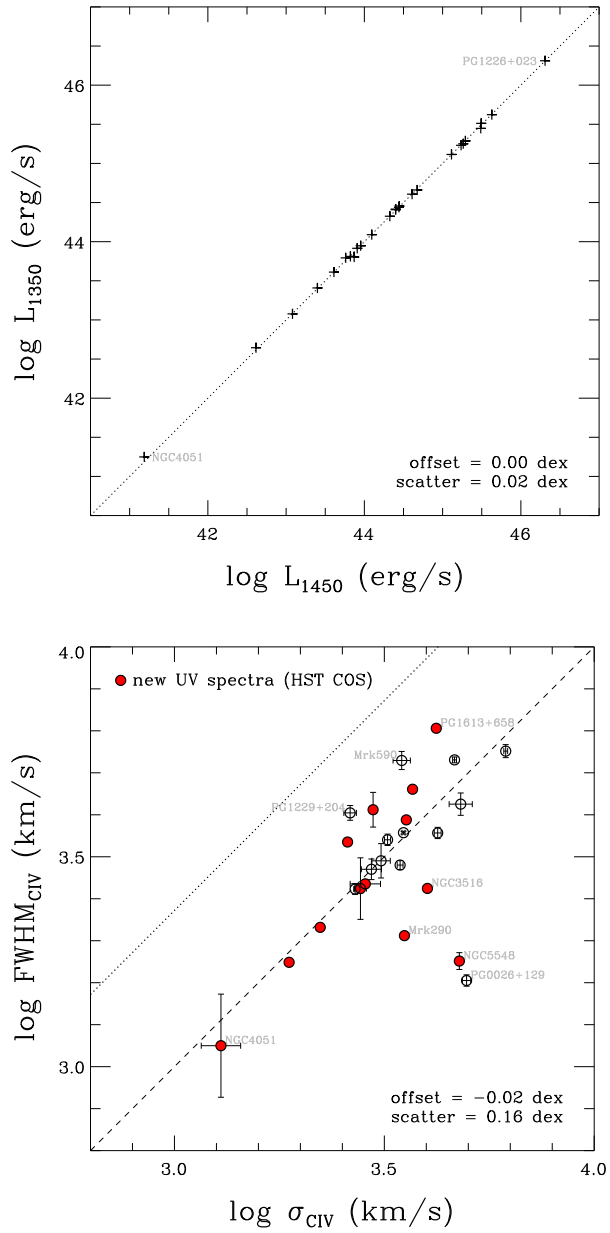

Figure 4.3 Comparison of UV measurements. The top panel shows the consistency of luminosities measured at 1350 Å and 1450 Å, respectively. The bottom panel compares the C IV FWHM and line dispersion (σ), where both were measured from the full line profile. The ratio between FWHM and σ is close to one (dashed line), indicating the line profile is more peaky than Gaussian (dotted line). Objects with new UV spectra from the *HST* COS is denoted with red filled circles. Average offset and 1σ scatter are given in the lower right corner in each panel.

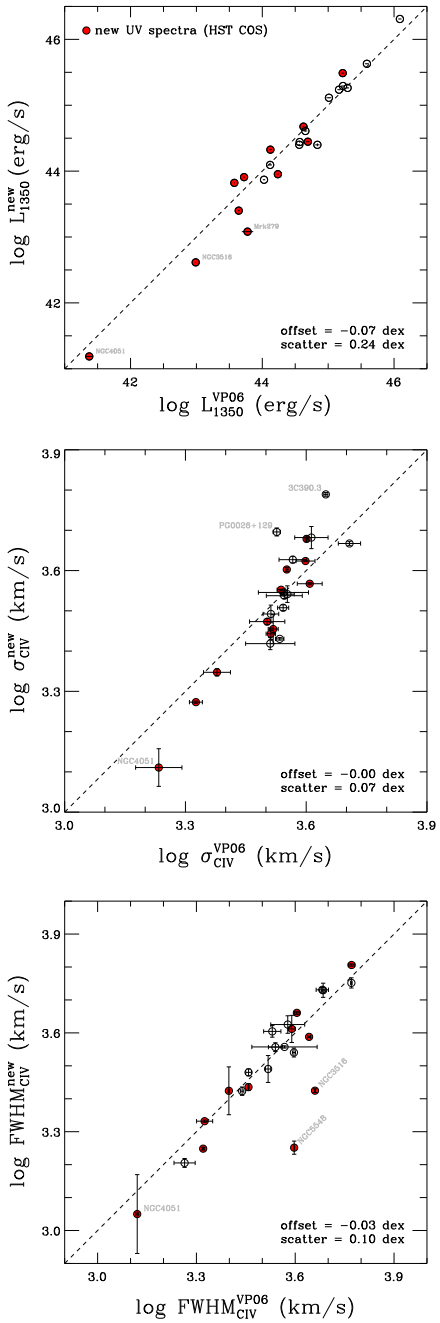

Figure 4.4 Comparisons of the luminosity (top) and line width (middle and bottom) measured in this study and those by VP06. For VP06 values, the weighted average is plotted for given objects using the listed values in their Table 2. Average offset and 1σ scatter are given in the lower right corner in each panel.

For the comparison of L_{1350}, there is 0.24 dex scatter, which may stem from a combination of the differences, e.g., adopted spectra and the Galactic extinction correction, between our study and VP06. We used the combined single spectra with the best quality while VP06 used all available SE spectra for each object. Especially for the objects with the new *HST* COS spectra (red filled circles) observed in different epochs, there could be an intrinsic difference due to the variability. In the case of the Galactic extinction correction, we utilized the recent values of $E(B-V)$ listed in the NED taken from the Schlafly & Finkbeiner (2011) recalibration, while VP06 used the original values from Schlegel et al. (1998).

When comparing our $\sigma_{\rm CIV}$ measurements to those of VP06, a slight positive systematic trend seems to be present (middle panel of Figure 4.4). The most likely origin of this trend is the difference in the adopted line width measurement methods between VP06 and this work. Based on the investigation by Fine et al. (2010), we modeled the C IV complex region with multiple components and measured line dispersion from the de-blended C IV line model profile, whereas VP06 measured line dispersion from the data without functional fits by limiting the C IV line profile range to $\pm 10,000$ km s^{-1} of the line center, regardless of the intrinsic line width of each CIV profile. Thus, the line dispersion measured by VP06 will be biased if line wings are extended much further than the fixed line limit (i.e., underestimation) or the wings are smaller than the fixed line limit (i.e., overestimation by including other features). We avoid these biases by de-blending the C IV line from other lines using the multi-component fitting analysis and measuring the line widths from the best-fit models. Since the line dispersion is more sensitive to the line wings than the line core, the decomposition and thus recovery of the line wing profile from contaminating lines is essential.

The bottom panel of Figure 4.4 compares FWHM$_{\rm C\ IV}$, indicating on average consistency between VP06 and this work, except for a few outliers. This is because FWHM is less sensitive to the line wings than $\sigma_{\rm C\ IV}$, hence the difference in the measuring method does not generate significant difference in measurements. Note that although FWHM is sensitive to the narrow-line component, both VP06 and our study used the full line profile without decomposing the broad and narrow components. Instead, another source of discrepancy comes from the fact that VP06 measured the line width directly from the data while in this study the best-fit models were used for line width measurements. Thus, there may be object-specific differences depending on how the absorptions above the "half-maximum" flux level were dealt with by VP06, and how well the functional fits represent the peak of the profile in our study.

4.4 Updating the Calibration of the C IV SE $M_{\rm BH}$ estimator

By adopting Hβ RM-based masses as true $M_{\rm BH}$ (see Table 1), we calibrate the C IV mass estimators by fitting

$$\log\left[\frac{M_{\rm BH}}{M_{\odot}}\right] = \alpha + \beta\,\log\left(\frac{L_{1350}}{10^{44}\ {\rm erg\ s^{-1}}}\right) + \gamma\,\log\left[\frac{\Delta V({\rm C\,IV})}{1000\ {\rm km\ s^{-1}}}\right], \qquad (4.1)$$

where L_{1350} is the monochromatic continuum luminosity at 1350 Å and ΔV(C IV) is the line width of C IV, either FWHM$_{\rm CIV}$ or $\sigma_{\rm CIV}$. We regress Equation 4.1 to determine the free parameters (α,β,γ) using the `FITEXY` estimator implemented in Park et al. (2012a). Note that this approach is different from that used by VP06, who adopted the luminosity slope from the size-luminosity relation and fixed the velocity slope to 2. Instead, this method is consistent with the recent approaches described by Wang et al. (2009), Rafiee & Hall (2011b), and Shen & Liu (2012). Because a non-linear dependence is often observed between the line widths of Hβ and C IV line (especially based on the FWHM; see Denney 2012 for a likely physical interpretation), leaving α, β, and γ as free parameters arguably results in a better statistical regression by accommodating the possible covariance between luminosity and line width.

4.4.1 New Calibrations

In Figure 4.5, we present the final best-fit calibration results for C IV-based mass estimators by directly comparing the C IV SE masses with the Hβ RM-based masses, using Equation 4.1. The regression results with various conditions and the previous calibrations from the literature are listed in Table 4.3. We adopt the regression results without NGC 4051, which is subject to the largest measurement errors among our sample since modeling the C IV line of this object is highly uncertain due to the strong absorption at the center (see Fig. 4.2). In addition, the variability of NGC 4051 is expected to have a large amplitude since it is the lowest-luminosity object in our sample. Thus, NGC 4051 can add large scatter to the regression and potentially skew the slope because there is only a single object at the low-mass regime. Thus, excluding this object possibly will lead to less biased results in terms of sample selection and measurement uncertainties. We will present the results without NGC 4051 hereafter unless explicitly stated.

The slope of the velocity term, when it is treated as a free parameter, is closer to the virial assumption (i.e., 2) for the $\sigma_{\rm C\,IV}$-based estimator, i.e., $\gamma = 1.74 \pm 0.55$ ($\gamma = 1.45 \pm 0.53$

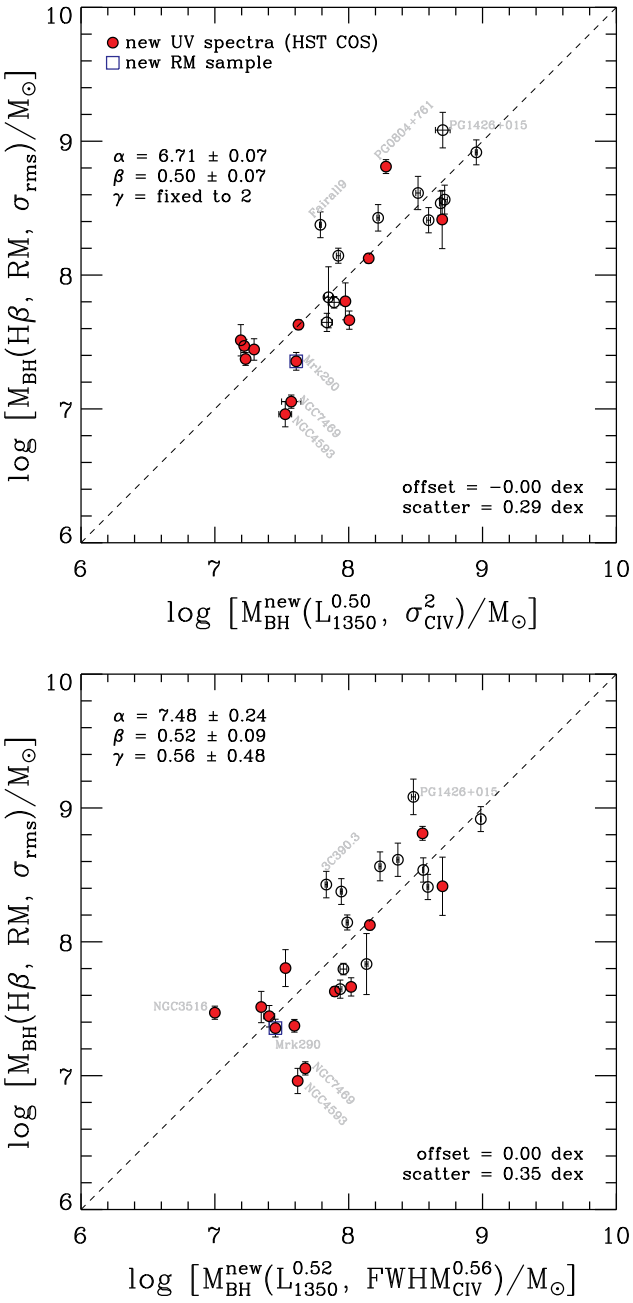

Figure 4.5 Calibrations of σ-based SE BH masses (top) and FWHM-based SE BH masses (bottom) to the Hβ RM-based BH masses. The new sample from the recent RM results is marked with a blue open square. The regressed parameters (α, β, γ) with the uncertainty estimates are given in the upper left part in each panel.

if NGC 4051 is included) than for the $\mathrm{FWHM_{C\,IV}}$-based estimator, i.e., $\gamma = 0.56 \pm 0.48$ ($\gamma = 0.52 \pm 0.46$ if NGC 4051 is included). This reinforces the use of σ for characterizing the line width of C IV, as suggested by Denney (2012, 2013; see also Peterson et al. 2004 and Park et al. 2012b for the case of Hβ). The slope of the luminosity term (i.e., $\beta = 0.51 \pm 0.08$ for σ; $\beta = 0.52 \pm 0.09$ for FWHM) is almost consistent to that of photoionization expectation (i.e., 0.5; Bentz et al. 2006) within the uncertainty. This may indicates that asynchronism between Hβ and C IV measurements does not introduce a significant overall difference for our high-luminosity, high-quality calibration sample.

In this calibration, we treat β and γ as free parameters in addition to α. Letting β be a free parameter is required to reduce luminosity dependent systematics since we are dealing with non-contemporaneous Hβ and C IV measurements, which is expected to be not necessarily linear. In addition, it is currently questionable to directly adopt the C IV size-luminosity relation (e.g., Kaspi et al. 2007) for the estimator since it is based on such a small sample. Relaxing the constraint of $\gamma = 2$ for $\mathrm{FWHM_{C\,IV}}$ can be corroborated by the investigation by Denney (2012), which shows that there are severe biases in measuring $\mathrm{FWHM_{C\,IV}}$ due to the non-variable component and dependence on the line shape. These systematic uncertainties may be properly calibrated out by taking γ as a free parameter. In the case of $\sigma_{\mathrm{C\,IV}}$, however, a similar systematic does not seem to be present for $\sigma_{\mathrm{C\,IV}}$ (see Denney 2012). Even if we allow γ to be free, the regression slope for $\sigma_{\mathrm{C\,IV}}$ is consistent to the virial expectation (i.e., 2) within 1σ uncertainty, thus we opt to fixing γ to a value of 2, avoiding systematic uncertainties due to small number statistics or sample-specific systematics. Thus, here we provide the best estimator for the C IV-based M_{BH} (see also, Fig. 4.5) as

$$\begin{aligned} \log\left[\frac{M_{\mathrm{BH}}}{M_{\odot}}\right] &= (6.71 \pm 0.07) \\ &+ (0.50 \pm 0.07)\ \log\left(\frac{L_{1350}}{10^{44}\ \mathrm{erg\ s^{-1}}}\right) \\ &+ 2\ \log\left[\frac{\sigma(\mathrm{C\,IV})}{1000\ \mathrm{km\ s^{-1}}}\right] \end{aligned} \tag{4.2}$$

with the statistical scatter against RM masses of 0.29 dex and

$$\begin{aligned}\log\left[\frac{M_{\rm BH}({\rm SE})}{M_\odot}\right] &= (7.48\pm0.24)\\ &+ (0.52\pm0.09)\,\log\left(\frac{L_{1350}}{10^{44}\ {\rm erg\ s^{-1}}}\right)\\ &+ (0.56\pm0.48)\,\log\left[\frac{{\rm FWHM(C\ IV)}}{1000\ {\rm km\ s^{-1}}}\right] \qquad (4.3)\end{aligned}$$

with the statistical scatter against RM masses of 0.35 dex. Apart from the interpretation of values of zero point and slopes, it is worth noting that these estimators are the best calibrated ones to reproduce Hβ RM masses as closely as possible for the current sample and data sets.

4.4.2 Comparison to Previous Recipes

In Figure 4.6, we present the systematic difference of $M_{\rm BH}$ estimates based on our new estimators (Equations 4.2 and 4.3) compared to the previous estimators from VP06 and SL12, respectively, using C IV line width and L_{1350} measurements. The $\sigma_{\rm C\ IV}$-based $M_{\rm BH}$ estimates show almost consistent results to VP06 with a slight offset of ~ 0.03, which is expected from a difference in the adopted values of the virial factor (i.e., $\log f = 0.71$ here versus $\log f = 0.74$ in VP06). In contrast, the comparison of FWHM$_{\rm C\ IV}$-based masses, respectively estimated with our recipe and with that of VP06, shows large scatter and a systematic trend that the VP06 recipe underestimates $M_{\rm BH}$ in the low-mass regime and overestimates $M_{\rm BH}$ in the high-mass regime, compared to our recipe. The bottom panel of Figure 4.6 shows that the SL12 recipe systematically overestimates $M_{\rm BH}$ over the whole dynamic range of the sample (i.e., $\lesssim 10^9\ M_\odot$). This is understandable because SL12 used the FWHM$_{\rm H\beta}$-based $M_{\rm BH}$ in VP06 as a fiducial one and recalibrate the estimator using their high-mass ($> 10^9\ M_\odot$) QSOs. Thus, the calibration performed by SL12 in their limited dynamical range inherits the overestimation behavior of the VP06 recipe with respect to our recipe, and propagates it into the low mass regime with larger effect. In addition, SL12 subtracted a narrow C IV component before measuring FWHM of C IV, leading to an overestimated FWHM$_{\rm C\ IV}$, compared to VP06 and our methods. We note that a large dynamic range is necessary for better calibration and investigation of the biases, as pointed out by SL12.

In order to explicitly compare the calibration methods used in here and VP06, we regress Equation 4.1 by fixing β and/or γ with the adopted values in VP06 as listed in Table 4.3. For the σ-based mass estimator, we obtain almost same calibration result ($\alpha = 6.72\pm0.06$)

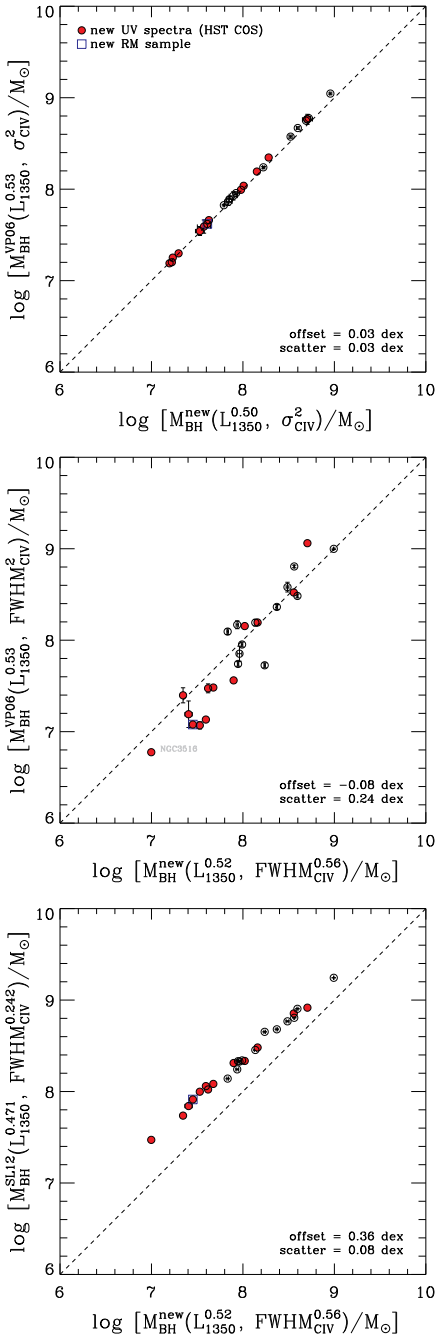

Figure 4.6 Comparison of σ-based (top) and FWHM-based (middle) $M_{\rm BH}$ respectively calculated using the estimators in this study and the estimators of VP06. In the bottom panel, $M_{\rm BH}$ calculated with the FWHM-based estimator from SL12 is compared to our mass estimates. Average offset and 1σ scatter are given in the lower right corner in each panel.

to that of VP06 (α = 6.73 $\pm$ 0.01) using the sample including NGC 4051. When NGC 4051 is exclude, the zero points reduces slightly (α = 6.69 $\pm$ 0.06) and intrinsic scatter becomes smaller. It is interesting to see the consistency of the σ-based calibration between our study and VP06, despite the systematic bias in $\sigma_{\rm CIV}$ measurements of VP06 as shown in Section 4.3.2. We interpret this as follows. Although there is a bias in the VP06 measurement method for σ, due to their choice of line limits (i.e., $\pm$10,000 km s^{-1}), their σ-based $M_{\rm BH}$ measurements serendipitously scatter evenly below and above the central point of the mass scale of the sample, consequently resulting in a similar zero point regardless of the bias in σ measurements. In the end the calibrations are very similar, however, the intrinsic scatter of our calibration is smaller than that of VP06, which demonstrates a general increase in accuracy of our σ-based masses over those of VP06, advocating for our σ measurement prescription.

4.4.3 Difference in SMBH Population using the SDSS DR7 Quasar Catalog

To demonstrate the effect of our new estimators on $M_{\rm BH}$ studies, we present in Figure 4.7 the $M_{\rm BH}$ distribution of the SDSS QSO sample as a function of redshift, based on various mass estimators. These masses are calculated using the FWHM$_{\rm C\ IV}$ measurements from Shen et al. (2011), who provides only FWHM measurements using SDSS DR7 spectra. Note that FWHM$_{\rm C\ IV}$-based $M_{\rm BH}$ determined with our new estimator is on average smaller by $\sim$ 0.25 dex than that calculated with the previous estimator by VP06, since the VP06 recipe tends to overestimate $M_{\rm BH}$ in the high-mass regime as explained in Section 4.2. In contrast, there is a smooth transition between Mg II-based masses estimated from the recipe of Wang et al. (2009) and C IV-based masses from our new calibration since both estimators are based on the same calibration scheme (see Section 4.4).

Kelly & Shen (2013) derived a predicted maximum $M_{\rm BH}$ of broad-line QSOs as a function of redshift (their Figure 7), showing a slight trend that the maximum $M_{\rm BH}$ was larger at higher redshift. However, this subtle trend may simply be a result of systematic overestimation of C IV masses at high redshift because their mass determination was based on the VP06 recipe. Adopting our new C IV mass estimator may eliminate such a trend.

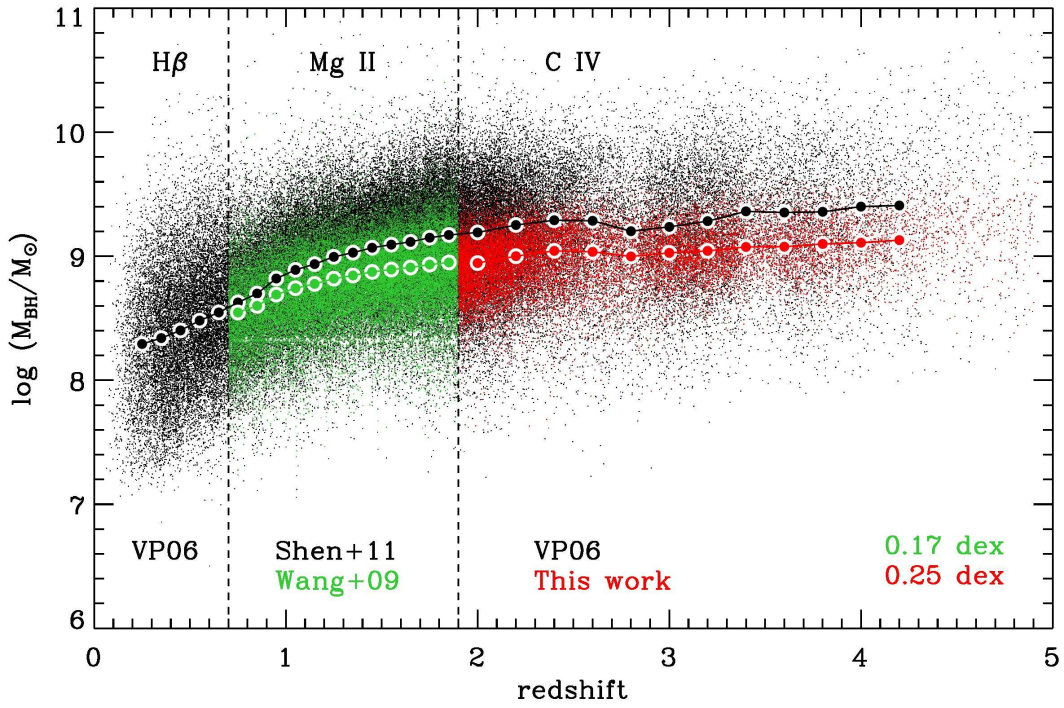

Figure 4.7 Comparison of FWHM-based $M_{\rm BH}$ distributions as a function of redshift between the previous calibrations and the new ones in this study. FWHM$_{\rm C\ IV}$ and L$_{1350}$ for $\sim 100,000$ QSOs are taken from the SDSS DR7 quasar catalog (Shen et al. 2011) to calculate $M_{\rm BH}$ using different estimators. Black dots represent $M_{\rm BH}$ estimates using previous recipes of VP06 (Hβ; $z < 0.7$), Shen+11 (Mg II; $0.7 \leqslant z < 1.9$), and VP06 (C IV; $z \geqslant 1.9$). Corresponding emission lines and $M_{\rm BH}$ recipes are indicated in upper and bottom parts with redshift separations marked with vertical dashed lines. For new $M_{\rm BH}$ estimates, green dots represent mass estimates using the calibration of Mg II by Wang et al. (2009), while red dots denote C IV-based $M_{\rm BH}$ estimates using our new recipe. Large filled circles indicate the median values in each redshift bin, with $\Delta z = 0.1$ for $z \leqslant 1.9$ and $\Delta z = 0.2$ for $z > 1.9$. Average offset values of green filled circles (Mg II) and red filled circles (C IV) from black filled circles are indicated in lower right corner.

4.5 Discussion and Conclusions

We investigated the calibration of C IV $M_{\rm BH}$ estimators based on the updated sample of 26 AGNs, for which both Hβ reverberation masses and UV archival spectra were available. The sample of AGNs with RM masses as well as the UV spectra including C IV have been expanded and updated since the calibrations performed by VP06; it is therefore useful to revisit the calibration of the C IV-based mass estimators to provide the most consistent virial $M_{\rm BH}$ estimates using the C IV emission line. Major differences of the calibration method between VP06 and the current study is twofold. First, we derived line widths (i.e., line dispersion and FWHM) from the spectral fits by performing multi-component fitting on the C IV complex region to accurately de-blend C IV from other contaminating lines while VP06 measured the line width of CIV directly from the spectra. When "applying" a SE scaling relationship to calculate $M_{\rm BH}$, it is important to use the same fitting and line width measurement prescriptions that were used in "calibrating" the scaling relationship because significant systematic differences can arise in $M_{\rm BH}$ estimates if different analysis and measurement techniques are utilized (e.g., Assef et al. 2011, Denney 2012, SL12, Park et al. 2012b). Second, we treated the slope parameters (i.e., β and γ) in the virial $M_{\rm BH}$ equation (i.e., Eq. 4.1) as free parameters as in Wang et al. (2009), which is particularly important for FWHM.

We provided the best-fit calibrations for both $\sigma_{\rm C\ IV}$- and FWHM$_{\rm C\ IV}$-based mass estimators. While we presented a consistent estimator for the σ-based masses to that of VP06, we obtained significantly different $M_{\rm BH}$ estimator for the FWHM-based masses, presumably due to relaxing the constraint of the virial expectation (i.e., γ = 2) to mitigate the FWHM-dependent biases. We generally recommend to use the σ-based mass estimator if the σ measurement is available, as it shows the better consistency with the virial relation, and σ-based masses show a smaller scatter than the FWHM-based masses when compared to Hβ RM-based masses. Using $\sigma_{\rm C\ IV}$-based estimator is also preferred by Denney (2012), who showed that the $\sigma_{\rm C\ IV}$ measured from mean spectra is the better tracer of the broad-line velocity field than the FWHM$_{\rm C\ IV}$ since FWHM of C IV is much more affected by the non-variable C IV core component.

Compared to the previously calibrated FWHM$_{\rm C\ IV}$ estimator by VP06, our new estimator shows a systematic trend as a function of mass. The VP06 recipe overestimates $M_{\rm BH}$ in the high-mass regime (i.e., $\gtrsim 10^8 M_\odot$) while it underestimate $M_{\rm BH}$ in the low-mass regime (i.e., $\lesssim 10^8 M_\odot$), compared to C IV masses based on our new estimator. This systematic

discrepancy is due to a combination of effects, including difference in the RM sample and updated RM masses, newly available UV spectra, emission-line fitting method, and calibration method. For the SDSS quasar sample (Shen et al. 2011), we find that $M_{\rm BH}$ estimates based on our new estimator are systematically smaller by ~ 0.25 dex than those based on the previous recipe of VP06.

One of the main differences in calibrating the FWHM$_{\rm C\ IV}$-based mass estimator is that we fit the exponent of velocity ($\beta = 0.56$) as in Eq. 3, instead of adopting $\beta = 2$ as in VP06. This provides effectively the same effect as adopting a varying virial factor. If a constant virial factor is used for mass determination, then FWHM-based masses will show systematic difference compared to σ-based masses, since the FWHM/σ ratio has a broad distribution, while the fiducial RM masses are derived with σ measurements from rms spectra. To resolve this issue, Collin et al. (2006), for example, introduced varying virial factors for the FWHM$_{\rm H\beta}$-based mass estimator depending on the range of the line widths. In our case, relaxing the virial (FWHM^2) requirement in calibrating FWHM$_{\rm C\ IV}$-based masses against $\sigma_{\rm H\beta}$-based RM masses provides virtually the same effect as adopting a varying virial factor, thus resulting in better consistency with σ-based masses. It also mitigates the bias caused by the contamination of the non-variable C IV emission component, where FWHM$_{\rm C\ IV}$-based masses in objects with 'peaky' ('boxy') profiles are under- (over-) estimated with previous FWHM$_{\rm C\ IV}$-based mass estimators.

The calibration of mass estimators provided in this study still suffers from a sample bias as in the case of VP06. The incompleteness or lack of low-mass objects (i.e., $\lesssim 10^7 M_{\odot}$) in the current sample will be resolved when new *HST* STIS observations become available for six low-mass reverberation-mapped AGNs (GO-12922, PI: Woo). However, the extrapolation of this calibration to high-luminosity, higher-redshift AGNs more similar to the SDSS sample can only be realized with the extension of the RM sample to this regime — an endeavor that we strongly advocate.

Apart from the calibration analysis performed in this and previous studies, several schemes to correct for the C IV-based masses have been suggested in the literature to reduce the large scatter between the C IV-based masses and the Hβ-based masses. For example, Assef et al. (2011) suggested a prescription to reduce mass residuals using the ratio of the rest-frame UV to optical continuum luminosities based on a sample of 12 lensed quasars. Shen & Liu (2012) reported a poor correlation with large scatter between FWHM$_{\rm H\beta}$ and FWHM$_{\rm CIV}$ using a sample of 60 high-luminosity QSOs, showing that some part of the scatter correlated with the blueshift of C IV with respect to Hβ. They suggested a correction for

the FWHM of C IV and C III] lines as a function of the C IV blueshift. Recently, Denney (2012) showed that the C IV line profile consists of both non-variable and variable components based on the sample of seven AGNs with C IV reverberation data, and concluded that this non-variable component is a main source of the large scatter of the C IV SE $M_{\rm BH}$. They provided an empirical correction for the FWHM-based mass depending on the line shape as parameterized as the ratio of FWHM to the line dispersion. Since the C IV line region is more likely to be affected by non-virial motions such as outflows and winds than the lower ionization line region, such as Hβ (e.g., Shen et al. 2008; Richards et al. 2011), aforementioned corrections are also important and worth investigating further with a larger sample with enlarged dynamic range.

In general, correcting for possible systematic biases and providing accurate $M_{\rm BH}$ estimates is crucial for studies of the cosmic evolution of BH population, particularly at high-redshifts (e.g., Fine et al. 2006; Shen et al. 2008, 2011, Shen & Kelly 2012; Kelly & Shen 2013). Thus, it is important to ensure a reliable calibration at the high-mass end ($\gtrsim 10^9\ M_\odot$) since the C IV mass estimators are most applicable to high-mass AGNs at high-redshift utilizing optical spectroscopic data from large AGN surveys. Note that the current RM sample used for calibrating C IV mass estimators still suffers from the lack of high-luminosity AGNs, suggesting that the RM sample may not best represent the high-luminosity QSOs at high-redshifts, i.e., SDSS QSOs. Thus, obtaining direct C IV reverberation mapping results for high-mass QSOs will be even more useful (see Kaspi et al. 2007 for tentative results), despite the practical observational challenges. Such measurements will be used to better determine a reliable C IV size-luminosity relation and to directly investigate non-varying component of C IV.

Table 4.1. Optical spectral properties from Hβ reverberation mapping

Object	z	$\tau_{\rm cent}$ (Hβ) (days)	$\sigma_{\rm rms}$ (Hβ) (km s^{-1})	FWHM$_{\rm rms}$ (Hβ) (km s^{-1})	$\log(M_{\rm BH}/M_\odot)$[a] (RM)	Ref.
(1)	(2)	(3)	(4)	(5)	(6)	(7)
3C120	0.03301	$27.2^{+1.1}_{-1.1}$	1514 ± 65	2539 ± 466	7.80 ± 0.04	6
3C390.3	0.05610	$23.60^{+6.45}_{-6.45}$	3105 ± 81	9958 ± 1046	8.43 ± 0.10	1
Ark120	0.03230	$39.05^{+4.57}_{-4.57}$	1896 ± 44	5364 ± 168	8.14 ± 0.06	1
Fairall9	0.04702	$17.40^{+3.75}_{-3.75}$	3787 ± 197	6901 ± 707	8.38 ± 0.10	1
Mrk279	0.03045	$16.70^{+3.90}_{-3.90}$	1420 ± 96	3385 ± 349	7.51 ± 0.12	1
Mrk290	0.02958	$8.72^{+1.21}_{-1.02}$	1609 ± 47	4270 ± 157	7.36 ± 0.07	4
Mrk335	0.02578	$14.1^{+0.4}_{-0.4}$	1293 ± 64	1025 ± 35	7.37 ± 0.05	6
Mrk509	0.03440	$79.60^{+5.75}_{-5.75}$	1276 ± 28	2715 ± 101	8.12 ± 0.04	1
Mrk590	0.02638	$24.23^{+2.11}_{-2.11}$	1653 ± 40	2512 ± 101	7.65 ± 0.07	1
Mrk817	0.03145	$19.05^{+2.45}_{-2.45}$	1636 ± 57	3992 ± 302	7.66 ± 0.07	1
NGC3516	0.00884	$11.68^{+1.02}_{-1.53}$	1591 ± 10	5175 ± 96	7.47 ± 0.05	4
NGC3783	0.00973	$10.20^{+2.80}_{-2.80}$	1753 ± 141	3093 ± 529	7.44 ± 0.08	1
NGC4051	0.00234	$1.87^{+0.54}_{-0.50}$	927 ± 64	1034 ± 41	6.20 ± 0.14	4
NGC4593	0.00900	$3.73^{+0.75}_{-0.75}$	1561 ± 55	4141 ± 416	6.96 ± 0.09	2
NGC5548	0.01717	$4.18^{+0.86}_{-1.30}$	3900 ± 266	12539 ± 1927	7.80 ± 0.14	3, 5
NGC7469	0.01632	$4.50^{+0.75}_{-0.75}$	1456 ± 207	2169 ± 459	7.05 ± 0.05	1
PG0026+129	0.14200	$111.00^{+26.20}_{-26.20}$	1773 ± 285	1719 ± 495	8.56 ± 0.11	1
PG0052+251	0.15500	$89.80^{+24.30}_{-24.30}$	1783 ± 86	4165 ± 381	8.54 ± 0.09	1
PG0804+761	0.10000	$146.90^{+18.85}_{-18.85}$	1971 ± 105	2012 ± 845	8.81 ± 0.05	1
PG0953+414	0.23410	$150.10^{+22.10}_{-22.10}$	1306 ± 144	3002 ± 398	8.41 ± 0.09	1
PG1226+023	0.15830	$306.80^{+79.70}_{-79.70}$	1777 ± 150	2598 ± 299	8.92 ± 0.09	1
PG1229+204	0.06301	$37.80^{+21.45}_{-21.45}$	1385 ± 111	3415 ± 320	7.83 ± 0.23	1
PG1307+085	0.15500	$105.60^{+41.30}_{-41.30}$	1820 ± 122	5058 ± 524	8.61 ± 0.12	1
PG1426+015	0.08647	$95.00^{+33.50}_{-33.50}$	3442 ± 308	6323 ± 1295	9.08 ± 0.13	1
PG1613+658	0.12900	$40.10^{+15.10}_{-15.10}$	2547 ± 342	7897 ± 1792	8.42 ± 0.22	1
PG2130+099	0.06298	$12.8^{+1.2}_{-0.9}$	1825 ± 65	2097 ± 102	7.63 ± 0.04	6

Note. — Col. (1) Name. Col. (2) Redshifts are from the NASA/IPAC Extragalactic Database (NED). Col. (3) Rest-frame Hβ time lag measurements. Col. (4) Line dispersion ($\sigma_{\rm line}$) measured from rms spectra. Col. (5) FWHM measured from rms spectra Col. (6) $M_{\rm BH}$ estimates from reverberation mapping: $M_{\rm BH}({\rm RM}) = f c \tau_{\rm cent} \sigma_{\rm rms}^2 / G$ where the virial factor f is adopted from Park et al. (2012a) (i.e., $\log f = 0.71$). Col. (7) References. 1. Peterson et al. 2004; 2. Denney et al. 2006; 3. Bentz et al. 2009; 4. Denney et al. 2010; 5. Park et al. 2012b; 6. Grier et al. 2012.

[a]Note that as in VP06 the $M_{\rm BH}$ taken from Table 8 in Peterson et al. (2004) are based on the weighted average virial products from RM results of all reliable different emission lines rather than Hβ only results.

Table 4.2. Ultraviolet spectral properties from C IV single-epoch estimates

Object	Telescope/Instrument	Date Observed	S/N (1450Å or 1700Å) (pix^{-1})	$E(B-V)$ (mag)	$\log(\lambda L_\lambda/\mathrm{erg\ s^{-1}})$ (1350Å)	σ_{SE} (C IV) ($km\ s^{-1}$)	$FWHM_{SE}$ (C IV) ($km\ s^{-1}$)	$\log(M_{BH}/M_\odot)$ (σ(C IV), SE)	$\log(M_{BH}/M_\odot)$ (FWHM(C IV), SE)	Notes
(1)	(2)	(3)	(4)	(5)	(6)	(7)	(8)	(9)	(10)	(11)
3C120	*IUE*/SWP	1994-02-19,27;1994-03-11	12	0.263	44.399 ± 0.021	3106 ± 157	3093 ± 291	7.89 ± 0.05	7.96 ± 0.03	···
3C390.3	*HST*/FOS	1996-03-31	18	0.063	43.869 ± 0.003	6154 ± 65	5645 ± 202	8.22 ± 0.01	7.83 ± 0.01	···
Ark120	*HST*/FOS	1995-07-29	17	0.114	44.400 ± 0.005	3219 ± 53	3471 ± 108	7.93 ± 0.01	7.99 ± 0.01	···
Fairall9	*HST*/FOS	1993-01-22	24	0.023	44.442 ± 0.004	2694 ± 20	2649 ± 77	7.79 ± 0.01	7.95 ± 0.01	···
Mrk279	*HST*/COS	2011-06-27	9	0.014	43.082 ± 0.004	2973 ± 53	4093 ± 388	7.20 ± 0.02	7.35 ± 0.02	···
Mrk290	*HST*/COS	2009-10-28	24	0.014	43.611 ± 0.002	3531 ± 32	2052 ± 36	7.61 ± 0.01	7.45 ± 0.01	···
Mrk335	*HST*/COS	2009-10-31;2010-02-08	29	0.032	43.953 ± 0.001	1876 ± 12	1772 ± 14	7.23 ± 0.01	7.59 ± 0.01	···
Mrk509	*HST*/COS	2009-12-10,11	107	0.051	44.675 ± 0.001	3568 ± 9	3872 ± 18	8.15 ± 0.01	8.16 ± 0.01	···
Mrk590	*IUE*/SWP	1991-01-14	17	0.033	44.094 ± 0.007	3479 ± 165	5362 ± 266	7.84 ± 0.04	7.94 ± 0.01	···
Mrk817	*HST*/COS	2009-08-04;2009-12-28	38	0.006	44.326 ± 0.001	3692 ± 23	4580 ± 48	8.01 ± 0.01	8.02 ± 0.01	···
NGC3516	*HST*/COS	2010-10-04;2011-01-22	20	0.038	42.615 ± 0.002	4006 ± 49	2658 ± 34	7.22 ± 0.01	7.00 ± 0.01	abs
NGC3783	*HST*/COS	2011-05-26	29	0.105	43.400 ± 0.001	2774 ± 91	2656 ± 444	7.30 ± 0.03	7.41 ± 0.04	···
NGC4051	*HST*/COS	2009-12-11	23	0.011	41.187 ± 0.001	1290 ± 139	1122 ± 309	5.53 ± 0.09	6.05 ± 0.07	abs
NGC4593	*HST*/STIS	2002-06-23,24	10	0.022	43.761 ± 0.005	2946 ± 162	2952 ± 166	7.53 ± 0.05	7.62 ± 0.01	···
NGC5548	*HST*/COS	2011-06-16,17	36	0.018	43.822 ± 0.001	4772 ± 80	1785 ± 82	7.98 ± 0.01	7.53 ± 0.01	abs
NGC7469	*HST*/COS	2010-10-16	32	0.061	43.909 ± 0.001	2849 ± 237	2725 ± 66	7.57 ± 0.07	7.68 ± 0.01	···
PG0026+129	*HST*/FOS	1994-11-27	25	0.063	45.236 ± 0.005	4965 ± 113	1604 ± 50	8.72 ± 0.02	8.24 ± 0.01	···
PG0052+251	*HST*/FOS	1993-07-22	21	0.042	45.292 ± 0.004	4648 ± 50	5380 ± 87	8.69 ± 0.01	8.56 ± 0.01	···
PG0804+761	*HST*/COS	2010-06-12	34	0.031	45.493 ± 0.001	2585 ± 20	3429 ± 23	8.28 ± 0.01	8.56 ± 0.01	···
PG0953+414	*HST*/FOS	1991-06-18	18	0.012	45.629 ± 0.005	3448 ± 55	3021 ± 74	8.60 ± 0.01	8.60 ± 0.01	···
PG1226+023	*HST*/FOS	1991-01-14,15	93	0.018	46.309 ± 0.001	3513 ± 29	3609 ± 29	8.96 ± 0.01	8.99 ± 0.01	···
PG1229+204	*IUE*/SWP	1982-05-01,02	28	0.024	44.609 ± 0.009	2621 ± 90	4023 ± 163	7.85 ± 0.03	8.14 ± 0.01	···
PG1307+085	*HST*/FOS	1993-07-21	14	0.030	45.113 ± 0.006	4237 ± 80	3604 ± 111	8.52 ± 0.02	8.37 ± 0.01	···
PG1426+015	*IUE*/SWP	1985-03-01,02	45	0.028	45.263 ± 0.004	4808 ± 305	4220 ± 258	8.71 ± 0.06	8.49 ± 0.02	···
PG1613+658	*HST*/COS	2010-04-08,09,10	37	0.023	45.488 ± 0.001	4204 ± 17	6398 ± 51	8.70 ± 0.01	8.71 ± 0.01	···

Table 4.2 (cont'd)

Object	Telescope/Instrument	Date Observed	S/N (1450Å or 1700Å) (pix^{-1})	$E(B-V)$ (mag)	$\log(\lambda L_\lambda/\mathrm{erg\ s^{-1}})$ (1350Å)	σ_{SE} (C IV) ($km\ s^{-1}$)	$FWHM_{SE}$ (C IV) ($km\ s^{-1}$)	$\log(M_{BH}/M_\odot)$ (σ(C IV), SE)	$\log(M_{BH}/M_\odot)$ (FWHM(C IV), SE)	Notes
(1)	(2)	(3)	(4)	(5)	(6)	(7)	(8)	(9)	(10)	(11)
PG2130+099	*HST*/COS	2010-10-28	22	0.039	44.447 ± 0.001	2225 ± 47	2147 ± 18	7.63 ± 0.02	7.90 ± 0.01	···

Note. — Col. (1) Name. Col. (2) Telescope/Instrument from which archival UV spectra were obtained. Note that the new COS spectra were obtained after 2009. Col. (3) Observation date for combined spectra. Col. (4) Signal-to-noise ratio per pixel at 1450Å or 1700Å in rest-frame. Col. (5) $E(B-V)$ are from the NASA/IPAC Extragalactic Database (NED) based on the recalibration of Schlafly & Finkbeiner (2011). Col. (6) Continuum luminosity measured at 1350Å. Col. (7) Line dispersion (σ_{line}) measured from SE spectra. Col. (8) FWHM measured from SE spectra. Col. (9) SE mass estimates based on σ_{line} from the new estimator. Col. (10) SE mass estimates based on FWHM from the new estimator. Col. (11) abs: The C IV line profile is affected by a strong absorption near the line center. Thus the emission-line modeling could be uncertain although that region was masked out.

Table 4.3. C IV Mass Calibration results

$\log[M_{\rm BH}({\rm RM})/{\rm M}_\odot] = \alpha + \beta \log({\rm L}_{1350}/10^{44}\ {\rm ergs}^{-1}) + \gamma \log[\Delta {\rm V(CIV)}/1000\ {\rm kms}^{-1}]$

ΔV(CIV)	α	β	γ	$\sigma_{\rm int}$	mean offset (dex)	1σ scatter (dex)	Ref.
Previous calibrations							
$\sigma_{\rm line}$	6.73 ± 0.01	0.53	2	0.33	···	···	VP06[a]
$\sigma_{\rm line}$	6.73 ± 0.02	0.53	2	0.37	···	···	VP06[b]
FWHM	6.66 ± 0.01	0.53	2	0.36	···	···	VP06[a]
FWHM	6.69 ± 0.01	0.53	2	0.43	···	···	VP06[b]
FWHM	8.021	0.471	0.242	···	0.03	0.28	SL12
This work							
$\sigma_{\rm line}$	7.02 ± 0.29	0.46 ± 0.07	1.45 ± 0.53	0.30 ± 0.04	0.00	0.298	
FWHM	7.51 ± 0.21	0.51 ± 0.08	0.52 ± 0.46	0.34 ± 0.05	0.00	0.340	
This work (fixing γ = 2)							
$\sigma_{\rm line}$	6.75 ± 0.07	0.43 ± 0.07	2	0.30 ± 0.05	0.00	0.308	
FWHM	6.81 ± 0.09	0.40 ± 0.08	2	0.41 ± 0.05	0.00	0.421	
This work (fixing β = 0.5)							
$\sigma_{\rm line}$	7.07 ± 0.27	0.5	1.34 ± 0.48	0.29 ± 0.04	0.00	0.301	
FWHM	7.50 ± 0.18	0.5	0.54 ± 0.36	0.33 ± 0.04	0.00	0.340	
This work (fixing β = 0.5 and γ = 2)							
$\sigma_{\rm line}$	6.73 ± 0.06	0.5	2	0.30 ± 0.04	0.00	0.318	
FWHM	6.78 ± 0.08	0.5	2	0.41 ± 0.05	0.00	0.439	
This work (fixing β = 0.53 and γ = 2 for the comparison to VP06)							
$\sigma_{\rm line}$	6.72 ± 0.06	0.53	2	0.31 ± 0.04	0.00	0.328	
FWHM	6.77 ± 0.08	0.53	2	0.42 ± 0.05	0.00	0.449	
This work (w/o NGC 4051)							
$\sigma_{\rm line}$	6.84 ± 0.30	0.51 ± 0.08	1.74 ± 0.55	0.29 ± 0.04	0.00	0.293	
FWHM	$\mathbf{7.48 \pm 0.24}$	$\mathbf{0.52 \pm 0.09}$	$\mathbf{0.56 \pm 0.48}$	0.35 ± 0.05	0.00	0.347	best-fit[c]
This work (w/o NGC 4051; fixing γ = 2)							

Table 4.3 (cont'd)

ΔV(CIV)	α	β	γ	$\sigma_{\rm int}$	mean offset (dex)	1σ scatter (dex)	Ref.
$\sigma_{\rm line}$	$\mathbf{6.71 \pm 0.07}$	$\mathbf{0.50 \pm 0.07}$	**2**	0.28 ± 0.04	0.00	0.295	best-fit[c]
FWHM	6.78 ± 0.10	0.45 ± 0.10	2	0.41 ± 0.05	0.00	0.419	
This work (w/o NGC 4051; fixing β = 0.5)							
$\sigma_{\rm line}$	6.84 ± 0.29	0.5	1.75 ± 0.51	0.28 ± 0.04	0.00	0.293	
FWHM	7.47 ± 0.23	0.5	0.59 ± 0.44	0.34 ± 0.04	0.00	0.347	
This work (w/o NGC 4051; fixing β = 0.5 and γ = 2)							
$\sigma_{\rm line}$	6.71 ± 0.06	0.5	2	0.28 ± 0.04	0.00	0.295	
FWHM	6.75 ± 0.08	0.5	2	0.40 ± 0.05	0.00	0.422	
This work (w/o NGC 4051; fixing β = 0.53 and γ = 2 for the comparison to VP06)							
$\sigma_{\rm line}$	6.69 ± 0.06	0.53	2	0.28 ± 0.04	0.00	0.296	
FWHM	6.74 ± 0.08	0.53	2	0.41 ± 0.05	0.00	0.425	

Note. — The mean offset and 1σ scatter for our calibrations are measured from the average and standard deviation of mass residuals between RM masses and calibrated SE masses, $\Delta = \log M_{\rm BH}({\rm RM}) - \log M_{\rm BH}({\rm SE})$.

[a]The VP06 calibration based on all individual measurements for each object.

[b]The VP06 calibration based on weighted averages of all measurements for each object.

[c]We suggest these calibrations as the best $M_{\rm BH}$ estimators. The viral factor is assumed as $\log f = 0.71$.

References

Assef, R. J., Denney, K. D., Kochanek, C. S., et al. 2011, ApJ, 742, 93

Barth, A. J., Nguyen, M. L., Malkan, M. A., et al. 2011a, ApJ, 732, 121

Barth, A. J., Pancoast, A., Thorman, S. J., et al. 2011b, ApJ, 743, L4

Baskin, A., & Laor, A. 2005, MNRAS, 356, 1029

Bennert, V. N., Treu, T., Woo, J.-H., et al. 2010, ApJ, 708, 1507

Bennert, V. N., Auger, M. W., Treu, T., Woo, J.-H., & Malkan, M. A. 2011, ApJ, 742, 107

Bentz, M. C., Peterson, B. M., Pogge, R. W., Vestergaard, M., & Onken, C. A. 2006, ApJ, 644, 133

Bentz, M. C., Peterson, B. M., Netzer, H., Pogge, R. W., & Vestergaard, M. 2009, ApJ, 697, 160

Bentz, M. C., Denney, K. D., Grier, C. J., et al. 2013, ApJ, in press, (arXiv:1303.1742)

Canalizo, G., Wold, M., Hiner, K. D., et al. 2012, ApJ, 760, 38

Collin, S., Kawaguchi, T., Peterson, B. M., & Vestergaard, M. 2006, A&A, 456, 75

Denney, K. D., Bentz, M. C., Peterson, B. M., et al. 2006, ApJ, 653, 152

Denney, K. D., Peterson, B. M., Dietrich, M., Vestergaard, M., & Bentz, M. C. 2009, ApJ, 692, 246

Denney, K. D., Peterson, B. M., Pogge, R. W., et al. 2010, ApJ, 721, 715

Denney, K. D. 2012, ApJ, 759, 44

Denney, K. D., Pogge, R. W., Assef, R. J., et al. 2013, ApJ, submitted, (arXiv:1303.3889)

Dietrich, M., Mathur, S., Grupe, D., & Komossa, S. 2009, ApJ, 696, 1998

Ferrarese, L., & Merritt, D. 2000, ApJ, 539, L9

Fine, S., Croom, S. M., Miller, L., et al. 2006, MNRAS, 373, 613

Fine, S., Croom, S. M., Bland-Hawthorn, J., et al. 2010, MNRAS, 409, 591

Fitzpatrick, E. L. 1999, PASP, 111, 63

Gebhardt, K., Bender, R., Bower, G., et al. 2000, ApJ, 539, L13

Graham, A. W., Onken, C. A., Athanassoula, E., & Combes, F. 2011, MNRAS, 412, 2211

Greene, J. E., Peng, C. Y., & Ludwig, R. R. 2010, ApJ, 709, 937

Grier, C. J., Peterson, B. M., Pogge, R. W., et al. 2012, ApJ, 755, 60

Hiner, K. D., Canalizo, G., Wold, M., Brotherton, M. S., & Cales, S. L. 2012, ApJ, 756, 162

Ho, L. C., Goldoni, P., Dong, X.-B., Greene, J. E., & Ponti, G. 2012, ApJ, 754, 11

Kaspi, S., Smith, P. S., Netzer, H., et al. 2000, ApJ, 533, 631

Kaspi, S., Maoz, D., Netzer, H., et al. 2005, ApJ, 629, 61

Kaspi, S., Brandt, W. N., Maoz, D., et al. 2007, ApJ, 659, 997

Keeney, B. A., Danforth, C. W., Stocke, J. T., France, K., & Green, J. C. 2012, PASP, 124, 830

Kelly, B. C., & Bechtold, J. 2007, ApJS, 168, 1

Kelly, B. C., & Shen, Y. 2013, ApJ, 764, 45

Leighly, K. M., & Moore, J. R. 2004, ApJ, 611, 107

Magorrian, J., Tremaine, S., Richstone, D., et al. 1998, AJ, 115, 2285

Marziani, P., Sulentic, J. W., Negrete, C. A., et al. 2010, MNRAS, 409, 1033

McGill, K. L., Woo, J.-H., Treu, T., & Malkan, M. A. 2008, ApJ, 673, 703

McLure, R. J., & Dunlop, J. S. 2004, MNRAS, 352, 1390

McLure, R. J., & Jarvis, M. J. 2002, MNRAS, 337, 109

Merloni, A., Bongiorno, A., Bolzonella, M., et al. 2010, ApJ, 708, 137

Metzroth, K. G., Onken, C. A., & Peterson, B. M. 2006, ApJ, 647, 901

Netzer, H., Lira, P., Trakhtenbrot, B., Shemmer, O., & Cury, I. 2007, ApJ, 671, 1256

Onken, C. A., Ferrarese, L., Merritt, D., et al. 2004, ApJ, 615, 645

Park, D., Kelly, B. C., Woo, J.-H., & Treu, T. 2012a, ApJS, 203, 6

Park, D., Woo, J.-H., Treu, T., et al. 2012b, ApJ, 747, 30

Peng, C. Y., Impey, C. D., Rix, H.-W., et al. 2006, ApJ, 649, 616

Peterson, B. M. 1993, PASP, 105, 247

Peterson, B. M., Ferrarese, L., Gilbert, K. M., et al. 2004, ApJ, 613, 682

Peterson, B. M., Bentz, M. C., Desroches, L.-B., et al. 2005, ApJ, 632, 799

Rafiee, A., & Hall, P. B. 2011a, ApJS, 194, 42

Rafiee, A., & Hall, P. B. 2011b, MNRAS, 415, 2932

Richards, G. T., Kruczek, N. E., Gallagher, S. C., et al. 2011, AJ, 141, 167

Salviander, S., Shields, G. A., Gebhardt, K., & Bonning, E. W. 2007, ApJ, 662, 131

Schlafly, E. F., & Finkbeiner, D. P. 2011, ApJ, 737, 103

Schlegel, D. J., Finkbeiner, D. P., & Davis, M. 1998, ApJ, 500, 525

Shen, Y., Greene, J. E., Strauss, M. A., Richards, G. T., & Schneider, D. P. 2008, ApJ, 680, 169

Shen, Y., Richards, G. T., Strauss, M. A., et al. 2011, ApJS, 194, 45

Shen, Y., & Liu, X. 2012, ApJ, 753, 125

Shen, Y., & Kelly, B. C. 2012, ApJ, 746, 169

Sulentic, J. W., Bachev, R., Marziani, P., Negrete, C. A., & Dultzin, D. 2007, ApJ, 666, 757

Trakhtenbrot, B., & Netzer, H. 2012, MNRAS, 427, 3081

Treu, T., Woo, J.-H., Malkan, M. A., & Blandford, R. D. 2007, ApJ, 667, 117

Vestergaard, M. 2002, ApJ, 571, 733

Vestergaard, M., & Peterson, B. M. 2006, ApJ, 641, 689

Vestergaard, M., & Wilkes, B. J. 2001, ApJS, 134, 1

Wandel, A., Peterson, B. M., & Malkan, M. A. 1999, ApJ, 526, 579

Wang, J.-G., Dong, X.-B., Wang, T.-G., et al. 2009, ApJ, 707, 1334

Woo, J.-H., Treu, T., Malkan, M. A., & Blandford, R. D. 2006, ApJ, 645, 900

Woo, J.-H., Treu, T., Malkan, M. A., & Blandford, R. D. 2008, ApJ, 681, 925

Woo, J.-H., Treu, T., Barth, A. J., et al. 2010, ApJ, 716, 269

Woo, J.-H., Schulze, A., Park, D., Kang, W.-R., Kim, S. C., & Riechers, D. 2013, ApJ, submitted

Chapter 5

Investigating the cosmic evolution of the black hole mass – bulge luminosity scaling relation

(A journal paper based on this chapter will be submitted soon for publication in ApJ.)

5.1 Introduction

The black hole – galaxy co-evolution framework is now one of the basic elements in the understanding of galaxy formation and evolution. The tight correlations between the masses of supermassive black holes (BH) and the global properties of the host galaxies discovered in the local universe (e.g., $M_{\rm BH}-\sigma_*$, $M_{\rm BH}-L_{\rm bul}$, and $M_{\rm BH}-M_{\rm bul}$ relations; Magorrian et al. 1998; Ferraresse & Merritt 2000; Gebhardt et al. 2000; Marconi & Hunt 2003; Häring & Rix 2004) imply a causal connection between the BH growth and galaxy evolution.

The AGN feedback mechanism has been suggested for a physical origin of this coupling (e.g., Kauffmann & Haehnelt 2000; Volonteri et al. 2003; Croton et al. 2006; Hopkins et al. 2009). It has also been suggested that a consequence of a statistical convergence from a hierarchical merging can reproduce the observed correlations without a physical coupling (e.g., Peng 2007; Hirschmann et al. 2010; Jahnke & Macciò 2011). However, the origin of this correlation is still unclear since these results from the theoretical modelings rely on many ad hoc assumptions and approximations due to too many physical processes involved

with huge degrees of freedom. Therefore the more and accurate observational constraints on how the black holes and galaxies co-evolve are required and it will be essential to investigate physical mechanisms involved in the BH-galaxy co-evolution. This can be achieved by investigating the empirical scaling relations as a function of cosmic time.

Many observational studies have been performed to measure the cosmic evolution of the scaling relations using a sample of active galaxies to probe the distant universe (e.g., Treu et al. 2004, 2007; McLure et al. 2006; Peng et al. 2006; Woo et al. 2006, 2008; Jahnke et al. 2009; Decarli et al. 2009; Merloni et al. 2010; Bennert et al. 2010, 2011b; Cisternas et al. 2011; Hiner et al. 2012; Canalizo et al. 2012; Schramm & Silverman 2013), which mainly report the tentative result that the BH growth precedes the growth of the host bulge.

However, many previous studies were still subject to small number of the sample and relying on relatively uncertain measurements for black hole mass and host galaxy properties. In this work, we study the cosmic evolution of the $M_{\rm BH}-L_{\rm bul}$ relation for the extended sample of 52 Seyfert 1 galaxies at z = 0.36 and z = 0.57 including all previous samples from Woo et al. (2006), Treu et al. (2007), Woo et al. (2008), and Bennert et al. (2010) for better statistics. Black hole mass is measured using the Hβ broad emission line and 5100Å nuclear luminosity from a combined analysis of the high-quality Keck spectra and *HST* images. Bulge luminosity is obtained with structural decomposition of the high-resolution *HST* imaging data.

We adopt the following cosmological parameters to calculate distances in this work: H_0 = 70 km s^{-1} Mpc^{-1}, $\Omega_{\rm m}$ = 0.30, and Ω_Λ = 0.70. Magnitudes are given in the AB system.

5.2 Sample and Data

5.2.1 Sample Selection

To simultaneously measure black hole masses ($M_{\rm BH}$) from broad emission line and continuum luminosity, stellar velocity dispersions (σ_*) from absorption lines in spectra, host galaxy bulge luminosities ($L_{\rm bul}$) from images, the objects with the comparable nuclear and stellar light fraction, such as Seyfert 1 galaxies, are essential with high S/N spectra and high-resolution images. A sample of Seyfert 1 galaxies (i.e., relatively low-luminosity broad-line AGNs) was carefully selected from the SDSS database with specific redshift windows in $0.35 < z < 0.37$ and $0.56 < z < 0.58$ to minimize the uncertainties from strong sky features. The following selection criteria were applied based on the SDSS data: (1) Hβ equivalent

widths greater than 5Å (2) spatially resolved in the Sloan images (3) $g'-r' > 0.1$ and $r'-i' > 0.3$ for a non-negligible stellar light fraction. Thus, our final sample contains a total of 52 AGNs (37 at $z \sim 0.36$; 15 at $z \sim 0.57$). Out of those 52, 40 objects were already analysed and the results were presented in the series of papers (Treu et al. 2004; Woo et al. 2006; Treu et al. 2007; Woo et al. 2008; Bennert et al. 2010). We here focus on the remaining 12 AGNs, which are located at $z \sim 0.57$ mostly. Table 5.1 lists the sample with all previous 40 objects.

5.2.2 Observations and Data Reduction

The Keck spectra for our sample of 12 objects as well as all previous 40 objects were obtained with the Low Resolution Imaging Spectrometer (LRIS) at Keck I telescope. The 900 lines mm^{-1} grating centered at 6700Å was used for objects at z = 0.36 with total exposure times ranging from 600 s and 3.5 hr, yielding a pixel scale of 0.85Å$\times$0.″215 and a Gaussian resolution (σ) of $\sim$55 km s^{-1} while for objects at z = 0.57 the 831 lines mm^{-1} grating centered at 7600Å was used with total exposure times ranging from 1.5 hr and 4.5 hr, yielding a pixel scale of 0.92Å$\times$0.″215 and a Gaussian resolution of $\sim$58 km s^{-1}. After that the standard spectroscopic reduction procedures including bias subtraction, cosmic ray removal, flat fielding, spectral extraction, wavelength calibration, and flux calibration were performed using IRAF, one-dimensional spectra were extracted with an window of $4-5$ pixels ($\sim 1''$). To compensate the uncertainties of long-slit spectrophotometry due to the slit losses and seeing effects, we performed a recalibration of the flux scale based on the corresponding SDSS DR7 spectra, which were obtained from the aperture of a 3" spectroscopic fiber with the better spectrophotometric calibration by taking advantage of their imaging data. Thus, reduced spectra were renormalized with the scale factors, which were determined by χ^2 minimization of the difference between the filter magnitudes calculated with the SDSS r (i) filter curve from the Keck and SDSS spectra for objects at z = 0.36 (z = 0.57). We then applied the Galactic extinction correction to spectra using the values of $E(B-V)$ from Schlafly & Finkbeiner (2011) listed in the NASA/IPAC Extragalactic Database (NED[1]) and the reddening curve of Fitzpatrick (1999). The final reduced spectra are presented in Figure 5.1 & 5.2. The average signal-to-noise ratio at rest-frame 5100Å for all spectra is S/N $\approx$ 61 pixel^{-1} (see Table 5.2).

The *HST* imaging data for the three objects at z = 0.36 were obtained as a part of GO-

[1] `http://ned.ipac.caltech.edu/`

11166 (PI: Woo) and those for the nine objects at $z = 0.57$ were obtained as a part of GO-11208 (PI: Treu). All 12 objects were observed with the WFC3 imager aboard the *HST* in F110W filter (wide YJ band) for a total exposure time of 2397 sec per object. Four separate exposures for each target were dither-combined with the `MultiDrizzle` within the `PyRAF` environment. The parameters of a final pixel scale of $0.09''$ and a pixfrac of 0.9 were adopted for the `MultiDrizzle` task. The final drizzled (distortion corrected, cosmic rays and defects removed, sky background subtracted) images for 12 objects are shown in the first column of Figure 5.3.

5.3 Measurements

To investigate the evolution of the BH scaling relations over the cosmic time, both the black hole property ($M_{\rm BH}$) and the host galaxy property ($L_{\rm bul}$) as a function of redshift are required. In this section, we present measurements for $M_{\rm BH}$ from a combination of spectral and imaging analysis and $L_{\rm bul}$ from high-resolution images.

5.3.1 Black Hole Mass

To estimate black hole masses, we applied the multi-component spectral decomposition technique, which was developed by Park et al. (2012b) and modified and improved for this work, to the obtained Keck spectra.

First, the spectra were converted to the rest-frame using the improved redshifts from Hewett & Wild (2010) (see Table 5.1). Second, the observed continuum was modeled with a combination of a single power-law, an Fe II template, and a host-galaxy template for the featureless AGN continuum, the AGN Fe II emission blends, the host-galaxy starlight respectively in the regions of 4430-4770Å and 5080-5450Å, which were slightly adjusted for each spectrum to avoid the contaminating absorption and emission features. The weak AGN narrow emission lines (e.g., He I λ4471, [Fe VII] λ5160, [N I] λ5201, [Ca V] λ5310) and He II λ4686 line in this continuum window were also masked out.

The Fe II template was adopted from I Zw 1 Fe II template of Boroson & Green (1992) and the stellar template was composed of seven stellar spectra of G and K giants with various temperatures from the Indo-US spectral library[2] (Valdes et al. 2004), which have been widely used for stellar velocity dispersion measurements on Keck spectra in many studies

[2] `http://www.noao.edu/cflib/`

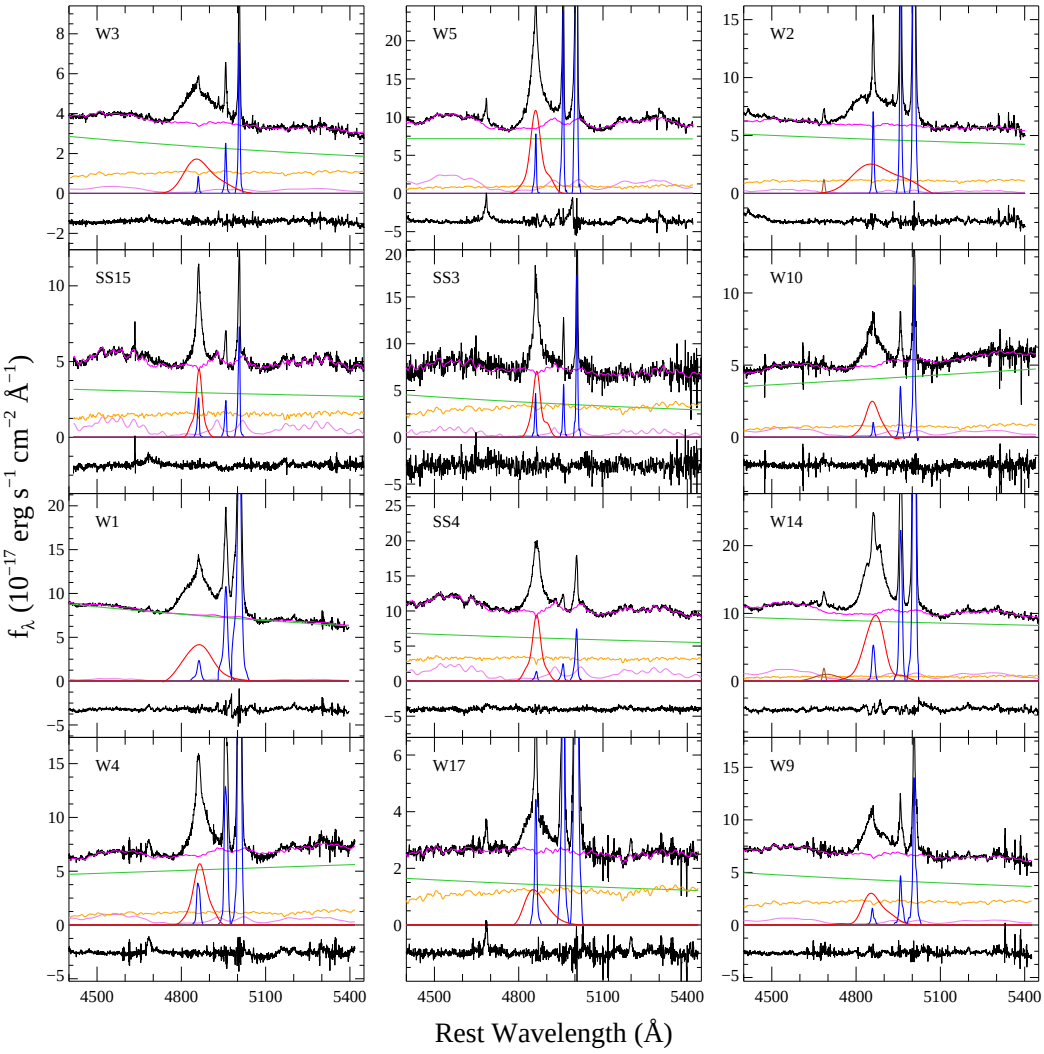

Figure 5.1 Multi-component spectral decomposition results for the sample of our 12 objects. The observed spectra are shown along with the best-fit models. In each panel, observed spectra (black) and the continuum+Fe II+stellar best-fit model (magenta) are shown in the upper part, and the best-fit power-law continuum (green), stellar template (yellow), and Fe II template (violet) models are presented in the middle part. Three narrow lines [Hβ, [O III] $\lambda\lambda$4959, 5007 (blue)], broad Hβ (red), and the broad and narrow He II λ4686 components (brown) are presented in the bottom part. The residuals (black), representing the difference between the observed spectra and the sum of all model components, are arbitrarily shifted downward for clarity.

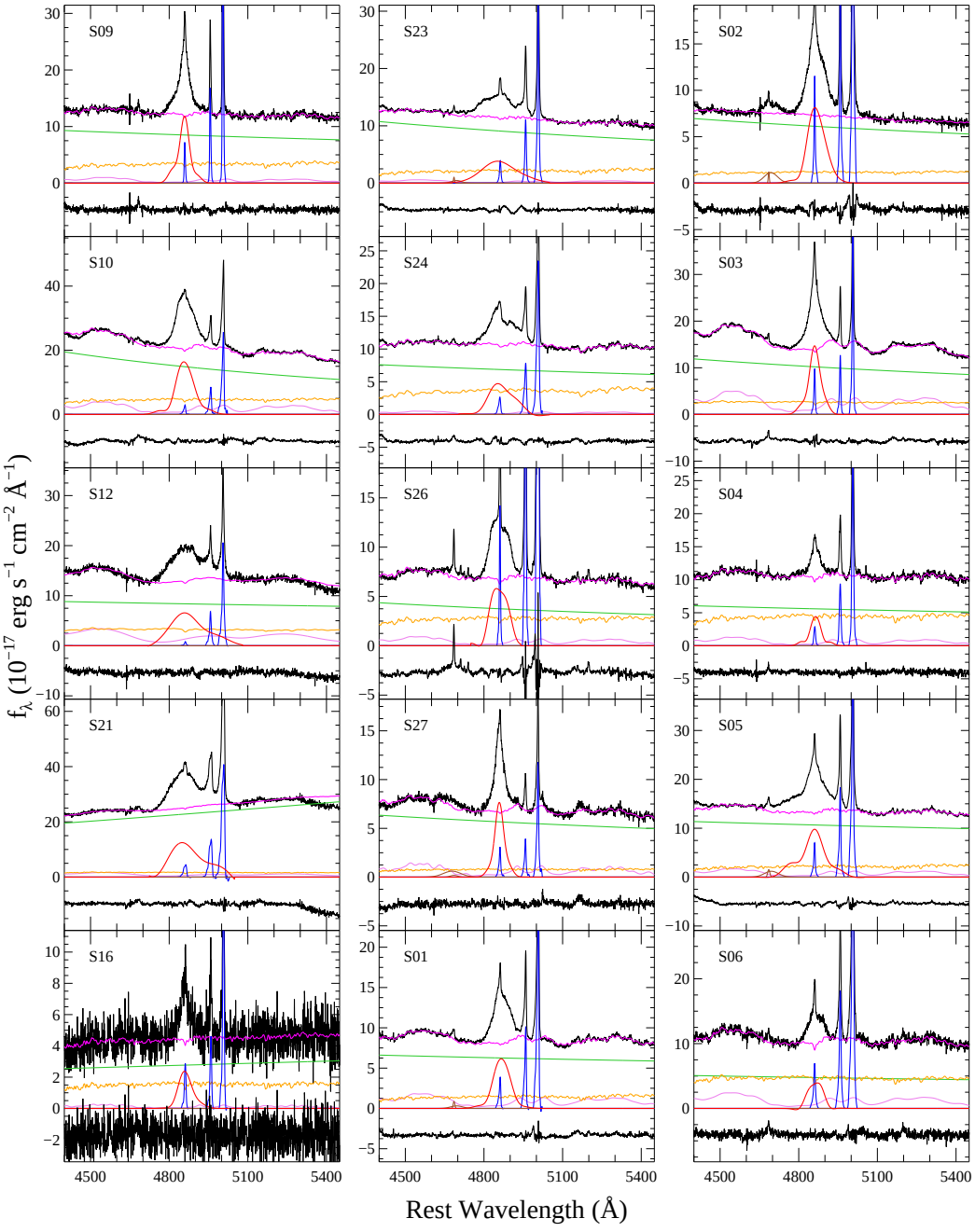

Figure 5.2 Same as Figure 5.1, but for the previous sample of 40 objects.

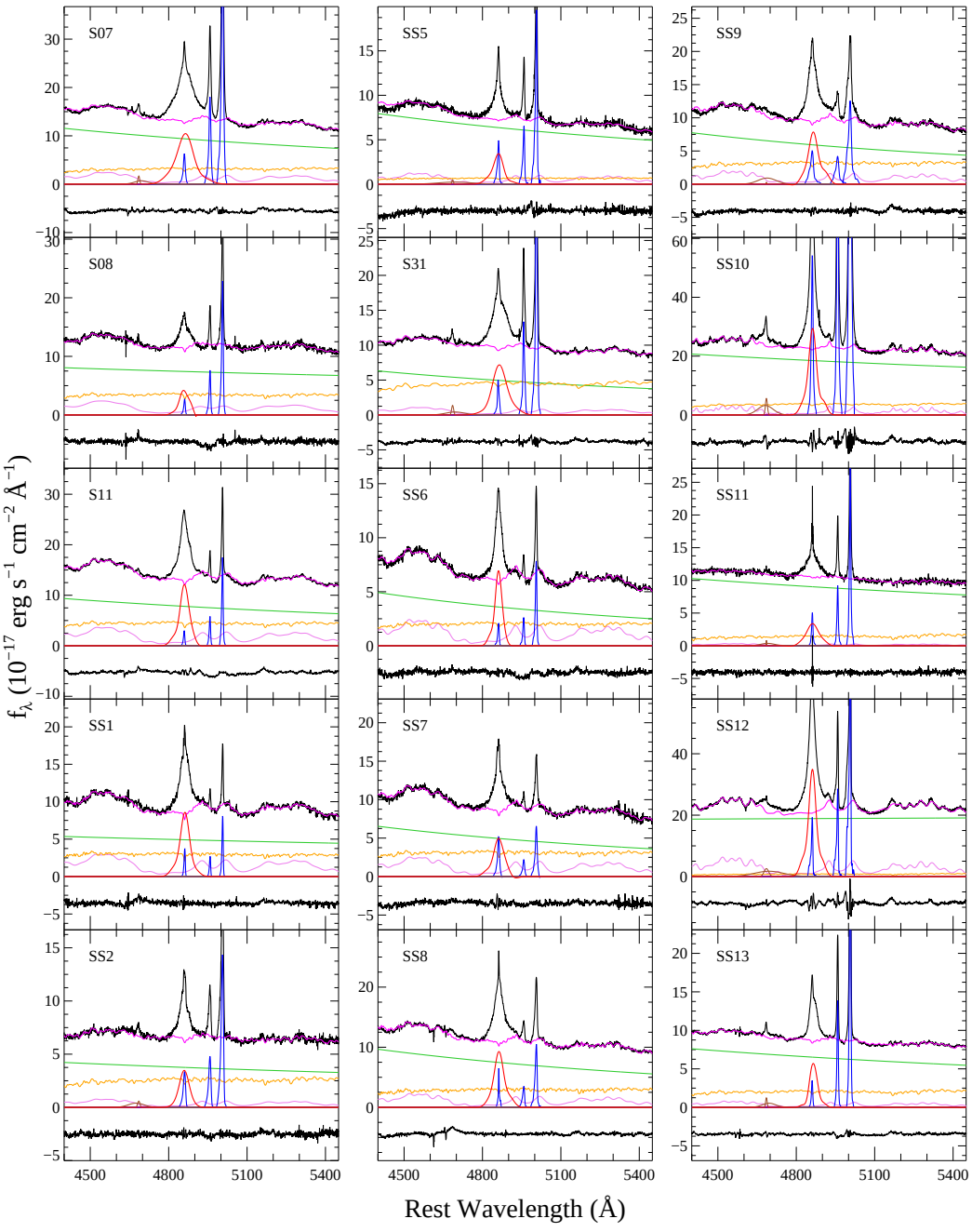

Figure 5.2 *Continued.*

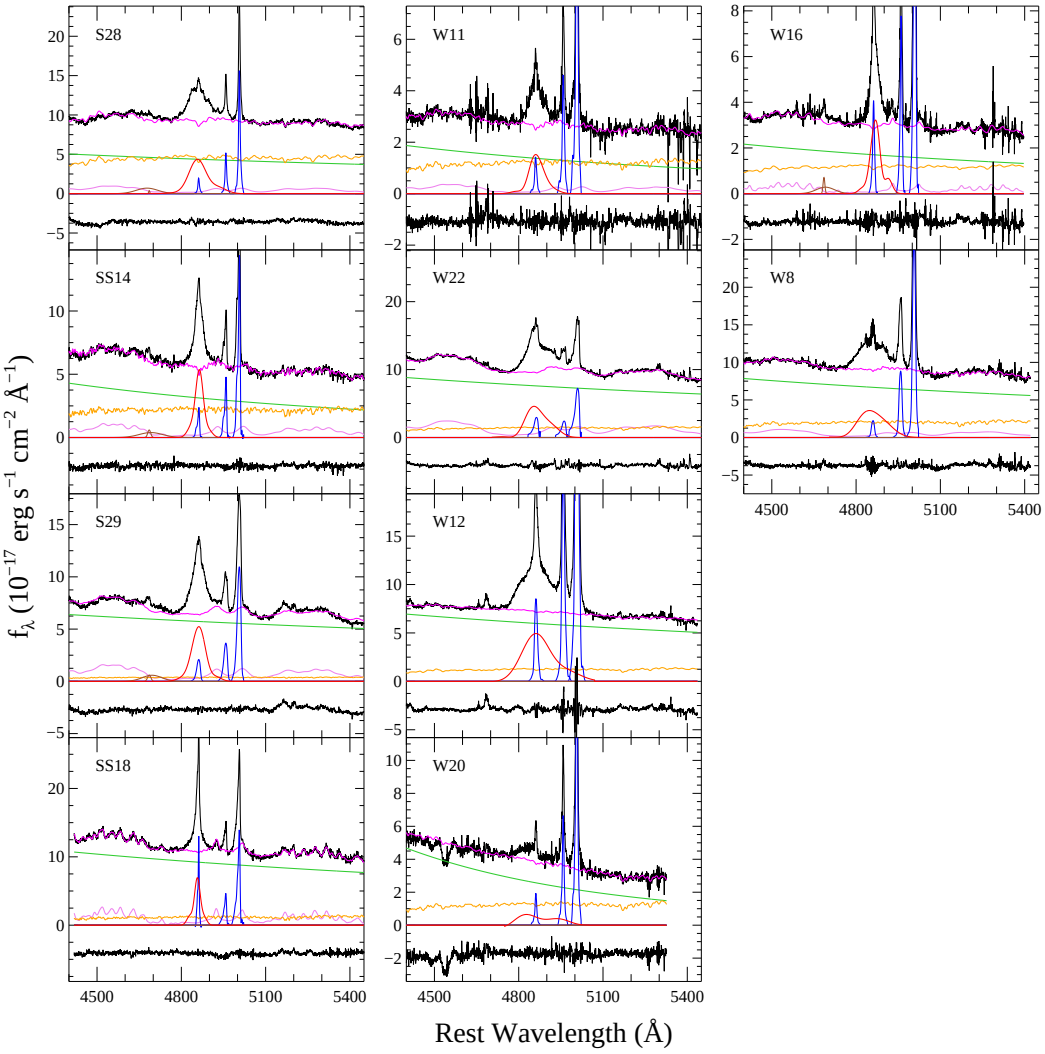

Figure 5.2 *Continued.*

(e.g, Wolf & Sheinis 2008; Suyu et al. 2010; Bennert et al. 2011; Fernández Lorenzo et al. 2011; Harris et al. 2012; Suyu et al. 2013). These high-resolution stellar template spectra ($\sim$ 34 km s^{-1}; Beifiori et al. 2011) were degraded to match the Keck spectral resolution. Note that our template for the host-galaxy starlight is different to that of Park et al. (2012b; a single synthetic template with solar metallicity and 11 Gyr old from Bruzual & Charlot 2003). This choice is motivated by the investigations of Treu et al. (1999, 2001), who showed G-K type stellar templates produced a best-fit galaxy model. Empirically it is also evidenced by that our spectral fitting ranges are dominated with the features of late-type stellar spectra such as Mg *b* triplet ($\sim$ 5175 Å) and Fe (5270 Å) absorption lines and by that our experiments show the better χ^2 values and residuals compared to the case of a single synthetic galaxy template.

The best-fit continuum models were determined with the χ^2 minimization using the nonlinear Levenberg-Marquardt least-squares fitting routine `mpfit` (Markwardt 2009) in IDL for the optimal parameters: the normalization and slope of the power-law model and the velocity shifts and widths of the Gaussian broadening kernels for the convolution of the Fe II and host-galaxy templates. The weights for a linear combination of the Fe II and stellar templates were internally optimized using a bounded-variable least-squares solver (`bvls`[3]) with the constraint for non-negative values during the fitting. We measured the AGN continuum luminosity at 5100Å from the power-law model.

Third, after subtracting the best-fit continuum model, the Hβ emission line region complex were modeled with a combination of a sixth-order Gauss-Hermite series for the Hβ broad component, a tenth-order Gauss-Hermite series with different flux scaling ratios for the Hβ narrow component and [O III] $\lambda\lambda 4959, 5007$ narrow lines, two Gaussian functions for the He II λ4686 line whenever it blends with the Hβ profile. Figure 5.1 shows the observed spectra with the best-fit models for our sample of 12 objects (see Fig. 5.2 for previous 40 objects). We measured line widths (ΔV), FWHM and line dispersion (σ), for the Hβ broad emission line from the best-fit profile of the sixth-order Gauss-Hermite series. The measured line widths were subsequently corrected for the instrumental resolution by subtracting it in quadrature.

Using the method described above we fitted all spectra for a total of 52 sample including all previous sample, thus we have updated spectral measurements for the samples presented in Treu et al. (2007) and Bennert et al. (2010) (also in Woo et al. 2006, 2008).

[3]It is implemented in IDL by Michele Cappellari and is available at `http://www-astro.physics.ox.ac.uk/~mxc/idl/`.

These measurements are listed in Table 5.2. For $M_{\rm BH}$ estimation, we use the following formalism, derived by combining the recent calibrations for the size-luminosity relationship (Bentz et al. 2009a; $R_{\rm BLR} \propto L^{0.519}$) and the virial factor (Park et al. 2012a; Woo et al. 2013; $\log f = 0.71$) from the virial equation ($M_{\rm BH} = f R_{\rm BLR} \Delta V^2 / G$ where G is the gravitational constant):

$$\log\left(\frac{M_{\rm BH}}{M_\odot}\right) = 7.536 + 0.519\ \log\left(\frac{\lambda L_{5100}}{10^{44}\ {\rm erg\ s^{-1}}}\right) + 2\ \log\left(\frac{\sigma_{\rm H\beta}}{1000\ {\rm km\ s^{-1}}}\right), \qquad (5.1)$$

where the overall uncertainty of SE BH masses are assumed to be 0.4 dex, estimated by summing in quadrature each source of uncertainties for 0.31 dex scatter of the virial factor (Woo et al. 2010), 0.2 dex additional variation of the virial factor depending on the direction of regression in its calibration (Park et al. 2012a), 0.05 dex scatter due to the variability (Park et al. 2012b), and 0.15 dex scatter of the size-luminosity relation (Bentz et al. 2009a). Although we noted that recently Bentz et al. (2013) have updated the $R-L$ relation with nine new low mass RM AGNs, we use the calibration of Bentz et al. (2009a) in order to be consistent with the local RM AGN sample adopted here from Bentz et al. (2009b; reanalysed in Bennert et al. 2010). The main result investigated in this work is not changed if we adopt the latest $R-L$ calibration (described in next section). Note that we use the AGN continuum luminosity measured from *HST* images described in next section for final $M_{\rm BH}$ estimates (Table 5.4).

5.3.2 Bulge Luminosity

We performed two-dimensional surface photometry on HST imaging data for our 12 objects to decompose AGN and host-galaxy light, thus determining the AGN and bulge luminosities of the AGN-host galaxies. The image fitting code written by Matthew W. Auger using Python, which is the modified version of the SPASMOID used in Bennert et al. (2011a,b), was used for structural decompositions of the images. This flexible code allows us to make use of linear combinations of different PSFs for the AGN model to account for the PSF-mismatch, which is particularly important for the *HST* image analysis of a galaxy with a bright unresolved point source (Kim et al. 2008b). To efficiently explore the multi-parameter space the code adopts the adaptive simulated annealing algorithm with the Markov chain Monte Carlo (MCMC) sampler in the `pymc`[4] framework, thus giving the better performance than an usual local χ^2 minimization method in the sense that it is much less sensitive to an

[4] `https://github.com/pymc-devs/pymc`

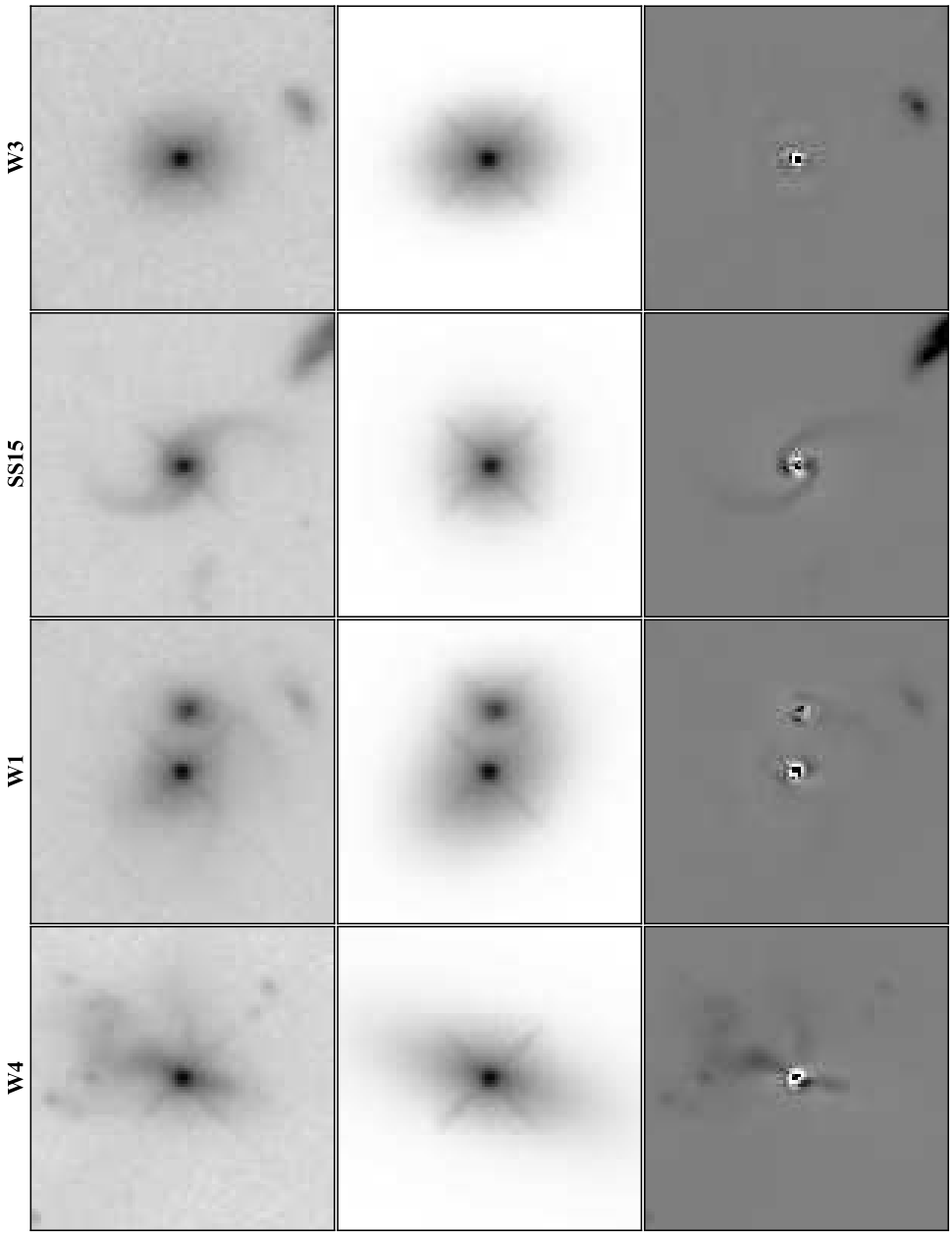

Figure 5.3 *HST* F110W images for the sample of 12 objects. In each row, obtained data (left), best-fit models (middle), and residuals (right) are presented with the object name. The data and models are displayed with an inverted asinh stretch, and the residuals are displayed with an inverted linear stretch centered around zero counts. The counts in residual images are only $\sim \pm 3\%$ level of original images except for a few cases. Each image is $9'' \times 9''$ size.

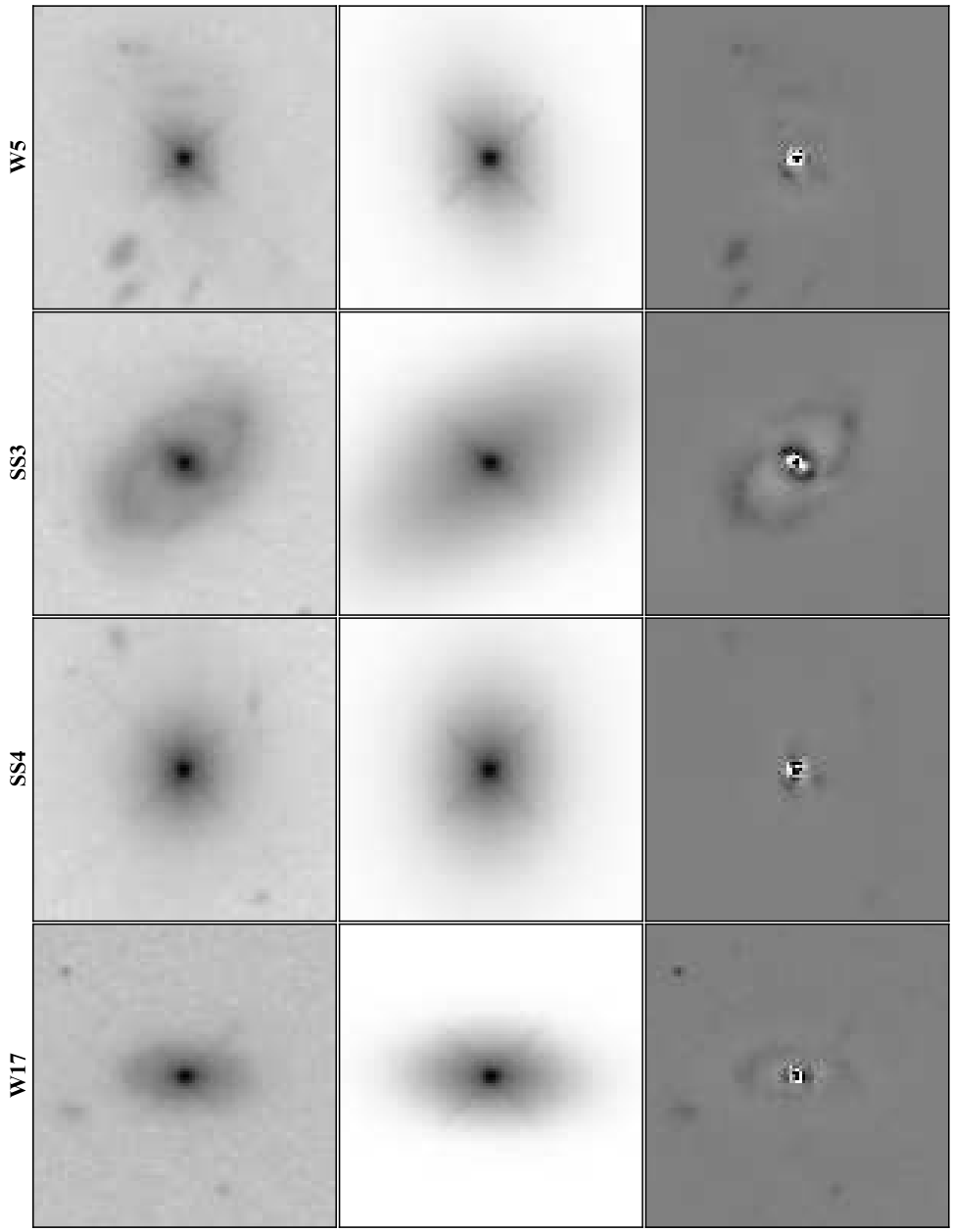

Figure 5.3 *Continued.*

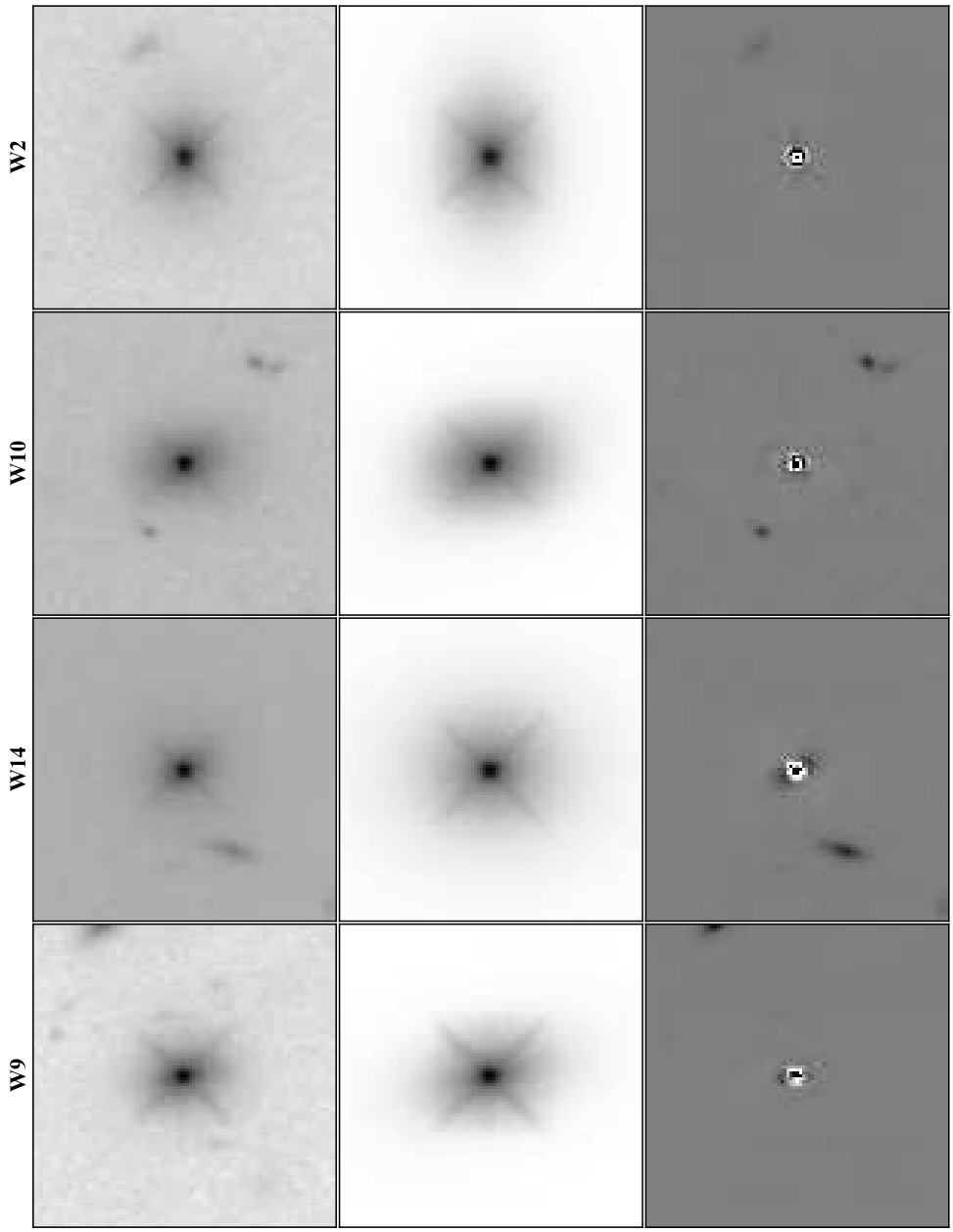

Figure 5.3 *Continued.*

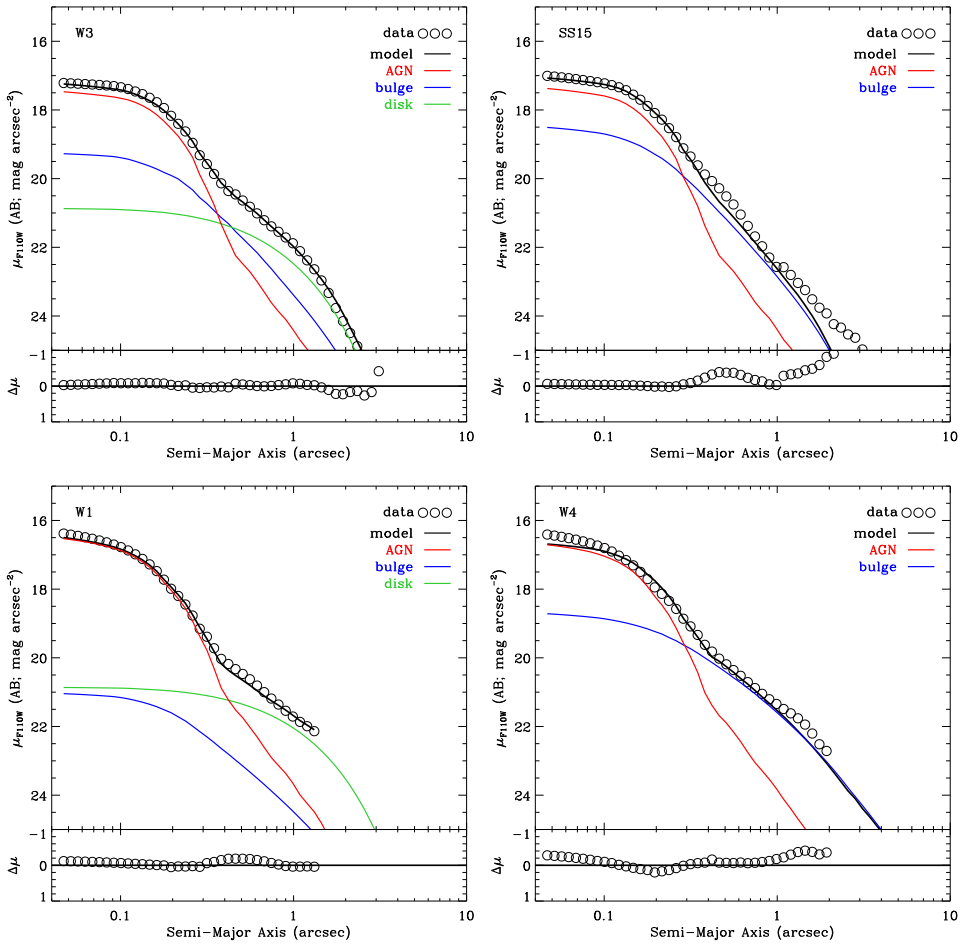

Figure 5.4 One-dimensional surface brightness profiles of *HST* F110W images for the sample of 12 objects. In each top panel, the profiles measured from the data (open circles), the best-fit model (black solid line), and the subcomponents of the model for bulge (blue solid line), disk (green solid line), PSF (red solid line) are shown. Residuals (open circles), the difference of the profiles between the data and the best-fit model, are presented in each bottom panel.

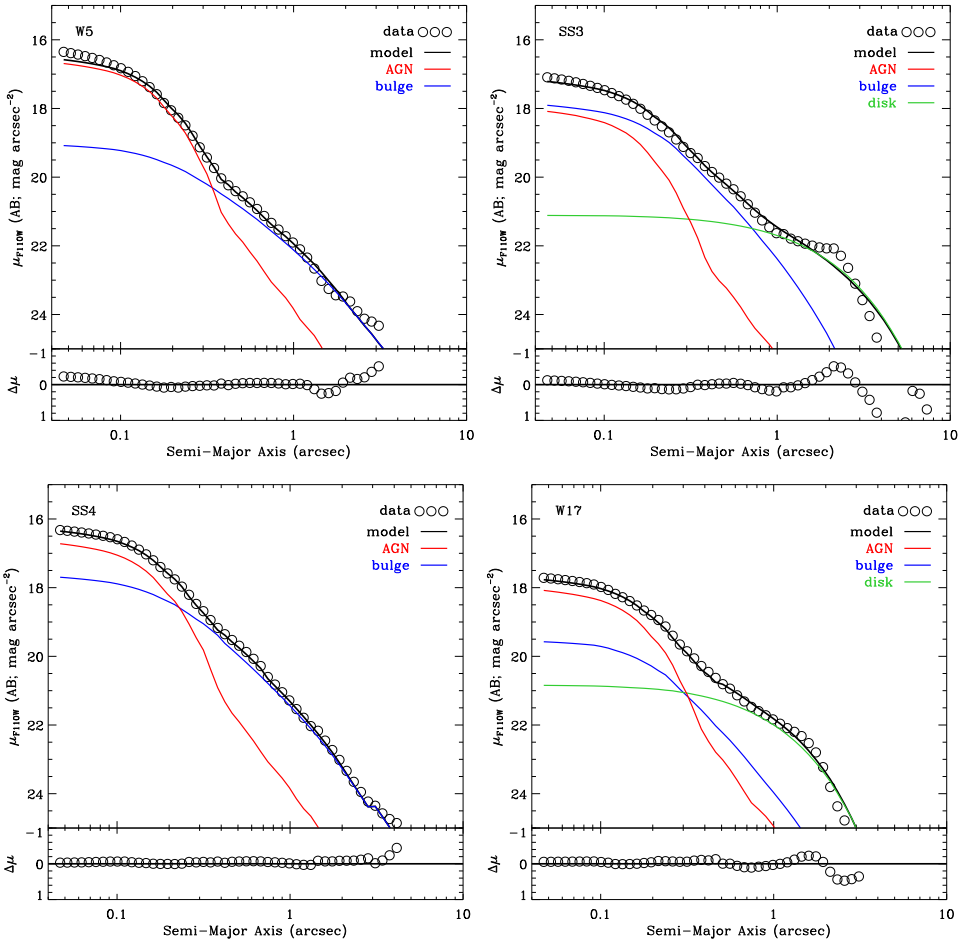

Figure 5.4 *Continued.*

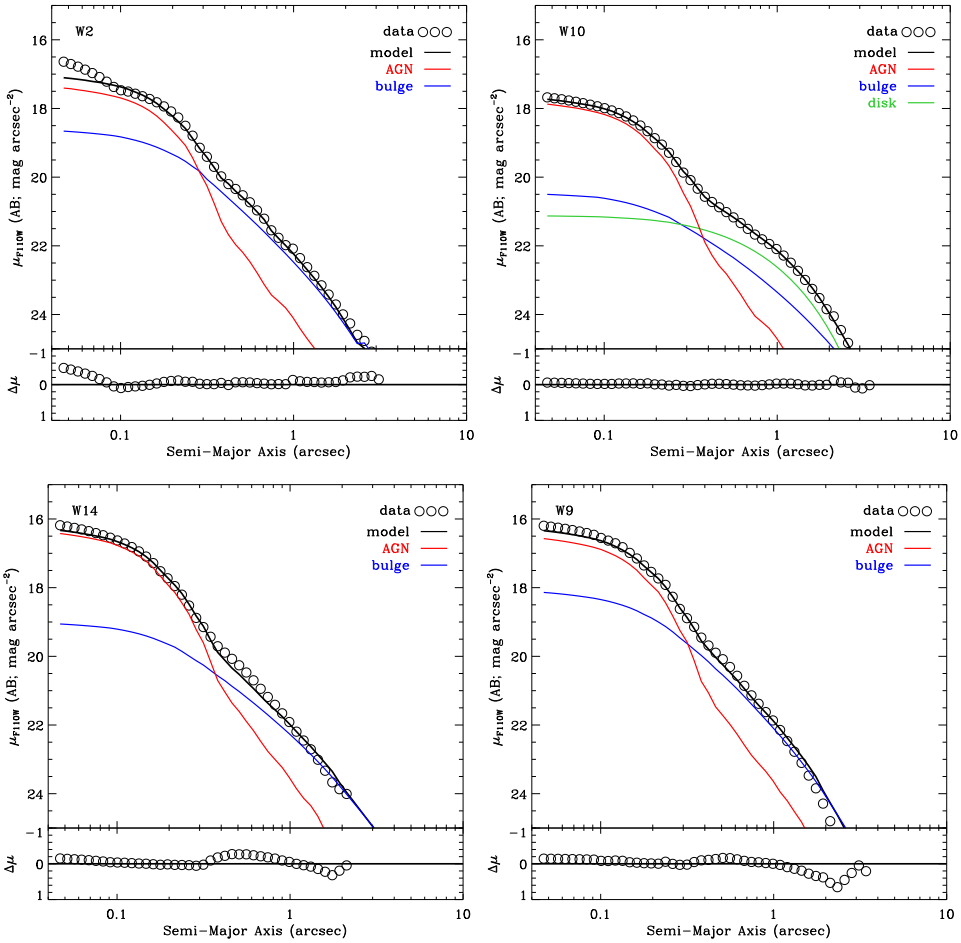

Figure 5.4 *Continued.*

initial guess for the parameters and it better ensures the true global minimum over the posterior distribution at a cost of longer execution time.

We created a library of 16 point-spread functions from nearby bright, isolated, unsaturated stars carefully selected over the science image fields, which was subsequently used to model the central point source (i.e., AGN) as an appropriately scaled linear combination of them. The PSF images were subsequently normalized and shifted each other using spline interpolation to obtain centroided images. These empirical stellar PSFs are the better choice than the synthetic TinyTim PSFs in the sense that they were observed and reduced in the same instrumental conditions at a same time (Kim et al. 2008b; Canalizo et al. 2012). Note that our 12 objects were usually fitted with 2 to 4 PSF combinations for the AGN. We first fitted the host galaxy with a de Vaucouleurs profile for a bulge component. We then added an additional exponential disk profile by carefully examining for clear evidence of a disk component based on the original and residual images (i.e., following the similar strategy adopted by Treu et al. 2007, Kim et al. 2008a, Bennert et al. 2010). Here 5/12 objects were modeled with an additional disk component. All model components for the host galaxy are concentric, but the offset between the AGN and host galaxy centroids is allowed. The minimum radius of the de Vaucouleurs profile was set to be 2 pixels (i.e., the minimum resolvable size for the given PSFs). The normalization of each profile (i.e., magnitude of each model component) is optimized by fitting the linear combination of all models given the structural parameters (i.e., centroid, effective radius, axis ratio, and position angle) to data with a non-negative least squares solver (`nnls`; Lawson & Hanson 1987). Note that the all model components were fitted simultaneously.

Out of the 12 objects, three host bulge components (i.e., W3, SS3, W17) resulted in small effective radii, approaching to the minimum size. Thus, we consider that these objects have the bulge luminosity as an upper limit. For the case of W1, a nearby object was fitted simultaneously since its light profile overlaps that of the science target, while all other objects that seems to be irrelevant to the science target in the field of the image were masked-out during the fitting. In Figure 5.3, we show the images, best-fit models, and residuals for the 12 objects. One-dimensional surface brightness profiles obtained with the IRAF `ellipse` task are also shown in Figure 5.4 for illustration only since the fits were done in two dimensions.

The apparent AB magnitudes were determined by converting counts to magnitude with Equation (11) in Sirianni et al. (2005), i.e., $\mathrm{ABmag} = -2.5\log(\mathrm{counts}[\mathrm{e}^{-1}\mathrm{s}^{-1}]) + \mathrm{Zeropoint}$, where the zero-point of AB mag for WFC3 F110W filter is 26.83. To obtain rest-frame

V-band luminosities of the host-galaxy bulges, we first applied the Galactic extinction correction to measured magnitudes using the values of $E(B-V)$ from Schlafly & Finkbeiner (2011) listed in the NED and assuming $A_{\rm F110W} = 0.902\ E(B-V)$ (Schlegel et al. 1998). The extinction-corrected F110W AB magnitudes were then transformed to rest-frame V-band by applying K-correction with an early-type galaxy template spectrum[5] of Coleman et al. (1980) extended to UV and IR regions using Bruzual & Charlot model spectra. The V-band luminosities were given by $\log L_V/L_{V,\odot} = 0.4(M_{V,\odot}-M_V)$ where $M_{V,\odot} = 4.83$. We adopt a conservative total uncertainty of 0.2 dex (~ 0.5 mag) for the bulge luminosity estimates as investigated in Treu et al. (2007) and Bennert et al. (2010). Note that our F110W band is corresponding to rest-frame R and I bands for redshifts of our sample. Thus the V-band bulge luminosity can be determined robustly because the F110W IR filter is better to decompose a bulge component as against the blue AGN light domination at shorter bandpass regime and is less affected by dust effects. The scatter of red colors of bulges (i.e., $V-R$ and $V-I$) are also known to be small.

For the more direct comparison of the samples at local and distant universe, the corrections for passive luminosity evolution to account for their fading as stellar populations age were also applied in a same manner as in Treu et al. (2007) and Bennert et al. (2010):

$$\log L_{V,0} = \log L_V - (0.62 \pm 0.09) \times z. \tag{5.2}$$

The sample of local RM AGNs was also corrected for passive luminosity evolution to zero redshift.

To measure the AGN monochromatic continuum luminosity at 5100Å from the *HST* image analysis ($\lambda L_{5100}^{\rm image}$), which is thought to be better than $\lambda L_{5100}^{\rm spec}$ from the spectra since it is not affected by the uncertainties from slit losses, seeing effects, and the difficulty of absolute spectrophotometric calibration in spectral measurements, we transformed the extinction-corrected PSF F110W AB magnitude to rest-frame 5100Å by assuming a single power-law SED ($f_\nu \propto \nu^{-0.5}$) as adopted by Bentz et al. (2006) and Bennert et al. (2010, 2011a). Note that the median value of power-law continuum slopes measured from our 52 spectra is also –1.49 (i.e., corresponding to $\nu^{-0.5}$) although they are based on the limited wavelength range. The uncertainty due to the fixed single slope (–0.5) was estimated to be less than 0.05 dex in the derived luminosity by changing the adopted slope between –0.2 and –1 (i.e., the range reported in literature; see Bennert et al. 2011a and references therein). Thus it is negligible

[5] This empirical observed SED templates are available at `http://webast.ast.obs-mip.fr/hyperz/`.

compared to the adopted total uncertainty for $M_{\rm BH}$ (i.e., 0.4 dex). The measured quantities from *HST* image analysis for the sample of 12 objects are listed in Table 5.3.

Table 5.4 provides final derived properties for black holes and host-galaxies related to our science. Results of surface photometry for the previous sample of 40 objects taken from the Table 2 in Bennert et al. (2010) are also presented. The black hole mass is derived with Equation (5.1) using $\sigma_{\rm H\beta}$ and $\lambda L_{5100}^{\rm image}$. The bulge luminosities are given for both cases of not-corrected and corrected for passive evolution.

5.4 Results

This section provides the main results for the relationship between nuclear black holes and host galaxy bulges by investigating the $M_{\rm BH}-L_{\rm bul}$ scaling relation of our intermediate-z sample, as well as for local comparison samples.

5.4.1 $M_{\rm BH}-L_{\rm bul}$ relation

Figure 5.5 shows the black hole mass–host bulge luminosity relation for a total of 52 intermediate-z objects with the local comparison sample. Note that the local baseline sample of RM AGNs is taken from the Table 3 in Bennert et al. (2010), which was re-analysed for the sample presented by Bentz et al. (2009b) with a consistent manner to reduce systematic uncertainties involved in bulge luminosity measurements. The offset on $\log M_{\rm BH}$ with respect to the local baseline is estimated with the `FITEXY` estimator implemented in Park et al. (2012a). By fixing the slope of the $M_{\rm BH}-L_{\rm bul}$ relation for our intermediate-z sample to be the same as that of the local relation, we perform a regression to determine the normalization and intrinsic scatter of the relation. The average offset is a difference of normalizations between the relations for our and local comparison samples, $\Delta\log M_{\rm BH} = +0.08\pm0.07\pm0.23$ dex (random and systematic errors adopted by an observed scatter$/\sqrt{N}$ and intrinsic scatter of the relation respectively). The observed offset is not significant to interpret it as an evolution signal in the sense that it is comparable to random error and less than systematic error and the intrinsic scatter of the local baseline relation (i.e., 0.21 dex). The offset in a direction of bulge luminosity is $\Delta\log L_{\rm bul} = -0.11\pm0.09\pm0.33$ dex. If we adopt the recent inactive relation from McConnell & Ma (2013) as a local baseline, the offset is $\Delta\log M_{\rm BH} = -0.21\pm0.08\pm0.29$ dex ($\Delta\log L_{\rm bul} = +0.19\pm0.07\pm0.26$ dex), which is still not a statistically significant for given errors.

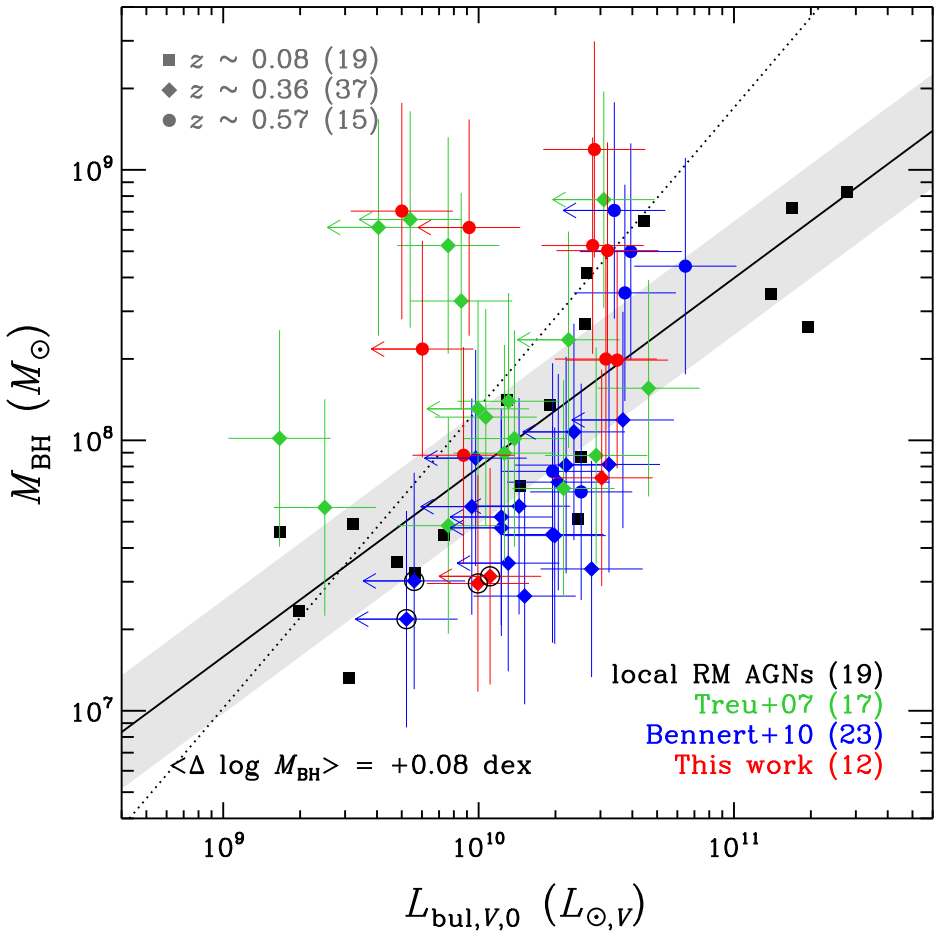

Figure 5.5 $M_{\rm BH}-L_{\rm bul}$ relation. Colored symbols indicate our intermediate-z sample (green: the sample of Treu et al. 2007; blue: that of Bennert et al. 2010; red: this work). Corresponding redshifts of the samples are expressed by different symbols (square: local ($\bar{z}\sim 0.08$); diamond: $z = 0.36$; circle: $z = 0.57$). Black filled squares are the local RM AGNs taken from Bennert et al. (2010) with the best-fit relation (black solid line) and its intrinsic scatter (0.21 dex; gray shaded region). Black dotted line represents the local baseline for inactive galaxies (44) from McConnell & Ma (2013). The objects which have bulge luminosities as upper limits (19) are indicated by a left-hand arrow in the horizontal error-bar. The narrow-line Seyfert 1 galaxies are marked with a open circle enclosing the corresponding symbol. The average offset in $\log M_{\rm BH}$ for the intermediate-z sample against the local base-line (black solid line) is given in the lower left corner.

This roughly zero or negative offset in $\log M_{\rm BH}$ could be affected by a particular subclass of typical broad-line AGNs such as Narrow-line Seyfert 1 (NLS1) galaxies, defined by their narrower broad line widths of Hβ FWHM < 2000 km s^{-1}, since they seem to have relatively low BH masses with high Eddington accretion rates and appear to fall below the BH-bulge scaling relation (Orban de Xivry et al. 2011; Mathur et al. 2012). This particular type of Seyfert galaxies is thus subject to possible underestimation of BH masses probably due to the effect of strong radiation pressure (Marconi et al. 2008; but see also Netzer 2009) and/or just from a selection of AGNs with a relatively low-inclination angle of the BLR. Here four galaxies (SS6, SS18, SS15, and SS3) were classified into NLS1s based on their narrow FWHM$_{\rm H\beta}$ (see Table 5.2). Although all four NLS1 galaxies are offset under the local baseline, they are not significant outliers compared to the other sample of typical Type-1 AGNs (see Fig. 5.5). Thus we do not exclude them for further analysis.

5.4.2 Treating $L_{\rm bul}$ of Upper Limits with Informative Priors

Note that 19 objects out of a total of 52 sample have upper limits for their bulge luminosities due to the resolution limit of *HST* images. Therefore, the offset measured above should be considered as a lower limit.

To derive the bulge luminosity from an upper limit, we applied the same method described in Bennert et al. (2010) for a sample of three upper limits (i.e., W3, SS3, W17) in this work. By taking advantage of the prior knowledge on the bulge-to-total luminosity ratios, which were measured from Benson et al. (2007) for a sample of 8839 SDSS galaxies, we derived the posterior distribution by combining the prior and likelihood for the B/T ratios as shown in Figure 5.6. A step function whose value is non-zero up to the measured upper limit B/T was adopted for the likelihood function. The prior was determined by making the B/T distribution of galaxies from Benson et al. (2007), whose total galaxy magnitudes are in the range of ± 0.5 mag to the total host galaxy magnitude for the sample of upper limits in this work. For each object, the mean value from the B/T posterior distribution was adopted to calculate the final bulge luminosity from the total host galaxy luminosity.

Figure 5.7 shows the final $M_{\rm BH}-L_{\rm bul}$ relation with the re-estimated $L_{\rm bul}$ for 16 upper limit objects in Bennert et al. (2010) as well as the three objects in this work. The final $L_{\rm bul}$ measurements are listed in Table 5.4. The average offset we obtain is $\Delta \log M_{\rm BH} = +0.15 \pm 0.07 \pm 0.27$ dex ($\Delta \log L_{\rm bul} = -0.22 \pm 0.09 \pm 0.39$ dex), which is still not significant to assure the positive evolution. For the local baseline from McConnell & Ma (2013), the

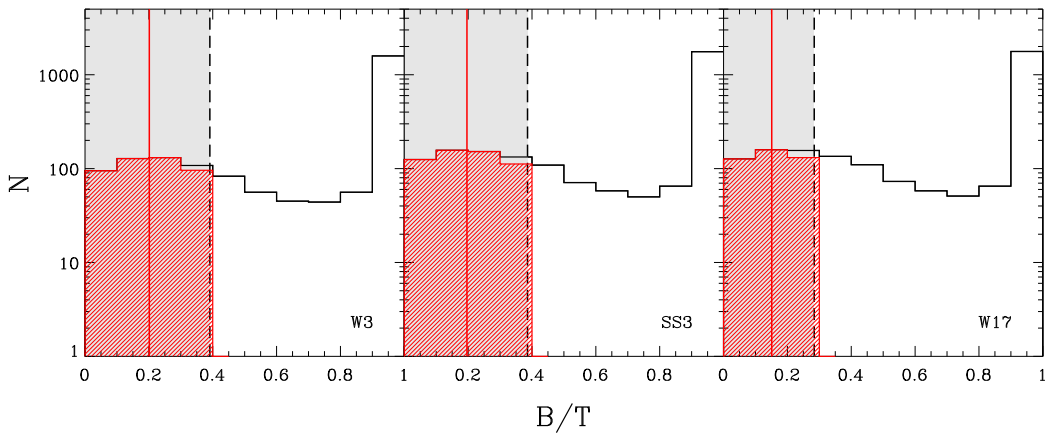

Figure 5.6 The bulge-to-total (B/T) luminosity ratio distributions from Benson et al. (2007) as informative priors for estimating $L_{\rm bul}$ from upper limits. The names of a sample of three upper limits in this work are given in the lower-right corner of each panel. The black histograms indicate B/T prior distributions from SDSS galaxies that have comparable total magnitudes of ± 0.5 mag to those of our Seyfert sample. The vertical black dashed line shows an upper limit value for the B/T measured from our surface photometry and the B/T likelihood function as the form of a step function is expressed as a grey shade. The posterior distribution for the B/T ratios, by combining the prior (black histogram) and likelihood (gray shade), is plotted as a red hashed histogram with its mean value (vertical red solid line) in each panel.

offset is found to be $\Delta \log M_{\rm BH} = -0.10 \pm 0.08 \pm 0.37$ dex ($\Delta \log L_{\rm bul} = +0.09 \pm 0.07 \pm 0.33$ dex).

5.4.3 Local Comparison Sample

Adopting the robust local baseline is crucial for an accurate characterization of the evolution of the scaling relation. Above we provide the results based on both local relations from active galaxies (Bennert et al. 2010) and inactive galaxies (McConnell & Ma 2013). However, a direct comparison of our intermediate-z active galaxies to the local-baseline of inactive galaxies for the $M_{\rm BH}-L_{\rm bul}$ relation may not be straightforward because it is subject to different selection biases for the two samples (Lauer et al. 2007). Comparison between two samples selected differently in a way that a sample of local inactive galaxies is selected

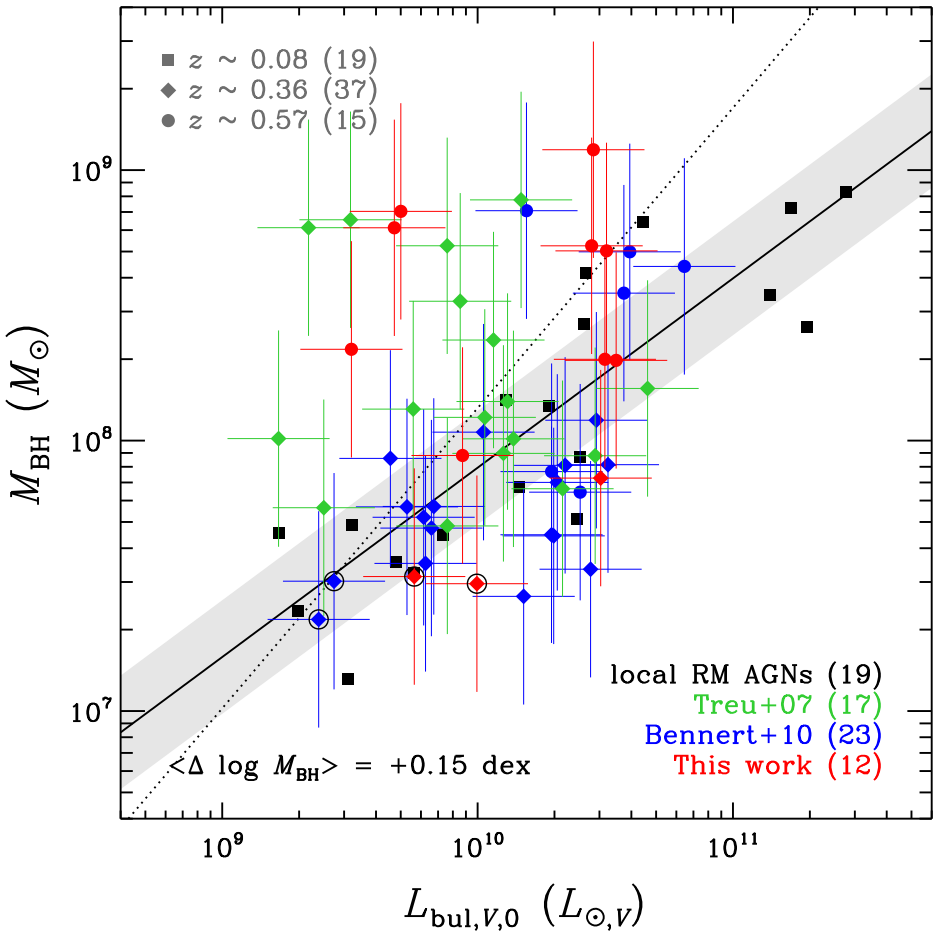

Figure 5.7 Same as Fig. 5.5, but for the final $M_{\rm BH}-L_{\rm bul}$ relation with bulge luminosities re-estimated from upper limits using informative priors.

by galaxy property (e.g., galaxy luminosity) while that of high-z active galaxies is selected by black hole property (e.g., nuclear luminosity and broad emission line, hence $M_{\rm BH}$) could introduces a substantial bias for an evolution signal. In addition, the recent sample of local inactive galaxies compiled in McConnell & Ma (2013) suffers a lack of low-mass objects (i.e., $M_{\rm BH} \lesssim 10^8 M_{\odot}$) and is limited only to early-type galaxies in the $M_{\rm BH}-L_{\rm bul}$ plane. Thus more appropriate comparison sample for this study is the reverberation-mapped local AGNs, for which both the reliable BH masses and host properties from *HST* images are available, selected on the same property. The dynamic ranges of $M_{\rm BH}$ and $L_{\rm bul}$ for our intermediate-z sample are also comparable and well covered by those of the local RM AGNs. Another point is a normalization of BH mass scale (i.e., related to the virial factor) for active galaxies since it is calibrated by forcing a sample of local RM AGNs into being agreement with the $M_{\rm BH}-\sigma_*$ relation of local inactive galaxies (see Park et al. 2012a), not with the $M_{\rm BH}-L_{\rm bul}$ relation because the former has smaller intrinsic scatter and better defined. Thus, the possible difference on the BH mass scales between inactive and active galaxies will be irrelevant to this work if we use local RM AGNs as a baseline sample and consistently apply the same virial factor for both samples of local and distant active galaxies, under the assumption that it does not change with redshift. Hereafter we will use the comparison sample of local RM AGNs as a fiducial baseline for further investigations.

5.4.4 Sample Dependency

Note that the SS* objects (16 at $z \sim 0.36$; most of blue and red diamonds in Fig.5.5) were actually selected with an additional selection criterion of $M_{\rm BH} \lesssim 10^8 M_{\odot}$ to extend the sample to lower mass range compared to our parent sample (S* and W* objects; 21 at $z \sim 0.36$ and 15 at $z \sim 0.57$). High mass objects in this sample, which could bring an offset above the $M_{\rm BH}-L_{\rm bul}$ relation, is deficient due to an artificial truncation by the sample selection limit. Thus, this mixture of samples selected differently precludes us from making conclusive answer for whether there is truly no evolution in the $M_{\rm BH}-L_{\rm bul}$ relation. Furthermore, the measured offset seems to be depend on BH mass and Eddington ratio as shown in Figure 5.8, where bolometric luminosity is estimated by $L_{\rm bol} = 9.26 \times \lambda L_{5100}^{\rm image}$ with the bolometric correction factor of $\rm BC_{5100} = 9.26$ (see Shen et al. 2008 and references therein). Above the BH mass of $10^8 M_{\odot}$ most objects show a positive offset, which seems to be increasing as a function of mass. This positive trend could be interpreted as a true physical effect with the AGN downsizing (i.e., anti-hierarchical BH growth) in a way that high BH mass objects evolve

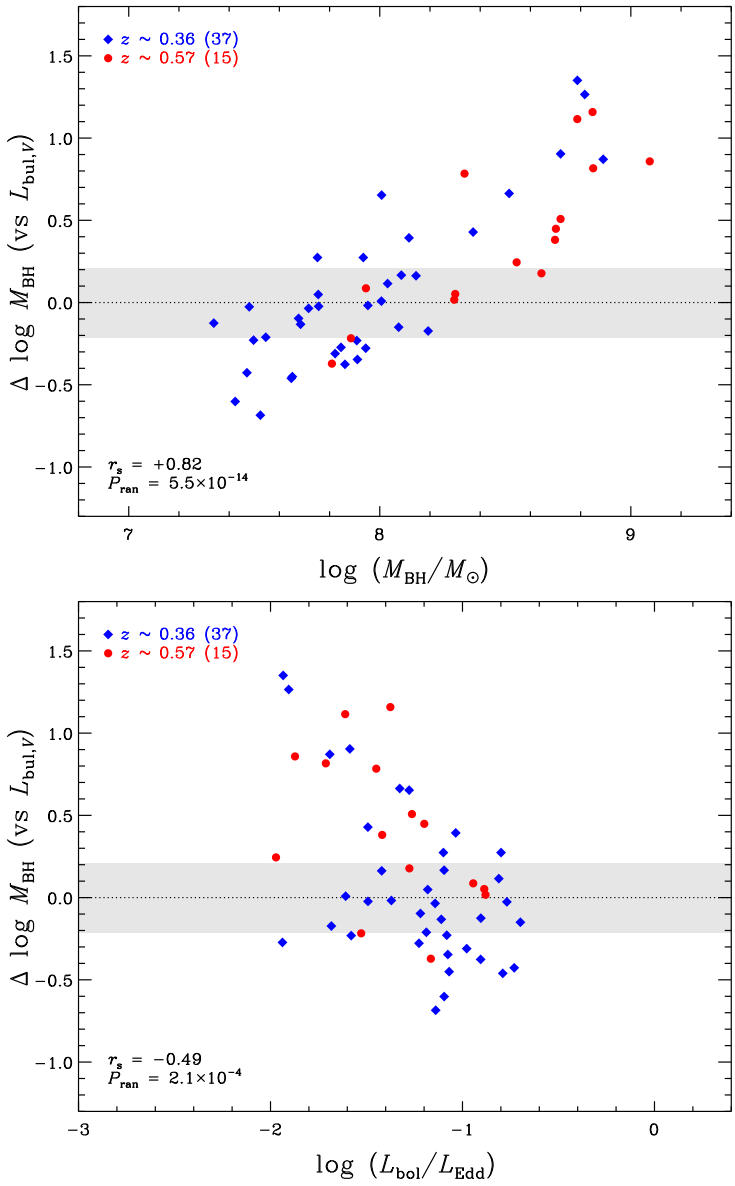

Figure 5.8 The measured offset in $\log M_{\rm BH}$ for a given $L_{\rm bul}$ with respect to local baseline $M_{\rm BH}-L_{\rm bul}$ relation (black dotted line with gray shaded region for the intrinsic scatter) as a function of black hole mass (top) and Eddington ratio (bottom). Blue diamonds indicate our sample at $z = 0.36$, while red circles show that of $z = 0.57$. Spearman rank correlation coefficient ($r_{\rm s}$) and the probability of being drawn from random distribution ($P_{\rm ran}$) are presented in the lower left corner in each panel.

faster thus having more chances to be offset above the local relation if there is a time offset to the corresponding bulge growth or an effect of selection bias by preferentially selecting more massive BHs at a given bulge luminosity under the steeply falling galaxy luminosity function and intrinsic dispersion of the scaling relation (cf. Lauer et al. 2007; see also Merloni et al. 2010 and Cisternas et al. 2011). Apart from the interpretation of the observed trend, we expect that most objects showing a negative offset in the low mass regime have black holes growing more actively (i.e., as indicated by relatively higher Eddington ratios) by accreting a substantial amount of mass for given their BH masses.

5.4.5 Redshift Evolution of the Relation

Figure 5.9 shows the measured offset of each object as a function of redshift. As a comparison, we show the local RM AGNs with black squares and intrinsic dispersion (i.e., 0.21 dex) of the local baseline as gray shaded region. The overall positive trend is observed although we note here that the observed offset is not very statistically significant, especially for the sample at $z = 0.36$. The best-fit trend of redshift evolution of the offset is modeled with a form of $\Delta \log M_{\rm BH} = \gamma \log(1+z)$, where we find $\gamma = +1.2 \pm 0.4$ with the intrinsic scatter of 0.3 ± 0.1 dex using the `FITEXY` estimator. Note that this estimate does not take into account selection effects.

As noted in Treu et al. (2007) and Lauer et al. (2007), there could be a bias in the inferred offset and evolution of the scaling relation due to selection effects. Our sample of intermediate-z Seyfert 1 galaxies is selected basically on the nuclear (AGN) luminosity and detectability of the Hβ broad emission line (i.e., black hole mass). This will cause a selection bias toward more galaxies with less luminous bulges at a given black hole mass, similar to the well-known Malmquist bias, under the steeply declining bulge luminosity function and the intrinsic dispersion of the $M_{\rm BH}-L_{\rm bul}$ relation. The distribution of black hole masses (e.g., lower and upper limits) of our sample on the entire population of supermassive black holes is also important to correct for selection effects in our estimate of the evolution. Note that our samples at $z = 0.36$ and $z = 0.57$ have different selection criteria on black hole mass as discussed in Section 5.4.4. Thus, selection limits on black hole masses for the sample should be taken into account to derive the selection-bias corrected evolution.

To this end, we adopted the Monte Carlo simulation method as employed in Bennert et al. (2010) to incorporate the effect of observational selection process on constraining the evolution trend and the intrinsic scatter. First we generate samples on the joint distribution of

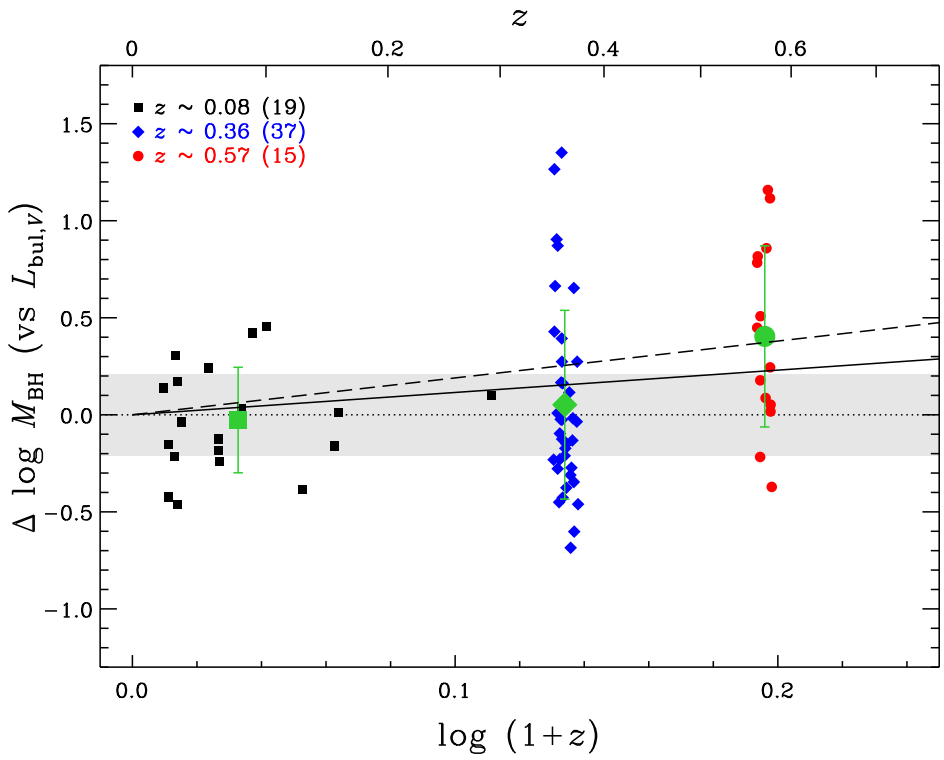

Figure 5.9 Redshift evolution of the offset in $\log M_{\rm BH}$ for a given $L_{\rm bul}$ with respect to local baseline $M_{\rm BH}-L_{\rm bul}$ relation (black dotted line with gray shaded region for the intrinsic scatter). Colored symbols indicate local RM AGNs (black squares at $\bar{z}\sim 0.08$) and our intermediate-z sample at $z = 0.36$ (blue diamonds) and at $z = 0.57$ (red circles). The mean and rms scatter of offsets for each sample are shown as green big symbols with error bars for reference. The black solid (dashed) line represents the best-fit of all intermediate-z objects in the functional form of $\Delta\log M_{\rm BH} = \gamma\log(1+z)$ without (with) taking into account for selection effects. The corresponding best-fit values for the evolution slope are $\gamma = 1.2\pm0.4$ ($\gamma = 1.9\pm0.7$).

black hole mass and bulge luminosity from a combination of the bulge luminosity function, transformed to V-band, from Driver et al. (2007; Ellipticals + bulges sample in their Table 1) and the local baseline $M_{\rm BH}-L_{\rm bul}$ relation from Bennert et al. (2010; local RM AGNs). The simulated samples, for which Gaussian random noises are added on both axes, are constructed as a function of the two free parameters of the γ and $\sigma_{\rm int}$. We then consider the observational selections on $\log M_{\rm BH}$, which are simply modeled by the lower and upper limit of [7.3, 8] for SS* objects (16 out of total 52) and [7.6, 9] for S* and W* objects (36 out of total 52), respectively. Note that this simple threshold is a practical approach at present since it is difficult to derive the selection function by including all the details involved in the observation and sampling processes. The likelihood for each object in our sample is calculated by making the probability distribution of black hole masses from the simulated sample which have the corresponding bulge luminosity within the measurement error. By adopting the uninformative uniform priors for the parameters, we evaluate the posterior distribution and take the best-fit values at the maximum posterior with 1σ uncertainties.

Figure 5.10 shows the results of the Monte Carlo simulations in the 2D plane of the γ and $\sigma_{\rm int}$. In a case of the uniform prior for $\sigma_{\rm int}$ (upper panel), the parameters are not well constrained since a dynamic range in redshifts of our sample is insufficient to determine the γ and $\sigma_{\rm int}$ simultaneously. If we adopt the log-normal prior (bottom panel) from Bennert et al. (2010; $\sigma_{\rm int} = 0.21 \pm 0.08$), the slope is found to be $\gamma = +1.9 \pm 0.7$ with $\sigma_{\rm int} = 0.4 \pm 0.1$. We obtain consistent estimates for the slope, $\gamma = +1.9 \pm 0.9$ and $\gamma = +2.0 \pm 1.1$, if we adopt the log-normal priors for $\sigma_{\rm int}$ from Gültekin et al. (2009; $\sigma_{\rm int} = 0.38 \pm 0.09$) and McConnell & Ma (2013; $\sigma_{\rm int} = 0.52 \pm 0.06$), respectively. This result can also be expressed as

$$\frac{M_{\rm BH}}{L_{\rm bul}} \propto (1+z)^{1.9\pm0.7}. \tag{5.3}$$

The positive trend reinforces the previous result that the BH growth precedes the assemble of bulge reported by Woo et al. (2006), Treu et al. (2007), Woo et al. (2008), and Bennert et al. (2010). Thus, to make our intermediate-z Seyfert galaxies falling on the local relation as an end-point of evolution, their bulge luminosities have to be increased by 0.25 dex (i.e., 80%) and 0.37 dex (i.e., more than a factor of two) by today from $z = 0.36$ ($\sim$ 4 Gyr) and $z = 0.57$ ($\sim$ 6 Gyr), respectively. This requires formation or injection of young stars into the bulge component without a significant BH growth.

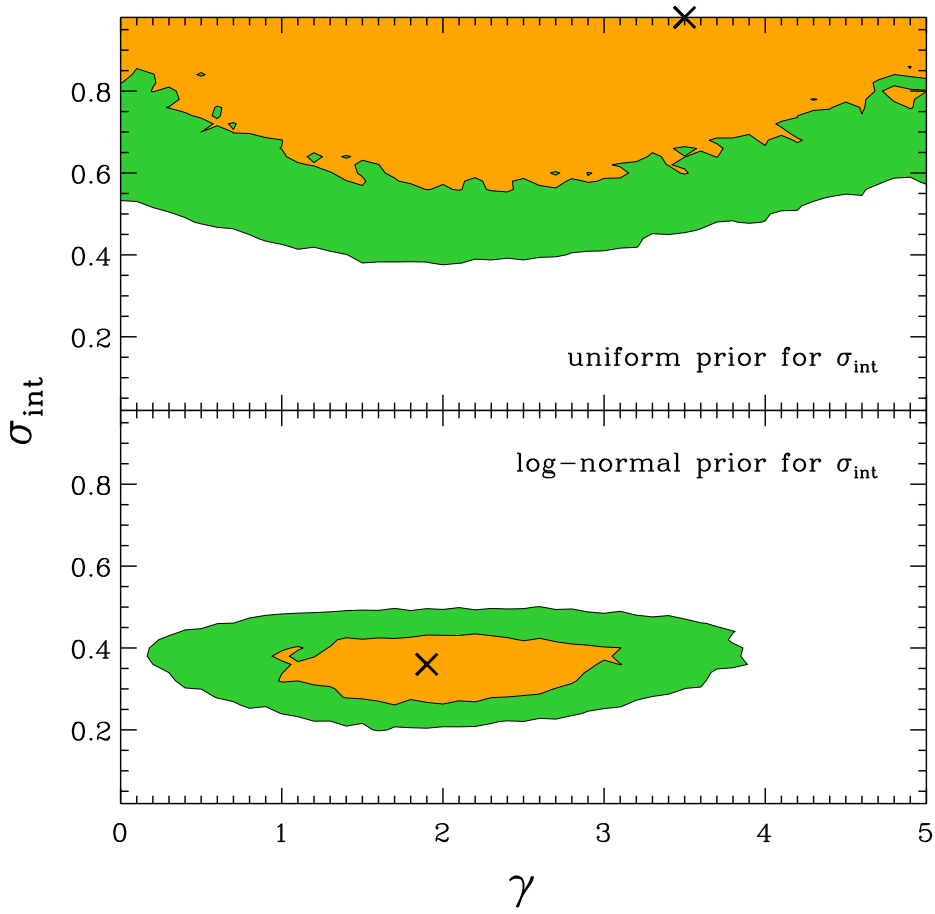

Figure 5.10 Monte Carlo simulation results accounted for selection effects on the slope γ and intrinsic scatter $\sigma_{\rm int}$ in the evolution trend, $\Delta \log M_{\rm BH} = \gamma \log(1+z)$. Upper panel: constraining the evolution trend by assuming an uniform prior for $\sigma_{\rm int}$. Both parameters are not well constrained. Bottom panel: the same as in the upper panel, but by assuming the log-normal prior for $\sigma_{\rm int}$ from Bennert et al. (2010; $\sigma_{\rm int} = 0.21 \pm 0.08$). The 2D joint confidence region is plotted with a yellow (green) filled contour corresponding to the 1σ (2σ) level of significance. The best-fit point at the maximum posterior is marked with a black cross symbol.

5.5 Discussion and Conclusions

We investigated the cosmic evolution of the black hole mass–bulge luminosity relation with a sample of 52 Seyfert 1 galaxies at $z\sim0.36$ and $z\sim0.57$ using high-quality Keck spectra and high-resolution *HST* images, which enables us to perform robust spectral and structural decompositions, thus leading to reliable $M_{\rm BH}$ and $L_{\rm bul}$ measurements. Taking into account selection effects, we find the evolutionary trend in the form of $M_{\rm BH}/L_{\rm bul}\propto(1+z)^{1.9\pm0.7}$. This means that black holes at distant universe reside in smaller bulges than today, thus implying that black holes grow first and then the host galaxies catch up in the context of the co-evolution of black holes and galaxies.

The overall trend of the positive evolution we detect is generally consistent with those observed by Treu et al. (2007; $\gamma=1.5\pm1.0$) and Bennert et al. (2010; $\gamma=1.4\pm0.2$) based on the $M_{\rm BH}-L_{\rm bul}$ relation and McLure et al. (2006; $\gamma=2.07\pm0.76$), Jahnke et al. (2009; $\gamma=1.2$), Decarli et al. (2010; $\gamma=1.4$), Cisternas et al. (2011; $\gamma=1.15\pm0.34$), Bennert et al. (2011b; $\gamma=1.96\pm0.55$) based on the $M_{\rm BH}-M_{\rm bul}$ relation and Woo et al. (2006; $\gamma=1.66\pm0.43$), Woo et al. (2008; $\gamma=3.1\pm1.5$) based on the $M_{\rm BH}-\sigma_*$ relation. Wyithe & Loeb (2003) also expect $M_{\rm BH}/M_{\rm bul}\propto(1+z)^{3/2}$ from a theoretical approach with a self-regulated BH growth model.

The results we found can be interpreted as that black hole tends to be completed their growth before the bulge growth under the assumption that the local relation is the final product of the BH-galaxy co-evolution. Thus a substantial bulge growth is expected between today and observed epochs. Out of our sample of 52 galaxies, $\sim30\%$ show a merger or interaction signature. This indicates merging can contribute the bulge growth in a faction of the sample. Treu et al. (2007) suggested that a merger with a disk-dominated system containing no black hole can explain substantial growth of bulge luminosity by transferring stars in a disk to a bulge. Recently the secular evolution driven by disk instabilities and/or minor merging are also suggested for the bulge growth mechanism by redistributing mass into the bulge component without a significant growth of black hole. (e.g., Parry et al. 2009; Jahnke et al. 2009; Cisternas et al. 2011; Bennert et al. 2010, 2011b; Schramm & Silverman 2013)

Although we found the tentative evolution signal from the samples of local and distant AGNs, in order to be considered as a conclusive detection it should be confirmed by the detailed tests for the selection biases or with the better defined samples of much more numbers and wider dynamic ranges. We note here that accounting for selection bias and other

potential biases properly is important for the study of the evolution of the scaling relations. First is the AGN luminosity selection bias noted in Treu et al. (2007) and Lauer et al. (2007). Selecting the broad-line AGN sample based on their luminosities (i.e., black hole masses) leads to a preferential selection of higher mass black holes than those of associated bulge luminosities under a presence of intrinsic scatter of the scaling relation, particularly in the high-luminosity regime where galaxy (and bulge) luminosity function is steeply decreasing. This selection effect is taken into account for constraining the evolution by performing the Monte Carlo simulations in the previous section. Second is a bias from the measurement uncertainty on black hole mass (Shen & Kelly 2010; but see also Schulze & Wisotzki 2011). This BH mass error-induced bias arises due to the large uncertainty in BH mass measured from the SE method. It is likely to detect more massive black holes at a given bulge luminosity since the true lower mass BHs have more chances to be scatted into the higher SE mass bin through the SE mass estimates with large uncertainty than the intrinsically higher-mass BHs under the steeply declining black hole mass function. The opposite effect may be expected for the uncertainty on bulge luminosity. These effects of measurement uncertainties are also incorporated in the Monte Carlo simulations performed in the previous section. Third is the active fraction bias suggested by Schulze & Wisotzki (2011). This causes a negative offset in a sample of AGNs by preferentially observing less massive black holes for a given bulge luminosity under a presence of intrinsic scatter of the scaling relation since the active fraction (i.e., the probability of black holes to be observed as broad-line AGNs) decreases as a function of mass. We will perform quantitative assessments for all selection effects by incorporating them properly in the better designed Monte Carlo simulations with the possibly more refined underlying distribution functions as well as the exact knowledge of the selection function in future works since we are noticing that the result in this work is not a completely free of the potential biases.

Aside from the selection biases, there are many limitations that should be further improved for the better estimation of evolution of the scaling relations. First, BH mass measurements for distant Seyfert galaxies are based on the empirically calibrated SE method, which is subject to relatively large random and systematic uncertainties although this method is only viable one beyond local universe. The largest systematic uncertainty is from the unknown virial factor related to the kinematics and geometry of the BLR, which is currently adopted from the empirically calibrated average virial factor for all population. A direct assessment of the virial factor for each active galaxy will greatly reduce the uncertainties in $M_{\rm BH}$ measurements (see, e.g., Pancoast et al. 2011, 2012; Brewer et al. 2011). In addition,

the results from our own image decomposition tool might be systematically different to those from the other program used in literature (e.g., GALFIT; Peng et al. 2002, 2010). The thorough comparison test for a reliability and performance between tools is left for future study.

The sample of local RM AGNs as the local baseline is still limited to small number and insufficient dynamic ranges. The extension of this sample and more complete establishment of the local scaling relation will ultimately shed light on the accurate characterization of the BH-galaxy co-evolution. On the other aspect, although the BH mass ranges in between our sample and local RM AGNs are almost same, we need to expend our sample to higher and lower $L_{\rm bul}$ regimes for a more direct comparison to the local RM AGNs.

Another possible explanation for the positive offset we detected is redshift evolution of intrinsic scatter of the relation (i.e., increasing with redshift). In the end, to extract the true redshift evolution (i.e., its normalization or intrinsic scatter) of the scaling relation from the contaminations of selection biases and systematic uncertainties we need larger sets of uniformly selected and consistently measured samples of local and distant active or inactive galaxies. This can be achieved with the next generation ground and space telescopes in near future.

Table 5.1. Sample list

Object	SDSS name	z	$D_{\rm L}$ (Mpc)	$E(B-V)$ (mag)
(1)	(2)	(3)	(4)	(5)
The sample presented in Treu et al. (2007)				
S09	SDSS−J005916.10+153816.0	0.354488	1884.8	0.089
S10	SDSS−J010112.06−094500.7	0.351342	1865.3	0.030
S12	SDSS−J021340.59+134756.0	0.358309	1908.6	0.104
S21	SDSS−J110556.18+031243.1	0.354551	1885.2	0.048
S16	SDSS−J111937.58+005620.3	0.370213	1983.1	0.033
S23	SDSS−J140016.65−010822.1	0.351314	1865.1	0.039
S24	SDSS−J140034.70+004733.3	0.361910	1931.1	0.032
S26	SDSS−J152922.24+592854.5	0.369242	1977.0	0.014
S27	SDSS−J153651.27+541442.6	0.366873	1962.1	0.020
S01	SDSS−J153916.24+032322.0	0.359351	1915.1	0.058
S02	SDSS−J161111.66+513131.1	0.354384	1884.2	0.021
S03	SDSS−J173203.08+611751.8	0.358429	1909.3	0.040
S04	SDSS−J210211.50−064645.0	0.357906	1906.1	0.076
S05	SDSS−J210451.83−071209.4	0.353505	1878.7	0.086
S06	SDSS−J212034.18−064122.2	0.368817	1974.3	0.186
S07	SDSS−J230946.07+000048.9	0.351999	1869.3	0.041
S08	SDSS−J235953.44−093655.6	0.358619	1910.5	0.030
The sample presented in Bennert et al. (2010)				
S11	SDSS−J010715.97−083429.4	0.355877	1893.4	0.049
SS1	SDSS−J080427.99+522306.2	0.356555	1897.7	0.043
SS2	SDSS−J093455.60+051409.1	0.367083	1963.4	0.033
SS5	SDSS−J100706.26+084228.4	0.373450	2003.5	0.029
S31	SDSS−J101527.26+625911.5	0.350568	1860.5	0.006
SS6	SDSS−J102103.58+304755.9	0.358781	1911.5	0.025
SS7	SDSS−J104331.50−010732.8	0.361284	1927.1	0.046
SS8	SDSS−J104610.60+035031.2	0.365515	1953.6	0.039

Table 5.1 (cont'd)

Object	SDSS name	z	$D_{\rm L}$ (Mpc)	$E(B-V)$ (mag)
(1)	(2)	(3)	(4)	(5)
SS9	SDSS−J125838.71+455515.5	0.370188	1982.9	0.012
SS10	SDSS−J133414.84+114221.5	0.365808	1955.5	0.023
SS11	SDSS−J135226.90+392426.8	0.373111	2001.3	0.016
SS12	SDSS−J150116.82+533102.1	0.362919	1937.4	0.013
SS13	SDSS−J150541.79+493520.0	0.374316	2008.9	0.013
S28	SDSS−J161156.29+451610.9	0.367841	1968.2	0.011
SS14	SDSS−J211531.68−072627.5	0.370558	1985.3	0.117
S29	SDSS−J215841.92−011500.3	0.357366	1902.7	0.083
SS18	SDSS−J234050.52+010635.5	0.358543	1910.0	0.029
W11	SDSS−J015516.18−094556.0	0.565000	3282.3	0.019
W22	SDSS−J034229.70−052319.4	0.565167	3283.5	0.042
W12	SDSS−J143955.10+355305.3	0.562309	3263.4	0.010
W20	SDSS−J150014.81+322940.4	0.576130	3360.7	0.014
W16	SDSS−J152654.93−003243.3	0.578015	3374.0	0.106
W8	SDSS−J163252.42+263749.1	0.571209	3326.0	0.043
The new sample in this work				
W3	SDSS−J002005.69−005016.3	0.576049	3360.1	0.024
SS15	SDSS−J014412.77−000610.5	0.359329	1914.9	0.024
W1	SDSS−J083654.98+075712.4	0.573637	3343.1	0.026
W4	SDSS−J093210.96+433813.1	0.576601	3364.0	0.018
W5	SDSS−J094852.73+363120.5	0.576728	3364.9	0.012
SS3	SDSS−J095553.14+633742.8	0.356623	1898.1	0.028
SS4	SDSS−J095850.15+400342.3	0.362909	1937.3	0.011
W17	SDSS−J100728.38+392651.8	0.561690	3259.0	0.012
W2	SDSS−J110641.86+614146.5	0.572026	3331.7	0.008
W10	SDSS−J111415.83−005920.4	0.571076	3325.0	0.035
W14	SDSS−J125631.89−023130.6	0.561702	3259.1	0.019
W9	SDSS−J155227.81+562236.4	0.565356	3284.8	0.010

Note. — Column 1: Object ID. Column 2: SDSS name. Column 3: Redshifts listed in the NASA/IPAC Extragalactic Database (NED) from the improved redshifts by Hewett & Wild (2010). Column 4: Luminosity distance. Column 5: $E(B-V)$ listed in the NED from the Schlafly & Finkbeiner (2011) recalibration of the Schlegel, Finkbeiner & Davis (1998) infrared-based dust map.

Table 5.2. Results from spectroscopic decomposition analysis

Object	S/N	FWHM$_{H\beta}$	$\sigma_{H\beta}$	$\lambda L_{5100}^{\rm spec}$	$\log M_{\rm BH}^{\rm spec}$
	(pix^{-1})	(km s^{-1})	(km s^{-1})	(10^{44}erg s^{-1})	($M_\odot$)
(1)	(2)	(3)	(4)	(5)	(6)
S09	39	2655	1748	1.76	8.15
S10	96	4850	2597	2.77	8.59
S12	39	8799	4255	1.82	8.93
S21	74	8295	3896	5.33	9.09
S16	6	3748	1866	0.69	8.00
S23	108	9628	4250	1.78	8.92
S24	100	7061	2635	1.49	8.47
S26	50	5385	1914	0.83	8.06
S27	42	2508	1408	1.26	7.89
S01	69	4662	2193	1.37	8.29
S02	44	4841	2274	1.25	8.30
S03	87	3018	1715	2.11	8.17
S04	46	2820	1748	1.19	8.06
S05	118	4908	3332	2.23	8.76
S06	30	4527	1412	1.10	7.86
S07	107	4634	2546	1.81	8.48
S08	54	2909	1217	1.59	7.81
S11	113	2595	1353	1.57	7.90
SS1	25	2620	1500	1.04	7.90
SS2	31	2814	1315	0.83	7.73
SS5	45	2790	1611	1.40	8.03
S31	79	4011	2116	0.93	8.17
SS6	47	1946	1031	0.69	7.48
SS7	54	2959	1370	0.98	7.81
SS8	82	2733	1532	1.54	8.00
SS9	69	2786	1569	1.25	7.98
SS10	83	2231	1431	4.09	8.16
SS11	48	3504	1465	2.07	8.03
SS12	115	2100	1371	4.34	8.14

Table 5.2 (cont'd)

Object	S/N	FWHM$_{H\beta}$	$\sigma_{H\beta}$	$\lambda L_{5100}^{\rm spec}$	$\log M_{\rm BH}^{\rm spec}$
	(pix^{-1})	(km s^{-1})	(km s^{-1})	(10^{44}erg s^{-1})	($M_\odot$)
(1)	(2)	(3)	(4)	(5)	(6)
SS13	108	2168	1143	1.49	7.74
S28	73	4600	2532	0.97	8.33
SS14	50	2143	1212	0.65	7.60
S29	54	3533	1846	1.20	8.11
SS18	63	1630	1028	1.90	7.71
W11	17	3811	2025	0.78	8.09
W22	80	5834	2654	4.65	8.73
W12	62	7697	3858	3.62	9.00
W20	26	10861	3805	1.33	8.76
W16	36	2392	1563	1.05	7.94
W8	56	7340	2976	4.17	8.81
W3	58	7461	3507	1.47	8.71
SS15	46	1604	1000	0.64	7.43
W1	79	7378	3152	4.71	8.88
W4	50	3489	1727	3.68	8.30
W5	71	2722	1738	4.94	8.38
SS3[a]	13	1952	1251	0.74	7.66
SS4	64	2212	1378	1.35	7.88
W17	24	5556	2483	0.86	8.29
W2	65	12647	4811	3.03	9.15
W10	31	3635	1477	2.92	8.12
W14	76	5000	2615	5.56	8.76
W9	61	5273	2746	2.64	8.63

Note. — Column 1: Object ID. Column 2: Signal-to-noise ratio averaged at the rest wavelength range of 5080–5120 Å. Column 3: Full width at half-maximum of Hβ broad emission line. Column 4: Line dispersion of Hβ broad emission line. Column 5: Continuum luminosities at 5100 Å measured from spectra. Column 6: Black hole mass derived from Eq (5.1) with the $\sigma_{H\beta}$ and $\lambda L_{5100}^{\rm spec}$ measurements.

[a]This object is measured from the SDSS DR7 spectrum because the Keck spectrum is not available.

Table 5.3. Results from photometric decomposition analysis

Object	Total	PSF	Host	Bulge	$r_{eff,bul}$	$r_{eff,bul}$	f_{AGN}	λL_{5100}^{image}	$\log L_{host,V}$	$\log L_{bul,V}$
	(mag)	(mag)	(mag)	(mag)	(")	(kpc)		(10^{44}erg s^{-1})	($L_{\odot,V}$)	($L_{\odot,V}$)
(1)	(2)	(3)	(4)	(5)	(6)	(7)	(8)	(9)	(10)	(11)
W3	18.86	19.69	19.55	20.56	0.21	1.38	0.47	2.04	10.73	10.32
SS15	18.81	19.64	19.48	19.48	0.33	1.67	0.46	0.75	10.22	10.22
W1	18.40	18.94	19.40	21.21	0.80	5.24	0.60	4.03	10.78	10.05
W4	18.35	19.09	19.12	19.12	0.63	4.13	0.51	3.55	10.90	10.90
W5	18.41	19.10	19.23	19.23	0.85	5.59	0.53	3.53	10.86	10.86
SS3	18.17	20.43	18.31	19.35	0.18	0.90	0.12	0.35	10.68	10.27
SS4	17.88	19.12	18.29	18.29	0.55	2.76	0.32	1.23	10.71	10.71
W17	19.16	20.35	19.60	20.97	0.18	1.17	0.34	1.05	10.68	10.13
W2	18.70	19.61	19.32	19.32	0.50	3.27	0.43	2.17	10.81	10.81
W10	19.13	20.11	19.70	20.60	0.87	5.68	0.41	1.36	10.65	10.29
W14	18.22	18.81	19.16	19.16	0.91	5.90	0.58	4.33	10.85	10.85
W9	18.36	18.94	19.32	19.32	0.28	1.85	0.58	3.90	10.80	10.80

Note. — Column 1: Object ID. Column 2: Total extinction-corrected F110W AB magnitude (Total=PSF+Bulge+Disk). Column 3: AGN extinction-corrected F110W AB magnitude. Column 4: Host galaxy extinction-corrected F110W AB magnitude (Host=Bulge+Disk). Column 5: Bulge extinction-corrected F110W AB magnitude. Column 6: Bulge effective radius in arcsec. Column 7: Bulge effective radius in kpc. Column 8: AGN-to-total light fraction in F110W. Column 9: AGN continuum luminosities at rest-frame 5100 Å in 10^{44} erg s^{-1}. Column 10: Host-galaxy luminosity in rest-frame V (solar units), not corrected for evolution. Column 11: Bulge luminosity in rest-frame V (solar units), not corrected for evolution.

Table 5.4. Derived quantities

Object	$\log M_{\rm BH}$	$\log L_{{\rm bul},V}$	$\log L_{{\rm bul},V,0}$
	$(M_\odot)$	$(L_{\odot,V})$	$(L_{\odot,V})$
(1)	(2)	(3)	(4)
S09	7.94	10.68	10.46
S10	8.37	10.28	10.06
S12	8.79	9.56	9.34
S21	8.89	10.39	10.17
S16	8.01	9.45	9.22
S23	8.82	9.72	9.50
S24	8.19	10.89	10.67
S26	7.95	10.33	10.10
S27	7.82	10.56	10.33
S01	8.14	10.34	10.12
S02	8.01	10.36	10.14
S03	8.12	9.97	9.75
S04	8.09	10.25	10.03
S05	8.72	10.10	9.88
S06	7.68	10.11	9.88
S07	8.52	10.15	9.93
S08	7.75	9.62	9.40
S11	7.65	10.51	10.29
SS1	7.68	10.04	9.82
SS2	7.52	10.67	10.44
SS5	7.93	9.89	9.66
S31	7.91	10.56	10.34
SS6	7.34	9.60	9.38
SS7	7.55	10.02	9.80
SS8	7.75	9.95	9.72
SS9	7.91	10.74	10.51
SS10	8.03	10.25	10.02
SS11	7.72	10.02	9.79
SS12	8.08	10.69	10.46

Table 5.4 (cont'd)

Object	$\log M_{\rm BH}$	$\log L_{{\rm bul},V}$	$\log L_{{\rm bul},V,0}$
	$(M_\odot)$	$(L_{\odot,V})$	$(L_{\odot,V})$
(1)	(2)	(3)	(4)
SS13	7.65	10.53	10.30
S28	7.85	10.54	10.31
SS14	7.42	10.41	10.18
S29	7.76	10.05	9.83
SS18	7.48	9.66	9.44
W11	7.89	10.64	10.29
W22	8.64	11.16	10.81
W12	8.85	10.54	10.19
W20	8.55	10.93	10.57
W16	7.81	10.76	10.40
W8	8.70	10.95	10.60
W3	8.79	10.03	9.67
SS15	7.47	10.22	10.00
W1	8.85	10.05	9.70
W4	8.30	10.90	10.54
W5	8.30	10.86	10.50
SS3	7.50	9.97	9.75
SS4	7.86	10.71	10.48
W17	8.34	9.85	9.51
W2	9.08	10.81	10.45
W10	7.94	10.29	9.94
W14	8.70	10.85	10.50
W9	8.72	10.80	10.45

Note. — Column 1: Object ID. Column 2: Black hole mass derived from Eq (5.1) with the $\sigma_{\rm H\beta}$ and $\lambda L_{5100}^{\rm image}$ measurements (solar units). Column 3: Bulge luminosity in rest-frame V (solar units) with the re-estimation for 19 upper limits using informative priors (see Section 5.4.2 for details). Column 4: Final bulge luminosity corrected for evolution by ageing of stellar population.

References

Beifiori, A., Maraston, C., Thomas, D., & Johansson, J. 2011, A&A, 531, A109

Bennert, V. N., Treu, T., Woo, J.-H., et al. 2010, ApJ, 708, 1507

Bennert, V. N., Auger, M. W., Treu, T., Woo, J.-H., & Malkan, M. A. 2011a, ApJ, 726, 59

Bennert, V. N., Auger, M. W., Treu, T., Woo, J.-H., & Malkan, M. A. 2011b, ApJ, 742, 107

Benson, A. J., Džanović, D., Frenk, C. S., & Sharples, R. 2007, MNRAS, 379, 841

Bentz, M. C., Peterson, B. M., Pogge, R. W., Vestergaard, M., & Onken, C. A. 2006, ApJ, 644, 133

Bentz, M. C., Peterson, B. M., Netzer, H., Pogge, R. W., & Vestergaard, M. 2009a, ApJ, 697, 160

Bentz, M. C., Peterson, B. M., Pogge, R. W., & Vestergaard, M. 2009b, ApJ, 694, L166

Bentz, M. C., Denney, K. D., Grier, C. J., et al. 2013, ApJ, in press, (arXiv:1303.1742)

Brewer, B. J., Treu, T., Pancoast, A., et al. 2011, ApJ, 733, L33

Bruzual, G., & Charlot, S. 2003, MNRAS, 344, 1000

Canalizo, G., Wold, M., Hiner, K. D., et al. 2012, ApJ, 760, 38

Cisternas, M., Jahnke, K., Bongiorno, A., et al. 2011, ApJ, 741, L11

Coleman, G. D., Wu, C.-C., & Weedman, D. W. 1980, ApJS, 43, 393

Croton, D. J., Springel, V., White, S. D. M., et al. 2006, MNRAS, 365, 11

Decarli, R., Falomo, R., Treves, A., et al. 2010, MNRAS, 402, 2453

Ferrarese, L., & Merritt, D. 2000, ApJ, 539, L9

Fernández Lorenzo, M., Cepa, J., Bongiovanni, A., et al. 2011, A&A, 526, A72

Fitzpatrick, E. L. 1999, PASP, 111, 63

Gebhardt, K., Bender, R., Bower, G., et al. 2000, ApJ, 539, L13

Greene, J. E., Peng, C. Y., & Ludwig, R. R. 2010, ApJ, 709, 937

Jahnke, K., Bongiorno, A., Brusa, M., et al. 2009, ApJ, 706, L215

Jahnke, K., & Macciò, A. V. 2011, ApJ, 734, 92

Harris, C. E., Bennert, V. N., Auger, M. W., et al. 2012, ApJS, 201, 29

Häring, N., & Rix, H.-W. 2004, ApJ, 604, L89

Hiner, K. D., Canalizo, G., Wold, M., Brotherton, M. S., & Cales, S. L. 2012, ApJ, 756, 162

Hirschmann, M., Khochfar, S., Burkert, A., et al. 2010, MNRAS, 407, 1016

Hewett, P. C., & Wild, V. 2010, MNRAS, 405, 2302

Hopkins, P. F., Murray, N., & Thompson, T. A. 2009, MNRAS, 398, 303

Kaspi, S., Smith, P. S., Netzer, H., et al. 2000, ApJ, 533, 631

Kaspi, S., Maoz, D., Netzer, H., et al. 2005, ApJ, 629, 61

Kaspi, S., Brandt, W. N., Maoz, D., et al. 2007, ApJ, 659, 997

Kauffmann, G., & Haehnelt, M. 2000, MNRAS, 311, 576

Kim, M., Ho, L. C., Peng, C. Y., et al. 2008a, ApJ, 687, 767

Kim, M., Ho, L. C., Peng, C. Y., Barth, A. J., & Im, M. 2008b, ApJS, 179, 283

Lauer, T. R., Tremaine, S., Richstone, D., & Faber, S. M. 2007, ApJ, 670, 249

Lawson C., Hanson R.J., 1987, Solving Least Squares Problems, SIAM

Magorrian, J., Tremaine, S., Richstone, D., et al. 1998, AJ, 115, 2285

Marconi, A., & Hunt, L. K. 2003, ApJ, 589, L21

Markwardt, C. B. 2009, Astronomical Data Analysis Software and Systems XVIII, 411, 251

Mathur, S., Fields, D., Peterson, B. M., & Grupe, D. 2012, ApJ, 754, 146

McConnell, N. J., & Ma, C.-P. 2013, ApJ, 764, 184

McGill, K. L., Woo, J.-H., Treu, T., & Malkan, M. A. 2008, ApJ, 673, 703

McLure, R. J., Jarvis, M. J., Targett, T. A., Dunlop, J. S., & Best, P. N. 2006, MNRAS, 368, 1395

Merloni, A., Bongiorno, A., Bolzonella, M., et al. 2010, ApJ, 708, 137

Onken, C. A., Ferrarese, L., Merritt, D., et al. 2004, ApJ, 615, 645

Orban de Xivry, G., Davies, R., Schartmann, M., et al. 2011, MNRAS, 417, 2721

Pancoast, A., Brewer, B. J., & Treu, T. 2011, ApJ, 730, 139

Pancoast, A., Brewer, B. J., Treu, T., et al. 2012, ApJ, 754, 49

Park, D., Kelly, B. C., Woo, J.-H., & Treu, T. 2012a, ApJS, 203, 6

Park, D., Woo, J.-H., Treu, T., et al. 2012b, ApJ, 747, 30

Parry, O. H., Eke, V. R., & Frenk, C. S. 2009, MNRAS, 396, 1972

Peng, C. Y., Ho, L. C., Impey, C. D., & Rix, H.-W. 2002, AJ, 124, 266

Peng, C. Y. 2007, ApJ, 671, 1098

Peng, C. Y., Impey, C. D., Rix, H.-W., et al. 2006, ApJ, 649, 616

Peng, C. Y., Ho, L. C., Impey, C. D., & Rix, H.-W. 2010, AJ, 139, 2097

Peterson, B. M. 1993, PASP, 105, 247

Peterson, B. M., Ferrarese, L., Gilbert, K. M., et al. 2004, ApJ, 613, 682

Schlafly, E. F., & Finkbeiner, D. P. 2011, ApJ, 737, 103

Schlegel, D. J., Finkbeiner, D. P., & Davis, M. 1998, ApJ, 500, 525

Schramm, M., & Silverman, J. D. 2013, ApJ, 767, 13

Schulze, A., & Wisotzki, L. 2011, A&A, 535, A87

Shen, Y., Greene, J. E., Strauss, M. A., Richards, G. T., & Schneider, D. P. 2008, ApJ, 680, 169

Shen, Y., & Kelly, B. C. 2010, ApJ, 713, 41

Suyu, S. H., Marshall, P. J., Auger, M. W., et al. 2010, ApJ, 711, 201

Suyu, S. H., Auger, M. W., Hilbert, S., et al. 2013, ApJ, 766, 70

Treu, T., Stiavelli, M., Casertano, S., Møller, P., & Bertin, G. 1999, MNRAS, 308, 103

Treu, T., Stiavelli, M., Møller, P., Casertano, S., & Bertin, G. 2001, MNRAS, 326, 221

Treu, T., Malkan, M. A., & Blandford, R. D. 2004, ApJ, 615, L97

Treu, T., Woo, J.-H., Malkan, M. A., & Blandford, R. D. 2007, ApJ, 667, 117

Valdes, F., Gupta, R., Rose, J. A., Singh, H. P., & Bell, D. J. 2004, ApJS, 152, 251

Vestergaard, M. 2002, ApJ, 571, 733

Vestergaard, M., & Peterson, B. M. 2006, ApJ, 641, 689

Vestergaard, M., & Wilkes, B. J. 2001, ApJS, 134, 1

Volonteri, M., Haardt, F., & Madau, P. 2003, ApJ, 582, 559

Wandel, A., Peterson, B. M., & Malkan, M. A. 1999, ApJ, 526, 579

Wolf, M. J., & Sheinis, A. I. 2008, AJ, 136, 1587

Woo, J.-H., Treu, T., Malkan, M. A., & Blandford, R. D. 2006, ApJ, 645, 900

Woo, J.-H., Treu, T., Malkan, M. A., & Blandford, R. D. 2008, ApJ, 681, 925

Woo, J.-H., Treu, T., Barth, A. J., et al. 2010, ApJ, 716, 269

Woo, J.-H., Schulze, A., Park, D., et al. 2013, arXiv:1305.2946

Wyithe, J. S. B., & Loeb, A. 2003, ApJ, 595, 614

Chapter 6

Conclusion and Summary

In this thesis, we perform four research projects ultimately for the better understanding of the BH-galaxy co-evolution. First, for the reliable measurements of BH masses as a fundamental physical quantity, we systematically study the uncertainties of the Hβ SE virial BH mass estimates (Chapter 2) and the virial factor constraining (Chapter 3), and thus present the improved BH mass estimators. We also update the calibration of the C IV SE virial BH mass estimators for high-redshift AGNs (Chapter 4). Then we investigate the redshift evolution of the $M_{\rm BH}-L_{\rm bul}$ relation and present the results in Chapter 5.

Improving black hole mass measurements in AGNs

By employing the multi-component spectral decomposition technique on the homogeneous and high-quality reverberation-mapping data for 9 local Seyfert 1 galaxies, we quantify that the random uncertainty of the SE BH mass due to the AGN variability is ~ 0.05 dex (12%) and the systematic uncertainty of the SE BH mass due to the line width difference is ~ 0.2 dex (60%). To correct for this systematic difference, we provide new line-width dependent recalibrated SE virial BH mass estimators. We also show that measured line widths and luminosities are in a good agreement with the expected theoretical relation from the virial theorem and size-luminosity relation, which further corroborates the use of the SE method for AGN BH mass estimation. Although we find the systematic trend in the sense that the line width measured in mean or SE spectra is systematically larger than that of rms spectra for the narrower line objects, its origin is still unclear, which consequently stimulates theoretical investigations for the nature. In future work we will extend this work

with more RM sample of larger dynamic ranges to account for possible selection biases and small sample size.

Using the recently compiled inactive and active galaxy data sets from literature, we derive the $M_{\rm BH}-\sigma_*$ relation and calibrate the virial factor with various linear regression methods. We find that a factor of two difference in the virial factors reported in recent studies is originated from a combined effect of the difference in sample selection (~ 0.1 dex) and the choice of independent variable in the regression analysis (~ 0.2 dex). This factor of two discrepancy can be considered as an additional systematic uncertainty in the AGN BH mass estimation from the current virial factor determination process. We also show that the FITEXY and Bayesian estimators are well performed in Monte Carlo simulations and the most recommendable ones for regression analysis in the scaling relation studies, while the maximum-likelihood estimate has a bias if it is based on the incorrect prior assumption. Although we present the updated $M_{\rm BH}-\sigma_*$ relation for local active galaxies based on the recent samples, this is still subject to selection effects in the AGN sample. For the better and complete determinations in a full dynamic range, it requires more RM AGN sample especially at high-mass regime ($\gtrsim 10^8 M_\odot$). In this regard, we will proceed the RM observation project for a sample of the carefully selected high-mass AGNs in near future.

We revisit the calibration of the C IV SE virial mass estimators with the most updated sample of the reverberation-mapped AGNs having archival UV spectra in order to obtain the most consistent C IV virial BH masses to the Hβ RM-based BH masses. By performing the multi-component spectral fitting analysis on the UV C IV region complex, we provide the updated best-fit calibrations for both the σ- and FWHM-based C IV SE virial BH mass estimators. We show that the FWHM-based BH masses using our updated calibration for high-redshift SDSS quasars are smaller on average by ~ 0.25 dex than those from the estimator commonly used in the literature. Since we are noticing that the current calibrations still suffer from a lack of low-mass AGNs ($\lesssim 10^7 M_\odot$), the calibrations will be updated with new *HST* STIS observations in future work. However, in the end, to perform a direct calibration for the C IV line as in the case of the Hβ line, conducting direct C IV RM studies for high-mass AGNs will be essential.

Constraining cosmic evolution of the $M_{\rm BH}-L_{\rm bul}$ relation

Carrying out the robust spectral and structural decomposition analysis on high-quality Keck spectra and high-resolution *HST* images for a sample of 52 Seyfert 1 galaxies at $z\sim 0.36$ and

$z \sim 0.57$, we obtain consistent measurements for black hole masses and bulge luminosities. Based on the measurements, we find the overall offset of the sample from the local relation as $\Delta \log M_{\rm BH} = +0.15 \pm 0.07 \pm 0.27$ dex, indicating on average that black holes at distant universe live in smaller bulges than today. Using the Monte Carlo simulations designed to account for selection effects, we obtain the evolution of BHs and host galaxy bulges in the form of $M_{\rm BH}/L_{\rm bul} \propto (1+z)^{1.9\pm0.7}$, which implies that black holes complete their growth before the bulge growth. This may suggest a different timescale for the galaxy bulge growth, which probably be driven by secular processes such as minor merging and disk instabilities. In future work, we will perform the better assessment for the evolution trend with the well defined and uniformly measured samples of more number and wider dynamic ranges in masses and redshifts since we note here that the results in this work is not a completely free of the potential biases and measurement systematics.

In conclusion, the results presented in this thesis will consequentially affect and improve our knowledge obtained from all studies based on BH mass measurements using AGNs, ranging from BH demographics to scaling relationships, and play a part in shedding light on the true nature of the co-evolution of the black holes and galaxies.

초 록

초거대 블랙홀의 성장과 그 모은하 간의 공동 진화를 이해하고자 다음과 같은 일련의 연구들을 수행하였다. 먼저 이 연구에서 핵심적인 물리량인 블랙홀 질량을 정확히 측정하기 위해, 수소 방출선의 한 시점 분광 관측을 통해 측정되는 비리얼 블랙홀 질량의 불확실성에 대해 체계적으로 연구하고 이러한 질량 측정법에 중요한 비리얼 계수를 추정하여 보다 향상된 질량 측정법을 제시하였다. 높은 적색편이에 존재하는 활동성 은하의 블랙홀 질량 측정에 유용한 탄소 방출선 기반 질량 추정법의 정확도를 향상시켰다. 이러한 경험과 기술을 바탕으로 먼 우주에 존재하는 블랙홀의 질량과 그 모은하의 팽대부 밝기를 측정하여 이들의 물리적 상관 관계에 대한 시간 진화를 연구하였다.

가까운 우주에 존재하는 9개의 활동성 은하에 대해 빛 반향 분포 측정법을 통해 얻어진 균질하고 고품질의 분광 자료에 다성분 분광 분해 기법을 적용하여, 은하의 밝기 변화에서 기인하는 임의적 오차(12%)와 방출선의 선폭 차이에서 기인하는 체계적 오차(60%)를 측정하고 이를 보정하는 새로운 질량 측정기법을 개발하였다. 또한 이 연구에 기반한 질량 측정치가 이론적인 비리얼 정리와 크기-밝기 관계에서 예측되는 값과 잘 부합함을 보였다.

최근 연구 문헌에서 정립된 활동성/비활동성 은하 자료에 다양한 선형회귀분석법을 적용하여 블랙홀질량-별속도분산 상관 관계식과 비리얼 계수를 유도하였다. 이러한 결과로부터 샘플 선택에서 기인하는 차이와 선형회귀분석의 독립변수 선택에서 기인하는 차이로 인해 현재 비리얼 계수 결정법에는 두배 가량의 체계적 오차가 존재함을 보였다. 또한 선형회귀분석법 중 FITEXY와 베이지안 방법론이 블랙홀 척도관계 연구에 가장 적합함을 보였다.

빛 반향 분포 측정법이 적용된 활동성 은하의 최신 샘플과 자료를 바탕으로 다성분 분광 분해 기법을 적용해 탄소 방출선 기반 블랙홀 질량 측정법의 정확도를 향상시켰다. 이러한 새 측정법이 기존의 측정법에 비해 얼마나 차이를 주는지 슬로안 분광전천탐사 자료에서 얻어진 퀘이사 목록에 적용하여 연구하였다.

지금으로부터 대략 40억년 전과 60억년 전에 존재하는 52개의 활동성 은하 샘플에 대해 Keck 지상 망원경과 허블 우주 망원경을 통해 관측하여 얻어진 고품질의 분광 자료와 고분해능의 측광 자료에 정교한 스펙트럼 분석 기법과 이미지 분석 기법을 적용하여 정확한 블랙홀 질량과 은하 팽대부 밝기 측정치를 얻었다. 이 결과에 기반해 먼 우주에 존재하는 블랙홀이 현재 우주의 블랙홀에 비해 상대적으로 작은 은하의 중심에 위치하고 있다는 관측적 증거를 제시하였다. 샘플 선택 효과를 보정하도록

설계된 몬테 칼로 시뮬레이션 기법을 적용해 블랙홀과 은하의 공동 진화 양상을 통계적으로 유도하여 블랙홀의 성장이 은하 진화에 선행한다는 것을 시사하였다.

주요어: 블랙홀 물리, 은하: 활동성, 은하: 핵, 방법론: 통계적

학 번: 2005-20522

List of Publications

- "Calibrating C IV-based Black Hole Mass Estimators",
  Daeseong Park, Jong-Hak Woo, Kelly D. Denney, Jaejin Shin,
  2013, ApJ, 770, 87

- "Recalibration of the Virial Factor and M_{BH}-σ_* Relation for Local Active Galaxies",
  Daeseong Park, Brandon C. Kelly, Jong-Hak Woo, Tommaso Treu,
  2012, ApJS, 203, 6

- "The Lick AGN Monitoring Project: Recalibrating Single-epoch Virial Black Hole Mass Estimates",
  Daeseong Park, Jong-Hak Woo, Tommaso Treu, Aaron J. Barth, Misty C. Bentz, Vardha N. Bennert, Gabriela Canalizo, Alexei V. Filippenko, Elinor Gates, Jenny E. Greene, Matthew A. Malkan, Jonelle Walsh,
  2012, ApJ, 747, 30